Linking the local and global flow fields around a fish-like robot

Ferns, Jennifer

Award date:
2015

Awarding institution:
University of Bath

Linking the local and global flow fields around a fish-like robot

Jennifer Catherine Ferns

A thesis submitted for the degree of Doctor of Philosophy

University of Bath
Department of Mechanical Engineering

August 2014

Acknowledgements

I would like to thank my supervisors, Dr. Carley, Dr. Megill and Dr. Chambers for the help that they gave me throughout my time working on my PhD. I would also like to thank the FILOSE project, and my colleagues within the project, for the funding to complete my PhD and for the help they gave me in my time at Bath.

To my friends Laura and Yvonne, thank you for help keeping me sane with the exercising, coffees and cut-short meals! To my manager Graham, thank you for the invaluable insight to the writing-up of my thesis.

To all of my family - thank you for all of your love and support. Vicki and James, thank you particularly for the encouragement and experience you shared with me; and to Mum and Dad I cannot repay your support, love and unfaltering belief in me, so all I can say is thank you.

Finally, to my husband Calvin. I am not sure there are the words to say thank you enough. For your support throughout everything, for your belief in me when I struggled to believe in myself and for your never-ending love, I will be forever grateful.

And to end, I will quote Douglas Adams:

So long, and thanks for all the fish.

Contents

List of Figures

Abstract

Underwater exploration is an important area of research, whether to expand our knowledge base of underwater environments, or to monitor and preserve structures both natural and man-made. Biomimetic fish-like robots are being developed to incorporate some of the aspects of live fish in the hope that more efficient machines can be produced by exploiting the energy available within flow phenomena such as vortices. However, in order for a fully autonomous robot to be able to swim in natural environments, a navigational strategy is needed that distinguishes between steady and unsteady flows. To develop an effective strategy, the link between the local flow fields measured by sensors on the robot and the global flow phenomena needs to be determined.

Therefore, the objective of this study was to link the local and global flow fields around a fish-like robot with an on-board pressure sensor array in both steady and unsteady flows. Two hypotheses were put forward: that the signal from pressure sensors towards the front of a fusiform-shape robot could be used to detect the relative position of vortices; and that the changing aspects of the Kármán vortex street could be identified by changing aspects of the pressure signals detected.

These hypotheses were tested by placing the fish-like robot in steady flows and in Kármán vortex streets, both whilst held stationary and whilst moving. The global flow field was measured using DPIV and the local flow field was measured using the pressure sensor array on-board the robot.

The results showed characteristic patterns within the pressure signals when the robot was within the Kármán vortex street. By combining different characteristics of the pressure signals, detection of the Kármán vortex street was possible, with the relative position and characteristics of the vortices able to be determined.

It is hoped that the results of this study could be used within navigational strategies for fish-like robots in order that they can identify and successfully navigate unsteady flows such as the Kármán vortex street, with the potential for this to reduce the energy usage of the robot in these flows.

Chapter 1

Introduction

1.1 Underwater exploration

Underwater exploration has been ongoing for centuries. With approximately 70% of the Earth's surface covered in water and less than 5% of it explored, there are vast areas of aquatic landscapes still to be discovered. Although exploration and discovery of these as yet unmapped areas, and their associated unknown flora and fauna, are key motivations for underwater expeditions, there are many other reasons to continue to develop underwater technologies. These include; monitoring of natural structures and habitats, such as coral reefs, for damage, decay or new growth; monitoring of waterways for pollution levels; protection and conservation of vulnerable species and environments; searching missions, including search and rescue, for sunken vessels and ship wrecks, or archaeological sites and finds; maintenance of both natural habitats as part of conservation work and man-made structures, such as oil-rigs or sub-sea turbines; and even for defence, with naval submarines.

Some of these activities can be carried out by divers, where human interaction is key. However, many of them are carried out by either manned submersibles, such as the naval submarines, or by unmanned submersibles. These latter vehicles are much safer (for humans) and can be much smaller than manned vehicles. Unmanned vehicles are split into two main designs; ROVs, Remotely Operated Vehicles, which are often tethered to the launching vessel; and AUVs, Autonomous Unmanned Vehicles. ROVs provide the opportunity for careful operations to be carried out remotely and closely monitored. They are, currently, the more common of the two vehicle designs. AUVs are less common, as they need more on-board programming for their missions but they provide the potential for greater manoeuvrability as they are not attached to a tether. AUVs can, therefore, be used for a wide range of applications that may involve, for example, swimming through difficult terrain.

One of the more recent areas of research and design of AUVs are those that take inspiration from, and mimic, nature; biomimetic robots. There are a number of advantages to be

gained from mimicking nature; the aim of biomimetics for fish-like robots are to improve the efficiency of the vehicle, decrease the size of the AUV and, additionally, produce a wake from the AUV that could be more natural and, consequently, less disruptive to its surrounding environment. Ultimately, the use of biomimetics permits engineering to tap into millions of years of natural evolution to improve man-made objects. There is also a huge variety of creatures that can inspire AUVs; from jellyfish, which have inspired Aquajelly (built by Festo [8]) to rays which inspired the Subsea Glider with fin ray effect (built by Evo Logics [9]). Fish have been the most common aquatic animal for inspiration for AUVs; with over 30,000 known species of fish, there is a lot of variety to choose from. The biological inspiration often comes from four main areas; the physiology, body motions or motor outputs, global movements and sensing system of a fish. The shape is determined by the intended use of the robot; this will, in turn, dictate the type of body motions present and the global movements possible by the robot. The shape and motions of the robot will impact the flows sensed by sensing system. The sensing system is a key aspect for an autonomous robot as it is the link to the global environment that will feed into the navigational strategy determined for the robot.

1.2 Fish

Fish are extremely adaptable; they live in a large variety of environments within oceans, lakes and rivers. They interact with their environment through their senses which, in turn, will alter their behaviour within the flow regimes they encounter. As noted previously, there are four key areas in which inspiration can be gained from fish for use in underwater robots; its shape; its body motions; its sensing systems and its behaviours, or global movements, within its environment.

1.2.1 Shape

Fish have evolved into many different shapes and sizes depending on their specific environment; the majority of fish have a fusiform shape, which gives a streamline body for swimming into the flow. This is illustrated in Figure 1-1 where key areas of the fish that will be discussed are also noted.

1.2.2 Body motions

There are two main ways for fish to swim – either the Median and Paired Fin (MPF) gait, where the fish propels itself using only its appendicular fins, or the Body and Caudal Fin (BCF) gait where the fish uses its whole body. In general, the MPF gait is used by smaller fish that do not travel long distances. The BCF gait is common amongst a wider variety of fish; therefore, the BCF gait will be focussed on here. The BCF gait is the overall gait for many fish and is then split into five smaller modes [10] which are illustrated in Figure 1-2.

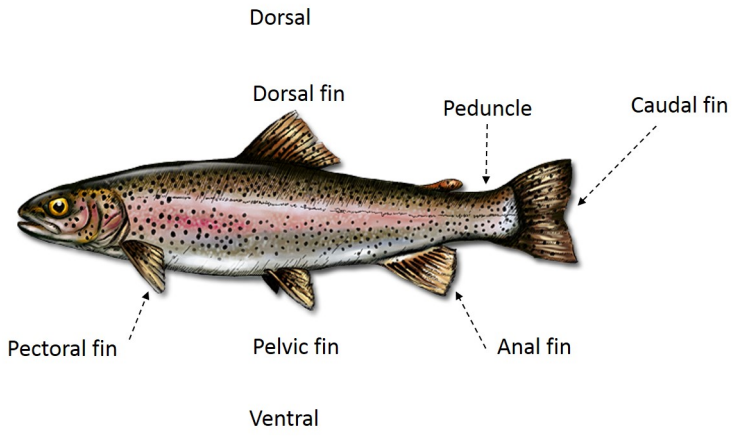

Figure 1-1: Rainbow trout, labelled with the main fin names. Image adapted from [1].

Anguilliform
Initially the anguilliform mode was described as the fish using the whole body to form the waveform, but recent data has shown that this is only true at high speeds or when accelerating [11]. Despite this, the anguilliform mode is still seen as the mode with the majority of the body involved in forming the waveform. An example of an anguilliform swimmer is the eel (*Anguilliformes*).

Subcarangiform In this mode, the posterior half to two thirds of the fish's body creates the waveform. This is considered a relatively more efficient mode than anguilliform. A rainbow trout (*Oncorynchus mykiss*) is classified as a subcarangiform swimmer.

Carangiform In this mode the rear of the body and tail (approximately one third) is used to form the waveform. Fish that swim in this mode, for example mackerel (*Scombrini*), generally have stiffer bodies and they travel at higher velocities than either the anguilliform or subcarangiform swimmers.

Thunniform These swimmers only use the caudal peduncle and fin as the propulsor; the name is taken from the most well known thunniform swimmer, the tuna (*Thunnus thynnus*).

Ostraciiform These swimmers, such as the electric rays (*Torpediniformes*), only use the caudal fin for propulsion.

All of these modes are periodic, with the first three motions taking the form of a sinusoidal bodywave passed in the rostro-caudal (head-to-tail) direction, with an increasing amplitude. As the fish's body moves forward with velocity U, the undulatory wave travels backwards with a velocity of $U - V_\lambda$. The velocity of the undulatory wave, V_λ , is always greater than that of the forward speed of the fish, U. The amplitude envelope of the waveform increases towards the tail; it shows the range of the caudal fin movement and is, therefore, directly related to the volume of water that is moved by the fish, meaning that it is related to the thrust produced as

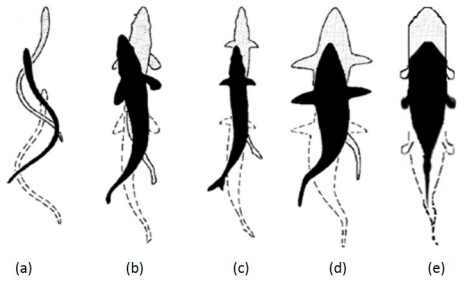

Figure 1-2: Swimming modes (a) Anguilliform (b) Subcarangiform (c) Carangiform (d) Thunniform and (e) Ostraciiform. Image adapted from [2] and [3].

well. For anguilliform swimmers the amplitude increase is not that large, but the carangiform and subcarangiform swimmers show a large increase in the amplitude of the caudal fin compared to further up the body.

As the undulatory wave is passed down the body of the fish, vortices are created along its side. These vortices grow in size and stay attached until they reach the tail. At this point they separate and the fish then 'pushes off' the vortex. The fish can stop the vortex or it can reverse the rotational direction [12]. It has been found that the body undulations and the tail beats both create vortices and in general the fish will shed two vortices per tailbeat at the point of maximum displacement of the tail. If the vortices created by the undulatory body movements and the tail merge then the circulation of the two vortices merge, thereby increasing the thrust produced by the fish. The majority of the energy shed into the wake is from the tailbeat as the energy from the body movements accounts for less than half of it [13, 14].

1.2.3 Sensing

Fish have highly developed senses; they have a very good sense of smell that helps them to find food, as well as having taste buds that are located not only in their mouths but can also be on the lips, on the skin covering the head and sometimes on the body fins. In addition, they have an elevated tactile sense, and most fish have sight, with diurnal fish often having colour vision. Fish can also hear and this sense is thought to be highly coupled with the final sensing system; the lateral line, together known as the acoustic-lateralis system. The lateral line system is of interest here as it allows the fish to sense the surrounding fluid flow.

Lateral line

The lateral line is made of neuromasts that can sense both velocity and pressure; the velocity sensors are surface neuromasts that stick out into the flow and move depending on the fluid velocity over them. The pressure sensors are neuromasts situated in canals, surrounded by fluid; these will then react to a pressure difference between pores in the skin. Empirical studies, as reviewed in [15], have found that the layout and morphology of the lateral line can be wildly

different over different species of fish; some fish have several thousand neuromasts covering their head, body and tail fin, whereas others may have fewer than fifty neuromasts along each side of their body [16]. Part of the reason for the differences of the layout would be the different environments that different species inhabit. A common layout of the lateral line over the head of fish such as the rainbow trout is shown in Figure 1-3; the lateral line canal continues down the length of the fish.

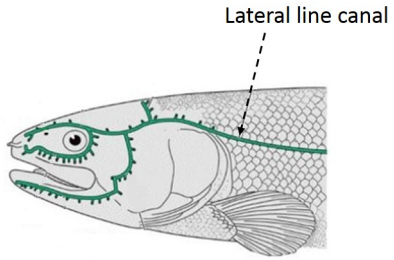

Figure 1-3: Illustration of the lateral line over the head of a fish similar to a rainbow trout. Image adapted from [4].

Each neuromast consists of dozens of individual hair cells, oriented in different directions, all surrounded by a cupula (Figure 1-4). As the cupula is bent by the flow the hair cells are also bent. Although the neuromast sends signals continuously, the hair cells are mechanoreceptors and have to reach a certain angle of bending before they transmit a signal. Each neuromast has directionality dependent on the orientation of the hair cells. This allows a fish to sense flow velocity and acceleration in different directions.

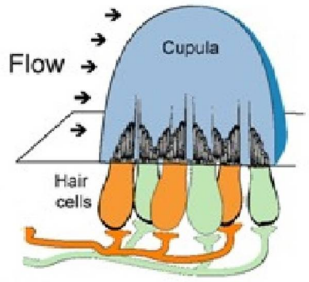

Figure 1-4: Neuromast of a fish. Image adapted from [5].

The lateral line has been well studied in more recent years, both empirically and theoretically. A theoretical study by McHenry et al [17] suggested that the sensitivity of a superficial neuromast is dependent on three main parameters; the hydrodynamics of the surrounding environment that acts as the stimulus to the neuromast; the boundary layer generated around the neuromast; and the fluid and structural dynamics of the cupula.

1.2.4 Global movements

The behaviour of fish is dependent on the fluid regimes present. Unsteady flows can either attract or repel fish; unsteady flows that are highly irregular, such as fully turbulent chaotic flows, are more likely to repel fish, whereas unsteady flow that has a level of regularity, such as the Kármán vortex street, will attract fish as they will be able to reduce their costs of locomotion by exploiting the turbulence. Fluid regimes and turbulence can affect the habitats chosen and the daily behavioural routine of fish. Fluid regimes can be caused by flow past objects in the flow or by other swimming fish. Schooling is an important behaviour and it is thought that the wakes behind swimming fish can be used by other fish to aid propulsion and efficiency [18]. It has also been found that fish change their swimming kinematics when swimming in a Kármán vortex street, the wake behind a shed cylinder (although it is also thought this pattern could emerge behind two fish swimming side by side), to match the fluid pattern [19,20]. It is not yet known whether the fish uses the low-speed 'street' between the two rows of vortices or whether it uses the vortices in a similar way to those that are self-generated.

These aspects of a fish were examined and some were reproduced on a robotic fish for this study. The swimming style and shape of a robot are interlinked; fish that swim in rivers and as such are more likely to encounter a variety of different flow regimes due to objects present that will obstruct the flow, are often carangiform or subcarangiform swimmers. By taking inspiration from these swimmers the shape of the robot was chosen to be a fusiform shape. The movement of the body of a fish is very complex due to its musculo-skeletal system, which comprises of a large number of muscles, tendons and bones. This was, therefore, not examined within this study. The lateral line sensing system of a fish can be broken down into pressure and velocity sensors present on the head and body of the fish; this is an aspect that can be mimicked on a robotic fish, giving it an artificial lateral line. For this study an array of pressure sensors was located in the head of the robot. Finally, the global movements of the fish were examined and mimicked to determine whether there could be a benefit, for example in terms of energy saving. Experiments examining these for both live fish and a fish-like robot are presented in Chapters 5 to 7.

1.3 Environment

A fish can be studied to provide inspiration for an underwater robot. However, a key parameter that must be examined is the environment in which the fish or robot is placed, as it is constantly interacting with its surroundings. Therefore, fluid characteristics and different flow regimes must be considered.

1.3.1 Fluid characteristics

A fluid is defined as a substance that will deform continuously when put under a net shear force [21]. A fluid flow can be considered to be either laminar or turbulent; if considering the

fully developed flow in a channel, laminar flow is smooth, with all the fluid particles travelling parallel to the channel walls. Turbulent flow is chaotic, where a fluid particle would follow an erratic path, although the average motion of the fluid is parallel to the channel walls. One of the key parameters used to help define whether a fluid is laminar or turbulent is the Reynolds number. This is a non-dimensional value, defined as the ratio of the inertial to viscous forces within the flow:

$$Re = \frac{\rho\, u\, l}{\mu} \tag{1.1}$$

where ρ is the density of the fluid; u is the velocity of the fluid; l is the characteristic length; and μ is the dynamic viscosity. For fluids such as water, at low Reynolds numbers (Re $\leq$ 2000), the flow is slow moving and laminar; as the speed increases the Reynolds number increases and the flow transitions from laminar to turbulent (Re $\geq$ 4000).

In addition to using the Reynolds number to demarcate the laminar and turbulent regimes, the turbulence intensity of a fluid may be calculated, to help characterise the flow. The turbulence intensity is calculated as the root-mean-squared value of the turbulent velocity fluctuations, u_{rms} $\mathrm{m\,s^{-1}}$, divided by the mean velocity value, U $\mathrm{m\,s^{-1}}$; $I \equiv \frac{u_{rms}}{U}$. This non-dimensional value can then be used to compare the levels of turbulence within a flow; in general if the turbulence intensity is less than 1% it is considered to be a low-turbulence case; if the value is calculated to be between 1 – 5 % then this is considered to have a medium level of turbulence, such as for low Reynolds number flows; and levels between 5 and 20% are considered high, likely to be found in complex geometries or for high Reynolds number flows.

A flow can also be defined in terms of uniformity and steadiness; these terms relate to the spatial and temporal variations of the flow at any given point and are detailed below.

- Uniform flow: where the flow velocity has the same magnitude and direction at every point in the fluid.
- Non-uniform flow: where the flow velocity is not the same at every point in the fluid.
- Steady flow: where the flow conditions of velocity and pressure may be different from point to point, but are constant with time.
- Unsteady flow: where the flow conditions of velocity and pressure may change from point to point and change with time.

Turbulent flow is time-varying and incoherent; however, the average of a turbulent flow is often considered as steady, or steady-in-the-mean, as it will not vary with time. To reduce the complexity of a problem, reference frames are often chosen to ensure that the flow with respect to them is steady; in this way, the majority of fluid flow problems can be analysed as steady-state cases. There are notable exceptions where the unsteady effects are particularly important; one of these exceptions is the flow past a circular cylinder, where the flow may be steady as it

approaches the cylinder, but is inherently unsteady in its wake. The flow behind a circular cylinder is described in greater detail in section 2.1.1.

The velocity of the fluid flow is a property that is often used to describe and define a flow, particularly when it is the key variable that changes between experiments. When this is the case, it is often the Reynolds number that is used to describe the flow. The governing equations for determining the velocity field are the Navier-Stokes equations. These equations were derived by applying mass conservation and Newton's Second Law to a fluid element, taking into account the velocity, pressure, temperature, density and viscosity of a fluid. Due to their non-linear nature at low Reynolds numbers, and the presence of turbulence at high Reynolds numbers, they are used primarily within Computational Fluid Dynamics (CFD) in a simplified form, the Reynolds-Averaged-Navier-Stokes (RANS) model, as the computational effort that is necessary to solve the standard equations is approximately of the order of Re^3. In many cases, simplifications are used to allow the Navier-Stokes equations to be solved; for example, when the flow can be considered incompressible or the fluid can be considered a Newtonian. Under these assumptions the following equations are obtained:

Continuity:

$$\nabla \cdot \mathbf{U} = 0 \tag{1.2}$$

Momentum:

$$\frac{\delta \mathbf{U}}{\delta t} + \mathbf{U} \cdot \nabla \mathbf{U} = -\frac{1}{\rho} \nabla P + \nu \nabla^2 \mathbf{U} \tag{1.3}$$

where $\mathbf{U}$ is the velocity vector; ν is the kinematic viscosity of the fluid; and P is the static pressure.

In addition to using the velocity itself to define flows, derivatives of the velocity can be used to give further information about the flow behaviour. One such property is the vorticity; this is defined as the curl of the velocity field:

$$\omega = \nabla \times \mathbf{U} \tag{1.4}$$

such that, in two dimensions,

$$\omega_x = \frac{\partial w}{\partial y} - \frac{\partial v}{\partial z}, \; \omega_y = \frac{\partial u}{\partial z} - \frac{\partial w}{\partial x}, \tag{1.5}$$

where ω is the vorticity; $\mathbf{U}$ is the velocity vector; u is the x-component of the velocity; v is the y-component of the velocity; and w is the z-component of the velocity.

The vorticity is "proportional to the rate of rotation of a small fluid element about its own axis" [22]. Therefore, it is not an indication of discrete vortices being present in the flow, but

is an indication of the type of fluid behaviour present, and gives the suggestion that vortices may be present. For two-dimensional flow the vorticity at a point is defined as "the ratio of the circulation round an infinitesimal circuit to the area of that circuit" [21]. This is discussed further in section 2.1.1.

Pressure is another defining flow property. Bernoulli derived an equation to describe the pressure of a flow, based on the application of Newton's second Law of Motion:

$$P + \frac{1}{2}\rho U^2 + \rho g z = constant \tag{1.6}$$

where P is the static pressure; g is the acceleration due to gravity; and z is the height of the fluid relative to a given datum. There were key assumptions made in the derivation;

- that the viscosity of the flow is negligible, i.e. the flow is frictionless;
- that the flow is steady; and
- that the flow is incompressible.

Although these assumptions only allow for the equation to be valid within limited scenarios, Bernoulli's equation can be used to give an initial insight into the possible flow behaviours present in a fluid. The terms given in equation 1.6 are known as the static pressure, dynamic pressure and the pressure head of a system respectively. From these it can be seen that the local static pressure will change with flow speed and with changing depth.

Given that the assumptions necessary for Bernoulli's equation were limiting, a more detailed expression was needed to calculate pressure in more complex situations. This expression is known as the pressure Poisson equation. It was derived from the solution to the Navier-Stokes equations; by taking the divergence of the momentum equation and using continuity, the pressure Poisson equation can be expressed as:

$$\nabla^2 P = -\rho \nabla \cdot (\mathbf{U} \cdot \nabla \mathbf{U}) \tag{1.7}$$

which is equivalent, in two dimensions, to

$$\nabla^2 P = -\rho \left\{ \left(\frac{\partial u}{\partial x} \right)^2 + 2 \left(\frac{\partial u}{\partial y} \frac{\partial v}{\partial x} \right) + \left(\frac{\partial v}{\partial y} \right)^2 \right\} \tag{1.8}$$

This equation is solved computationally, as with the Navier-Stokes equations, due to the complexity of the flow fields. It can give a much clearer picture of the behaviour of pressure in a flow field as it is not so limited by assumptions as Bernoulli's equation, and includes more complex fluid behaviours such as turbulence.

1.3.2 Vortices

Examining the flow characteristics, such as velocity and pressure, can help to define the flow. However, further flow behaviours can be determined when looking at the derivatives of the characteristics; this is shown in equations 1.4 and 1.5 where the vorticity within the flow has been calculated. The level of vorticity, as mentioned, gives a good indication of whether vortices could be present in a flow. Vortices are an important fluid behaviour to examine as they are discrete areas of turbulence that advect with the bulk flow and can cause local perturbations.

There are two fundamental types of vortices; free (irrotational) or forced (rotational) vortices. A free vortex has a tangential velocity that decreases hyperbolically with the radius of the vortex meaning the velocity is greatest in the centre of the vortex and gradually decreases with increasing radial distance. Conversely, a forced vortex has a tangential velocity that is proportional to the radius; that is, the velocity increases with increasing radial distance. Consequently, the static pressure within a free vortex is lowest at the centre and increases with increasing radial distance; the static pressure within a forced vortex decreases with increasing radial distance. In reality, a vortex is similar to a Rankine vortex, which has rotational flow at the core, and irrotational flow outside of this. In addition, in real flows the viscosity of the fluid causes vortices to dissipate and, therefore, progressively increase in size whilst the velocity and vorticity values decrease with time.

In addition to defining a vortex in terms of its size, its circulation, or strength, can also be calculated. This parameter gives a measure of the vorticity within a given area. The circulation, Γ, is the integral around a closed path of a component of velocity tangential to the path:

$$\Gamma = \oint q_s ds \tag{1.9}$$

where q_s is the component of velocity along the closed path.

It is convention that the anticlockwise direction is taken as positive and the clockwise direction as negative. As vorticity is the ratio of the circulation around a path to the area of that path, it is given that circulation, Γ, is equal to the vorticity within a path multiplied by the area enclosed by the path.

For a two-dimensional case, in which a circular element of fluid is considered, equation 1.10 can be derived, showing that the vorticity is twice the mean angular velocity at the centre of the circle:

$$\Gamma = \oint q_s ds = \oint \omega r^2 d\theta = 2\overline{\omega} r^2 \pi \tag{1.10}$$

where ω is the vorticity, $\overline{\omega}$ is the angular velocity and r is the radius of the circle.

Vortices can be produced in a fluid when it interacts with a body; a well-researched area of this is when a fluid flows around a bluff body, such as a cylinder. At very low Reynolds numbers, the flow is laminar and stays attached to the body, Figure 1-5 (a); as the Reynolds number increases, the fluid begins to separate at the back of the body Figure 1-5 (b), giving two stable areas of counter-rotating flow; once a critical Reynolds number is reached, vortices begin to form behind the bluff body and are shed in a periodic fashion from alternating sides of the body Figure 1-5 (c). This is known as the Kármán vortex street.

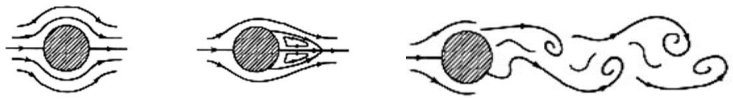

(a) (b) (c)

Figure 1-5: Images illustrating the different regimes of flow around a circular cylinder: (a) the laminar regime, with no separation; (b) separation from the cylinder, forming a separation bubble; (c) the Kármán vortex street. Adapted from [6].

1.3.3 Flow visualisation

There have been a wide variety of methods used to visualise fluid flows; techniques have included adding dyes to the flow [23], adding milk to the flow [24], illuminating aluminium flakes in the flow [25] and also using dilute solutions to provide a suitable flow visualisation environment, such as a dilute solution of the tobacco mosaic virus [26]. These techniques allowed the fluid behaviours to be visualised but only gave qualitative results; very few accurate, quantitative values could be calculated. As technology advanced, other techniques such as hot wire anemometry were developed to derive quantitative measurements from the flow [27–30]. Hot wire anemometry operates on the principle of convective heat transfer away from the hot wire; as the flow rate across the wire alters, the convective heat transfer coefficient varies which changes the heat transfer from the wire. The output of a hot-wire anemometry circuit will, in general, be a voltage, which will be calibrated to changes in flow rate. Although it has many advantages, such as good response at high frequencies, its main drawback is that it is an intrusive method of measuring the velocity field that can only measure a small area of flow. The intrusive nature of the equipment means that it disturbs the flow, which could have a knock-on effect for the results; with pointwise measurements, statistical data can be gained when a whole flow domain is mapped, but temporally synchronised information, which is necessary for understanding complex flows, is not available.

As technology developed, other methods were conceived to give non-intrusive measurements of flow fields; these had the advantages of not disturbing the flow during the measurement capture and, in addition, can allow a much larger flow area to be captured giving temporally synchronised information. These include, among many others, Laser Doppler Velocimetry, (LDV), Particle Tracking Velocimetry (PTV) and Particle Image Velocimetry (PIV). LDV uses the Doppler effect to determine particle velocity; by using monochromatic light and creating

an interference fringe pattern, the scattered light of particles in the flow can be compared to the incident light of the laser beam. The change in wavelength that is detected between the two light sources is a function of the particle's relative velocity. With PTV individual particles are tracked (using a camera) by size, within a flow field through successive images, to determine position, trajectory, and instantaneous velocity. Therefore, the images here are sparsely populated with particles. PIV uses much greater concentrations of particles, as small groups of particles are tracked (using a camera) between two quick-succession images to determine the flow velocity; this technique is described in more detail in Chapters 2 and 3. These three techniques capture two-dimensional information about the flow field i.e. in the plane of the laser sheet. They can also be extended to capture information in three dimensions. For PIV these include stereoscopic and scanning set-ups. Stereoscopic PIV uses two cameras focussed on the same point, but from different angles. The extra information provided by the second camera allows the movement within the third dimension to be calculated, giving a three-dimensional result. Scanning PIV takes images of a number of different planes within a volume in quick succession; the information from each of the planes can then processed to give a quasi-volumetric result as there is a slight time-lag between the capture of the different planes.

To produce a fully three-dimensional result, Holographic PIV (HPIV) can be used. This captures the position of all of the particles in the field-of-view onto a holographic plate. The light scattered from the particles is then made to interfere with a reference beam, and this information is recorded onto the holographic plate. The plate can then be developed and the particle images reconstructed to give velocity vectors in three dimensions. The three-dimensional techniques are extremely useful when investigating three-dimensional flow phenomena; however, when the flow field can be assumed to be two-dimensional, the standard techniques can give sufficient information to understand the flow behaviour; two-dimensional PIV is discussed in more detail in Chapter 3.

1.3.4 Pressure measurement

There are many different pressure measurement devices which include barometers, manometers and pressure transducers. Barometers are used to measure atmospheric pressure whereas manometers measure the pressure difference between a fluid and an outside source – often the atmosphere. In general these systems would be used to measure a gas pressure; for measuring the pressure underwater the main piece of equipment used is the pressure transducer. It is designed to measure the pressure difference between any two fluids. This makes it an ideal candidate for measuring the pressure at a point in a flow tunnel. The most common transducer used is the strain-gauge transducer, where strain gauges are placed on a diaphragm. When differential pressure is applied, the diaphragm is displaced so that the gauges record a strain. These strain gauges will, in general, be connected as Wheatstone bridges as this can give high accuracy in the measurements. The strain is then output directly as an electrical signal, which is often linearly proportional to the pressure applied so that a simple calibration can be applied

to output the pressure values. Consequently, by using a pressure transducer to measure the pressure of the flow, the total pressure at the wall can be quickly calculated.

All of these pressure measurement techniques are intrusive; a physical probe must be positioned in the fluid, which can change the fluid behaviour. When the fluid behaviour is also an important aspect of the investigation this can cause inaccuracies in the results. Therefore, a system to measure, or calculate, the pressure that is non-intrusive would be ideal for many situations. Initial work has been carried out to calculate pressure from DPIV, which would circumvent this issue; this is discussed in more detail in Chapter 2.

1.4 Thesis objectives

The underwater environment of a fish or a robot is the source of its interactions and sensor signals. Understanding the fluid characteristics and flow phenomena that occur in different flow regimes is an important part of understanding the fish, its shape, sensing systems and global movements. Inspiration can be taken from the fish to design a robot, but only with an understanding of the fluid flows that it will encounter and how these flows will be sensed by the on-board systems.

The aim of this work was to determine the correlation between the global fluid phenomena and the local pressure measurements taken from on-board a fish-like robot. Inspiration was taken from fish in terms of the shape, sensing system and global movements of the robot within the flow. The body motions of the fish were not examined here due to the complexity of the design necessary to mimic the fishes motions. Table 1.1 indicates the complexity of different machines in different environments, from stationary rigid robots to a highly complex autonomous flexible robot. The study presented in this thesis covers the first four topics (up to the dotted line) with the later topics of interest for future work.

The focus of the work is the fluid flows that the fish and robot interact with, how they are sensed using the on-board systems which gives the local measurements, and the global fluid phenomena to which the signals correlate. A fusiform shaped fish-like robot with an artificial lateral line, comprising of a pressure sensor array on the head of the robot, was placed within steady flows and Kármán vortex streets. The local and global flows were measured throughout the experiments so that the correlation between the two could be examined once the measurements had been processed. It is hoped that the results of this work will contribute to the knowledge used by roboticists in the design and implementation of robots, specifically for navigational strategies for autonomous machines. By linking local flow fields sensed on-board a robot to the global phenomena that occur within the flow, strategies to use artefacts such as vortices to increase swimming efficiency can be implemented. Additionally, the studies carried out with fish may contribute to the knowledge of the behaviours of fish within Kármán vortex streets.

Machine	Environment
Stationary rigid robot	Steady flow
Stationary rigid robot	Kármán vortex street
Moving rigid robot	Steady flow
Moving rigid robot	Kármán vortex street
Flexible robot	Steady flow
Flexible robot	Kármán vortex street
Autonomous flexible robot	Steady flow
Autonomous flexible robot	Kármán vortex street

Increasing complexity ↓

Table 1.1: Table indicating the increasing complexity of systems involving both a machine and its environment.

1.4.1 Hypotheses

There are a large number of characteristics of fish that can be looked to for inspiration for underwater robots, including their movements, their behaviours and their sensing systems.

A fish's movements within a Kármán vortex street are of interest, as it shows that there is the possibility of harvesting energy from the vortices present, reducing the energy usage of the robot. The Kármán vortex street has been extensively studied, and the effects behind a circular cylinder well defined. This is a useful phenomenon to use for unsteady flow experiments, as it is periodic and predictable. Therefore, changes in the generation of the vortex street due to changes in the environment around the cylinder can be more easily defined.

The lateral line system is also an area of growing interest for researchers; being able to create similar systems with simple sensors, or mimicking the sensors themselves, may allow for more sensing systems on board underwater robots, giving them more capabilities. A gap was found within the literature for sensing the Kármán vortex street with an artificial lateral line system; sensing vortices with a pressure sensor array on-board a vessel has not been covered extensively. Consequently, there has been very little work carried out that compares the velocity measured around a fish-like robot, in a global field, to the pressure measured at the robot body, in the local field. Some work by Bartol [31,32] and Windsor [33,34] has begun this, but it has focussed on the relevance to fish and has not specifically linked the two flows together.

This thesis links the global flows as measured by DPIV to the local flows measured using a pressure sensing array on-board a fish-like robot. A novel fusiform-shaped robot, with an embedded pressure sensing artificial lateral line, was placed in various different Kármán vortex streets (developed using different flow rates and different sized cylinders), both when held stationary and when moving to mimic the movements of a fish in a Kármán vortex street. Inspiration has been taken from fish in the shape of the robot, the type of sensing system that has been modelled on a lateral line system and the movements that a fish makes within a Kármán vortex street. Experiments showing the fish swimming within a Kármán vortex street will also be presented.

Two hypotheses are proposed to investigate this area:

1. That the pressure signal detected at, or near, the front of a fusiform shape can be used to determine the relative position of vortices to the fusiform shape.
   As vortices are discrete areas of rotational flow, it is assumed that they will have a specific effect on the pressure sensed by an on-board sensor. From literature [31], vortices present as a low pressure signal. By determining the position of a vortex relative to the front of the robot, a navigational strategy can be determined to allow the robot to intersect, avoid or otherwise interact with the vortices in a pre-determined way. However, the pressure signal that correlates with the Kármán vortex street must first be defined and understood.

2. That the properties of the pressure signal alter corresponding to changing properties of the vortices present in the flow.
   As the Kármán vortex street is changed, by varying the flow speed and the size of the cylinder, the vortex characteristics change. The aim of this hypothesis was to test whether this can also be determined through the pressure signal measured by the artificial lateral line.

These hypotheses were tested by placing the robot within various different Kármán vortex streets, in a number of different scenarios. These included stationary positions close to and far from the cylinder, and also at angles behind the cylinder. Additionally, moving experiments were undertaken, with a simplified global movement similar to that of the fish, to determine the pressure signal from the artificial lateral line. Across all of these experiments, DPIV captures were taken and synchronised with the pressure signal so that the global and local flow patterns could be linked.

It is hoped that this work will enable engineers and roboticists to better understand the link between the sensing of local flows on fusiform shapes when compared to the global flows around the body and, therefore, allow them to develop navigational strategies for underwater robots in unsteady flows. By being able to link a local signal to a global flow phenomenon, the robot behaviour can be pre-determined to ensure that the correct action can be taken in more complex flow situations. In addition, biologists may be able to link some of the results to the fishes' behaviour, to enable them to better understand the sensing system and behaviours of fishes.

1.5 Publications

Here follows a list of the publications to which the author has contributed (note, the author is J. Brown in these publications). The work contributed consisted of DPIV work within the flow tunnel and analysis work to determine the hydrodynamic events present in the flow, but does not include the specific results and analysis presented in this thesis. The two final items listed were presented as posters by the author at international conferences.

- R. Venturelli, O. Akanyeti, F. Visentin, J. Jeov, L. Chambers, G. Toming, J. Brown, M. Kruusmaa, W. Megill and P. Fiorini, *Hydrodynamic pressure sensing with an artificial lateral line in steady and unsteady flows*, Bioinspiration and Biomimetics, Vol. 7 (2012) [35].

- O. Akanyeti, L. Chambers, J. Jeov, J. Brown, R. Venturelli, M. Kruusmaa, W. Megill and P. Fiorini, *Self-motion effects on hydrodynamic pressure sensing; Part I. Forward-Backward Motion*, Bioinspiration and Biomimetics, Vol 8 (2013) [36].

- L. Chambers, O. Akanyeti, R. Venturelli, J. Jeov, J. Brown, M. Kruusmaa, P. Fiorini, W. Megill, *A fish perspective: detecting flow features while moving using an artificial lateral line in steady and unsteady flow*, Journal of the Royal Society Interface Vol 11 (2014) [37].

- J. Brown, L. Chambers, K. Collins, O. Akanyeti, F. Visentin, R. Ladd, P. Fiorini and W. Megill, *The Interaction Between Vortices and a Biomimetic Flexible Fin*, Towards Autonomous Robotic Systems – 12th Annual Conference, TAROS 2011, Proceedings. Vol. 6856. Heidelberg: Springer, pp. 418-419

- J. Brown, L. Chambers, W. Megill, *DPIV analysis to investigate turbulent fluid structure interactions*, Congress Flow Sensing in Air and Water, Bonn, Germany, July 17-21, 2011

1.6 Thesis structure

The thesis is structured into seven further chapters, the contents of which is as follows:

- Chapter 2 presents the literature review, focussing on: steady and unsteady fluid flows, particularly the Kármán vortex street, and how they can be measured; studies of fish and how they can provide inspiration for roboticists; and fish-like robots.

- The experimental methods used for the project are described in Chapter 3, detailing the set-ups and equipment used and how the data was captured, processed and analysed.

- Chapter 4 details the initial experiments carried out to characterise the flow tunnel used, for both steady flows and Kármán vortex streets.

- The experiments with fish, from which inspiration for the movement of the robot were taken, are described and the results presented in Chapter 5.

- The results of the experiments with the fish-like robot held stationary in steady and unsteady flows are given in Chapter 6.

- The results of the experiments with the fish-like robot whilst moving in steady and unsteady flows are presented in Chapter 7.

- The final chapter, Chapter 8, presents the conclusions of the work and suggests future work to be carried out.

Chapter 2

Literature Review

This chapter provides a review of the literature in relation to the underwater environment, fish within steady and unsteady flows and underwater fish-like robots.

2.1 Environment

Many of the characteristics of interest of the underwater environment used for this study were introduced in Chapter 1. Further detail is given here on the literature surrounding vortices, the Kármán vortex street and the means of measuring the pressure and velocity components within the flow.

2.1.1 Vortices and the Kármán vortex street

Examining the flow characteristics, such as velocity and pressure, can help to define the flow. However, further flow behaviours can be determined when looking at the derivatives of the characteristics; this was shown in equations 1.4 and 1.5 where the vorticity is calculated. The level of vorticity, as mentioned, gives a good indication of whether vortices could be present in a flow. Vortices are an important fluid behaviour to examine as they are discrete areas that advect with the bulk flow and can cause local perturbations in flow conditions.

Vortices

A vortex, in general, is considered to be a continuous area of rotating fluid, with the streamlines mapped in concentric circles. Although they are a well-known phenomenon, they have proven difficult to define. There are a number of different definitions used within the literature. The definition that fits best with the intuitive grasp that many have of what a vortex is was stated by Lugt in 1979, who defined a vortex as a collection of particles rotating around a common centre [38]. Chong et al defined a vortex as a region of strong vorticity [39] and Hunt et al defined a vortex as a region containing strong swirling zones with vorticity and low pressure [40].

Jeong and Hussain used a similar definition to Hunt et al, but refined it so that they only considered the vortical contributions to the local minima [41]. Cantwell and Coles [29] and Sung and Yoo [42] used the centroid of a region of vorticity to calculate the centre of a vortex. Kim et al [43] used a combination of previous definitions: they followed the method presented by Chong et al [39] to define the centre of the vortex during the early stages of vortex formation, and then once the vortex was shed from the cylinder, they used the the centroid of the region of vorticity to track the trajectory of the vortex.

These latter definitions have only specified a vortex core; therefore, a further definition is needed for the size of a vortex. This is addressed by Kim et al [43], Cantwell and Coles [29] and Sung and Yoo [42]. Kim et al and Sung and Yoo both used a limit of 50% of the maximum vorticity value to define the outer edge of their vortex; Cantwell and Coles used a value of 10% of the peak vorticity captured.

Kármán Vortex Street

The Kármán vortex street, illustrated in Figure 2-1, was first described by its namesake Theodore von Kármán in 1911 [44]; he presented a theoretical approach to the drag experienced by a body in a uniform flow. He reduced the effects to a two-dimensional problem and demonstrated that the only mathematically stable result was to have two lines of vortices, with opposing vortices placed at half-wavelength positions and with either line having vortices of opposite rotational direction. He stated that, for a stable street, the spacing ratio, h/a – that is the ratio of the distance between the rows to the distance between two vortices on the same row – needed to be 0.283 (Figure 2-1).

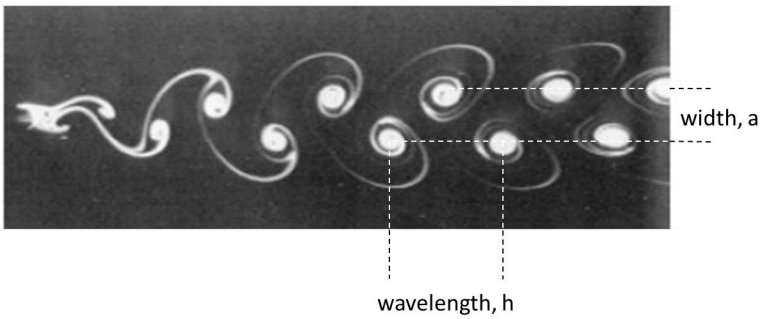

Figure 2-1: The Kármán vortex street, showing the width and wavelength characteristics. Adapted from [7].

Since this initial description of the Kármán vortex street in 1911 up to the present day there has been an extensive body of research carried out on the wakes behind bluff bodies. Studies, both experimental and numerical in nature, have been undertaken and published. Experimentally, these have ranged from studies of the trajectory of the vortices behind a circular cylinder by Walton [45] to studies using different shaped cylinders [46–54], multiple cylinders and cylinders near objects [55–61], rotating or oscillating cylinders [62–67] and onto the three-dimensional

behaviour of the flow behind bluff bodies [25, 68–70].

Numerically, many models have been developed to simulate the Kármán vortex street. Glauert investigated the effect of a finite channel width on the Kármán vortex street in 1928 [71]; the effects of viscosity were then included within the calculations by Hooker et al and Ponta et al [72, 73]. Others also described the evolution and breakdown of the vortex street in two-dimensions [74] and examined more complex situations such as the transition from steady to periodic fluid motion [75], or worked on calculations to determine the vorticity [76] or circulation [77] present in the flows. As the amount of experimental work continued to grow and present more information about the vortex street, the numerical simulations were used to look into other aspects of the flow, such as more complex shedding mechanisms than those initially described [78], or the inclusion of turbulence modelling within numerical simulations [79]. Other models have studied various different numerical methods, increasing the complexity of the models until they have been able to represent the three-dimensional effects in the wake [30, 80–91].

This vast range of research has allowed a much deeper level of understanding to be developed on the fluid behaviours behind bluff bodies. This was so much that case that in 1990 Zdravkovich wrote a paper [92], which he later expanded into a book [93], that defined a new terminology for the wake and shedding regimes of a circular cylinder. The flow past a circular cylinder was split into three transition states:

- the steady laminar wake;
- the transition-in-wake state; and
- the transition-in-boundary-layers state.

These three transition states were then split up again into different regimes; these regimes are dominated by the types of vortices that form, how they form and where they form in relation to the cylinder. This gave a much more extensive description of the wake behind a circular cylinder that could be used to further understand the behaviours, such as secondary wake formation [94], that were seen.

Throughout much of this work, various parameters were presented to describe and characterise the wake of a bluff body. Kármán had already defined the width, wavelength and spacing ratio [44]. As more research was carried out into the vortex shedding phenomenon, more parameters were used to describe the fluid flows observed. These parameters include the velocity distribution in the wake [68,95,96], vorticity distribution in the wake [67,68,76], trajectory of the vortices [67], convection speed of the vortices [67,97], vortex shedding frequency [50,55,98–100], vortex size [29,42,43,67], vortex shedding point or vortex formation point [101] and the strength or circulation of the vortices [62, 64, 66–68, 76, 96]. These characteristics are described more in Table 2.1.
Some of these characteristics can now be calculated using numerical models, but many can

Characteristic	Description
Width	The distance in the y-direction between two opposing vortices (Figure 2-1).
Wavelength	The distance in the x-direction between two vortices of the same rotational direction (Figure 2-1).
Spacing Ratio	The ratio of the width of the street to the wavelength of the street.
Vortex strength	The vortex strength is also known as the vortex circulation (described in Chapter 1).
Vortex size	The size of the vortex is dependent on the way that the vortex has been defined (Section 2.1.1). It is the area over which the vortex is seen.
Vortex shedding point	The point at which the vortices are shed from the attached cylinder wake and begin to travel downstream. This distance will change dependent on the size of the cylinder and speed of the flow.
Vortex shedding frequency	The frequency at which a pair of vortices (one of each rotation) are shed from the cylinder.
Average vortex convection speed	The speed at which the vortices travel downstream once they have been shed from the cylinder.

Table 2.1: Kármán vortex street characteristics.

still only be determined by experiments or predicted by empirical relationships. The vortex shedding frequency is one of these parameters; investigations showed that there was a strong relationship between the Strouhal number (a dimensionless number that is used to describe oscillating unsteady fluid flows, equation 2.1) and the Reynolds number (equation 1.1) at low Reynolds numbers, equation 2.2:

$$St = \frac{fd}{V} \tag{2.1}$$

$$St = 0.198\left(1 - \frac{19.7}{Re}\right) \tag{2.2}$$

where d is the diameter of the cylinder, V is the flow speed, and f is the frequency.

The Kármán vortex street is a useful experimental phenomenon as it is an unsteady, but periodic flow regime. It presents a more complex flow behaviour than steady, laminar flow, but one that can be well predicted compared to the chaotic nature of fully turbulent flow.

2.1.2 Sensing Flows

Whilst modelling can give a useful insight into flow behaviour, much of the current understanding comes from experiments and empirical relationships. Therefore, it is important to understand what is available and how the flows can be measured. The two main measurement systems focussed on here will be flow visualisation using DPIV and pressure.

Digital Particle Image Velocimetry

Digital particle image velocimetry (DPIV) is a non-intrusive, optical method of flow measurement; it is a flow visualisation technique that has been used to calculate the fluid velocities in a wide range of applications; flow around a cylinder [43,61,67,94,102]; boundary layer flows [103]; medical flows [104]; flow around animals in flight [105]; and flows around aquatic animals [106]. It was originally conceived using camera film, but the main advances came with digital CCD (Charge-Coupled Device) cameras and processing. The DPIV technique illuminates seeded particles within the flow field and captures two images of them in quick succession; these images are then processed to determine the distance the particle images have moved within the time-gap between the two images, which can then give the velocity of the flow distribution within a plane. The technique has been well detailed in Raffel et al [107], Adrian et al [108], Keane and Adrian [109] and Westerweel [110]. The main advantages of DPIV are: that it is non-intrusive, thereby allowing the user to measure velocities in areas where, for instance, a probe may directly affect the flow; that it can capture an image of a wide flow area; the data capture is efficient; and spatially synchronised data can be recorded. The main disadvantage of the technique is that it measures the fluid flow indirectly, as it measures the velocity of tracer particles added to the flow. Therefore, the equipment must be considered carefully to ensure that the best quality DPIV images possible are captured.

The main pieces of equipment necessary, and some of their associated considerations, are:

- a high speed, digital camera;
- a laser, with necessary lenses to create a thin sheet of light;
- image capturing and processing software; and
- neutrally buoyant particles.

A high speed camera is necessary to ensure that it can capture the images at a sufficient framerate. The time delay between the two quick-succession captures must be long enough that the particles are able to move between image captures, but short enough that there is minimal out-of-plane movement of the particles. The shutter speed of the camera also needs to be taken into account; the duration must be long enough to ensure sufficient light is captured to produce a clear image, but short enough to capture sharp image particles. If the shutter speed is too long, the particle images could blur, making it difficult to calculate the velocities. A laser is most often used in DPIV as the output is collimated and can easily be manipulated to give a thin light sheet with sufficient brightness to illuminate the in-plane particles. If the laser is pulsed, the same issues that could arise with the pulsed camera could occur, such as blurred particle images. Once images have been captured, software is needed to process them to derive the velocity data. Some packages will enable capture and processing through the same software; there are also some open-source DPIV codes available. An important consideration of the software, and more-so of the computer system, is the storage available for the images. This

will have a large impact on the temporal resolution of the data sets. The images are processed using cross-correlation algorithms; this is a mathematical construct that compares the particle images between the two quick-capture frames [110]. Initially, the images are subdivided into small areas called Interrogation Regions (IRs). Typical IRs for CCD cameras comprise of 16 $\times$ 16 or 32 $\times$ 32 pixels. The pattern of particle images in each IR from the first exposure of the image pair is taken and compared to the patterns found in the regions close to originating IR in the second exposure of the pair. Once a close match is found, the distance travelled by the group of particles within the interrogation region can be calculated, thereby giving the velocity of the fluid.

The particles chosen are particularly important; ideally they would be uniform in size and shape, highly reflective and have exactly the same density as the fluid. These properties will ensure that the light intensity is equal throughout the field-of-view and the particles will travel at the same velocity as the fluid. If not neutrally buoyant, they could be pulled out of the image plane due to gravitational forces.

Pressure measurement

As presented in Chapter 1, pressure measurements of flows consist of including intrusive instruments into the flow which can cause disruption to the flow field. However, recently work has begun to calculate the pressure from DPIV results which would allow for a non-intrusive method which can capture large areas of flow to be used for pressure calculation. There are three main methods in the literature: solving the pressure Poisson equation [111–114], solving the Navier-Stokes equations [115] or using a SIMPLER algorithm [116]. The SIMPLER (Semi-Implicit Method for Pressure Linked Equations – Revised) algorithm is an algorithm used in computational fluid dynamics (CFD) programs. It is a numerical, iterative procedure to solve the Navier-Stokes equations. The Navier-Stokes equations can be solved to get the pressure as the main coefficient in the equations. With this system the acceleration data also needs to be calculated for use in the equation.

The pressure Poisson equation is the most common method used to date. The right hand side of equation 1.7 can be calculated directly from the velocity vectors that are the results from the DPIV captures. Some of the literature available that uses the pressure Poisson equation to calculate the pressure from DPIV has used a stereo-DPIV set-up [112, 113], but others have shown that this is not necessary for the calculations [114].

The pressure Poisson equation, 1.7, has fewer assumptions than Bernoulli's equation, making it a more accurate calculation. To calculate the whole flow field using the pressure Poisson equation the pressure values at the boundaries must be known. This can be an issue if there are objects in the flow field, as current DPIV systems do not show solid boundaries, except as masks applied during the processing. This situation would, therefore, involve further com-

plexity to ensure that the boundary conditions are available. This is a situation that has been solved in [111] and [112], testing a circular cylinder and a NACA0018 aerofoil. The test with the aerofoil gave very close results to those that measured the pressure directly, but they were not identical.

All of the solutions found to calculate pressure from DPIV have their advantages and disadvantages. As there are relatively few studies published, it has yet to be determined which will prove to be the most accurate although all currently show that the solutions used do give fairly accurate results. Currently the pressure Poisson equation has been shown to be the most popular and this has also allowed for objects to be present in the flow field. However, calculating pressure from DPIV is still in the early stages of research, with the results close to, but not yet equal to, the measured values. Objects are more difficult to include and many, particularly complex geometries or moving objects, have not yet been tested.

2.2 Fish

Fish have been studied for many years so that we may gain a better understanding of their kinematics, locomotion, and sensing systems. As technologies are continually improving, more complex and detailed information can be captured, meaning better understanding can be derived, which in turn allows for improved biomimetic machines, especially in marine propulsion systems. In general, when looking for inspiration for underwater vehicles, the many different species of fish are investigated as they have evolved differently dependent on their environment. The rainbow trout (*Oncorynchus mykiss*) will be focused on here as it is a species that lives in streams, so will naturally come into contact with differing flow regimes.

2.2.1 Global movements

The way fish move has been well documented as in [11] and [2] which review the modes of swimming as described in Chapter 1. Much of the work that has been presented in the literature has focused on the gaits and movements in steady, laminar flow. This has allowed for descriptions and definitions of modes to be formed. Although steady flow is encountered by fish in their natural environment, there are also many instances where unsteady flow is encountered. Consequently, studies which include unsteady flow can reveal the natural diversity of the swimming abilities of fish. Some of these were completed by Liao et al [19, 20, 117, 118]; he investigated the movements of fish swimming in a Kármán vortex street and has defined the movements as a new gait as the fish voluntarily change their kinematics as they interact with the vortex street. He found that the fish slalomed between the vortices within the Kármán vortex street. Additionally, their tail-beat cycle changed to match the vortex shedding frequency and the amplitudes and curvature of their bodies increased when compared to the values for steady swimming in laminar flow. However, this was not considered as a passive movement as the wavelength of the fish body is longer than that of the wake and the trout did not match their

body wave speed to the speed of the oncoming vortices. This behaviour is interesting, as it was found that the fish decrease their muscle activity when they exploit vortices [20]. Therefore, there is the potential for fish-like robots to mimic this behaviour which may allow for energy extraction from the vortices.

2.2.2 Sensing

Empirical studies, as reviewed in [15], have found that the layout and morphology of the lateral line can be wildly different over different species of fish. There has also been evidence that the lateral line is used for prey detection [119], predator avoidance, schooling and entrainment, among others. It has also been found that fish can use the lateral line to detect vortices and, therefore, use the energy that is in vortices that are present in turbulent flows [20, 120, 121]. It has even been found that the neurological responses match the vortex shedding frequency of the Kármán vortex street when the fish has been introduced to that flow regime [122].

Some studies have tried to estimate and measure the pressure over a swimming fish; most notably Dubois [123], Lighthill [124] and McHenry et al [125]. Dubois measured the pressure over swimming bluefish using surgically inserted catheters and found gauge pressures (relative to atmosphere, at depth) up to 8826 Pa along the side of the swimming fish. Lighthill gives a mathematical solution to estimate the pressure differences over the head of a clupeid fish and puts forward the hypothesis of active drag reduction. McHenry et al found that, for the golden shiner (*Notemigonus crysoleucas*) the lateral line does not seem to be used for active drag reduction over the head. They concluded that the fish may use the lateral line sense to modulate the lateral amplitude of the body when swimming at low speeds, so as to allow the the fish to respond rapidly to any changes in the environmental flows. They nullified the hypothesis put forward by Lighthill.

Although it was found that the lateral line is not used for active drag reduction, it has been shown that it is used in a large variety of other situations. By sensing vortices, a fish can use the energy in the flow to aid in propulsion and efficiency. This would be a useful addition to robotic fish as it would increase the efficiency of the machine and could, therefore, allow greater usability than is currently available by, for example, increasing the operational range.

2.2.3 Fish in flows

A key area of research of a fish in a fluid has been to visualise the wake behind the fish. This was initially completed by using seeding particles or dye-tracers to qualitatively show the patterns created [13]. However, with DPIV technology now available the wakes can be visualised and quantified, allowing a much broader knowledge base to become available. Values such as momentum transfer from the fish to the fluid can be approximated from DPIV data, from the caudal fin and from the paired fins. Investigations into the wakes behind paired fins by Drucker and Lauder [126], found that the flow velocities throughout the wake structure were not uniform.

Stereo-DPIV studies have been able to show the shape of the vortices within the wake of a swimming fish as well as allowing further information on the wake in three dimensions. Sakakibara et al [127] found that both a side jet and a thrust jet were created in the vertical plane of the wake, with the height of both of these jets being of similar height to that of the tail fin. They also found that there were counter rotating vortices at the top and bottom of each of these jets. They made an estimate of the momentum and propulsive forces from the vortices in the wake of a swimming fish using techniques presented by Drucker and Lauder and their results were of the same order of magnitude [126].

Three-dimensional, or holographic, DPIV, which is a development of stereo-DPIV, enables a better understanding of the fluid structures developed behind a swimming fish. Nauen and Lauder [128] found strong oscillating jets in the wakes of swimming fish, with large lateral elements present. This concurs with the previous results found by two-dimensional DPIV, that there is a wake of linked vortex rings shed from the caudal fin of the fish.

In addition to studying the wakes of fishes, studies of the flow around fish have been carried out. Windsor et al [33,34] studied the flow around a blind Mexican cave fish in open water and when moving towards a wall whilst the fish was gliding through still water. Using DPIV and CFD they were able to couple the velocity measured and the pressure predicted around the fish so that they could determine the stimuli to the lateral line of the fish.

Aquatic animals are good sources of inspiration for those looking to create underwater vehicles. Having evolved to suit that environment, fish have developed movements and behaviours to allow them to fully exploit the opportunities around them to gain advantage such as reducing their energy usage. One aspect of this is their behaviour in the Kármán vortex street, termed by Liao the Kármán gait [19]. This new gait, and the slaloming movement between vortices, could be one way in which the design and movement strategy of autonomous robots could incorporate lessons learned from fish in order to reduce their energy usage. In addition to the movements and behaviours of the fish its physiology is also of interest, in particular its sensing system, the lateral line. This is a system that can detect both velocity and pressure within the fluid, allowing the fish to react to what is around it. If an artificial system with similar capabilities could be produced for a robotic fish, it could enable much greater flexibility and autonomy in an underwater environment.

2.3 Underwater fish-like robots

There are many different aspects that can be used as inspiration from a fish for developing underwater robots; they include its shape; its movements and behaviours; its musculature, which enables those movements; and its sensing systems. Various aspects have been taken and studied independently; some studies have looked to improve underwater robotic capabilities,

others have looked to better understand the systems of fish.

The characteristic movement of a fish, that of the oscillating wave along its body, has been simulated using flapping foils both experimentally and computationally [129–141]. These studies have mainly investigated the wakes behind the flapping foils in steady flow. To take this work further, others have developed flexible robots [142–151]. These studies have tried to emulate the body stiffness profile of the fish so that a wave-like movement can be produced, propelling the robot forward. Other studies have focused on the force, or thrust, that can be produced by using a fish-like motion [152–157]. Barrett et al [153] found that the power needed to propel a swimming model was considerably smaller than that needed to tow a model that was held straight and rigid. They also found that to reduce drag there must be an actively controlled transverse motion. These studies have all focussed on the body motions of the fish, not the global movements of the fish in flow.

Although many of these studies were carried out with the foil or fish-like robot in uniform flow, some studies have been carried out placing the foil or similar in a Kármán vortex street [36,132,136,149,158–161]. The majority of these papers have presented the phase angles and optimum positions for minimal energy usage to create maximum thrust. These have all, also, used fixed or constrained models centrally within the flow except for the experiments carried out by Akanyeti et al [36] (which the author is included), in which a simple fusiform-shaped robot was positioned laterally through and longitudinally up and down a Kármán vortex street to determine the sensing capabilities of a pressure sensing lateral line system.

In addition to investigating the motion of a fish, the sensing system has also been investigated and artificial lateral lines have been developed. Various different approaches have been taken to replicate the lateral line sensors; initially Yang et al [162] presented a proof-of-concept using a large number of small hot wire anemometers set in a straight line to sense the velocity of the flow and Peng and Zhou [163] developed a design that would very closely mimic that of the superficial neuromast of a fish. Further studies investigated using MEMS (Micro-Electro-Mechanical Systems) technology to develop velocity sensors [164, 165] and pressure sensors [166, 167], or even using optical sensors to detect water motions and subsequently calculate the pressure and velocity [161]. Additionally, studies using arrays of off-the-shelf sensors have also been carried out. These sensors have been tested in straight lines [161, 162], around cylinders [164], on torpedo-shaped bodies [166,167] or on a flat body with a streamlined upstream section [35,161]. These studies have shown that an artificial lateral line can be developed by mimicking the sensors, or neuromasts, found on fish. Additionally they have used off-the-shelf sensors to create an array and have shown that they can be used to successfully identify cylinder wakes [35,161], dipole sources [162, 164] or the size and shape of nearby objects [166, 167].

A key area of research relevant to this project has been that carried out by Bartol et al [31,32]. The research was focussed on the flow patterns around boxfishes as their mechanisms for pro-

ducing smooth swimming trajectories was unknown. They produced four models of boxfishes and studied them using DPIV, pressure distribution measurements and force balance measurements. They found that there was a strong correlation between areas of concentrated vorticity created along the bodies of the models to low pressure detected by the pressure tappings within the models [31]. These studies were, again, carried out in steady flow conditions.

Having examined the work carried out so far, it can be seen that the area of underwater robotics inspired by marine life is of growing interest. By examining the natural solutions that have evolved to best suit their specific environments, engineers may be able to develop more suitable, efficient means of exploring the marine world. The research into biomimetic fish-like robots is ongoing; a gap found in the literature surrounds the topic of exploring unsteady flows using a fusiform-shaped fish-like robot with an on-board sensing system. Two hypotheses were presented in Chapter 1, to explore this gap. Experiments were carried out to investigate the Kármán vortex street using a fish-like robot, both stationary and when moving through the flow; these are presented in the following chapters.

Chapter 3

Experimental Methods

This chapter details the equipment and the set-ups used and the experiments carried out for this research. The chapter has been divided into five main sections; the first section describes the experiments completed over the course of the research; the second section describes the environmental set up used for the experiments; the third section describes the flow visualisation technique and equipment used; the fourth section details the static and dynamic objects that were present in the flow; and the fifth details the data analysis techniques used.

3.1 Experiments

To answer the questions posed by the hypotheses stated in Section 1.4.1, the experiments carried out for this research investigated the link between the global and local flow behaviours around a fish-like robot in Kármán vortex streets. The global (velocity) flow field was measured using DPIV and the local (pressure) flow field was measured using an on-board pressure sensor array. These systems were correlated by an LED so that the two experimental measurements could be temporally synchronised. This is described in more detail in the following sections.

There were three key stages of experimentation; the characterisation of the fluid environment for both the background flow and the Kármán vortex streets (Chapter 4); experiments with fish to understand of the movements that a fish made in steady flow compared to in a Kármán vortex street (Chapter 5); and then experiments using a fish-like robot, both held stationary and moved within the flow tunnel, when in steady flow and in Kármán vortex streets (Chapters 6 and 7). These experiments, respectively, give the background flow within the flow tunnel used for the later experiments, look at how fish move within the environment present and use the knowledge gained to move the robot in a similar manner. The final experiments with the robot take a step-by-step approach, increasing the complexity of the system, to determine whether the pressure signal on-board a fish-like robot could detect the presence of a vortex and its characteristics and position relative to the robot.

3.2 Environmental set up

All of the experiments were carried out in a custom-made flow tunnel, Figure 3-1 [1]. It had a working section with maximum dimensions of 40 × 40 × 100cm and overall dimensions of 120 × 240 × 40cm, meaning it could hold approximately 1000 litres of water. It was made out of 6mm clear Perspex to allow for flow visualisation, with the base edges reinforced with steel angle bar and the lid edge reinforced with 2.5cm perspex beading. Two curves of 2mm perspex were fixed into each end of the flow tunnel to create a continuous-width circuit as a water path. The propeller (F18 Kangle 12V electric trolling motor, Cixi Kangle Sports Tackle Co., Ltd.) was positioned towards the back right of the flow tunnel which provided the maximum possible distance to dissipate the turbulence introduced before the flow had to travel around the curve of the tank and enter the working section. The propeller was able to produce up to about 30cm s^{-1} of flow speed around the flow tunnel (see Chapter 4 for more details).

The continuous-width circuit design did not provide smooth, uniform flow; therefore, additions were made to the flow tunnel to produce a steadier flow. These additions included vanes of 1mm thick polypropylene set in the left-hand curve, upstream of the working section, to support flow turning. Flow straighteners of 5cm thick aluminium honeycomb, of approximately 0.7cm cross-section, were also added to reduce the turbulence present in the flow. The flow straighteners also acted as end-points, or barriers, to the fish restricting access to the rest of the tank and thereby avoiding any harm from the propeller or the chiller pumps.

Various different configurations of vanes and flow straighteners were tested using simple flow visualisation; the flow was seeded with particles and a projector light used to visualise the general flow patterns present. Once any differences that occurred due to the change in set up were not discernible by eye, DPIV was used to determine the most uniform flow field that could be achieved. The final set-up of the flow tunnel (Figure 3-1) had the addition of: two sets of three vanes, set at equal distances apart (10cm) across the flow tunnel to support flow turning; and three flow straighteners, two upstream and one downstream of the working section. The two inward-facing surfaces of the flow straighteners flanking the working section were covered with a thin, coarse netting to prevent injury to the fish if they were to swim into them or rest against them. This gave the working section dimensions of 36 × 40 × 93cm. Full results for the flow characterisation of the flow tunnel are presented in Chapter 4.

Due to its use as an experimental platform for fish, the temperature of the water in the flow tunnel was kept to 15°C ± 1°C. This allowed the fish to be moved directly from their home tank into the flow tunnel, without a dramatic change in environment, which can cause them undue stress. For this same reason an air-line was continuously operating to ensure an oxygen-rich environment. Due to the air-line and the pump used to feed the water through the chiller system,

[1] Flow tunnel was designed and built by Nathan Sell (third-year undergraduate engineering student), Dr. Lily Chambers (post-doctoral researcher) and Steve Dolan (Ocean Technologies Laboratory Technician).

more turbulence was introduced into the system. The pump output was positioned directly next to the propeller, which was at the farthest point from the working section, and the air-line sat at the back of the working section so any bubbles that occurred had dissipated before reaching the working section. Therefore, the effects of the added turbulence were mitigated as much as possible, while maintaining a healthy environment for the live fish.

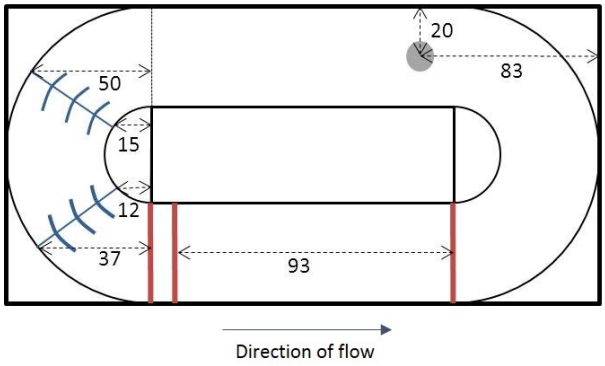

Figure 3-1: The flow tunnel final set-up showing the flow straighteners (in red) and the dimension of the working section between them. The two upstream flow straighteners were used to provide as uniform a flow as possible within the working section. The downstream flow straightener acted as an end barrier to the working section. The grey circle at the back indicates the position of the propeller used. The blue sections on the left show the positions of the vanes used to direct the flow. All dimensions given in cm.

3.3 Flow visualisation

The flow visualisation was carried out using a two-dimensional DPIV system; the following section details the equipment and configurations used for the experiments.

3.3.1 Equipment

The DPIV equipment used was:

- An excel laser (Laser Quantum, UK).
  This is a DPSS (diode-pumped solid state), continuous wave green-light laser (wavelength 532 nm), with a high power of 2W and variable control so that the output power is controlled by the user.

- A PCO 1200hs camera (PCO, Germany).
  This is a high speed, CCD (charge-coupled device) camera, with a maximum aquisition rate of 636 fps (frames per second) and a resolution of 1280 x 1024 pixels.

- A laser pulse synchroniser, model 610035 (TSI Inc. (USA)).
  The synchroniser enabled the camera to capture two images in quick succession.

- Insight 3G software (TSI Inc. (USA)) for capturing and processing the DPIV images.
- Vestosint 1301 particles (Evonik Industries, Germany)
  These were used as the reflective particles for the fluid visualisation. They are a 'fluidised bed coating power based on polyamide 12' [168], with a mean diameter of 100µm and a density of $1.06\,\mathrm{g\,cm^{-3}}$. These particles were recommended by TSI, who supplied the DPIV equipment.
- A front-silvered mirror, set at a 45 degree angle below the working section of the flow tunnel. It was important to use a front-silvered mirror so that no 'shadow' images were captured. Shadow images are caused by a second reflection occuring on the glass that often cover the silver mirror; these images can be captured on camera and can cause a 'shadow' to appear in the image. This can affect DPIV data as the shadow can obscure particle images and the true edge of any structures in the flow.

The main limitation of the DPIV equipment used was that it was a two-dimensional system; however, the Kármán vortex street can be considered to be a two-dimensional phenomenon as the vortices are produced along the full length of the cylinder. Therefore, sufficient information to test the proposed hypotheses can be captured with this system. Another limitation was the power of the laser sheet; the power of the laser was sufficient to illuminate a suitable camera field-of-view for the desired experiments, but with a stronger laser power, particle size can decrease (up to a point) and this can give more accurate results as the particles are better able to follow the flow. The particles used for this study were large and were not all of the same size or shape, which can cause errors to occur in the calculations due to light being reflected at angles away from the camera lens. However, the limitations of the equipment did not diminish the number of possible experiments and good results were still possible to obtain.

3.3.2 Set-up

This section describes the set-up of the necessary hardware, in terms of positioning with respect to other pieces of DPIV equipment and the flow tunnel. Also detailed here will be the software set-up for capture and processing of the images.

Laser and lens setup

The laser outputs a beam of green light, but for use in DPIV a sheet of laser light must be produced to enable capture of the velocity field in a plane. To do this a set of lenses is used, placed in front of the laser. This set up can be seen in Figure 3-2. First there are three diverging lenses, with focal lengths of -20mm, -20mm and -15mm. These lenses cause the beam to be spread into a sheet. The fourth and final lens used is a focusing lens, of focal length 1000mm, which thins down the sheet so its thickness is 1 to 2mm. This is necessary as the camera captures the particle images within the laser sheet; if the sheet is thicker, the focus of the particle images is poorer, leading to poorer quality images. In addition, a thicker sheet

would dilute the strength of the beam in the illuminated area. The width of the sheet, for usable bright light, is of the order of 30cm.

Ideally the camera is focused at the focal point of the laser sheet, as this point gives the thinnest point of the laser sheet. This is important as it gives the lowest likelihood of out-of-focus particles to be imaged which cause errors in the data. In reality there has to be a compromise between having a sheet wide enough to fill a suitable field of view of the camera and focusing at the optimal point. Therefore, the camera is usually focussed within the laser sheet produced with a sufficient depth of field for the images required.

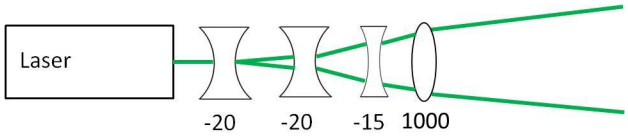

Figure 3-2: All focal lengths given in mm. This shows the laser-lens set-up, with three diverging lenses first to produce a wide sheet of laser light (of the order of approximately 30cm) and a focusing lens at the end to narrow the thickness of the sheet to 1 or 2mm.

The laser and lenses were attached to a heat sink, a safety measure to ensure that the laser did not overheat, which was then securely bolted on to a lab jack (Wolfram labs) to allow for easily adjustable height changes of the laser. This gave a flexibility to the set-up so that the laser sheet could be positioned in the centre of the water column, even if this changed due to a change in configuration. The lab jack was mounted securely to another heat sink, attached to the table, so that the lab jack could be moved to the left or right to allow various different areas of the flow tunnel to be imaged.

DPIV-to-flow-tunnel

To capture DPIV images, the equipment had to be set-up so that the laser sheet would illuminate a horizontal slice of the working section, with the camera pointing towards this area. Consequently, there were two positions in which the camera could be used:

- Directly under the flow tunnel, pointing upwards towards the light sheet (Figure 3-3 (a)). This configuration gave a much smaller field-of-view of the camera (approximately 10× 9cm) so it would have been very good for close-up work, but larger scale phenomena would have been harder to follow as there was only a small window for them to pass through.

- Under the laser, capturing the images through a front-silvered mirror set at 45° below the flow tunnel (Figure 3-3 (b)). This configuration gave a much larger field-of-view at approximately 30 × 28cm. This set up allowed full length objects to be seen in the flow and the larger, global fluid effects could be captured.

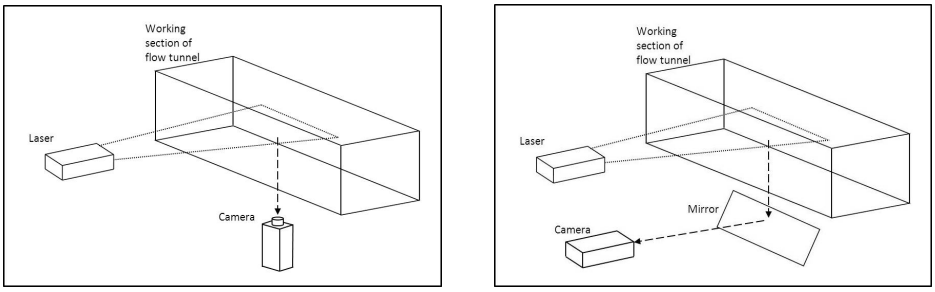

(a) (b)

Figure 3-3: Schematics of the set-up of the DPIV equipment around the flow tunnel. The laser is shown producing the horizontal light sheet that was used for experiments. (a) The camera is positioned directly below the flow tunnel, facing up towards the laser sheet. The field-of-view for this set-up is approximately 10 × 9cm. (b) A front-silvered mirror is positioned at 45° below the working section of the flow tunnel. The camera captures the image through the mirror. Although the image is of below the tank, the final image should be considered as though seen from above the flow tunnel. The field-of-view for this set-up is approximately 30 × 28cm.

Due to the large differences in field-of-view possible, a single set-up needed to be chosen to ensure continuity within the experiments. The main limitation of set-up (a) is the size of the field-of-view: the larger scale objects and flow phenomena could not be easily tracked; for set-up (b) it is that the flow very close to the body would not be captured in detail. A simple DPIV image was captured for each of the different field-of-views, with a cylinder as the main focal point of the image. By examining these captures, it was determined that the closest point to the body that could be imaged in set-up (a) was 1.65mm away; for set-up (b) the distance was 3.68mm. The closer field-of-view still did not allow the flow behaviours on the body to be captured; therefore, the main benefits of using a smaller field-of-view were annulled. In consequence, the larger field-of-view has been chosen for all of the experimentation. The larger flow behaviours can be captured and tracked, without significant loss of detail compared to a smaller field-of-view.

To allow for the synchronisation of the pressure and velocity measurements, an LED light was placed on the mirror so that it would be imaged by the camera during the DPIV capture. It showed obviously when lit, but was not visible when off.

3.3.3 Capturing the images

This section describes the set-up used within the Insight 3G software, to capture the DPIV images. To ensure that the best possible DPIV image is captured there are four different variables that must be set (Table 3.1); Delta T, Pulse rep rate, PIV exposure and laser pulse delay. The values chosen for these parameters were kept constant throughout all of the experiments.

Delta T

The time between the pair of images that are taken in quick succession. It was recom-

mended (TSI PIV Webinars) that this value should be set to allow the particle images to have moved a maximum distance of 25% of the interrogation region between the images. The value of Delta T used was the largest possible value, as it was constrained by the equipment, to allow the particle images to move, whilst still being able to capture a full-screen image. The range of flow speeds used for the experiments was small and so the movement of the particle images was approximately within range for all of the experiments.

Pulse Rep Rate

The frequency of the captures, or the number of image pairs captured in one second. Although this value was not limited, the number of image pairs that could be captured was limited by the space available on the camera and computer. Initially this was approximately 300 image pairs, but then more space was purchased so that approximately 700 image pairs could be captured. This value, therefore, had to be carefully selected so that it would give a good length of time to capture the fluid behaviour, but would also be quick enough to capture the detail in time as the flow is changing. The pulse rep rate was changed between experiments, largely due to the number of image pairs that could be captured. It will be noted in the specific experimental descriptions which value was used.

PIV exposure

The exposure time for each image. This was set to ensure that crisp particle images were produced, whilst capturing enough light so that the particle images were visible.

Laser pulse delay

The delay from when the capture is started to the first pulse. This parameter is much more important for a pulsed laser as it times the pulse to occur at the correct point of the capture for the camera. This value was set to that recommended by TSI when the equipment was first set up; as a continuous laser was used, changing this value made little difference to the images captured.

Laser pulse delay (µs)	400
Pulse rep rate (Hz)	50 or 100
Delta T (µs)	1700
PIV exposure (µs.)	1700

Table 3.1: Table of values for capturing DPIV images

3.3.4 Processing the images

Once the DPIV images had been captured they needed to be processed to calculate the velocity vectors. The processing software used in this study was Insight 3G software. Three steps were used to process the images in this study: pre-processing, processing and post-processing; these are detailed below.

Pre-processing

A background correction was necessary on the images, to delete spurious light effects that were inherent within the camera, thought to be due to differences in the sensitivity across the surface of the CCD chip. This was completed within the pre-processing stage. An image pair was captured with the lens cap on the camera, which was then subtracted from the DPIV image pairs in the pre-processing stages.

Processing

The velocity vectors were calculated in the processing stage. The images were processed using cross-correlation algorithms; this is a mathematical construct that compares the particle images between the two quick-capture frames. Initially, the images are subdivided into small areas called interrogation regions. The pattern of particle images in each interrogation region from the first exposure of the image pair is taken and compared to the patterns found in the regions close to originating interrogation region in the second exposure of the pair. Once the best close match is found, the distance travelled by the package of image particles within the interrogation region can be calculated, thereby giving the velocity of the fluid as the value of the time-step between the images is known. For good practice, the interrogation regions can be set up to follow a Nyquist grid, such that the interrogation regions overlap by 50% to ensure that no alias velocities are calculated, which would give incorrect results.

In each interrogation region the particle images are distributed randomly, given by equation 3.1.

$$\Gamma = \begin{bmatrix} X_1 \\ X_2 \\ \vdots \\ X_n \end{bmatrix} \qquad \text{where} \qquad X_i = \begin{pmatrix} X_i \\ Y_i \\ Z_i \end{pmatrix} \tag{3.1}$$

where X_i is the position of the particle in three-dimensional space and Γ describes the particle distribution at any time, t.

It is also assumed that the particle position and the particle image position are related by a magnification factor, M, that gives:

$$X_i = \frac{x_i}{M} \ , \ and \quad Y_i = \frac{y_i}{M} \tag{3.2}$$

where

$$x = \begin{pmatrix} x \\ y \end{pmatrix} \tag{3.3}$$

is the co-ordinate system of the image plane.

These mathematical expressions can then be used to determine the intensity of the image

particle and are used within the equation for cross-correlation. The intensity is used to determine whether a particle image is present, and in many software applications can be carried out to enhance the intensity of the particle images and, therefore, reduce the relative background noise. To calculate the intensity of the particle image, a Gaussian point spread function of the imaging lens, $\tau(x)$, is convolved with the particle image at any position x_i. As it is assumed that small particles and magnification factors are used, the Dirac delta function can be utilised. The image intensity field of the first exposure is given by (equation 3.8):

$$I(x, \Gamma) = \sum_{i=1}^{N} V_0(X_i)\tau(x - x_i) \tag{3.4}$$

where

$$\tau(x - x_i) = \tau(x) * \delta(x - x_i) \tag{3.5}$$

and $V_0(X_i)$ is the transfer function to convert the light energy of a particle image into an electronic signal.

Once the intensity and positions of the particle images have been determined, the cross-correlation can be carried out. It is assumed that all of the particle images within an interrogation region are displaced by the same amount. Within the time periods given between the captures in an image pair, and the relative distance moved compared to an interrogation region, this is a reasonable assumption. Recognised best practice is to have a time that allows the particle images to move $\approx 25\%$ of the width of the interrogation region [169].

The particle locations in the second exposure can be expressed as in equation 3.6, where $\mathbf{D}$ is the particle displacement, with the particle image displacement, $\mathbf{d}$, given as in equation 3.7:

$$X_i^* = \begin{pmatrix} X_i + D_x \\ Y_i + D_y \\ Z_i + D_z \end{pmatrix}, \tag{3.6}$$

$$\mathbf{d} = \begin{pmatrix} MD_x \\ MD_y \end{pmatrix}. \tag{3.7}$$

The image intensity of the second exposure is given in equation 3.8:

$$I^*(x, \Gamma) = \sum_{j=1}^{N} V_0^*(X_j + \mathbf{D})\tau(x - x_j - \mathbf{d}) \tag{3.8}$$

In the situation where $i = j$, that is where the first and second exposures are the same, the cross-correlation equation is as given in equation 3.9, where $\mathbf{s}$ is the separation vector in the correlation plane:

$$R_{II}(\mathbf{s},\Gamma,\mathbf{D}) = \frac{1}{a_1}\sum_{i,j} V_0(X_i)V_0(X_j+\mathbf{D})\int_{a_1}\tau(x-x_i)\tau(x-x_j+\mathbf{s}-\mathbf{d})dx \tag{3.9}$$

This equates to:

$$R_{II}(\mathbf{s},\Gamma,\mathbf{D}) = \sum_{i,j} V_0(X_i)V_0(X_j+\mathbf{D})R_\tau(x_i-x_j+\mathbf{s}-\mathbf{d}) \tag{3.10}$$

If the terms where $i \neq j$ are then examined, equation 3.11 can be determined. This has been decomposed into three expressions (equation 3.12):

$$R_{II}(\mathbf{s},\Gamma,\mathbf{D}) = \sum_{i,j} V_0(X_i)V_0(X_j+\mathbf{D})R_\tau(x_i-x_j+\mathbf{s}-\mathbf{d}) + R_\tau(\mathbf{s}-\mathbf{d})\sum_{i=1}^{N} V_0(X_i)V_0(X_i+\mathbf{D}) \tag{3.11}$$

$$R_{II}(\mathbf{s},\Gamma,\mathbf{D}) = R_C(\mathbf{s},\Gamma,\mathbf{D}) + R_F(\mathbf{s},\Gamma,\mathbf{D}) + R_D(\mathbf{s},\Gamma,\mathbf{D}) \tag{3.12}$$

R_c represents the mean intensities, R_F represents the fluctuating noise components and R_D represents the terms for which $i = j$ expressing the correlation of the image particles between exposures. The correlation peaks when $\mathbf{s} = \mathbf{d}$.

Once these calculations have been completed, the velocity vectors are output; the number of vectors output will depend on the number of interrogation regions chosen during the processing. If fewer interrogation regions are used, the processing is quicker; using more interrogation regions gives greater resolution. If objects are present in the flow field, masks can be used so that no vectors are calculated in these areas. These are described in the following section. Once output, the velocity vectors can be further processed and analysed to determine other characteristics of the flow field, such as vorticity and, more recently, pressure.

Here there were three main values to be set; the grid engine chosen was a recursive Nyquist grid, the correlation engine used was a Fast Fourier Transform (FFT) correlator and the peak engine was set to a be a Gaussian peak, Table 3.2.

Processing parameter	Description
Grid engine	The grid engine determines the type of grid that is used to split up the images for the cross correlation. Four different options are available: Nyquist grid, Recursive Nyquist grid, Rectangular grid or Deformation grid. A Nyquist grid uses a 50% overlap of interrogation regions to ensure no spurious vectors are created. This will give the fastest processing time. A recursive Nyquist grid uses the same overlap technique, but it uses two passes, one with a larger grid size the second with a smaller grid size (e.g. 64 × 64 down to 32 × 32 pixels). The processing time will increase with this setting, but the results are more accurate. The rectangular grid setting allows for more control of the recursive Nyquist grid, allowing for different overlap settings to be used, but also different shaped interrogation regions. The deformation grid uses multiple passes to calculate the velocity vectors and performs image deformation between each pass. This will give the greatest accuracy in the results, but increases the processing time significantly.
Correlation engine	The correlation engine determines which set of correlation equations should be used when calculating the velocity vectors. There are three different options in Insight 3G: The FFT correlation, the Hart correlation and the Direct correlations. The FFT correlation uses a Fast Fourier Transform (FFT) to calculate the correlation. This is the fastest option, but cannot be used if a rectangular interrogation region is defined. This correlates the whole image inside the interrogation region to find the point of 'best fit' to determine the velocity. The Hart correlation uses only the most significant pixels[2] to calculate a correlation. It is a version of the Direct correlation method, but reduces the processing time. The Direct correlation has the longest processing time associated with it. It carries out multiple tasks on the interrogation regions to give a high accuracy result.
Peak engine	The peak engine searches the correlation area for the peak location. Either a Gaussian peak or a Bilinear peak can be used. The Gaussian peak fits a Gaussian curve to the highest pixel and the four pixels nearest to it. It is the recommended peak engine for use with either the FFT or the Direct correlation engine. The Bilinear peak fits a set of linear functions to the highest pixel and the next four pixels nearest to it.

Table 3.2: Processing descriptions.

Post-processing

Post-processing was used to carry out checks on the calculated vectors to determine whether they are within a specified limit compared to those around them. During the processing step, large vectors can be calculated that are much greater than those around them; these are errors within the calculation, often due to an imperfect image. Therefore, two checks were carried

[2]Insight 3G User's Guide, pp 9-9.

out: global and local validations. The global and local validations check each vector against the rest of the field, to within a standard deviation of 3 and within a range of a 3×3 square of vectors around it respectively. These settings will define whether a vector seems correct in its value. If it is termed a 'bad', or incorrect, vector it is deleted and replaced by an interpolated vector; this is known as vector conditioning. The vector conditioning also checks the vector field for holes and fills these using interpolated vectors; these are calculated as the median value from a 3×3 surrounding neighbourhood. The interpolated vector count is kept under 5% of the total vector count, to ensure that the overall data sets were not skewed due to large numbers of interpolated data. It was decided that post-processing should be used so that for any visualisation, using Matlab or Tecplot, there were no erroneous vectors that masked the flow effects. As mathematical calculations would be carried out using the entire vector field, it was important to keep the interpolated vector count to a minimum.

Outside of these three steps, spatial calibration and masks were defined; these are described below.

Spatial calibration

A spatial calibration was necessary so that the output from the software could be given in terms of metres, rather than pixels. The spatial calibration was determined by taking a calibration image of a ruler held in the flow tunnel at the focal point of the camera. A line was drawn between two points along the image of the ruler, within the software, to define how far the distance was in millimetres. The pixel values were then converted to millimetre values for the velocity vectors.

Another important parameter to be set within the spatial calibration was the point of origin for the calculations; for all of the data processing, this point was set to the lower left-hand corner of the image so that any measurements taken from visualisation could be referenced to a suitable point.

Masks

Masks were used when there was an object present in the image. An object, whether static or moving, would obstruct the laser sheet. Therefore, there would be an area equal to the size of the object and its shadow within the image that would contain no particle images. This area could be masked off so that no vectors were calculated; this could save on processing time and also meant that the area of the object was obvious during image analysis. A mask could be created in one of two ways; by drawing a mask within the software on the image or by using threshold values of when a vector should be calculated.

Drawing a mask within the software was useful when a static object was present; an accurate representation of the object and its shadow could be created. However, if a moving object

was present, this process was extremely time consuming as a new mask would have to be drawn in every image captured.

For moving image captures, thresholding could be used instead. Two limiting values needed to be set; Minimum Average Intensity and Peak-to-Noise-Peak. The Minimum Average Intensity indicated whether there was a particle image at each pixel; the higher the value, the brighter the image such that a limit could be set as to what value constituted the presence of a particle image. The Peak-to-Noise-Peak value showed the measure of confidence in the chosen maximum peak. A high value indicated that there was a clear distinction between the peak found and the next peak, which was the noise peak, meaning there could be a high level of confidence that a particle image was present. A low peak-to-noise-peak value demonstrated that the highest peak and next highest peak values were similar; this could, therefore, indicate that there is no particle image present. Any vectors that fall outside of these limits would be deleted, thereby creating a mask within the image. However, the mask created cannot be pre-determined and if the correct values are not chosen then gaps may appear where vectors are needed, or vectors may be calculated over the object. Either of these outcomes can cause a large number of interpolated vectors to be created; in this case, new thresholds would need to be set and the processing repeated until less than 5% of the total vector count are interpolated vectors.

3.4 Static and dynamic objects

This section describes the different objects placed in the flow tunnel. There are two sets of objects used; firstly, cylinders are used to create Kármán vortex streets; secondly fish, including both live fish and fish-like robots, are used placed in the flow tunnel to interact with and sense the flow behaviours.

3.4.1 Cylinders

To create the Kármán vortex streets, three different solid Nylatron nylon cylinders were used of 25, 45 and 100mm diameters. They had a black finish so that they would not reflect the laser light during DPIV captures and were held securely in place during experiments using wedges between the cylinder and the flow tunnel. These sizes of cylinder were chosen as they gave a good range of vortex street sizes. Additionally, the larger sizes were chosen so that they would create Kármán vortex streets that the fish would respond to; Liao et al [19] found that a body length to cylinder diameter ratio (BL/D) of 2 would allow a fish to Kármán gait. Due to the width of the flow tunnel, and the largest field-of-view size available with the set-up, the largest cylinder size was restricted to 100mm.

3.4.2 Fish

Fish

Fish experiments were carried out in the flow tunnel. The fish used were female rainbow trout, from a South West England trout farm. The experiments were carried out when they were within the sizes of body-length BL 18±2cm. All experiments were carried out in accordance with the University of Bath animal care policy [170].

Robot fish

Experiments were also carried out with a fusiform robot with an ellipsoidal cross-section.[3] Figure 3-4 shows an exploded view of the robot model giving the important aspects as numbered items. The full robot length is 26.4cm, with an aspect ratio of 6.2:1:1.75.

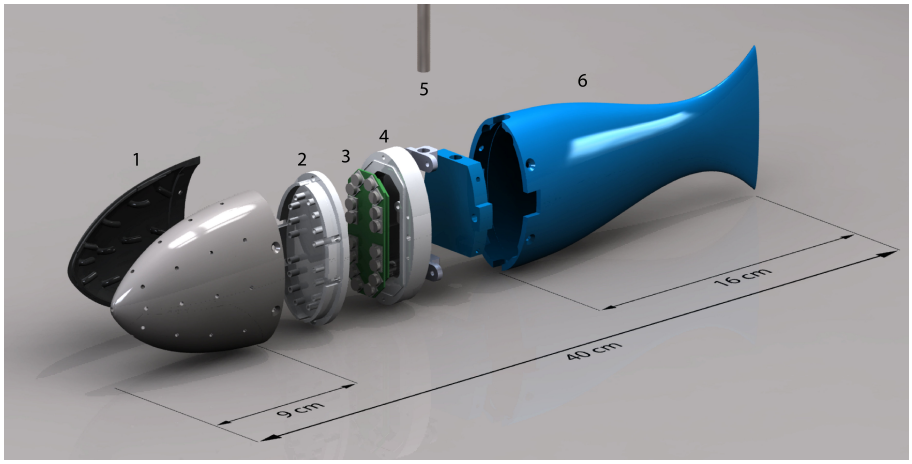

Figure 3-4: The robot fish used in the experiments. When fully assembled the robot was 26.4cm long. The robot was made up of; (1) a rigid head with tapped holes at 33 locations; (2) the connections from the sensors to silicone tubing that attached to the head; (3) the pressure sensors and associated electronics; (4) the connector to attach the head; the tail and the holding rod; (5) the rigid rod to connect the robot to apparatus above the tank; and (6) the tail.

The head was rigid, printed from polyamide powder and then coated with wood varnish and finished with a black spray paint. There were 33 possible pressure sensor locations on the head, all tapped into the head casing. These holes, of pore diameter 2mm, were attached to the pressure sensors housed in a watertight casing at the back of head using 2mm diameter flexible silicone tubing. For the experiments in this project, only nine pressure sensors were used, in the positions that gave a horizontal line directly along the head as this matched the plane of the laser light sheet and, therefore, the DPIV captures. The other possible pressure sensor locations were blocked off.

[3]The robot was designed and made by Jaas Ježov from Tallinn University of Technology.

The pressure sensors used were commercial pressure sensors, MS5401-AM (Measurement Specialities). They have a 0 to 1 bar (absolute) range scale and 240mV bar^{-1} sensitivity. The sensors were connected as Wheatstone bridges. High frequency noise was then filtered out of the differential signal from the sensor using a C filter. This filtered signal was amplified, with a gain of 13.67, using an instrumentation amplifier AD8226ARMZ (Analog Devices). A single-ended signal was produced which was passed through an RC filter with a time constant of 1ms. This signal was then digitised with a 16-bit accurate ADC (analogue-to-digital converter, ADS8332IBRGET, Texas Instruments). This digital signal was sent over SPI (Serial Peripheral Interface) to a microcontroller (MC, AT32UC3B1128-AUT, Atmel), where the data was oversampled 50 times and then forwarded to a PC, through RS-232 that sampled at 200Hz. The data received at the computer was 16-bit accurate and the least significant bit (LSB) value was approximately 2Pa, which equates to the data resolution value. In addition to the pressure data, the LED used for synchronisation was linked into the data capture, so that there was a log synchronised to the pressure data of when the LED was on or off.

The head casing was attached to the watertight box that housed the sensors and the associated acquiring electronics. At the back of the watertight casing was an attachment to fit a 6mm diameter rigid rod, to position the robot at the correct depth in the water column. The tail used was secured over the rod and attached to the back of the head; it was printed using gypsum powder and then coated using lacquer.

Figure 3-5 illustrates the positions of the sensors on a cross-section of the fish-like robot. They are numbered with sensor 1 in the left-most position and sensor 9 in the right-most position. The sensor pairs indicated are those used to calculate the difference in pressure across the head, which is used within the analysis.
A linear motor rig (BLM-142-B, Aerotech, with associated Soloist software) was positioned above the flow tunnel to allow a range of movement of the robot during experiments. The robot could either be held still and steady at a fixed point in the water column, or it could be moved in either the x (forward-backward) or y (lateral) directions within the flow tunnel.

3.5 Data analysis

Once the data had been captured and processed it had to be further analysed to provide the relevant results. For this project, this has been done using a number of different techniques. These are described here for both the DPIV data and pressure data.

3.5.1 DPIV data analysis

The DPIV data was captured and processed using Insight 3G. To analyse the data further, the vector files (the output from Insight 3G) were analysed in three ways; using Tecplot associated with Insight 3G, using a Matlab package associated with Insight 3G and using a custom-written

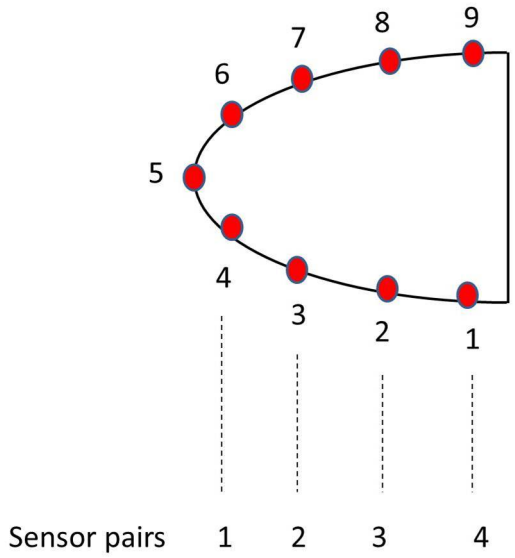

Figure 3-5: An illustration of the cross-section of the fish-like robot indicating the position of the pressure sensors and numbering them from 1 on the left-hand side of the head, to 5 positioned on the nose and 9 on the right-hand side of the head.

toolbox, based in Matlab. By using these three different software packages, the various different aspects of the flow field could be determined; the Tecplot software gave good visualisation of the data; from the Matlab package the velocity or vorticity of each of the vector points can be determined; and the custom-written toolbox gave much more detailed information from the vector field. These packages are described in more detail below.

Tecplot associated with Insight 3G

Included with the Insight 3G software was a link to Tecplot software; by loading up Tecplot through Insight 3G, an additional data loading script was executed so that the vector file output from Insight 3G could be loaded easily into Tecplot. The velocity vectors were then visualised as a two-dimensional plot. Parameters such as velocity in x and y and velocity magnitude; vorticity; and the velocity gradients could then be plotted. These could be displayed as line or flood contours, or as coloured arrows. In addition to these plots, stream lines could be added to the visualisation. Exporting the data was limited to images and videos; therefore, this software package was useful as a visualisation aid to determine which areas or frames should be investigated more closely, but often the specific values would be output from the Matlab package.

Matlab associated with Insight 3G

A custom Matlab package for Insight 3G, provided with the software, was able to read in the vector files and display them as vector arrows. Also, a number of different fluid flow parameters

could be calculated; x or y velocity, or velocity magnitude; vorticity; or the velocity gradients. These parameters could be exported as values or displayed as a flood contour or line contours overlaid on the vectors or as a graph and then exported. A useful aspect of the Matlab package was that a specific row, column, area or point could be selected to determine the parametric values. This gave a good level of control over the data extracted. In addition, the Matlab package could be used to gain knowledge of the time averaged values within the flow field by loading up multiple frames or an individual frame could be examined to determine the flow characteristics at a specific time step. This allowed a large variety of data analysis to be carried out with this package.

Custom-written toolbox

As an additional tool, a custom-written toolbox was developed, with close collaboration with a colleague, Francesco Visentin (University of Verona). This was developed as a toolbox to analyse the velocity vectors from Insight 3G, so that it could:

- calculate the vorticity field (among others) from the velocity field;
- identify and track vortices throughout a DPIV data set; and
- calculate for each vortex, in each frame, its position, size and circulation.

The toolbox identified a vortex as a circular area about a maximum point of vorticity to a value of 30 to 40% of the maximum. It would track the maximum vorticity point and create the circular area around it for each frame and subsequently calculate the size of the vortex and the circulation of the vortex dependent on the vorticity present within the circular area using the equations presented in Chapter 1. This definition of a vortex is in line with Cantwell and Coles [29] and Sung and Yoo [42]. A circular area was chosen for ease of modelling and calculation. The centroid of the area of circulation was taken to be the centre of the vortex for the position output from the toolbox:

$$x_c = \frac{1}{\Gamma}\int_A x\omega_z dA, \qquad y_c = \frac{1}{\Gamma}\int_A y\omega_z dA \tag{3.13}$$

Once the data had been processed with the toolbox, it could be further analysed to determine the parameters desired to characterise the Kármán vortex street, which were described in Chapter 2. This work was done by hand, using Microsoft Excel and Matlab.

3.5.2 Pressure data analysis

The raw pressure data from the sensors were in volts (V) and had to be calibrated to give a pressure (pascals, Pa). To do this, calibration experiments were carried out with each experimental set; they consisted of multiple runs of pressure capture at two different depths within the static water column. As the pressure at these points was known from hydrostatic variation, the output values from the sensors were calibrated to the correct pressure values. The experimental data sets were calibrated and then plotted against time to give the pressure signals

present over the time-window of the experiment. The pressure signals, once calibrated, were also processed to carry out a detailed frequency analysis using the fast fourier transform (FFT). The dominant frequency of each pressure sensor signal could then be determined, along with the magnitude of that frequency. This was done using the FFT code built-in to Matlab. The FFT processing was carried out on the pressure difference calculated between the sensor pairs illustrated in Figure 3-5 as this gave more consistent results than processing the individual sensor signals.

3.5.3 Synchronised DPIV and pressure

The DPIV data and pressure data were captured simultaneously and synchronised using an LED; this could be seen visually within the DPIV frames and was recorded together with the pressure data set as to whether it was turned on or off. The light was turned on within a couple of seconds from the start of the DPIV capture (as the longest capture only lasted for 7 seconds) and left on until the capture was over. Therefore, the frames could be processed to ensure the DPIV frames and the pressure signals were matched in time.

The data, once processed separately, were then examined together; this was carried out using the synchronised time-steps. The flow behaviour could then be linked between the DPIV data and the pressure signal.

3.6 Summary

This chapter has detailed the equipment used and the experiments carried out. The experiments use both DPIV and an on-board pressure sensor array to capture the flow behaviours in steady flow and in Kármán vortex streets. The measurements were correlated so that the frames could be synchronised between the two measurement systems.

The flow tunnel was designed and built in house, giving a working section of $36 \times 40 \times 93$cm. The flow path was altered using vanes and flow straighteners to produce the most uniform flow possible, although it was expected that variations across the tank and turbulence would be present. The flow characterisation of the flow tunnel is given in Chapter 4.

The DPIV equipment has been listed, and was initially set-up using guidance from TSI. Through exploratory use of the equipment and the software, the specific set-ups necessary for the experiments were determined. Variables such as camera field-of-view were taken into account when setting up the equipment, and it was determined that a larger field-of-view was necessary to capture the desired data and would not have significant limitations compared to the other possible field-of-views that could be used. The variables within the software were also tested and set to ensure that the best possible data was captured. The processing steps taken have also been described, using Insight 3G software (TSI INc, USA) to reduce spurious light effects

within the camera, calculate the velocity vectors and delete and replace any anomalous vectors.

Objects that were placed in the flow tunnel have also been described: three different sized cylinders to create a number of different Kármán vortex streets; and live and robotic fish that were placed in steady flows and the Kármán vortex streets. The live fish used were rainbow trout *Oncorhynchus mykiss* of body length BL = 18±2cm. The robotic fish was a fusiform shape with a pressure tapped head so that pressure signals on the body could be determined, whether it was held still at a specific location or moved in either the x or y directions within the flow tunnel. These experiments, combined with those using live fish which provided the inspiration for the specific experiments carried out, were used to determine a global–local link between the velocity vectors calculated using DPIV around the bodies with the pressure signals detected along the bodies. These experiments, and the results, are presented in Chapters 5 - 7.

The DPIV data analysis was carried out using three different methods; a custom-written toolbox in Matlab, a Matlab program associated with Insight 3G and a Tecplot program associated with Insight 3G. These software packages allowed a variety of parameters to be calculated and analysed so that both the steady flows and the Kármán vortex streets could be characterised effectively. Using these software packages the average velocity and vorticity in the x or y directions, or across an entire field-of-view and across the full capture range could be calculated; the flow could be easily visualised, as velocity magnitude or vorticity, so that the flow behaviours could be determined; and vortices could be defined and tracked so that the relevant parameters, such as width, wavelength, speed, size and strength, could be determined. The pressure data analysis was completed using Matlab and Microsoft Excel, to determine the pressure patterns and dominant frequencies.

Chapter 4

Flow Characterisation

This chapter describes the characterisation of the flow tunnel, for both steady flows and the Kármán vortex streets created. Details of the flow speeds achieved within the flow tunnel and the parameters used for characterisation are given.

4.1 Steady Flow

This section details the steady flow experiments that were carried out. It is important to understand the bulk flow behaviour within the working section; if the flow is very turbulent, or is highly non-uniform across the working section for example, this could create problems when more complex flow regimes are needed. Therefore, the flow tunnel has been characterised at various positions to give a detailed insight into the fluid behaviour.

Using the flow tunnel and DPIV equipment described in Chapter 3, the experiments were carried out with 600 images captured at 100Hz giving 6 seconds of data capture. An initial calibration had been carried out to determine the bulk flow speeds that resulted from different voltage inputs to the propeller. This was then used to determine the inputs necessary to reach the desired bulk flow speeds for the experiments; the more detailed steady flow experiments using DPIV gave a better indication of the bulk flow speeds reached for each voltage input that would be used throughout, in addition to providing information on the flow behaviour

To characterise the working section, nine different field-of-view positions were used; left, centre and right positions in the longitudinal (x) direction of the flow tunnel at each of three positions in the z (depth) direction of the flow tunnel; top, middle and bottom. The field-of-views used were able to capture the majority of the width of the flow tunnel; there was up to an 11cm gap between the edge of the field-of-view and the edge of the flow tunnel. These positions are illustrated in Figure 4-1, with the dimensions and locations further detailed in Table 4.1. The variation of flow speed within the working section of the tank in both the x and z directions could then be determined. Given that the single-camera DPIV set-up can only give results in

two dimensions, this set of experiments gave an indication to the three-dimensional behaviour within the flow tunnel.

		Left position	Centre position	Right position
Top Position				
FOV size ($x \times y$)	(cm)	29.6 x 23.7	28.9 x 23.1	29.8 x 23.8
Distance from the floor of the tank	(cm)	27	27	27
Distance from left edge of tank	(cm)	11	31	52
Distance from front edge of tank	(cm)	7	8	8
Middle Position				
FOV size ($x \times y$)	(cm)	28.4 x 22.8	30.5 x 24.4	28.1 x 22.5
Distance from the floor of the tank	(cm)	18	18	18
Distance from left edge of tank	(cm)	11	32	52
Distance from front edge of tank	(cm)	8	8	8.5
Bottom Position				
FOV size ($x \times y$)	(cm)	26.5 x 21.2	26.2 x 21.0	25.9 x 20.7
Distance from the floor of the tank	(cm)	9	9	9
Distance from left edge of tank	(cm)	12	31	51
Distance from front edge of tank	(cm)	6.5	8	9

Table 4.1: Positions of the field of views captured at the left, centre and right positions at each height used.

4.1.1 Steady flow results

There are three main aspects that have been considered within the flow characterisation:

- the flow speeds measured;
- the variation in flow speed in all three directions (x, y and z); and
- the turbulence intensity.

Flow speeds

The flow speeds achieved are given in Table 4.2. These values are averaged over 600 captures at all nine positions for each flow speed (i.e. a single tunnel bulk measurement), with errors of standard deviation given. The associated Reynolds numbers are also given.

Voltage input, V	4.8	6.8	8.8	10.8	12.8
Flow speed, cms^{-1}	9.92 ± 1.44	14.97 ± 2.12	19.65 ± 2.96	23.52 ± 3.58	26.09 ± 4.43
Reynolds number, $\times 10^3$	11.0 ± 1.6	16.7 ± 2.4	21.9 ± 3.3	26.2 ± 4.0	29.0 ± 4.9

Table 4.2: Velocity values, and their associated Reynolds numbers, for each of the different input voltages, given as an average value with error of standard deviation. The values are averaged over the matrix of the nine field-of-views used.

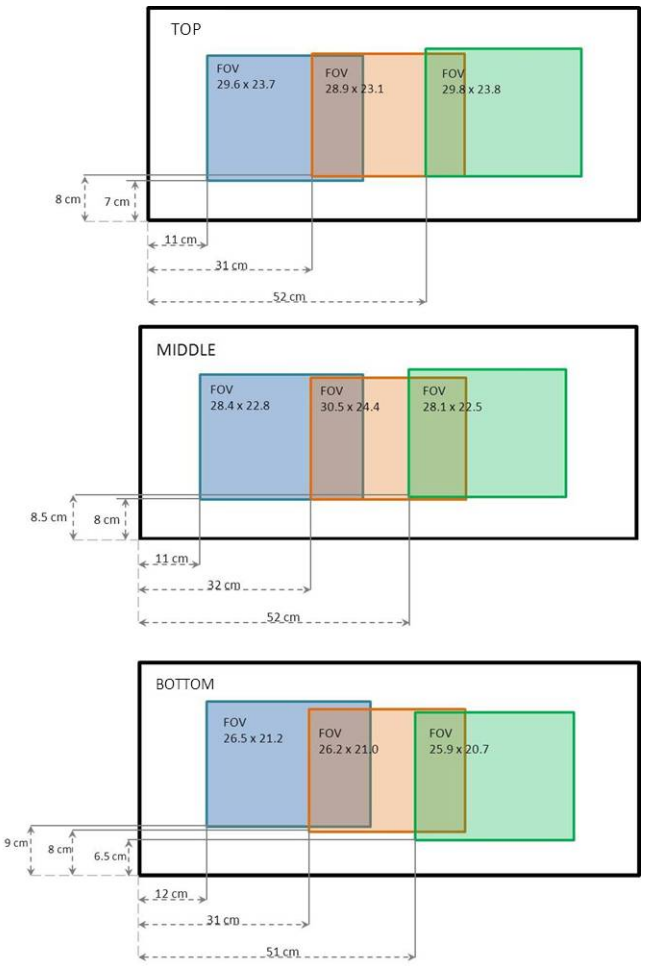

(a)

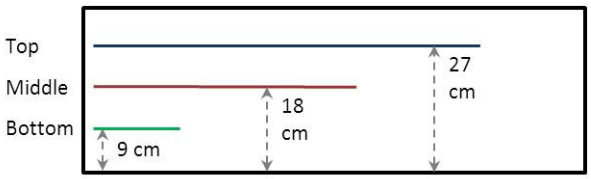

(b)

Figure 4-1: Positions of the field-of-views used to characterise the working section of the flow tunnel; flow travels from left to right. Image (a) shows the left, centre and right positions used for the three height levels: top, middle and bottom of the tank as though from above. Image (b) shows the height levels within the flow tunnel (top, middle and bottom), relative to the height of the water column, as though from the side.

Variation in flow speed

The variation in the flow speed can be seen in the graphs in Figure 4-2. These graphs are the averages over the experiments at Re = 21.9 $\times 10^3$ for (a) the left, centre and right captures and (b) the top, middle and bottom captures, but are indicative of the variation at all of the flow speeds. These graphs show that the pattern is of a stream of slower flow towards the back of the flow tunnel; then an area of increased speed at approximately the centre of the working section; and finally an area of reduced speed again. The pattern is very similar when looking along a single plane comparing the left, centre and right field-of-views (Figure 4-2 (a)); by the right-hand side of the working section, the area of high velocity has moved towards the back of the working section, but the values remain constant. When comparing the flow patterns between the top, middle and bottom field-of-view sets, the pattern is the same, but there is greater disparity between the values. The captures at the bottom of the tank present lower flow speeds that those captures taken at the top of the working section; therefore, care was taken in future experiments not to use the bottom of the flow tunnel during experiments. These variations are captured in the stated errors of the flow speeds.

The flow pattern seen within the flow tunnel is due mainly to the set-up of the flow tunnel; as noted in Chapter 3, the flow tunnel was configured such that the flow was driven by a propellor around a curved section and then through a flow straightener situated at the start of the working section. The propellor did not produce a steady speed across the width of the tunnel, but rather produced a jet of faster water that was then turned around the curve. This faster jet was split into sections by the vanes added around the curve; however, it could not be split to form a uniform cross-section of steady flow, shown by the variation in speed across the tank.

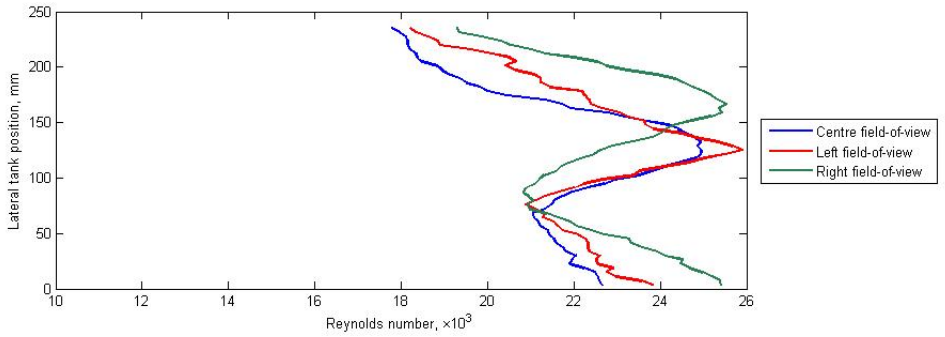

(a)

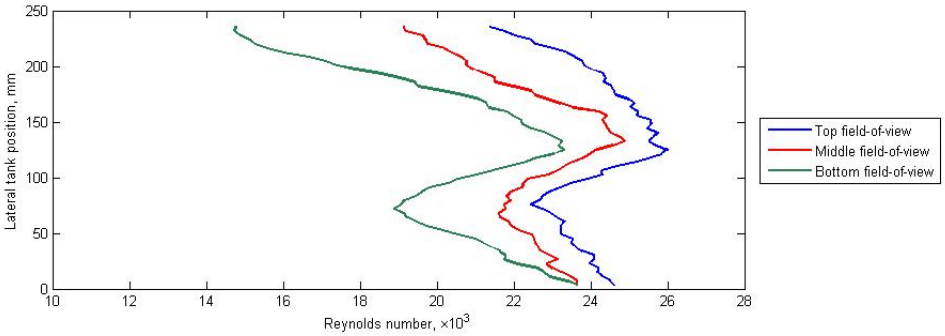

(b)

Figure 4-2: The variation in the flow speed measured at Re = 21.9 $\times 10^3$. (a) Velocity results for the left, centre and right field-of-view positions; values have been averaged over the top, middle and bottom captures. (b) Velocity results for the top, middle and bottom field-of-view positions; values have been averaged over the left, centre and right captures.

Turbulence intensity

The final aspect looked at was the turbulence intensity present at each flow speed. The turbulence intensity is calculated as the ratio of the standard deviation to the mean value of the velocity field. This calculation is carried out by the custom-written toolbox described in Chapter 3. The turbulence intensity values for each flow speed are given in Table 4.3 and are calculated as averages over each capture of 600 frames and then over the nine field-of-views used, with errors of standard deviation given. By examining the values in Table 4.3 it can be seen that the turbulence intensity stays relatively stable throughout the flow speeds, with the maximum value and maximum variation occurring at the highest flow speed.

Reynolds number $\times 10^3$	11.0	16.7	21.9	26.2	29.0
Turbulence Intensity %	12.5 $\pm$ 3.6	11.3 $\pm$ 3.3	12.5 $\pm$ 4.0	12.9 $\pm$ 3.9	14.6 $\pm$ 4.6

Table 4.3: Turbulence intensity for each flow speed, taken as an average value over each capture set and then over each different field-of-view. The errors given are the standard deviations.

4.1.2 Steady flow: summary

It can be seen from these results that the standard flow within the flow tunnel was steady and uniform; it did not vary with time throughout the captures taken. The standard deviations of the velocity for all the flow speeds is approximately 15%. It should be noted that the increase in flow speed is approximately linear for the first four speeds, but the final speed breaks this trend. At this flow speed the propeller used was working outside its specified working range, so increasing the flow speed was not an option. This is also the reason that the flow speed does not continue to increase linearly with increasing voltage inputs as it did for the lower voltages and flow speeds. There is variation within the tank in the y-direction remaining within 17% of the main flow speed value. The turbulence intensity for the flow tunnel is high for a free stream flow; however, this creates a realistic situation for the fish, both robotic and real, as turbulent flows are prevalent in nature.

4.2 Kármán vortex street

By introducing a bluff body to the flow tunnel, an alternating pattern of vortices was produced in its wake with an area of reduced speed between them; the Kármán vortex street [44]. The Kármán vortex street is a useful phenomenon for investigating fluid dynamics as it gives a regular, predictable pattern that incorporates areas of high rotation in the presence of vortices. This section details the experiments carried out to create Kármán vortex streets, and characterises the streets using various parameters.

Three different cylinder sizes were used to create the Kármán vortex streets; 25, 45 and 100mm diameters. They were set up in the flow tunnel with the centre of the cylinder 11.5cm downstream from the first collimator for the 25mm and 45mm cylinders and 27cm for the 100mm cylinder. The discrepancy here is due to the relative cylinder sizes; the largest cylinder had to be placed further downstream to allow for a large enough gap after the collimator before the water reached the cylinder, to ensure the flow remained as steady as possible.

The DPIV captures were taken in the centre of the water column (the middle position detailed in Section 4.1). The captures were 200 frames long, taken at 50Hz for the 25mm and 45mm diameter cylinders, giving 4 seconds of capture time, and 600 frames at 100Hz for the 100mm cylinder, giving 6 seconds of capture time (the frequency and number of frames was increased for the 100mm cylinder due to an upgrade of equipment). Two field-of-view positions were used for each of the Kármán vortex streets created; one that took in the cylinder and the near wake; and one that captured the wake further downstream (Figure 4-3).

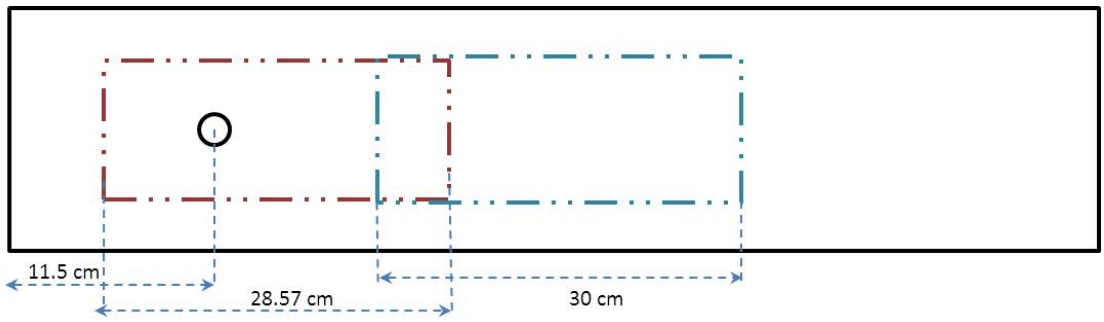

(a) 25mm cylinder

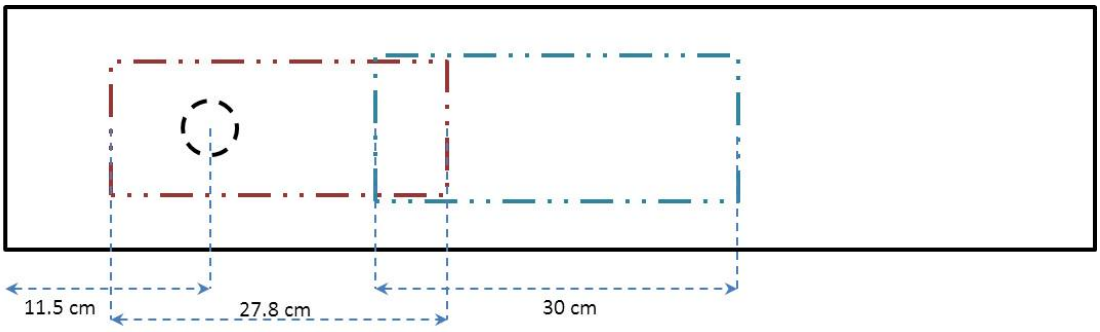

(b) 45mm cylinder

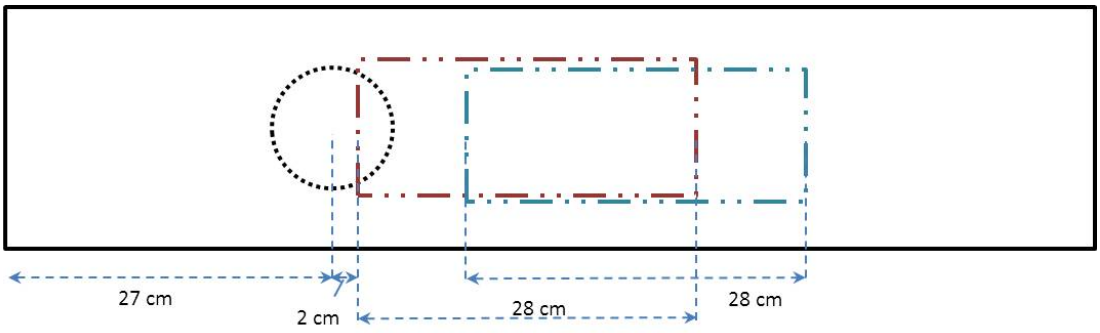

(c) 100mm cylinder

Figure 4-3: Field-of-view positioning used for each of the three different cylinder sizes used to create Kármán vortex streets. The discrepancy of positioning between the smaller cylinders, (a) and (b), and the largest cylinder (c) is due to the size of the cylinder relative to the size of the flow tunnel. The flow is travelling from left to right, with the origin taken to be the lower left corner.

The cylinders were tested at each of the five flow speeds detailed in Section 4.1. The results were then processed and analysed looking at the following characteristics of the Kármán vortex street;

- wake wavelength ($\frac{\lambda}{D}$);
- wake width ($\frac{w}{D}$);
- flow speed variation across the wake ($\frac{u}{U_\infty}$);
- vortex shedding frequency (f,Hz);
- the size of the vortices, given as a circle diameter ($\frac{d}{D}$); and
- the circulation, or strength, of the vortices ($\frac{\Gamma}{\pi U_\infty D}$, positive = anticlockwise direction).

These characteristics can be used to fully describe and compare the different Kármán vortex streets created in the flow tunnel; they are, barring the frequency, dimensionless numbers. The frequency can also be given using the dimensionless Strouhal number. They have been calculated using the custom-built toolbox and also by looking at the vector files in Matlab or Tecplot; these techniques were described in Chapter 3.

4.2.1 Kármán vortex street: results

Flow regime

The flow around a circular cylinder is split into different flow regimes depending on the Reynolds number of the flow; these are detailed by Zdravkovich [93]. The cylinder diameter is used as the characteristic length for the Reynolds number calculations here; the results are presented in Table 4.4 for the 25, 45 and 100mm diameter cylinders at 9.92, 19.65 and 26.09cm s^{-1}.

Freestream flow velocity, cm s^{-1}	9.92	19.65	26.09
25mm	2.2	4.3	5.6
45mm	3.9	7.7	10.2
100mm	8.6	17.0	22.6

Table 4.4: Reynolds numbers $\times 10^3$ for the flow around the 25, 45 and 100mm diameter cylinders at freestream flow velocities of 9.92, 19.65 and 26.09cm s^{-1}.

By comparing these values to those given by Zdravkovich [93] for the different flow regimes, it was found that the Kármán vortex streets produced span the intermediate subcritical shedding regime: $(1000 - 2000) < Re < (20,000 - 40,000)$. In this regime, the vortices are formed and shed closer to the cylinder than for regimes with lower or higher Reynolds numbers. It was found that the strength of the vortices decreases with increasing distance downstream of the cylinder and also with increasing Reynolds number. Additionally, the Strouhal number was found to stay constant, at approximately 0.2, across the range of Reynolds numbers within the regime. This showed that the frequency of the vortex shedding changed linearly with respect

to the free stream velocity. Figure 4-4 shows the vortices shed behind the three different cylinder sizes and the position at three cylinder diameters downstream. The vortices mature as they move away from the cylinder, until they are shed and begin to travel downstream in the characteristic pattern of the Kármán vortex street. It can be seen that by three cylinder diameters downstream, the vortices and the Kármán vortex street are well formed.

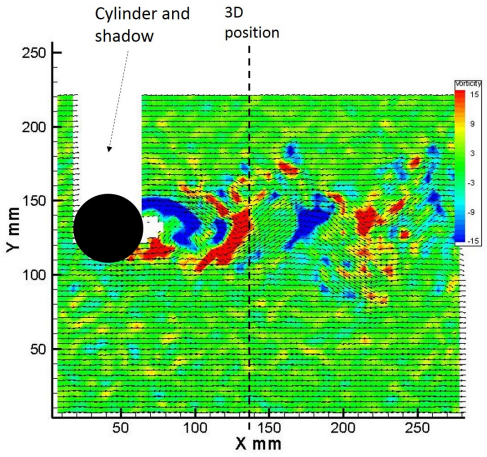

(a)

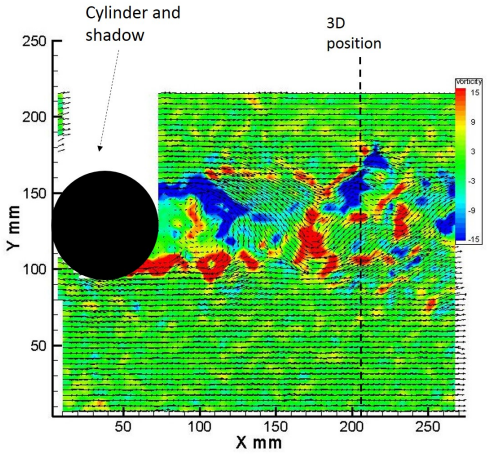

(b)

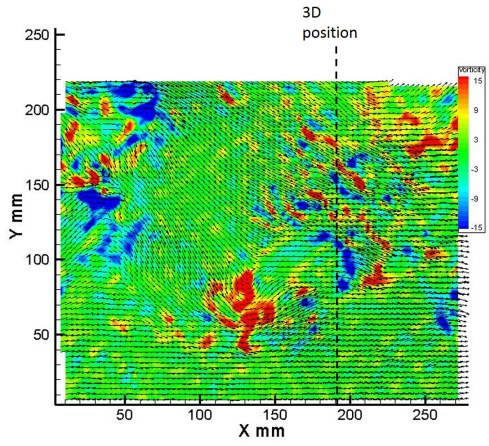

(c)

Figure 4-4: DPIV images of vorticity illustrating the position three cylinder diameters downstream of (a) 25mm, (b)45mm and (c)100mm diameter cylinders. The red areas shown are positive vorticity and the blue areas are negative vorticity. This study has considered areas of concentrated vorticity to indicate vortices present within the flow.

Wake wavelength

The wavelength is the distance between two vortices of the same directional rotation; it has been calculated using the average position of the vortices in x as they travel down the flow tunnel, and has been averaged over the values for both the positive and negative vortices. The wavelength was also normalised by the diameter of the cylinder. Figure 4-5 shows the normalised wavelength relationship for each cylinder size with increasing speed.

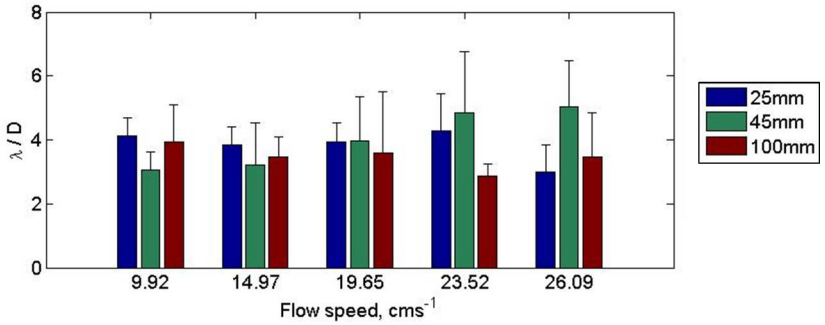

Figure 4-5: Normalised wake wavelength, taken as average values for each cylinder size with increasing speed plotted against the tested flow speeds. The error bars show the standard deviation of the normalised data.

The figure shows that, in general, the wavelengths stay approximately constant with increasing flow speed for each cylinder size. The exception to this is the 45mm cylinder where the values seem to increase. Due to the small size of the cylinder, the wavelength can increase by a small amount and it will appear to cause a large variation in the normalised wavelength of the vortices. It is also possible that, due to the positioning and size of the cylinder and the flow speed variation across the tank, some vortices are carried along by slightly faster streams within the flow tunnel, which increases the wavelength with increasing speed. The 25mm and 100mm cases show a decrease in the wavelength values at the highest flow speed. This is likely due to the steady flow characteristics at this flow speed; the turbulence present at the highest flow speed is much greater than for the lower flow speeds, which will affect the production of a Kármán vortex street.

Brede et al [94] calculated a normalised wake wavelength of 1 for low Reynolds number flows and values between 4 and 8 for higher Reynolds number flows. Karasaduni and Funakoshi [171] calculated the normalised wavelengths within a Kármán vortex street to be approximately 5. The values presented here, of between 2.5 and 5, fit with the second category of values from Brede et al and with the values presented by Karasaduni and Funakoshi.

Wake width

The wake width was calculated using the average y positions of the positive and negative vortices downstream of the cylinder and calculating the difference between them. This was

calculated as an average over the whole capture time, and is presented in Figure 4-6. Again, the values have been normalised by the cylinder diameter.

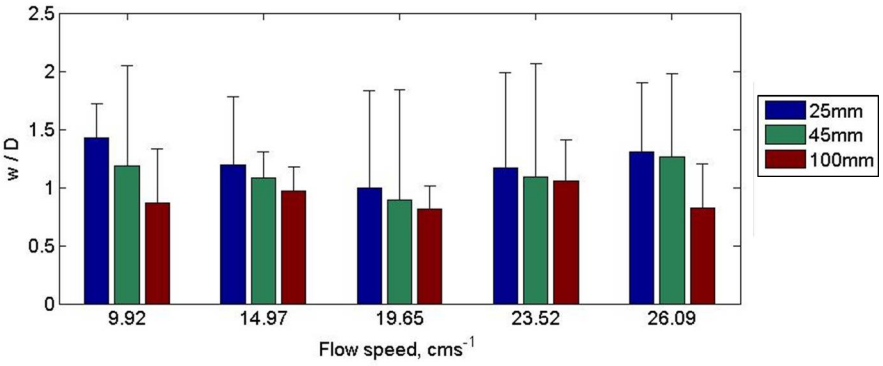

Figure 4-6: Normalised wake width, taken as average values for each cylinder size plotted against the tested flow speeds. The error bars show the standard deviation of the normalised data.

The values here stay approximately constant around 1.1 ± 0.3. Therefore, the width of the streets are approximately the same as the diameter of the cylinders.

Velocity distribution across the wake

The velocity distribution across the wake of the 100mm cylinder at Re = 17.0 $\times 10^3$, Figure 4-7, shows a typical, symmetrical pattern of approximately free-stream values at the edges of the wake, a possible slight increase in velocity and then a significant decrease in speed towards the centre of the wake in the reduced velocity zone. This is representative of the velocity distribution across the wakes for each cylinder at each speed. It can be seen that the lowest normalised velocity shown here is at approximately 0.5 – 0.6 at the centre of the wake, with the greatest speed reaching approximately 1.1.

This pattern of flow was shown in Liao [19], Anagnostopoulous [76] and Nishioka and Sato [172]. The normalised values range from approximately 0.2 [172] for the lowest speed in the centre of the wake, up to 1.3 [76] for the values at the edge of the wake. The values from this study are close to those presented by Anagnostopoulous [76].

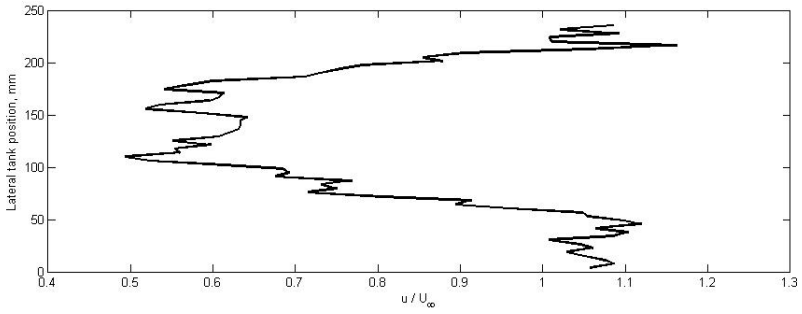

Figure 4-7: Normalised velocity distribution across the wake of the 100mm cylinder at Re = 17.0 $\times 10^3$.

Figure 4-8 shows the minimum flow speeds in the centre of wake relative to the freestream flow speed for each cylinder size. It can be seen that the lowest flow speeds are at the centre of the widest wake - for the 100mm cylinder - and the highest values are at the centre of the 25mm cylinder. As the wake width increases with increasing cylinder size, it would be expected that the flow speed at the centre of the wake would decrease proportionally, as can be seen here.

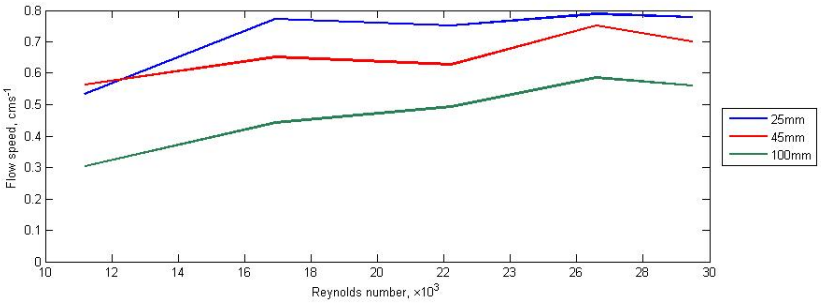

Figure 4-8: Minimum flow speeds for each of the cylinder sizes at steady flow Reynolds numbers 11.0 $\times 10^3$ to 29.0 $\times 10^3$

.

Vortex shedding frequency

The vortex shedding frequency values for each cylinder at each flow speed are presented in Figure 4-9. It can be seen that the values measured using the toolbox from the DPIV captures closely match the values calculated using the equation for the Strouhal number, $St = \frac{fd}{V}$. The vortex shedding frequency increases linearly with flow speed over each cylinder size; if the values are compared between cylinder sizes, it can be seen that the smaller cylinder sizes have a greater value of vortex shedding frequency for any given flow speed.

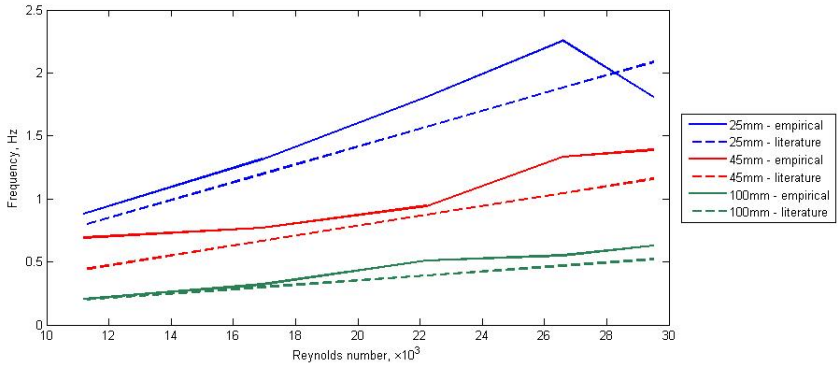

Figure 4-9: The vortex shedding frequencies for each of the cylinder sizes, at each of the five speeds tested plotted against steady flow Reynolds numbers. The values calculated using the Strouhal number are also shown on the graph.

Size of vortices

The size of the vortices have been normalised by dividing the calculated diameter of the vortex by the diameter of the cylinder, Figure 4-10. The normalised sizes of the vortices are within the range of 0.3 –1.1, which are of a similar order to those calculated by Lam [67] of A/D^2 of 0.2 – 0.7. There is a trend in the experimental data that, with an increase in the diameter of the cylinder, there is a decrease in the normalised size of the vortices. The size remains approximately constant with increasing flow speed, although the vortices for the 100mm diameter cylinder show greater variation with flow speed. It is likely that this is due to the larger vortices dissipating much more quickly than the smaller ones as the total rate of viscous dissipation is proportional to the integral of the square of the vorticity produced [173]. This can be seen when the captures are visualised in Tecplot, as the 25mm runs show much more coherent vortex structures than either the 45mm or the 100mm cylinders, Figure 4-4.

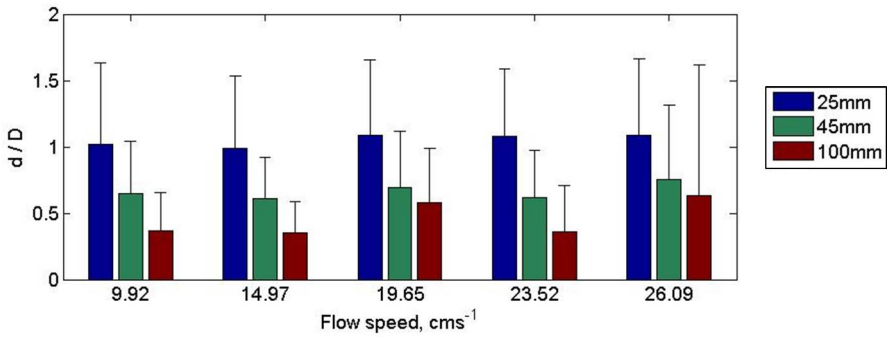

Figure 4-10: Average normalised size of vortices for each cylinder size plotted against the tested flow speeds. The error bars show the standard deviation of the normalised data.

Circulation of vortices

The circulation of the vortices can also be termed the strength of the vortices. The normalised circulation values are calculated as $\frac{\Gamma}{\pi U D}$. These are presented in Figure 4-11, which shows that the greatest normalised circulation occurs for the 25mm diameter cylinder, with a general trend of decreasing with increasing cylinder size but remaining approximately constant with increasing flow speed. There is an anomalous result for a Reynolds number of 17.0 $\times 10^3$ as the value for the 100mm diameter cylinder is high. It is unclear why this run would have a greater value than the other runs, and break the trend seen. The values, sitting approximately between 0.15 and 0.35, are within the same range as those presented by Brede et al [94] of 0.16 – 0.3, Williamson [174] of 0.13 – 1.11, and at the lower range presented by Obasaju et al [62] of approximtaely 0.25 – 1.

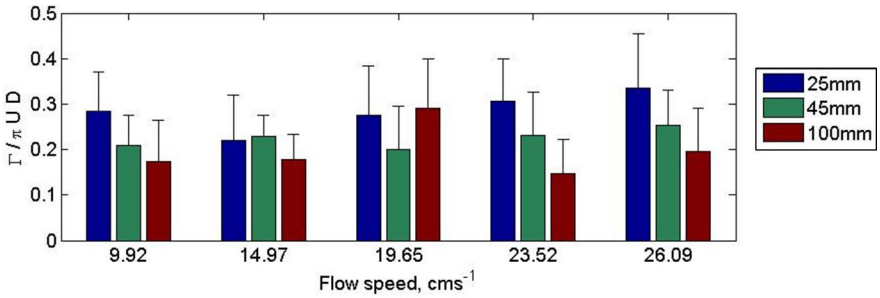

Figure 4-11: Average normalised strength of vortices for each cylinder size at each tested flow speed plotted the tested flow speeds. The error bars show the standard deviation of the normalised data.

4.2.2 Kármán vortex street: summary

The Kármán vortex street has been characterised using the wake wavelength and width, the vortex shedding frequency, the size and circulation of the vortices and the flow speed variation across the wake, including the minimum flow speed present. The normalised wake wavelengths and widths remain approximately constant for each cylinder size, and all collapse around similar values between the cylinder sizes. The velocity distribution across the wake shows a significant decrease at the centre of the wake, rising to the free stream velocity at the edge of the wake, similar to those presented in the literature. The vortex shedding frequency matches the analytical values calculated from the Strouhal number closely. The normalised size of the vortices show distinct relationships between the vortex size and the cylinder size, and combined with the flow visualisation suggests that the larger vortices (from the larger cylinders) are dispersing much more quickly than the smaller. The normalised circulation was calculated to be within the range of 0.15 – 0.35; the general trend shows a decrease with increasing cylinder size, but it remains approximately constant with flow speed. The values presented here match the values found in the literature well; this gives confidence for the analysis techniques used to determine the parameters that characterise the Kármán vortex street.

4.3 Flow characterisation: discussion

Steady flow experiments were carried out to determine the flow behaviours in the tank with no objects present. Five different flow speeds were tested between 9.90 and 26.09cm s^{-1}, giving Reynolds numbers between 11.0 $\times 10^3$ and 29.0 $\times 10^3$, at nine different positions in the tank. This gave an indication of the three-dimensionality of the flow. It was found that the velocities towards the bottom of the flow tunnel were slightly lower than those towards the top of the water column; however, the disparity between the results is within the error of the flow speed and as such can be considered as a negligible difference. The values along the full length of the flow tunnel remained constant, with the pattern of fast and slow velocities only altering slightly by the extreme right-hand-side of the flow tunnel. The turbulence intensity within the flow tunnel was also calculated, and found to be approximately 12%, although it is greater than this at the highest flow speed. It can be concluded that whilst the flow within the flow tunnel is turbulent flow, with a constant speed variation across the tank that is within 4cms^{-1} of the target velocity, the overall trends are that of a steady flow. There is a variation shown in the horizontal direction within the water column, but the variation is small and within the error calculated for the flow speed. This flow behaviour presents a natural environment for a fish and, therefore, a realistic situation in which to capture data from a swimming fish and also a robot fish.

The Kármán vortex street experiments were carried out using three different cylinder sizes and all five flow rates, giving Reynolds numbers between 2.2 $\times 10^3$ and 22.6 $\times 10^3$ all of which lie within the immediate subcritical shedding regime as defined by Zdravkovich [93]. Two different field-of-view areas were captured for each street; a view which included the cylinder and the near-field wake and a far-field view, to capture the downstream behaviour of the vortices. These captures were analysed to determine six different parameters within the street; the wake width and wavelength, the velocity variation across the wake, the vortex shedding frequency and the strength and size of the vortices. The values calculated matched well with those reported in the literature; the normalised width and normalised wavelength values stayed approximately constant across cylinder sizes and flow speeds; the velocity decreased towards the centre of the wake, increasing back to the free stream value at the edge of the wake; the vortex shedding frequencies calculated from the velocity field closely matched the values calculated from literature; the normalised size and circulation of the vortices showed a trend of decreasing with increasing cylinder size, but remaining approximately constant with increasing flow speed.

The flow characterisation has provided detail on the behaviour of the global flow within the flow tunnel when no downstream obstacles are present; two different flow regimes have been created and characterised so that the behaviours can be categorised and understood. The variable that has been investigated has been the velocity, and by extension the vorticity, of the flow. An important aspect of the flow that has not yet been studied is the pressure; studies of calculating pressure from DPIV data have been carried out [111–116], but these are still

in the early stages and only simple situations have been used for the calculations. Therefore, a measurement system must be placed in the flow to determine the pressure signals present; however, the presence of an object will alter the fluid behaviour. This is true of a swimming fish in all situations and, consequently, inspiration was taken from the shape of fish such that a fusiform, pressure tapped robot was used to represent a fish within the flow.

The following chapters detail the experiments carried out; firstly, a swimming fish used as inspiration; latterly, experiments carried out with the fish robot both stationary and when moving in steady and Kármán vortex streets are presented. These experiments have been used to determine a global-local link between the velocity vectors calculated using DPIV around the bodies with the pressure signals detected along the bodies. Therefore, a coherent picture of the information available within the flow to local flow sensors can be presented.

Chapter 5

Experiments with Fish

The following chapter details the experiments carried out with the fish. Small rainbow trout were placed in steady flows and Kármán vortex streets and DPIV was used to capture the flow fields around them. The focus of these experiments was to determine the global movements of the fish within the flow tunnel and determine whether there was a pattern to the position of the fish relative to the vortices present in the cylinder wakes. This information was then used to help design the experiments carried out with the fish-like robot in Chapters 6 and 7.

5.1 Background

The biomimetics of fish uses nature and the evolutionary advances that have allowed fish to survive in many difficult and complex locations as the inspiration for the design of a man-made robot. The objective is to incorporate any advantages the fish gains through its locomotory adaptations into the design of an underwater robot. The robot could, therefore, move through environments in a natural way causing minimal disturbance to the environment around it, and coping with more difficult flow fields in a more efficient way. One of these flow fields is the Kármán vortex street.

The motion of a fish in a Kármán vortex street was termed the Kármán gait by Liao et al [19]. They studied rainbow trout behind a 2.5 and a 5cm diameter half-cylinder at flow speeds of 2.5 and 4.5 BLs^{-1} (body lengths per second). They found that the fish altered their kinematics when it was swimming within the Kármán vortex street. The fish decreased their tail-beat frequency and increased their body wavelength, as well as increasing body amplitudes, although this was due to the increased lateral motion of the fish within the tank. The tail-beat frequencies were found to generally match the vortex shedding frequency of the Kármán vortex street, whereas the body wavelength was found to be greater than wake wavelength of the street. Liao et al [19] theorised from their work that the fish swim behind the cylinders to capture energy from the vortices present. The trout were found to slalom between the vortices in the street.

If the movement of the fish within the Kármán vortex street is due to it capturing energy from the vortices, so that it can hold station within the flow with very little energy usage, this could be a beneficial movement for a robot to mimic. It could allow an autonomous robot fish to save energy in certain situations, rather than expending more as would be usual within turbulent flows.

The experiments carried out in this study have provided inspiration for the movements of the robot, presented in Chapter 7. By studying the literature surrounding fish swimming in Kármán vortex streets, it can be seen that the global movements of a fish have not previously been tracked and the position of the fish with respect to the vortices has not been studied extensively. Therefore, these few experiments, although with a focus on extracting useful information in regards to the robot fish used within the later studies, can also benefit biologists in further understanding the motions and behaviours of fish when they Kármán gait.

5.2 Experimental details

The fish used for these experiments were rainbow trout (*Oncorhynchus mykiss*), of approximate length 18±2cm. They were placed in the working section of the flow tunnel in steady flows with flow speeds of 1.82, 0.92 and 0.69 BLs^{-1} giving Reynolds numbers of 17.9 $\times 10^3$, 35.4 $\times 10^3$ and 47.0$\times 10^3$ relative to the fish length. In addition they were placed within Kármán vortex streets created using the 100mm diameter cylinder at the same range of flow speeds. The 100mm diameter cylinder was used as it gave a body-length-to-cylinder-diameter (BL/D) ratio of 1.8, which is close to that used by Liao et al (BL/D = 2) [19].

DPIV captures were taken, with a maximum of seven seconds captured in a single data set. The laser sheet was set up at a height that the fish would usually swim so that the images could capture the fish within the Kármán vortex street. It was observed during the experiments that the fish would avoid the laser light, and generally swim just above or just below it. Therefore, captures with the fish within the laser sheet in the Kármán vortex street were rare.

Overall, four different fish were used, and each was placed within the steady flows and Kármán vortex streets using varying flow speeds and cylinder sizes. In total over one hundred and forty experiments were captured. For most of the captures the fish would be just above or just below the street, but a few captures caught the fish in the laser sheet whilst it was swimming. A number of these data sets did not capture sufficient information and so could not be used; a selection of 34 successful experiments are presented here.

5.3 Results

There were two main characteristics that were drawn from these experiments; the overall movement of the fish in the steady flows and Kármán vortex streets; and whether the fish avoided

or approached the vortices within the cylinder wake. These two parameters could then be used to determine the positions of the robot when it was placed within the flow fields.

The global motion of the fish was determined by looking at the head position within the captured field-of-view. The nose of the fish was tracked to give a position in both x (longitudinally) and y (laterally).

5.3.1 Steady Flow

The results of the fish swimming in steady flow are shown in Figure 5-1. These plots show the movement of the fish within the flow tunnel, in both x and y, during the DPIV captures at each of the tested flow speeds. At a Reynolds number of 17.9 $\times 10^3$ relative to the fish, the fish swam laterally across the flow tunnel or moved backwards within the flow tunnel. For many of the experiments at this lowest flow speed, it was observed that the fish would swim all around the tank; it is suggested that this flow speed did not present significant resistance to the fish. When the Reynolds number was increased to 35.4 $\times 10^3$ relative to the fish similar behaviour was seen, but the fish was observed to hold station in x and y more frequently. This is shown by the straighter path lines shown in Figure 5-1. By increasing the Reynolds number again, up to 47.0×10^3 relative to the fish, the fish was observed to hold station in x but would also drift across the tank. By examining these graphs together, it can be seen that the range of motion is comparable at each of the tested flow speeds. There is no clear pattern of movement within the flow tunnel; the fish would often hold station, or would drift slowly across the flow tunnel or backwards within the flow tunnel.

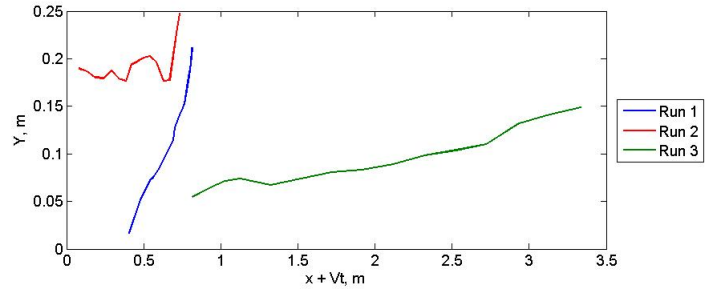

(a)

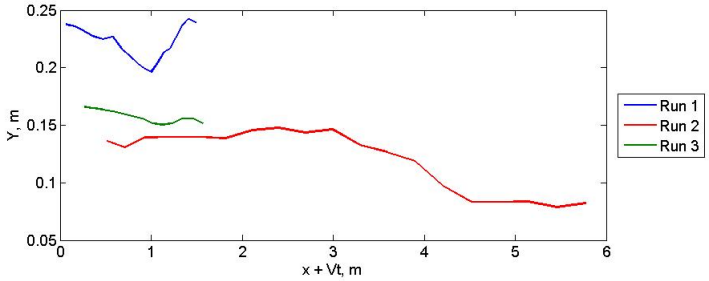

(b)

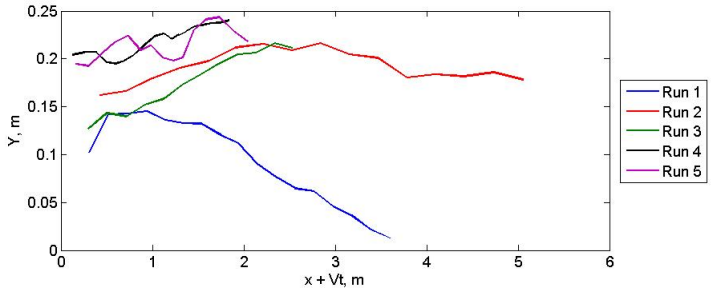

(c)

Figure 5-1: Plots showing the global movement of the fish when places in steady flows at Reynolds numbers relative to the fish of (a) 17.9 $\times 10^3$, (b) 35.4 $\times 10^3$ and (c) 47.0$\times 10^3$. These different plots were taken from successful captures of the fish at each of the tested flow speeds, with the different lines illustrating different experiments.

5.3.2 Kármán vortex street

The global motions of the fish in Kármán vortex streets are given in Figure 5-2. A number of different experimental results have been plotted which have been time–shifted so that the pattern of motion more closely matches between lines as the experiments were not always captured over the same pattern of vortices. The plots in Figure 5-2 show a clear oscillatory trend. At the lowest flow speed the wavelength is long and as such only a small portion is captured within the experiment. At the higher flow speeds, there is a clear distinction between

the movements in a Kármán vortex street and the movements presented in Figure 5-1 for the fish in steady flow. By examining the movement waveforms it was found that the frequency of the fish's motion was similar to that of the Kármán vortex street in which it was swimming, Table 5.1.

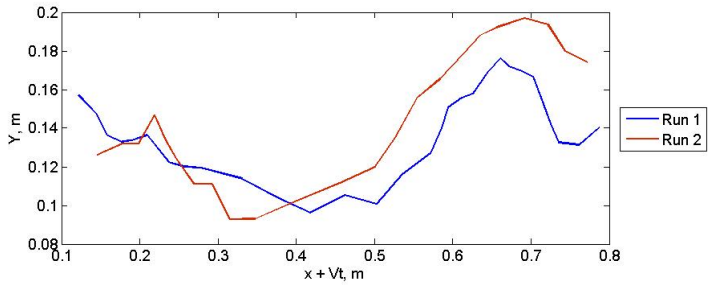

(a)

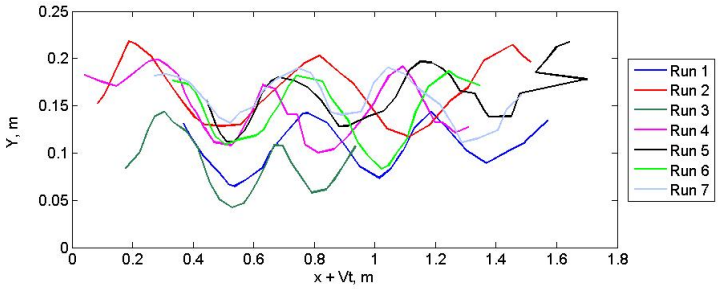

(b)

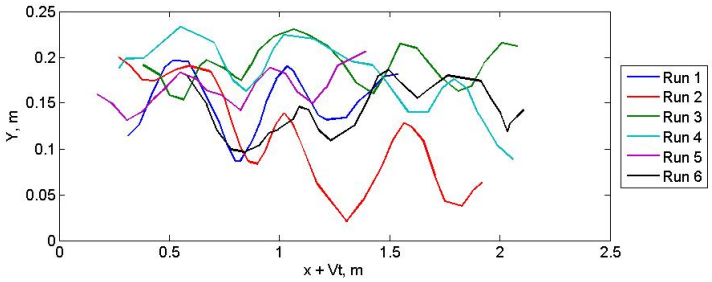

(c)

Figure 5-2: Plots showing the global movement of the fish when places in Kármán vortex streets at Reynolds numbers relative to the fish of (a) 17.9 $\times 10^3$, (b) 35.4 $\times 10^3$ and (c) 47.0$\times 10^3$. These plots show the various successful experiments of the fish captured with the DPIV data.

The amplitudes of the motion, Table 5.2, calculated as the maximum position in y minus the minimum position in y averaged over the experiments at each flow speed, match closely with the value of wake width, which was approximately 10cm (Chapter 4).
These results show a marked distinction between the movements of the fish when swimming in steady flow compared to the Kármán vortex street. The characteristics of the movement in the

Flow speed,cm s^{-1}	Fish, Hz	Kármán vortex street, Hz
9.92	0.16	0.19
19.65	0.41	0.39
26.09	0.50	0.52

Table 5.1: Frequency of the motion of the fish and vortex shedding frequency for the associated Kármán vortex streets.

Flow speed,cm s^{-1}	Motion amplitude, cm
9.92	9.2±1.7
19.65	9.6±1.1
26.09	10.7±2.7

Table 5.2: Average amplitudes of the motion of the fish within Kármán vortex streets.

Kármán vortex streets indicate that the fish is swimming to approach or avoid the vortices; the amplitude of the movement matches that of the cylinder wake width and the frequency of the movement matches the vortex shedding frequency.

By examining the DPIV data captured, it was found that the fish moved along the Kármán vortex street behind the cylinder, and seemed to approach the vortices. This is illustrated for each of the flow speeds in Figures 5-3 (a) – (c) and in Figures 5-4 which presents a plot of the fish nose in y within the working section of the flow tunnel behind the 100mm cylinder at Re = 35.4 $\times 10^3$ relative to the fish, with the vortex positions at frames where the vortex and fish were both present. This is representative of the behaviour seen at all flow speeds. It can be seen that the fish nose is positioned so that the fish approaches each of the vortices, rather than moving to avoid them. This case shows an interesting result, where the fish appears to be swimming around the outside of the negative (blue) vortices; this occurred for a number of the experiments, but not in all. The behaviour shown by the fish here do not match the behaviours presented in the literature, where the fish slaloms around the vortices. This change in behaviour could be due to the lower relative flow speeds used in these experiments; the fish could need the extra thrust produced by using the vortices to help them hold station within the Kármán vortex street rather than avoiding them as they do at higher flow speeds.

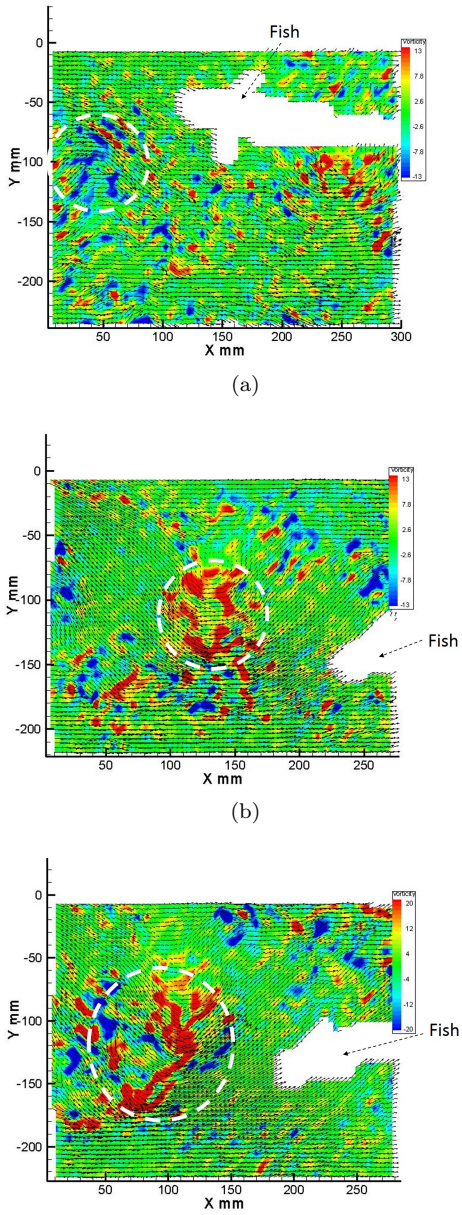

(a)

(b)

(c)

Figure 5-3: Images illustrating the position of the fish relative to the vortices at (a) 1.82 BLs^{-1}, (b) 0.92 BLs^{-1}, and (c) 0.69 BLs^{-1}. The contour plot shown is vorticity, with red indicating positive (anti-clockwise) vortices and blue indicating negative (clockwise) vortices. The fish (indicated) is shown as a white region, absent from velocity vectors.

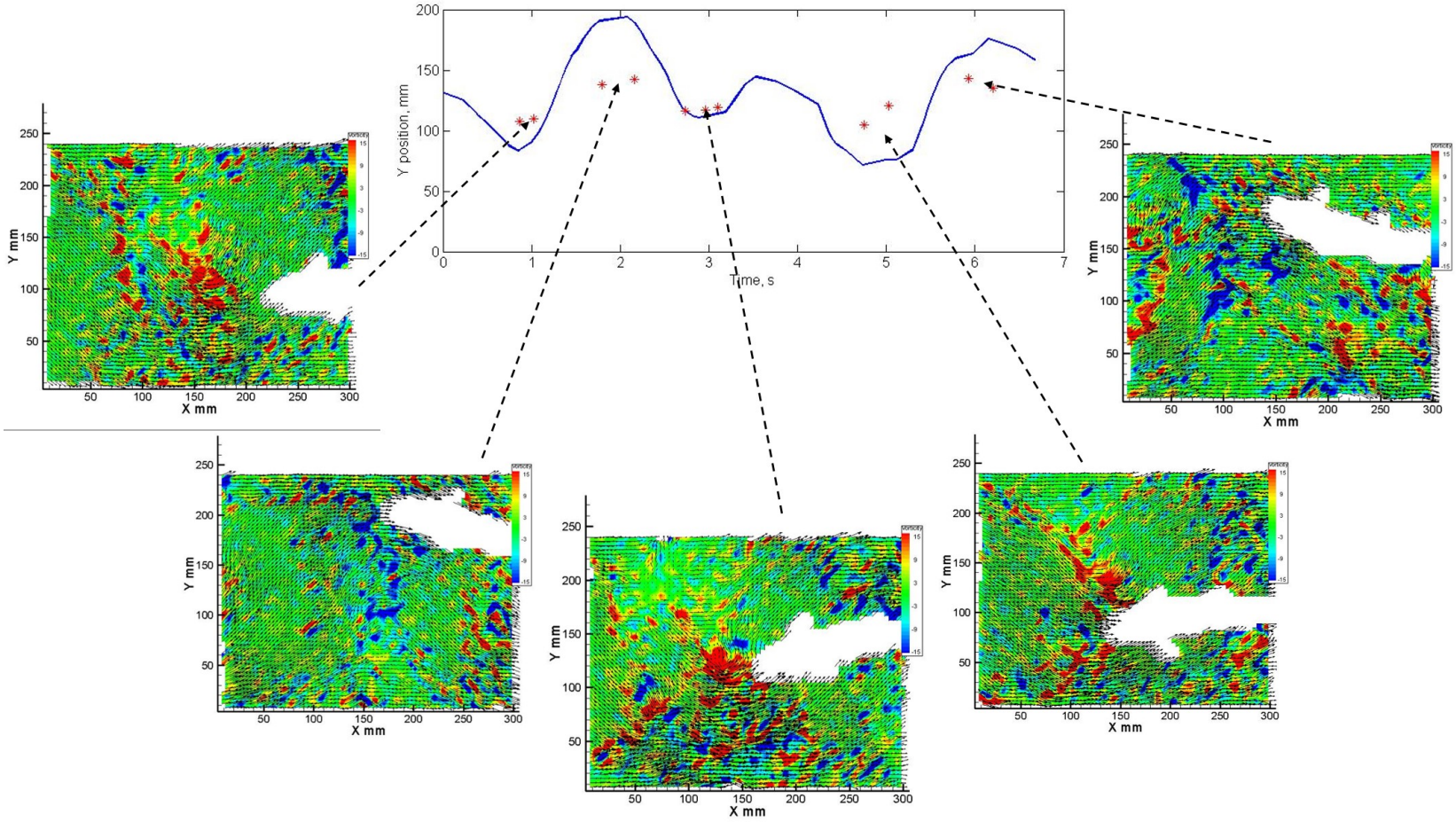

Figure 5-4: Illustration of the fish position relative to the vortices within the Kármán vortex street behind the 100mm diameter cylinder at a flow speed giving Re = 35.4 $\times 10^3$ relative to the fish. The contour plot shown is vorticity, with red indicating positive (anti-clockwise) vortices and blue indicating negative (clockwise) vortices. The fish is shown as a white region, absent from velocity vectors.

5.4 Discussion

The experiments carried out here have used DPIV to examine the flow field around the fish when swimming in steady flow and in Kármán vortex streets. It was found that the fish presents a very different movement within the flow tunnel when comparing steady flow swimming to swimming within a Kármán vortex street. In steady flows, the fish would often hold station in x but drift across or backwards within the flow tunnel. In comparison, when in the Kármán vortex street, the fish exhibited a marked oscillatory pattern. The frequency of this oscillation was similar to that of the vortex shedding frequency of the Kármán vortex street, and the amplitude of this motion matched the wake width closely. It was also found that the fish moved to approach the vortices, rather than avoid them. These findings do not agree with those presented by Liao et al [19], who showed that the fish moved to slalom around the vortices within the Kármán vortex street.

The purpose behind these experiments was to investigate the movement of the fish within these different flows which can be mimicked using a fish-like robot. Although it is currently unclear as to why the fish would Kármán gait, either when approaching or avoiding the vortices, it is possible that it can extract energy from the vortices and therefore reduce their locomotory costs [20]. By mimicking this behaviour with a fish-like robot that can swim effectively within unsteady flows, this could be further investigated. If energy harvesting from the vortices is possible, this could be used to increase the efficiency of fish-like robots.

The following chapters detail experiments with a fish-like robot, also placed in steady flows and Kármán vortex streets, with an on-board artificial lateral line system of pressure sensors; firstly with the robot stationary and then, taking inspiration from the fish's motion, with the robot moving within the flow tunnel.

Chapter 6

Experiments with the Robot Held Stationary

This chapter details the experiments in which the fish-like robot was held stationary. These first experiments were of simplified situations so that different flow regimes could be captured without the complexity of a moving robot. Initial experiments were carried out when no cylinder was present ahead of the robot, to give a baseline behaviour for the pressure sensors and fluid flow around the robot. Once these were completed, further experiments with the robot placed in a Kármán vortex street were carried out. A number of configurations were tested in order to investigate the global and local flows around the robot in different flow regimes: the flow was changed by either changing the flow speed or the cylinder size; or the robot position relative to the cylinder was changed to give a different pressure sensor profile. These experiments are described in detail below.

6.1 Steady flow

Initially the robot was placed in steady flow. Two sets of experiments were carried out: firstly with the robot facing into the flow and secondly with the robot placed at various angles to the direction of flow. The first experiment, facing the robot into the direction of flow, gave the pressure signals for the simplest situation; the signals are indicative of a robot swimming either in still water or into a flow. In addition, the behaviour of the flow around the robot can be determined. This gives a baseline against which to compare later results.

It is unlikely that a robot placed within an unsteady flow environment would consistently be facing directly into the direction of the flow. Therefore, experiments in which the robot head is angled relative to the oncoming flow are of interest. Initially experiments were conducted in steady flow to provide a basis of understanding before further complexities of the flow, such as the Kármán vortex street, are introduced.

6.1.1 Facing into the flow

The robot was placed in the centre of the working section of the flow tunnel. Three different flow speeds were tested, at Reynolds numbers relative to the robot of 39.7 $\times 10^3$, 78.6 $\times 10^3$ and 104.4 $\times 10^3$.

An image from the DPIV capture is shown in Figure 6-1, with streamlines showing the flow around the robot. The flow travels smoothly around the robot, due to its fusiform shape. The velocity magnitude, taken 10mm away from the nose of the robot, Figure 6-2, also shows that there is little disturbance to the bulk flow field due to the presence of the robot. The values of flow speed taken at this point are very similar to the overall values given in Chapter 4, with only slight variation in the flow pattern compared with the previous results, Table 6.1. The near-field values presented here were taken over three columns of data at 10mm in front of the nose of the robot; the far-field values were taken over the entire field-of-view when no robot was present.

	Flow speed, cms^{-1}		
Near-field	8.8±1.4	18.9±2.3	25.9±2.1
Far-field	9.92 ± 1.44	19.65 ± 2.96	26.09 ± 4.43

Table 6.1: The velocity values within the steady flow field at Reynolds numbers relative to the robot of 39.7 $\times 10^3$, 78.6 $\times 10^3$ and 104.4 $\times 10^3$, taken in the near-field and far-field.

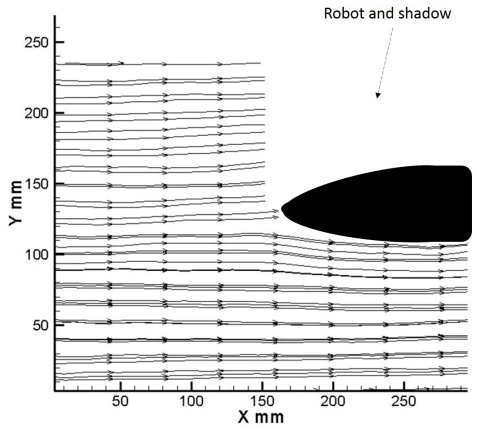

Figure 6-1: Image from the DPIV data set showing the streamlines around the robot when in steady flow at Re = 78.6 $\times 10^3$. It is representative of all the flow speeds.

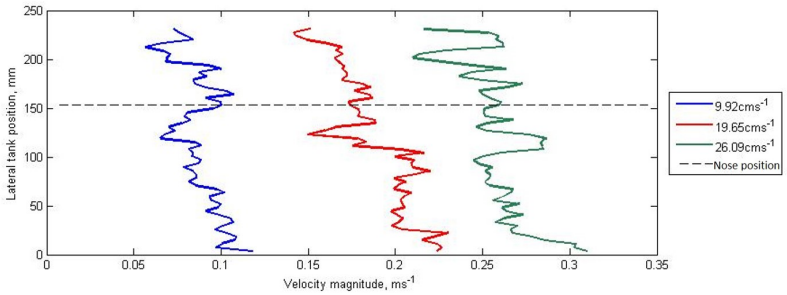

Figure 6-2: Velocity magnitude 10mm in front of the nose of the robot when in steady flow at Reynolds numbers relative to the robot of 39.7 $\times 10^3$, 78.6 $\times 10^3$ and 104.4 $\times 10^3$. The nose position of the robot is also indicated.

The pressure signals for each of the different flow speeds are shown in Figure 6-3; these signals are gauge pressures, calibrated as detailed in Chapter 4 and normalised by subtracting the mean value of the pressure signal so that they oscillate around zero. There is no discernible pattern, although some peaks and troughs are present, particularly at the higher flow speeds. These variations are likely to correspond to slight variations in the flow speed within the working section of the flow tunnel as there is no clear correlation to any flow behaviour found in the DPIV data. The pressure results also show that the peak-to-peak amplitude of the pressure increases with increasing flow speed, Table 6.2. Additionally, the signals were processed to extract the dominant frequencies; no clear pattern is seen across the four sensor pairs to give a clear dominant frequency at any of the flow speeds tested. The magnitudes of the frequencies were all below 2.5, showing that there is no strong signal present.

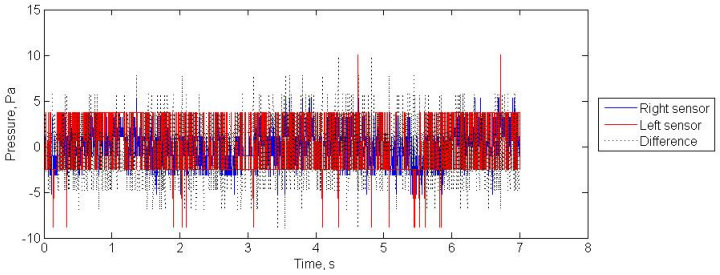

(a)

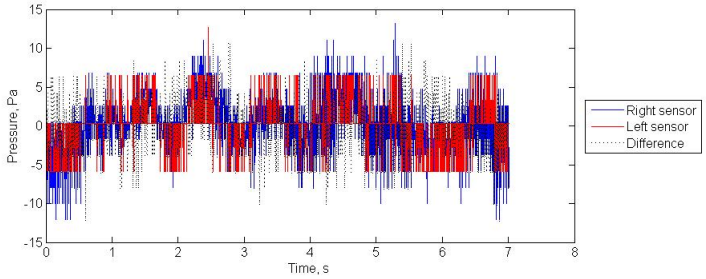

(b)

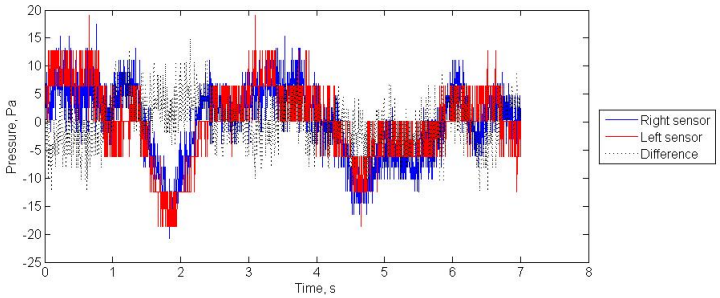

(c)

Figure 6-3: Pressure plots from the robot placed in steady flow at Reynolds numbers of (a) 39.7 $\times 10^3$, (b) 78.6 $\times 10^3$ and (c) 104.4 $\times 10^3$. The blue line indicates the sensor next to the nose on the right-hand side of the robot, the red line indicates the sensor next to the nose on the left-hand side of the robot. The dotted line shows the difference between these two sensor signals.

Reynolds number $\times 10^3$	39.7	78.6	104.4
Peak-to-peak amplitude, Pa	10	15	25

Table 6.2: Peak-to-peak pressure amplitudes for each of the Reynolds numbers relative to the robot of 39.7 $\times 10^3$, 78.6 $\times 10^3$ and 104.4 $\times 10^3$.

6.1.2 Head angled to the flow

The robot was placed at angles up to ±40° in 5° increments, Figure 6-4, at a Reynolds number relative to the robot of 78.6 $\times 10^3$. Both positive and negative angles were considered as only the left side of the head could be illuminated by the laser sheet.

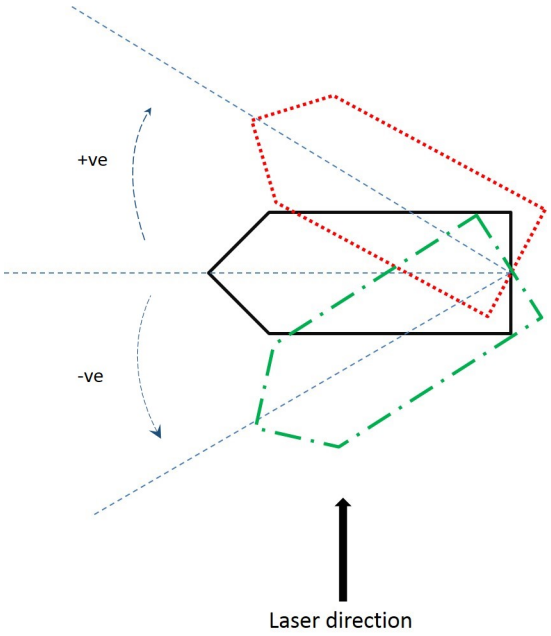

Figure 6-4: Positive and negative angles at which the robot was placed, with 0° being the centre-line. The laser position is at the bottom of the image, so only the left-hand side of the robot is illuminated. Positive angles are shown by the red diagram and negative angles are shown by the green diagram.

Figure 6-5 shows the streamlines around the robot at (a) -30° and (b) +30° for a single time-step within the data; however, they are representative of the whole dataset. It can be seen that the flow is smooth around the robot; the contraction of the streamlines indicates some faster flow around the nose (a) and along the side (b) of the robot, but no large areas of recirculation appear.

The pressure signals, Figure 6-6, show no clear distinction of pattern between either side of the head. The values of the peak-to-peak pressure amplitudes, equal to 20Pa, fall into that bounded by the previous experiments where the robot was facing into the flow. The frequencies and their magnitudes extracted from the pressure signals match those from the experiments with the robot facing into the flow.

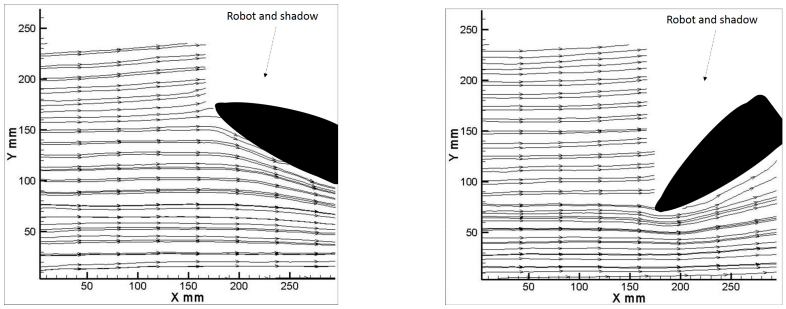

(a) (b)

Figure 6-5: Images showing the flow around the robot when in steady flow at a Reynolds number of 78.6 $\times 10^3$ with the robot positioned at (a) $+30°$ and (b) $-30°$.

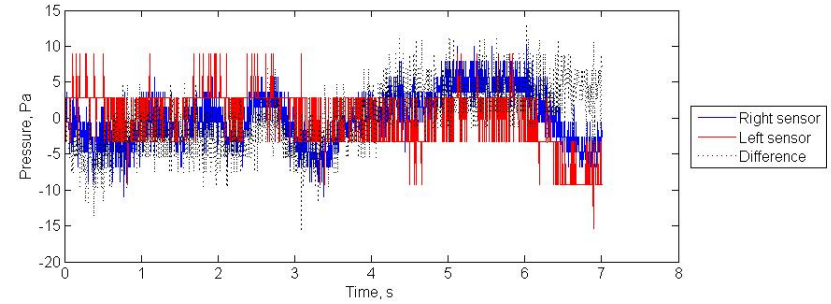

(a)

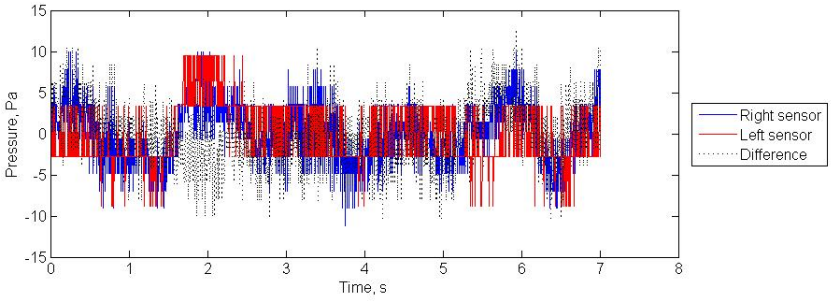

(b)

Figure 6-6: Pressure plots from the robot when placed at (a) $30°$ and (b) $-30°$, in a steady flow at a Reynolds number of 21.9 $\times 10^3$. The blue line shows the result from the sensor to the right-hand side of the nose; the red line shows the result from the sensor on the left-hand side of the nose. The dotted line gives the difference of right-hand to left-hand side.

Steady flow: summary

The steady flow experiments show that the flow travels smoothly around the robot both when it is facing into the flow and when it is angled relative to the direction of flow. The pressure signals showed some variation with time, with the peak-to-peak amplitude increasing with increasing

flow speed. No clear pattern was discernible in the pressure signal and any peaks or troughs are assumed to be slight variations within the flow field occurring with time, or noise within the pressure signal.

6.2 Kármán vortex street

Once the steady flow experiments were completed, the robot was placed in Kármán vortex streets. A number of different scenarios were tested which explored:

- changing the flow speed;
- changing the cylinder size;
- moving the robot close towards the cylinder;
- moving the robot laterally away from the centre-line of the Kármán vortex street; and
- angling the head within the cylinder wake.

These different experimental sets cover a range of situations that allow both hypotheses presented in Chapter 2 to be tested for a stationary robot. By changing the flow speed and the cylinder size, different Kármán vortex street parameters are produced, thereby allowing hypothesis 2 to be tested. Moving the robot into different positions will change the distance of some sensors to the vortices allowing hypothesis 1 to be tested.

6.2.1 Changing the flow speed

Changing the flow speed, around a single cylinder, changes the parameters of the Kármán vortex street produced, such as the vortex strength. This has been shown in Chapter 4.

The robot was placed centrally behind the 100mm diameter cylinder at three diameters (300mm) downstream (Figure 6-16). This distance allows for the vortices to form and be fully shed from the cylinder before they reach the robot. Three different flow speeds were tested, giving Reynolds numbers relative to the cylinder of 8.6 $\times 10^3$, 17.0 $\times 10^3$ and 22.6 $\times 10^3$. These Reynolds number flows are all situated within the intermediate subcritical shedding regime [93].

The results of the flow characterisation experiments showed that the normalised size and circulation of the vortices stayed approximately constant with increasing flow speed. Figure 6-7 presents the normalised size and circulation of the vortices calculated when the robot was present compared to the uninterrupted wake presented in Chapter 4. It can be seen that the values of normalised circulation match well, in general, between the two data sets. The anomalous result in the normalised circulation, at a Reynolds number of 17.0 $\times 10^3$, from the flow characterisation is clear here.

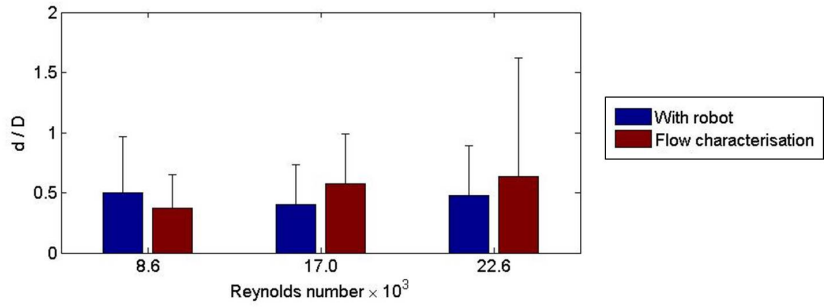

(a)

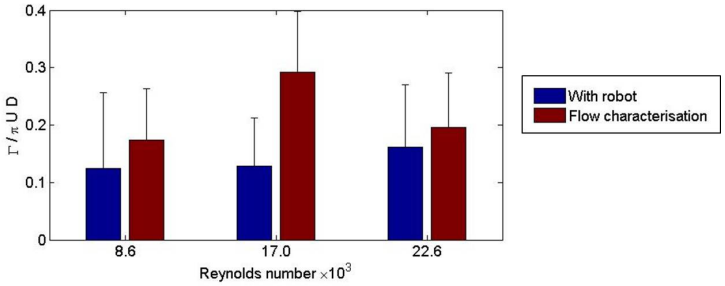

(b)

Figure 6-7: Normalised size (a) and normalised circulation (b) for the vortices at Reynolds numbers relative to the cylinder of 8.6 $\times 10^3$, 17.0 $\times 10^3$ and 22.6 $\times 10^3$ for flow characterisation data and when the robot is present in the wake of the cylinder. The error bars show the standard deviation of the normalised data set.

The pressure signals at Reynolds numbers relative to the cylinder of 8.6 $\times 10^3$, 17.0 $\times 10^3$ and 22.6 $\times 10^3$ are shown in Figure 6-8 (a), (b) and (c) respectively. In addition, plots of the signal from all of the sensors on each side of the head is shown in Figure 6-9, with the right-hand sensors in (a) and the left-hand sensors in (b). These plots show that, in general, there is a 180° phase difference between either side of the head; this is most clear at the highest flow speed, where Re = 22.6 $\times 10^3$. By examining the plots presented in Figure 6-9 it can be seen that the pressure signal is repeated by each of the sensors on each side of the head, at a slight time delay. This is indicative of the sensors each detecting the vortex as it travels down the length of the head.

The peak-to-peak amplitudes of the pressure were also examined and found to increase with increasing flow speed from approximately 10Pa at a Reynolds numbers of 8.6 $\times 10^3$, to approximately 50Pa at a Reynolds numbers of 17.0 $\times 10^3$ and up to 100Pa at a Reynolds numbers of 22.6 $\times 10^3$. This is the same trend as found when the robot was placed in steady flow; however, the amplitudes have increased significantly when the robot is in the Kármán vortex street compared to steady flows.

In addition to examining the sensor signals in the time domain, these signals were also processed to investigate their frequency component. It was found that the dominant frequency detected at each of the flow speeds was similar to the experimental vortex shedding frequency calculated from the DPIV data and presented in Chapter 4 and to that calculated from the Strouhal number; Table 6.3. The greatest variation in the numbers here is 23%, at the centre Reynolds number, between the two empirical results; the absolute difference is only 0.12Hz at this point. It can, therefore, be concluded that the vortex shedding frequencies are being detected by the pressure sensors when the robot is positioned within the Kármán vortex street. The magnitudes of the dominant frequencies were examined and found to increase with increasing flow speed, and were also greatest for the sensor pair nearest to the nose, Table 6.4.

Reynolds number, $\times 10^3$	8.6	17.0	22.6
Dominant frequency, Hz	0.195	0.391	0.586
Flow characterisation frequency, Hz	0.204	0.511	0.631
Strouhal frequency, Hz	0.198	0.393	0.522

Table 6.3: Dominant frequencies detected by the pressure sensors for each of the flow speeds with Reynolds numbers relative to the cylinder of 8.6 $\times 10^3$, 17.0 $\times 10^3$ and 22.6 $\times 10^3$. The values calculated from the DPIV data within the flow characterisation and from the Strouhal number are also given.

Sensor pair Reynolds number, $\times 10^3$	1	2	3	4
8.6×10^3	1.62	1.17	1.26	1.19
17.0×10^3	17.69	12.41	9.46	7.65
22.6×10^3	59.90	32.19	22.23	19.02

Table 6.4: Magnitudes of the dominant frequencies for each of the four sensor pairs at Reynolds numbers relative to the cylinder of 8.6 $\times 10^3$, 17.0 $\times 10^3$ and 22.6 $\times 10^3$.

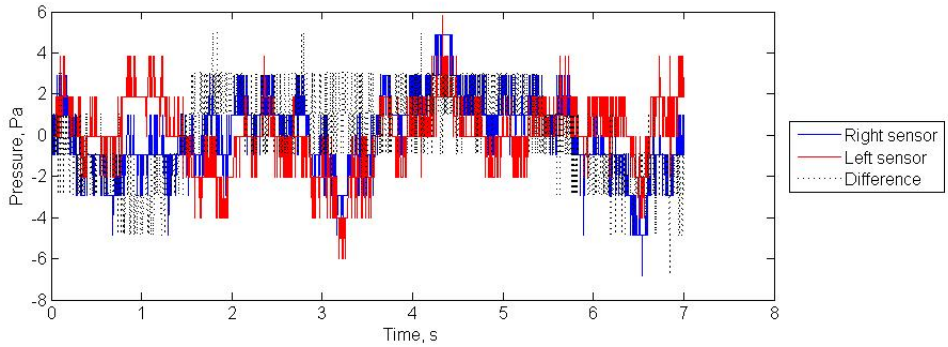

(a)

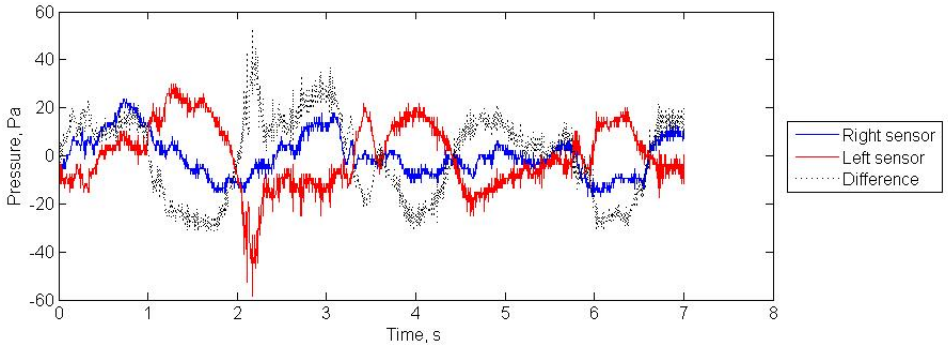

(b)

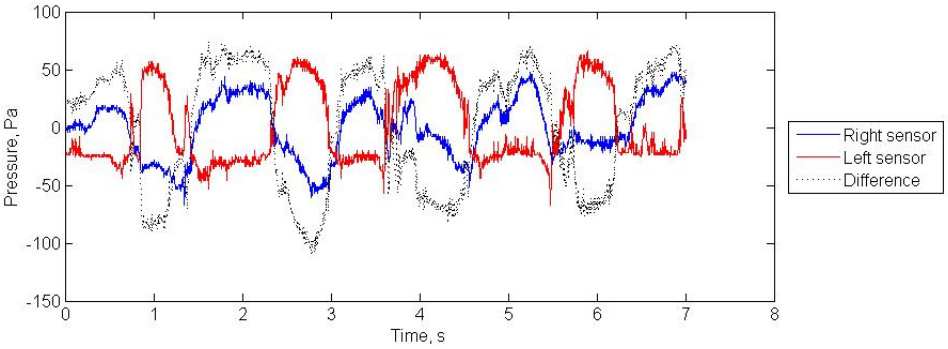

(c)

Figure 6-8: Pressure plots from the robot placed in the Kármán vortex street using the 100mm diameter cylinder at Reynolds numbers of (a) 8.6 $\times 10^3$, (b) 17.0 $\times 10^3$ and (c) 22.6 $\times 10^3$. The blue line indicates the sensor next to the nose on the right-hand side of the robot, the red line indicates the sensor next to the nose on the left-hand side of the robot. The dotted line shows the difference between these two sensor signals.

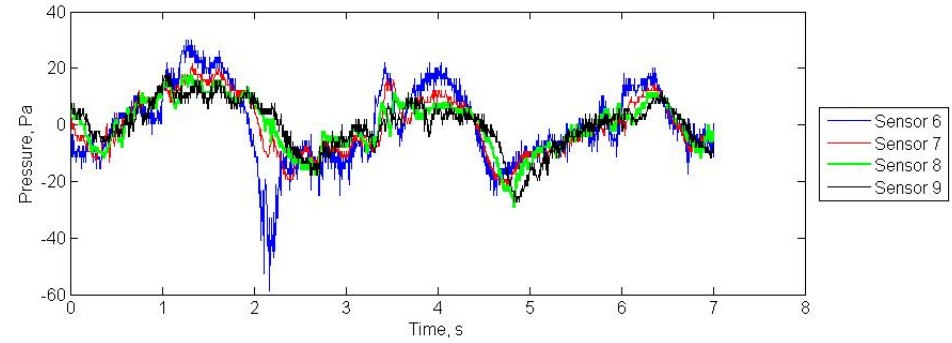

(a)

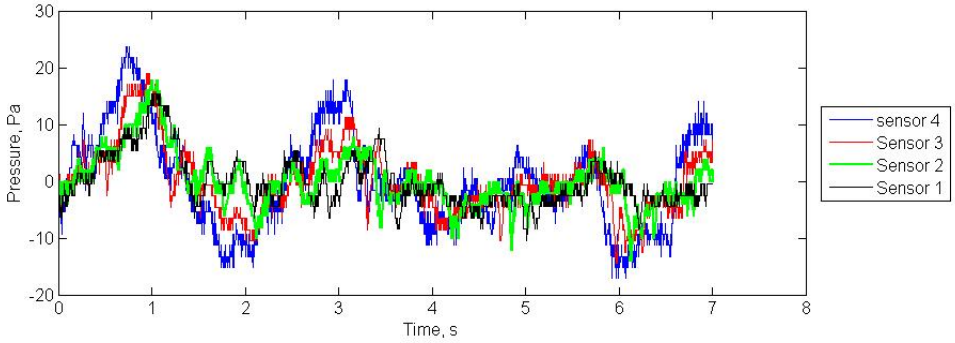

(b)

Figure 6-9: Pressure plots from the robot placed in the Kármán vortex street using the 100mm diameter cylinder at Re = 17.0 $\times 10^3$ for (a) the right-hand sensors and (b) the left-hand sensors. The pressure pattern is repeated for each of the sensors along the side of the head.

The pressure plots of the two sensors next to the nose on either side of the head were examined further by synchronising the DPIV and the pressure data using an LED. The nose sensor, being at the very front of the robot, intercepted both the positive and negative vortices whereas the side sensors only intercepted either the positive or the negative vortex. The frames at which the peaks and troughs of the pressure signals occurred for the two sensors on either side of the nose were extracted. These frames were matched to the synchronised DPIV frames to determine the position of the vortex relative to the sensors on the robot. The pressure plots showed that the start of a pressure peak on the right-hand sensor, which equates to a pressure trough on the left-hand side sensor, occurred when a negative (clockwise) vortex was approaching the robot; the start of a pressure trough from the right-hand sensor, and a pressure peak from the left-hand sensor, occurred when a positive (anticlockwise) vortex was approaching the robot, Figure 6-10. This observation holds true for each of the different flow speeds tested. Note that it is the oncoming vortex that is examined, as the vortex that is present on/around the body of the robot cannot be visualised on the right-hand side of the robot due to the experimental set-up.

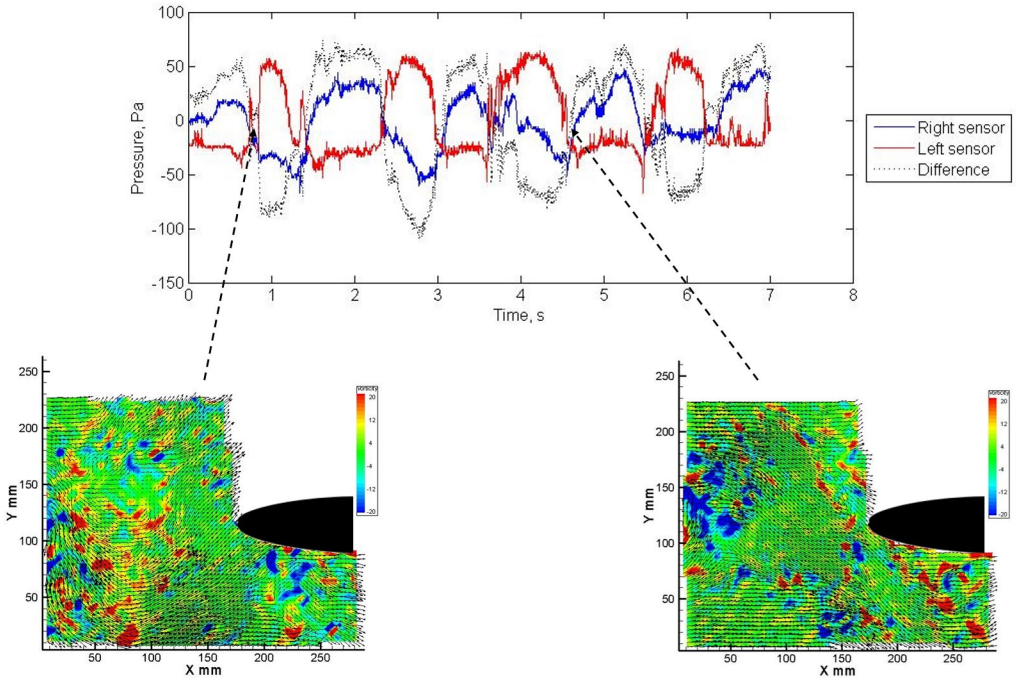

Figure 6-10: Pressure plots with synchronised DPIV images at selected frames from the robot placed in the Kármán vortex street using the 100mm diameter cylinder at a Reynolds number relative to the cylinder of 22.6 $\times 10^3$. The red areas indicate positive (anti-clockwise) vorticity and blue indicating negative (clockwise) vorticity. The DPIV images shown represent, on the left, the point at which there is a peak on the left-hand pressure signal and a corresponding trough on the right-hand pressure signal. At this point there is a large area of positive (red) vorticity, defined in this study as a positive vortex, approaching the robot. The right-hand image illustrates the point at which there is a peak on the right-hand pressure sensor and a corresponding trough on the left-hand sensor. At this point a concentrated area of negative (blue) vorticity is approaching the robot. This is indicative of the behaviour seen at all flow speeds.

In addition to correlating the presence of the vortices to the peaks and troughs of the pressure plot, the distance of the vortex away from the nose at the time of a pressure peak or trough was determined. The frames at the start of the peaks and troughs of the pressure for the two side sensors closest to the robot nose were extracted from the datasets. These frames were then examined in the DPIV data and the position of the vortex calculated, giving the distance of the vortex away from the nose. These values were normalised by the size of the cylinder, and are given in Table 6.5. It can be seen that, on average, the vortex is approximately one cylinder diameter in front of the nose when the pressure pattern records the start of a peak or trough. This value is shorter than the wavelength (the longitudinal distance between two vortices of the same rotational direction), or half the wavelength (the longitudinal distance between two vortices of differing rotational directions), of the associated Kármán vortex street.

Reynolds number, $\times 10^3$	8.6	17.0	22.6
Normalised wavelength	3.94	3.60	3.46
Normalised vortex distance from nose	0.87±0.19	0.84±0.14	1.33±0.3

Table 6.5: Distances of the vortices from the nose of the robot, with changing flow speed. The frames chosen are those at the start of the peaks and troughs of the pressure plots. The values are normalised by the cylinder diameter. The error given is the standard deviation.

Changing the flow speed: summary

By changing the flow speed the parameters which describe the Kármán vortex street change. Three different flow speeds were tested to present a variety of different parameter changes. It was found that the normalised size and circulation of the vortices stayed approximately constant with increasing flow speed as was found in the flow characterisation experiments. In addition it was found that the peak-to-peak pressure amplitudes increased with increasing flow speed and showed greater values and variation than when the robot was in steady flow. The pressure patterns showed a 180° phase difference between the two sides of the head; this is a good indicator that vortices are being sensed. This is supported by the results from examining the synchronised pressure and DPIV frames. The pressure plots show peaks from the right-hand side, equating with troughs on the left-hand side, when a negative vortex is approaching the robot; the opposite is also true, giving a trough from the right-hand side and a peak from the left-hand side, when a positive vortex is in front of the robot. These peaks and troughs occur when the vortex is approximately one cylinder diameter in front of the robot's nose; this value is shorter than the calculated wavelength, or half of the wavelength, of the Kármán vortex street when no robot was present.

6.2.2 Changing the size of the cylinder

Changing the size of the cylinder also changes the parameters of the Kármán vortex street. To investigate this, three different cylinder sizes were tested; 25, 45 and 100mm diameters. The robot was placed three diameters downstream of the cylinders (Figure 6-16) at a single flow speed of 21.9cm s^{-1} giving Reynolds numbers of 4.3 $\times 10^3$, 7.7 $\times 10^3$ and 17.0 $\times 10^3$ for the cylinder sizes respectively. These Reynolds numbers are lower than for the previous experiment, where the flow speed was altered, but they remain in the intermediate subcritical shedding regime.

From the flow characterisation it was found that the overall trend of the normalised size and strength of the vortices decreased with increasing cylinder size, although with an anomalous result for the circulation behind the 100mm diameter cylinder at a Reynolds number of 7.7 $\times 10^3$. This same trend is shown when the robot is positioned behind the cylinder, with a greater disparity within the results between the cylinder sizes; Figure 6-11.

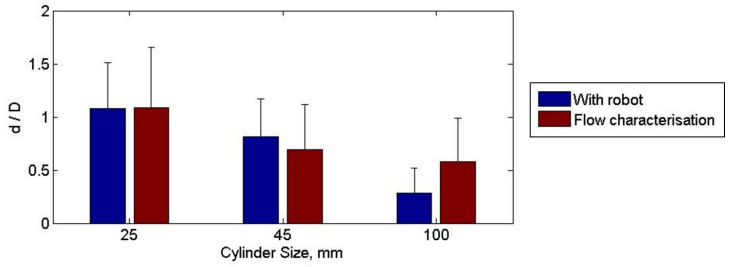

(a)

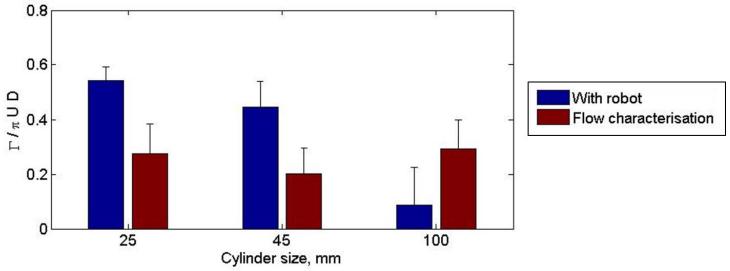

(b)

Figure 6-11: Normalised size (a) and normalised circulation (b) with the robot positioned three cylinder diameters downstream of the 25, 45 and 100mm diameter cylinders, compared to the results of the flow characterisation where no robot was present.

The pressure signals, Figure 6-12 (a), (b) and (c), show a 180° difference between the two sides of the head, as in Section 6.2.1. There is a clear distinction, as well, between the number of peaks and troughs present when the 25mm diameter cylinder was used compared to the larger cylinders. This matches the trend of the vortex shedding frequency, which decreases with increasing cylinder size. The peak-to-peak amplitudes of the pressure signals were examined and found to remain approximately constant at around 30Pa for each of the cylinder sizes. The dominant frequency detected from the pressure sensors is similar for each cylinder to the experimental frequency calculated in Chapter 4; these are presented in Table 6.6. The magnitudes of the dominant frequencies were examined and found to remain approximately constant with cylinder size with the greatest values in the sensor pair closest to the nose, Table 6.7.

Cylinder size, mm	25	45	100
Dominant frequency, Hz	1.66	0.88	0.391
DPIV frequency, Hz	1.81	0.94	0.51
Strouhal frequency, Hz	1.57	0.87	0.39

Table 6.6: Dominant frequencies detected by the pressure sensors for each of the cylinder sizes 25, 45 and 100mm. The values calculated from the DPIV data within the flow characterisation and values calculated from the Strouhal relationship are also given.

The frames at which the peaks and troughs were present in the pressure data were also analysed

Sensor pair Cylinder size	1	2	3	4
25mm	17.51	7.18	4.19	2.03
45mm	15.14	7.67	6.68	5.34
100mm	19.47	10.96	9.77	8.04

Table 6.7: Magnitudes of the dominant frequencies for each of the four sensor pairs behind the 25, 45 and 100mm diameter cylinders at Reynolds numbers relative to the cylinders of 4.3 $\times 10^3$, 7.7 $\times 10^3$ and 17.0 $\times 10^3$.

in DPIV. The start of a peak on the right-hand sensor, and trough on the left-hand sensor, occurs when a negative (clockwise) vortex is approaching the nose and a right-hand trough, and left-hand peak, occur when a positive (anticlockwise) vortex is approaching the nose, Figures 6-13 to 6-15. This is the same pattern as seen in the previous experimental set, when the flow speed was changed around a single cylinder (section 6.2.1). The distances of the vortices upstream of the robot at these points were also determined; Table 6.8. These values show a slightly greater average than the results when the flow speed was altered, of 1.37 cylinder diameters. As previously, the normalised distance of the vortex away from the nose is lower than the normalised wavelength, or half wavelength, of the Kármán vortex street.

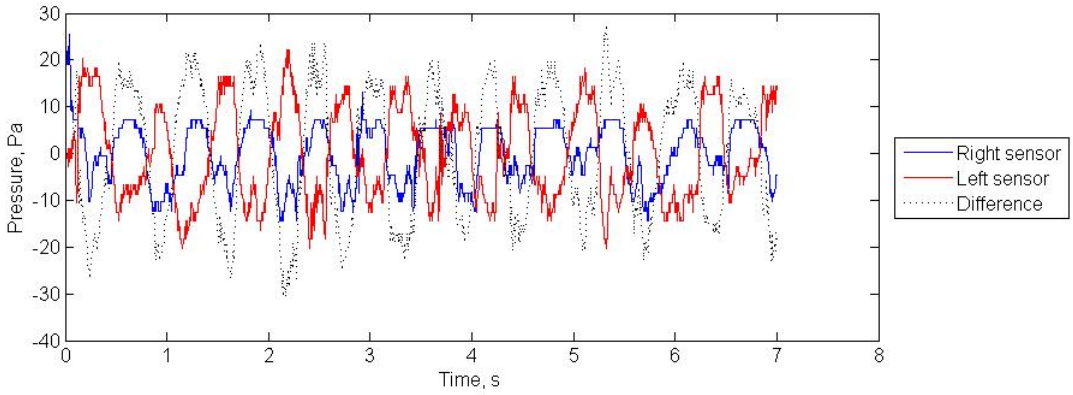

(a)

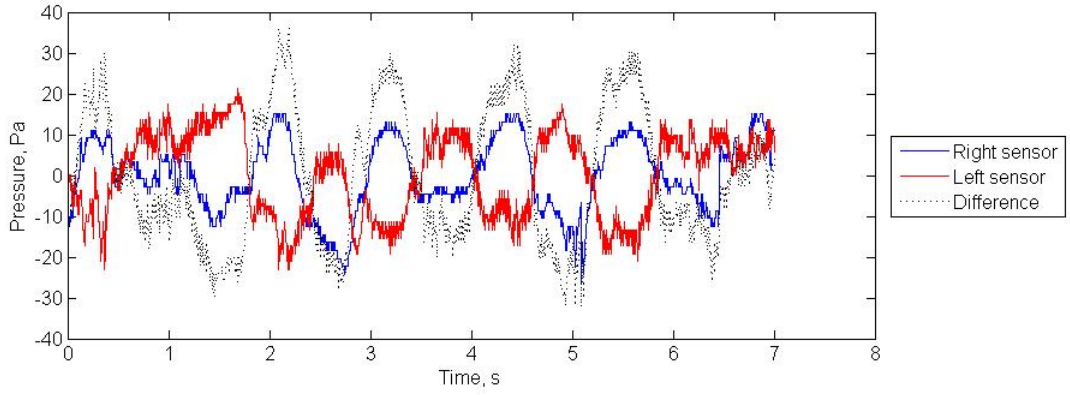

(b)

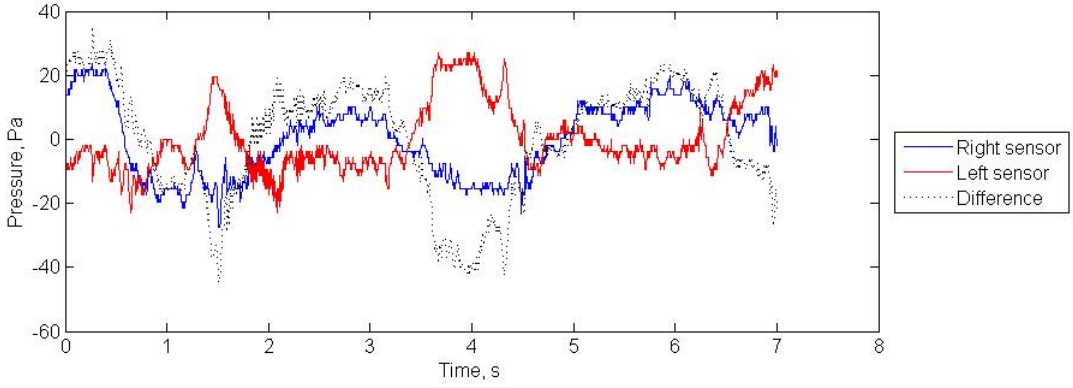

(c)

Figure 6-12: Pressure plots from the robot placed in the Kármán vortex street behind the (a) 25mm, (b) 45mm and (c) 100mm diameter cylinders. The blue line indicates the sensor next to the nose on the right-hand side of the robot, the red line indicates the sensor next to the nose on the left-hand side of the robot. The dotted line shows the difference between these two sensor signals.

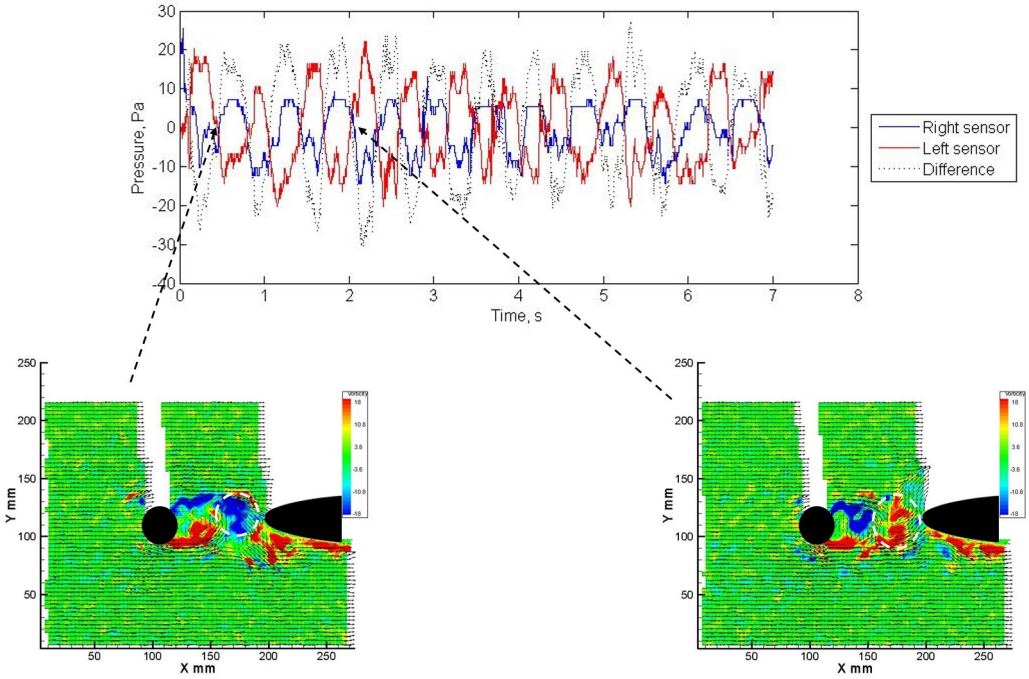

Figure 6-13: The pressure plot, with associated DPIV frames, from the robot placed in the Kármán vortex street behind the 25mm diameter cylinder. Within the DPIV image, the left-hand area of white is the cylinder and its shadow in the laser sheet and the right-hand white image is the robot and its shadow in the laser sheet. The red areas indicate positive (anti-clockwise) vorticity and blue indicating negative (clockwise) vorticity. The DPIV images show, on the right the point at which there is a peak on the left-hand pressure signal and a corresponding trough on the right-hand pressure signal. At this point there is a positive (red) vortex approaching the robot. The left-hand image illustrates the point at which there is a peak on the right-hand pressure sensor and a corresponding trough on the left-hand sensor. At this point a negative (blue) vortex is approaching the robot. The vortices are highlighted in the images.

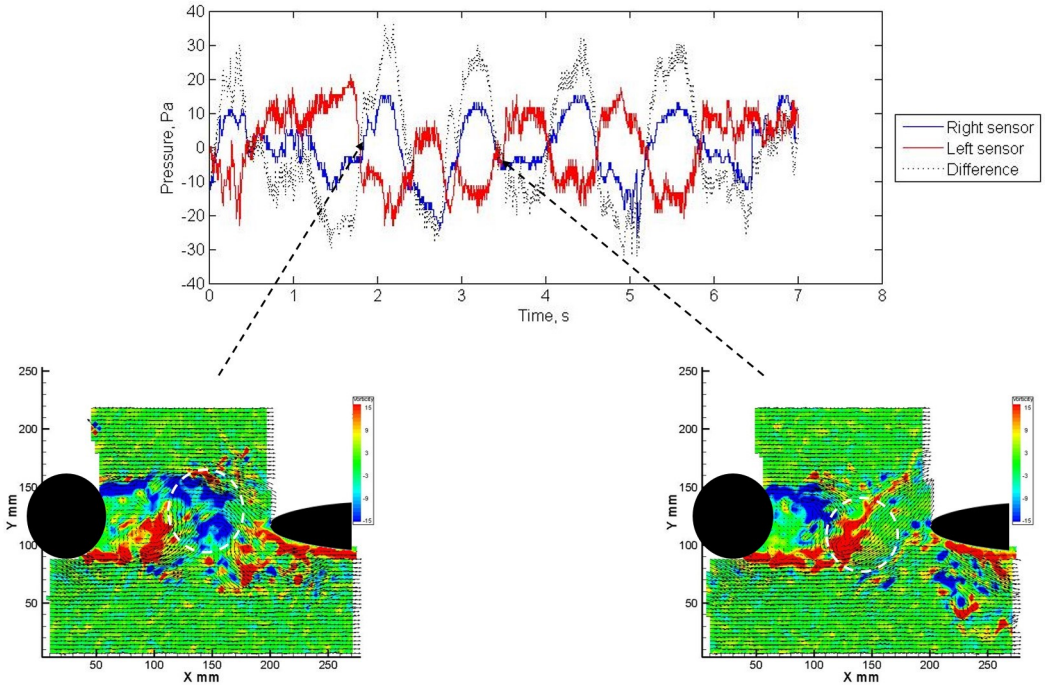

Figure 6-14: Pressure plots, with associated DPIV frames, from the robot placed in the Kármán vortex street behind the 45mm diameter cylinder. Within the DPIV image, the left-hand white area is the cylinder and its shadow and the right-hand white are is the robot and its shadow. The larger right-hand area indicates the larger size cylinder. The DPIV images show, on the right the point at which there is a peak on the left-hand pressure signal and a corresponding trough on the right-hand pressure signal. At this point there is a positive (red) vortex approaching the robot. The left-hand image illustrates the point at which there is a peak on the right-hand pressure sensor and a corresponding trough on the left-hand sensor. At this point a negative (blue) vortex is approaching the robot. The vortices are highlighted in the images.

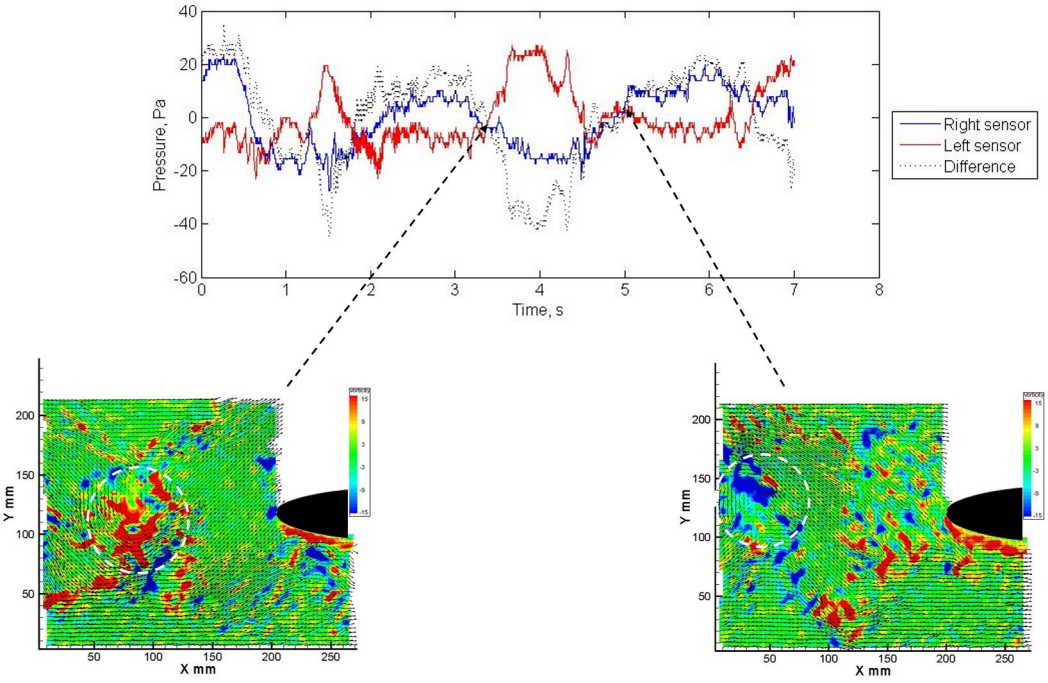

Figure 6-15: Pressure plots, with associated DPIV frames, from the robot placed in the Kármán vortex street behind the 100mm diameter cylinder. Within the DPIV image the right-hand white are is the robot and its shadow. The cylinder is not visible for this experiment. The DPIV images show, on the left the point at which there is a peak on the left-hand pressure signal and a corresponding trough on the right-hand pressure signal. At this point there is a positive (red) vortex approaching the robot. The right-hand image illustrates the point at which there is a peak on the right-hand pressure sensor and a corresponding trough on the left-hand sensor. At this point a negative (blue) vortex is approaching the robot. The vortices are highlighted in the images.

Cylinder Size mm	25	45	100
Normalised wavelength	3.93	3.96	3.6
Normalised vortex distance from nose	1.30±0.14	1.36±0.17	1.45±0.27

Table 6.8: Distances of the vortices from the nose of the robot with changing cylinder size. The frames chosen were those at the start of the peaks and troughs of the pressure plots. The values were normalised by the cylinder diameter. The error given is the standard deviation.

Changing the cylinder size: Summary

By changing the cylinder used to create the Kármán vortex street, the parameters of the Kármán vortex street change; three different cylinder sizes were used. It was found that the normalised size and circulation results followed the general trend of the flow characterisation data, decreasing with increasing cylinder size. The different vortex shedding frequencies produced by the different cylinders were clear in the pressure signals, where the frequency of the

peaks and troughs approximately matched the frequencies calculated from the DPIV data in the flow characterisation. The dominant frequencies extracted from the pressure signals support this, as they were close to the values from the DPIV data and calculated from the Strouhal number. The magnitude of the frequencies remained approximately constant with increasing cylinder size. The peak-to-peak amplitude of the pressure signal also remained approximately constant with increasing cylinder size and the pressure signals showed a 180° phase difference between the sides of the head. The peaks and troughs of the right-hand sensor and left-hand sensor occur with an approaching negative and positive vortex respectively; the vortex is, on average, 1.37 cylinder diameters upstream of the robot nose when a pressure peak starts.

6.2.3 Moving the robot towards the cylinder

This study was used to determine whether the change in vortex characteristics associated with the maturity of the Kármán vortex street could be detected by the pressure sensors. Experiments were carried out with the robot placed at one, two and three cylinder diameters downstream of all three cylinder sizes, 25, 45 and 100mm, Figure 6-16. A single flow speed of 21.9cm s^{-1} was used, giving Reynolds numbers of 4.3 $\times 10^3$, 7.7 $\times 10^3$ and 17.0 $\times 10^3$ for the three cylinder sizes respectively.

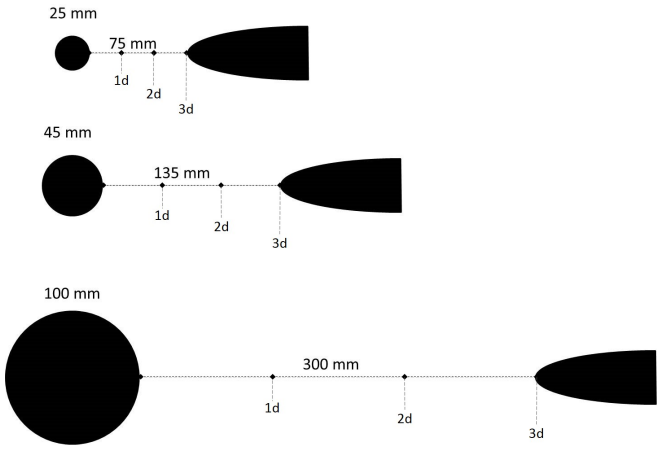

Figure 6-16: Image illustrating the 3D position of the robot behind the 25, 45 and 100mm diameter cylinders.

No clear information could be determined from the DPIV data of the robot at one diameter downstream of the cylinder; the robot was so close to the cylinder in this position that the vortices did not fully form before interacting with the robot.

The normalised vortex size and circulation results are presented in Figure 6-17 for the robot positioned at two and three diameters downstream, compared to the results from the flow characterisation experiments. The normalised size and circulation values decrease with increasing cylinder size which matches the pattern within the previous experiments, where the robot was

placed behind different sized cylinders. For both of these parameters, the values are highest when the robot is positioned three diameters downstream, except for the largest cylinder where the values are approximately equal.

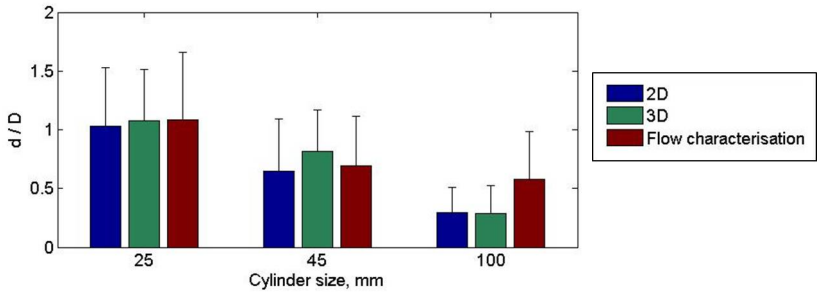

(a)

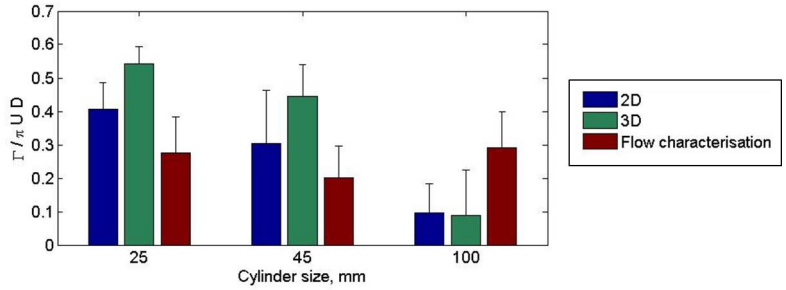

(b)

Figure 6-17: Normalised size (a) and normalised circulation (b) with the robot positioned at two and three cylinder diameters downstream of the 25, 45 and 100mm diameter cylinders. The error bars shown are the standard deviation over the number of vortices detected.

The pressure plots at one, two and three diameters for each of the cylinders are shown in Figures 6-18 to 6-20. At one diameter downstream, there is very little pattern shown; the 100mm cylinder shows the greatest indication of vortices sensed, but no individual vortex could be determined from the DPIV data. Clearer patterns can be seen for all cylinder sizes at two and three diameters with a 180° phase difference between either side of the head as before. The peak-to-peak pressure amplitudes remain approximately constant at 30 – 40Pa for all of the cylinder sizes at each of the downstream positions tested. In addition, the dominant frequency was extracted from the pressure signals, Table 6.9. At one diameter downstream, only the results behind the 100mm diameter cylinder captures the vortex shedding frequency. The results behind the 25 and 45mm diameter cylinder are both low compared to the previous empirical results, or those calculated using the Strouhal number. At two diameters downstream, both the 25 and 100mm diameter cylinder results show the vortex shedding frequency, but the 45mm diameter cylinder results match those at one diameter which are low. At three diameters downstream, the vortex shedding frequencies are detected behind all of the cylinder sizes. The magnitudes of the frequencies remained approximately constant for each of the positions tested.

At one diameter downstream, there is a trend of increasing magnitude with increasing cylinder size but this is not repeated at the other positions, Table 6.10

Position downstream	1D	2D	3D
25mm	0.39±0.19	1.56	1.66
45mm	0.73±0.05	0.684	0.879
100mm	0.391	0.488	0.391

Table 6.9: Dominant frequencies from the pressure signals behind the 25, 45 and 100mm diameter cylinders at positions of one, two and three diameters downstream.

Sensor pair	1	2	3	4
1D				
25mm	3.75	2.32	1.3	1.58
45mm	7.81	5.15	7.80	4.92
100mm	17.96	16.64	21.21	15.20
2D				
25mm	22.46	7.49	3.56	2.25
45mm	20.85	9.94	8.11	6.11
100mm	22.21	11.96	10.59	8.43
2D				
25mm	17.51	7.18	4.192	2.03
45mm	15.14	7.67	6.68	5.34
100mm	19.47	10.96	9.77	8.04

Table 6.10: Magnitudes of the dominant frequencies for each of the sensor pairs along the side of the robot head for each of the three positions behind the 25, 45 and 100mm diameter cylinders.

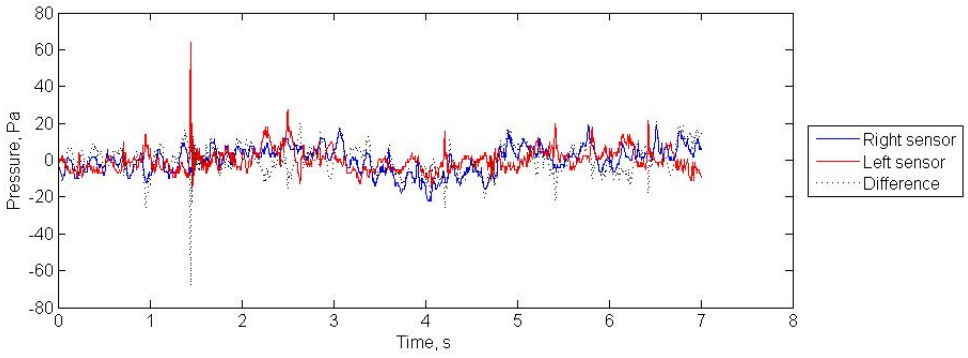

(a)

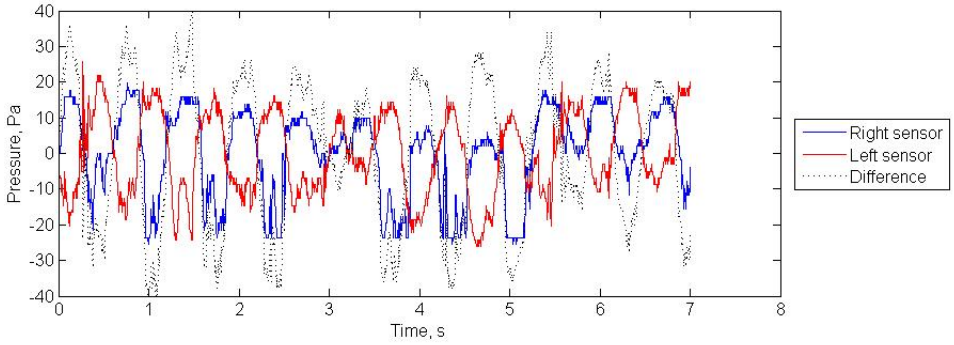

(b)

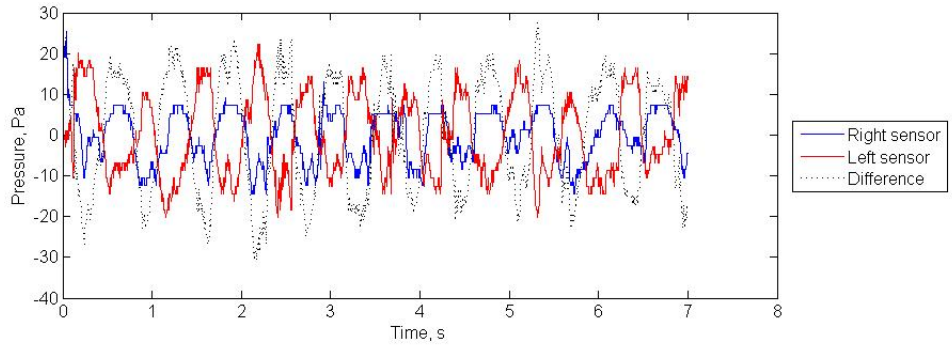

(c)

Figure 6-18: Pressure plots from the robot placed in the Kármán vortex street behind the 25mm diameter cylinder at (a) one diameter, (b) two diameters and (c) three diameters downstream. The blue line indicates the sensor next to the nose on the right-hand side of the robot, the red line indicates the sensor next to the nose on the left-hand side of the robot. The dotted line shows the difference between these two sensor signals.

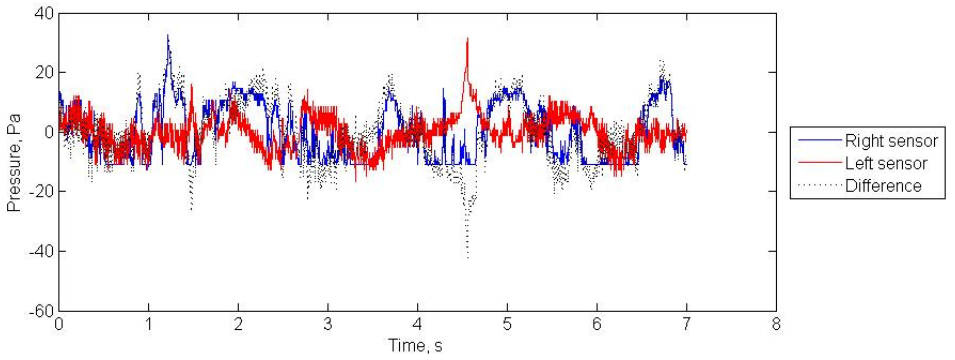

(a)

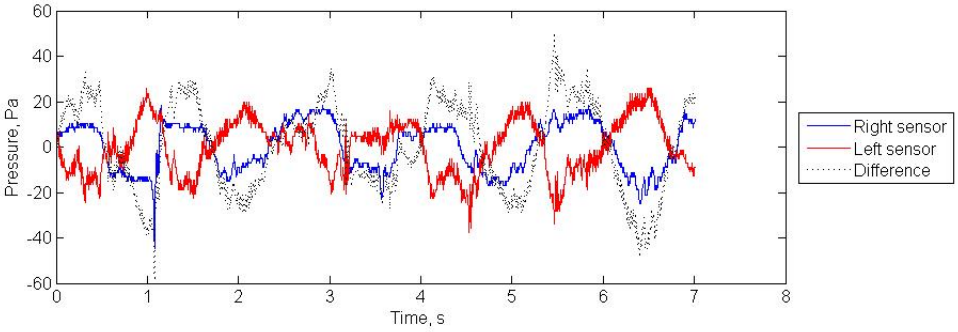

(b)

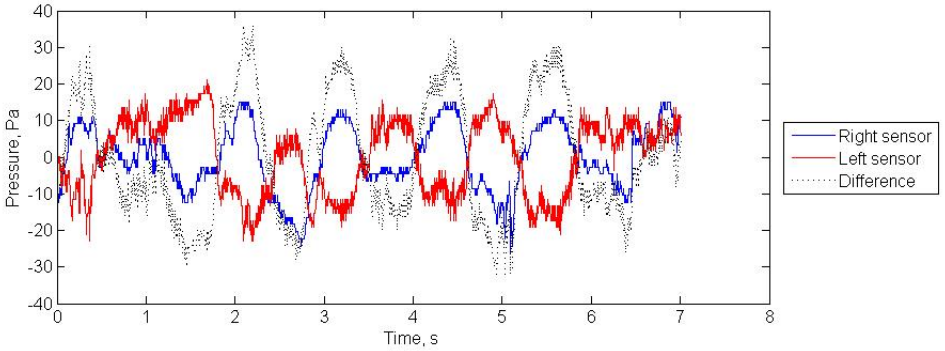

(c)

Figure 6-19: Pressure plots from the robot placed in the Kármán vortex street behind the 45mm diameter cylinder at (a) one diameter, (b) two diameters and (c) three diameters downstream. The blue line indicates the sensor next to the nose on the right-hand side of the robot, the red line indicates the sensor next to the nose on the left-hand side of the robot. The dotted line shows the difference between these two sensor signals.

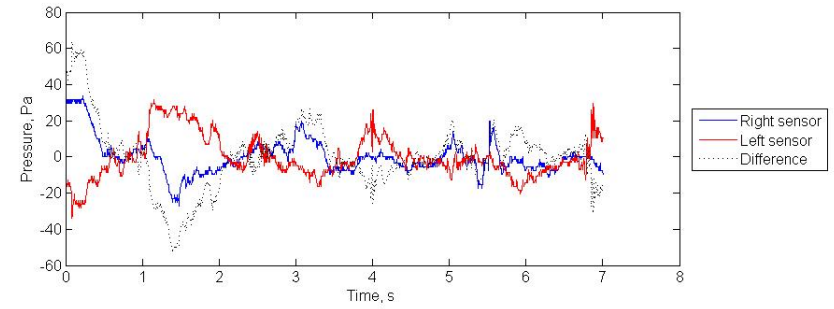

(a)

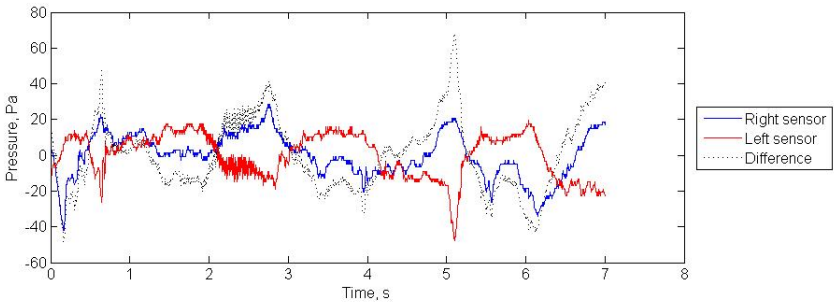

(b)

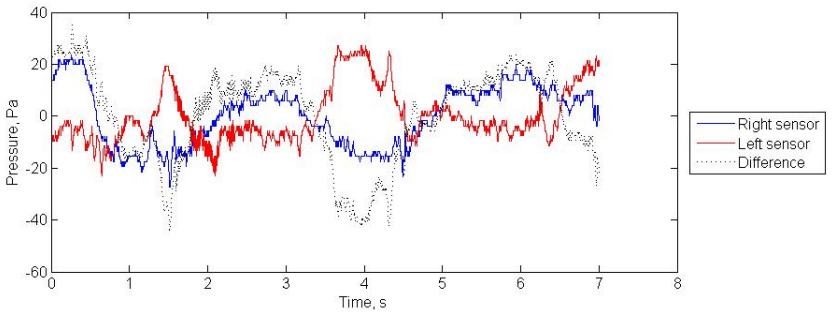

(c)

Figure 6-20: Pressure plots from the robot placed in the Kármán vortex street behind the 100mm diameter cylinder at (a) one diameter, (b) two diameters and (c) three diameters downstream. The blue line indicates the sensor next to the nose on the right-hand side of the robot, the red line indicates the sensor next to the nose on the left-hand side of the robot. The dotted line shows the difference between these two sensor signals.

The frames at which the pressure registered peaks and troughs were examined within the DPIV data. A negative (clockwise) vortex approaching the robot created a peak on the right-hand sensor and a trough on the left-hand sensor; a positive (anticlockwise) vortex approaching the robot created a peak on the left-hand sensor and a trough on the right-hand sensor. The results at two diameters and three diameters downstream are shown in Figures 6-21 to 6-26.

In addition, the distance between the approaching vortex and the nose of the robot was extracted; these values, normalised by the cylinder diameter, are given in Table 6.11. Only the values for when the robot was positioned two diameters and three diameters downstream of the cylinders are given, as no conclusive results could be obtained when the robot was one diameter downstream. The Kármán vortex street wavelengths are also given. These results show that the vortices were, on average, 1.1 and 1.4 cylinder diameters upstream of the robot at the two diameter and three diameter positions respectively.

	Two diameters	Three diameters	Kármán vortex street wavelength
25mm	1.13±0.21	1.30±0.14	3.93
45mm	1.33±0.27	1.36±0.17	3.96
100mm	0.90±0.07	1.45±0.27	3.6

Table 6.11: Normalised distance of the vortex in front of the nose of the robot at the start of the peaks and troughs within the pressure signals. The normalised wavelength for the associated Kármán vortex street is also given.

Moving towards the cylinder: Summary

The robot was positioned at one, two and three cylinder diameters downstream of the 25, 45 and 100mm diameter cylinders at Reynolds numbers relative to the cylinder size of 4.3 $\times 10^3$, 7.7 $\times 10^3$ and 17.0 $\times 10^3$ respectively. In general, the position at one diameter downstream meant that the robot was too close to the cylinder for the DPIV or the pressure sensors to capture any useful data. The normalised size and circulation were calculated and found to increase slightly with increasing distance from the cylinder but decreased with increasing cylinder size, as was found in the previous section where the cylinder size was changed. The pressure signals showed approximately 180° phase difference between the sides of the head. The peak-to-peak amplitudes of the pressure signals showed no significant change with either cylinder size or position behind the cylinder. The pressure patterns follow the same trend as found previously, where a peak in the right-hand pressure sensor signal, and, therefore, a trough in the left-hand pressure sensor signal, occurs when a negative vortex is approaching the robot, and vice versa. In addition, it was found that the vortices were detected by the pressure sensors when they were, on average, 1.1 and 1.4 cylinder diameters in front of the robot for the two diameter and three diameter positions respectively, which are shorter than the wavelength and half-wavelength of the Kármán vortex streets calculated from the flow characterisation.

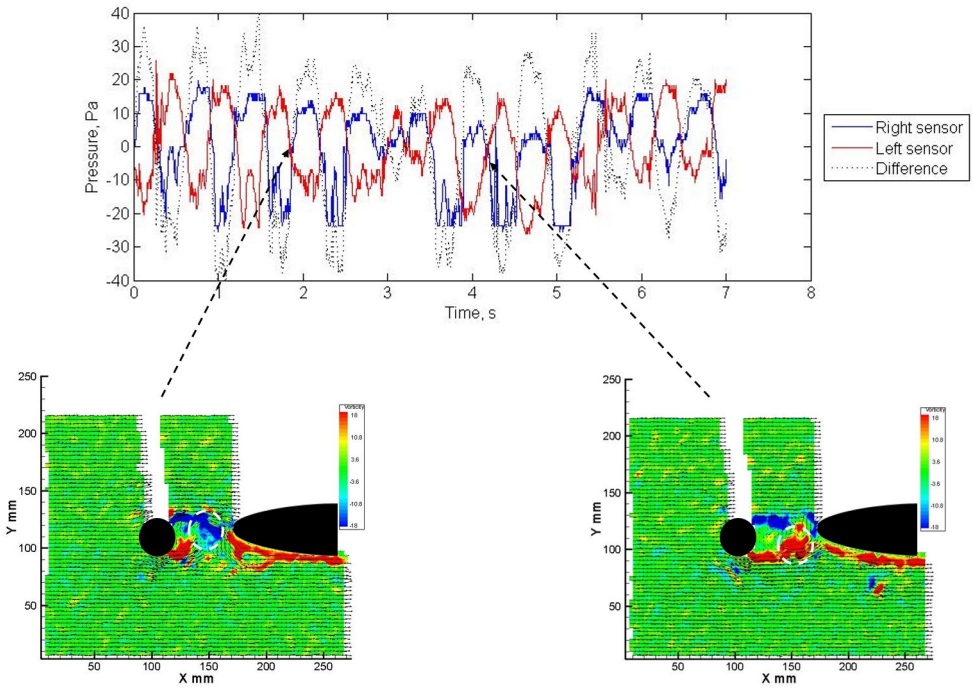

Figure 6-21: Pressure plots and linked DPIV frames from the robot placed in the Kármán vortex street behind the 25mm diameter cylinder at two diameters downstream. Within the DPIV image the left-hand white image is the cylinder and its shadow and the right-hand white image is the robot and its shadow. The DPIV images show, on the left the point at which there is a peak on the right-hand pressure sensor and a corresponding trough on the left-hand sensor. At this point a negative (blue) vortex is approaching the robot. The right-hand images show a peak on the left-hand pressure signal and a corresponding trough on the right-hand pressure signal. At this point there is a positive (red) vortex approaching the robot. The vortices are highlighted in the images.

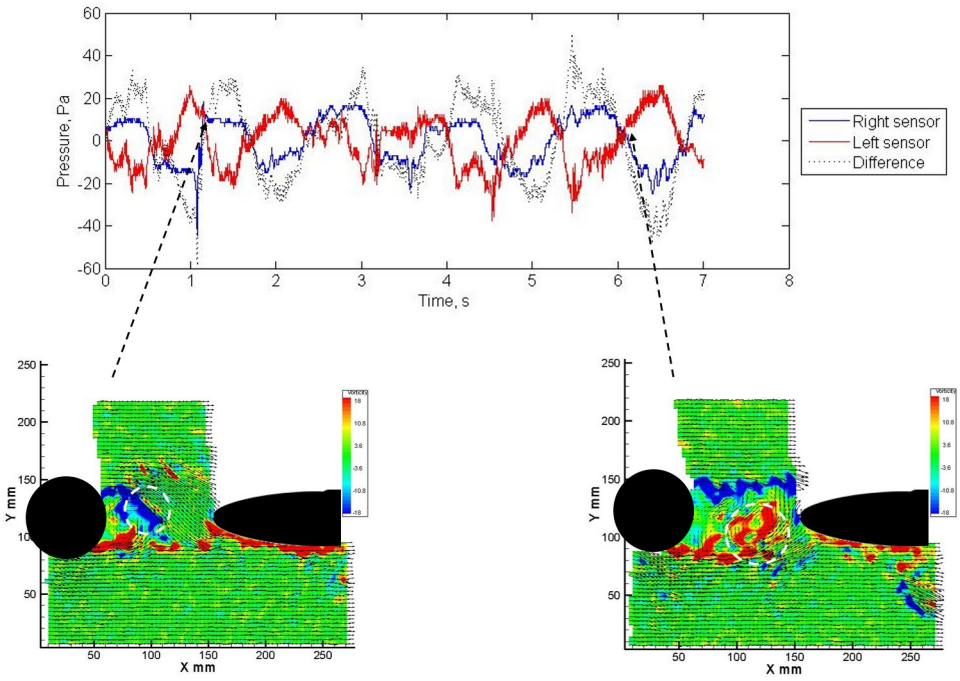

Figure 6-22: Pressure plots and linked DPIV frames from the robot placed in the Kármán vortex street behind the 45mm diameter cylinder at two diameters downstream. Within the DPIV image the left-hand white image is the cylinder and its shadow and the right-hand white image is the robot and its shadow. The DPIV images show, on the left the point at which there is a peak on the right-hand pressure sensor and a corresponding trough on the left-hand sensor. At this point a negative (blue) vortex is approaching the robot. The right-hand images show a peak on the left-hand pressure signal and a corresponding trough on the right-hand pressure signal. At this point there is a positive (red) vortex approaching the robot. The vortices are highlighted in the images.

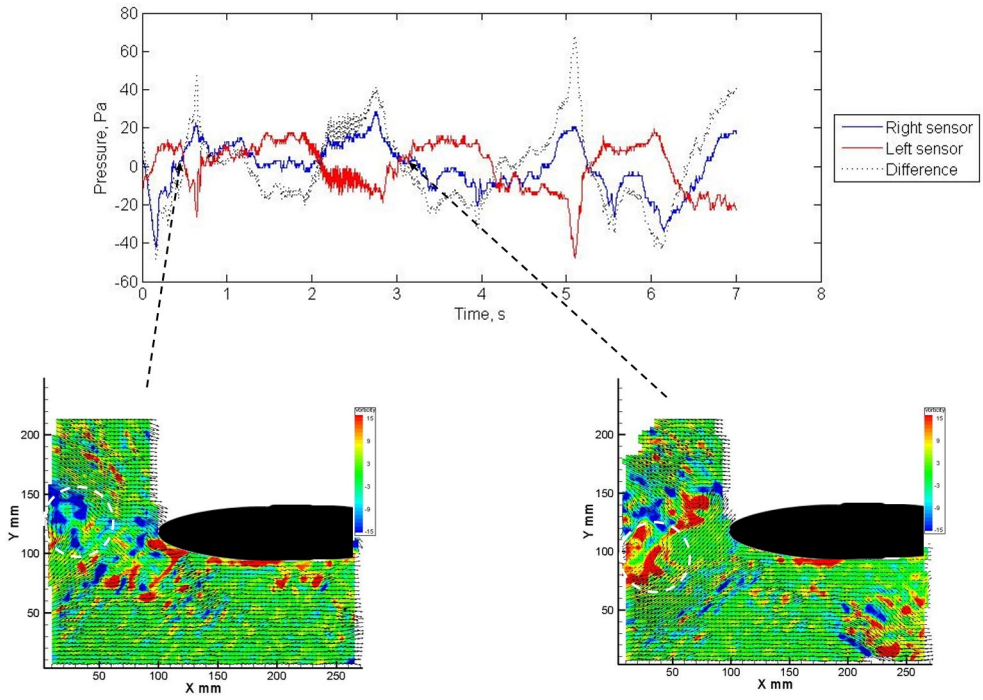

Figure 6-23: Pressure plots and linked DPIV frames from the robot placed in the Kármán vortex street behind the 100mm diameter cylinder at two diameters downstream. Within the DPIV image the white image is the robot and its shadow. The cylinder is not visible. The DPIV images show, on the left the point at which there is a peak on the right-hand pressure sensor and a corresponding trough on the left-hand sensor. At this point a negative (blue) vortex is approaching the robot. The right-hand images show a peak on the left-hand pressure signal and a corresponding trough on the right-hand pressure signal. At this point there is a positive (red) vortex approaching the robot. The vortices are highlighted in the images.

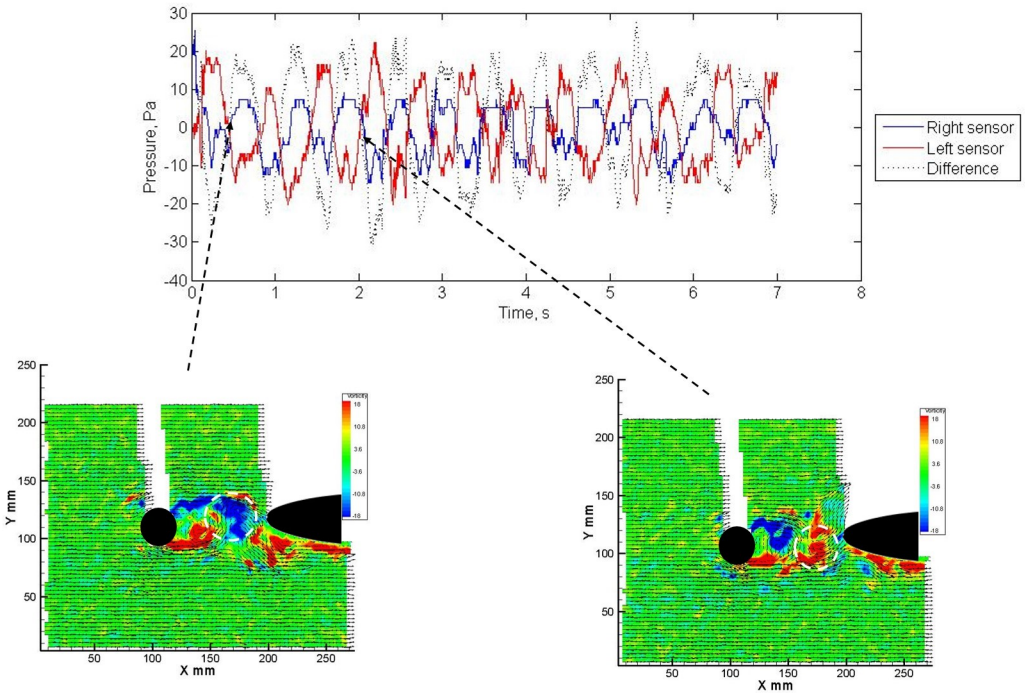

Figure 6-24: Pressure plots and linked DPIV frames from the robot placed in the Kármán vortex street behind the 25mm diameter cylinder at three-diameters downstream. The DPIV images show the approaching vortices corresponding to the peaks and troughs of the pressure sensors. A peak on the left-hand pressure sensor is linked to an oncoming positive vortex and a peak on the right-hand sensor is linked to an oncoming negative vortex.

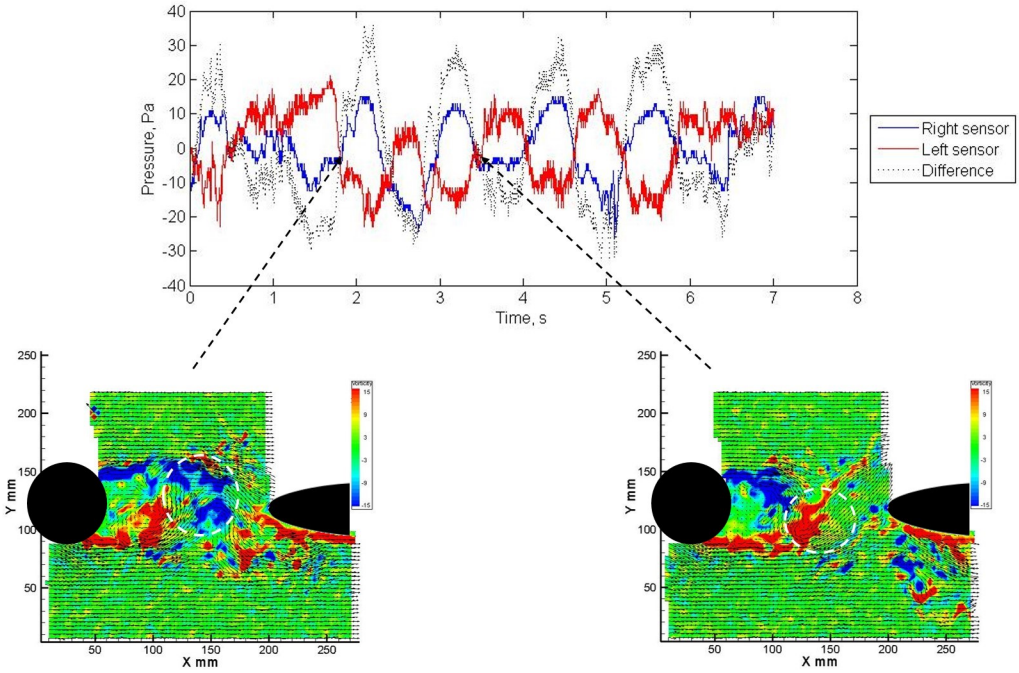

Figure 6-25: Pressure plots and linked DPIV frames from the robot placed in the Kármán vortex street behind the 45mm diameter cylinder at three-diameters downstream. The DPIV images show, as before, the approaching vortices corresponding to the peaks and troughs of the pressure sensors. A peak on the left-hand pressure sensor is linked to an oncoming positive vortex and a peak on the right-hand sensor is linked to an oncoming negative vortex.

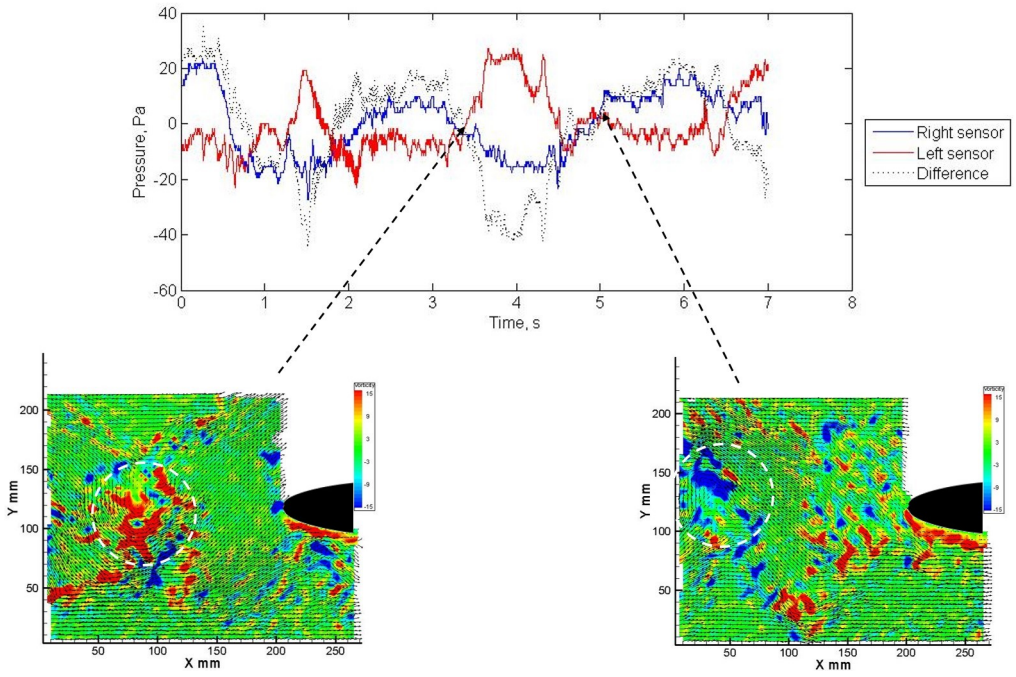

Figure 6-26: Pressure plots and linked DPIV frames from the robot placed in the Kármán vortex street behind the 100mm diameter cylinder at three-diameters downstream. As previously, the DPIV images show the approaching vortices corresponding to the peaks and troughs of the pressure sensors. A peak on the left-hand pressure sensor is linked to an oncoming positive vortex and a peak on the right-hand sensor is linked to an oncoming negative vortex.

6.2.4 Moving laterally out of the Kármán vortex street

A fish or a robot swimming within a natural environment is not guaranteed to approach an object, and experience the wake, from directly behind. To emulate this, the robot was moved laterally away from the centre line of the Kármán vortex street so that the effect on the pressure signals could be determined. This could potentially be used in navigational strategies in autonomous robot control. These experiments can also be used to determine whether the pressure signals can be used to determine the vortex position, with respect to which side of the head a vortex is present on (hypothesis 1). The experiments carried out placed the robot at the centre of the Kármán vortex street, 0cm; at the edge of the Kármán vortex street, 5cm away from the centre line; and then outside of the Kármán vortex street, 10cm from the centre line of the Kármán vortex street; Figure 6-27. The 100mm cylinder was used, at Reynolds numbers relative to the cylinder of 8.6 $\times 10^3$, 17.0 $\times 10^3$ and 22.6 $\times 10^3$.

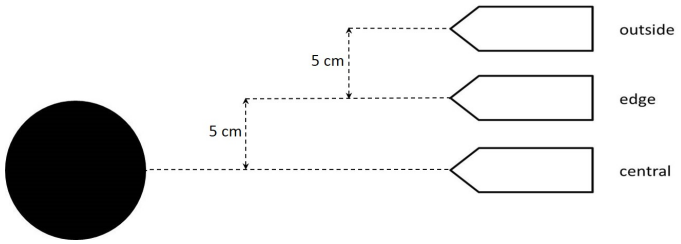

Figure 6-27: Positions of the robot behind when in the centre, at the edge and outside of the Kármán vortex street, with respect to the position of the 100mm cylinder.

The Kármán vortex street characteristics for these experiments were processed from DPIV and found to match those in section 6.2.1; the normalised size and circulation of the vortices remained approximately constant with increasing flow speed. These results are given in Figure 6-28.

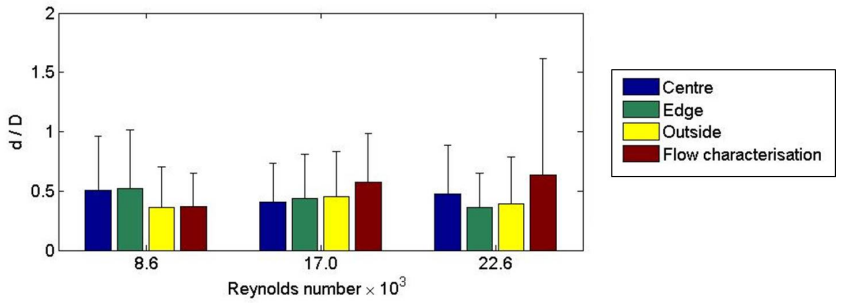

(a)

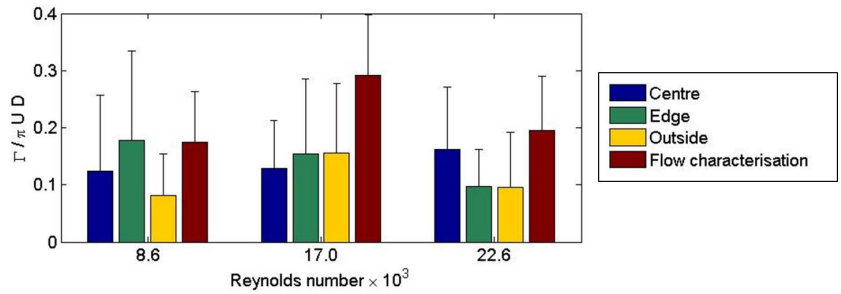

(b)

Figure 6-28: The normalised size and circulation of the vortices calculated when the robot was placed in the centre, at the edge and outside of the Kármán vortex street, along with the results from the flow characterisation data.

Figure 6-29 shows the pressure plots from the right-hand and left-hand side of the head respectively at the centre, edge and outside positions, at Re = 22.6 $\times 10^3$. It can be seen from these graphs that there is a clear pattern when the robot is in the centre, but this pattern reduces in clarity as the robot moves laterally out of the Kármán vortex street. This occurs at all flow

speeds tested, but at the lower Reynolds number of 17.0 $\times 10^3$ the reduction in clarity occurs only when the robot is moved to the outermost position. Figure 6-30 shows the pressure plots with both sides of the robot head on each graph, for all three positions. These show that the phase difference between the sides of the head decreases to nearly 0° with increasing distance from the centreline, where it is 180°. This is as expected, as the vortices will stop travelling down one side of the head as it moves out of the Kármán vortex street.

The peak-to-peak amplitudes of the pressure signals were examined and were found to increase with increasing flow speed when the robot was in the centre position, but this pattern reduced as the robot was moved to the edge and outside positions, Table 6.12. From examining the frequency from the pressure sensors, Table 6.13, it can be seen that they match the experimental values well when in the centre position, as found in previous experiments. As the robot is moved further out of the Kármán vortex street, the frequencies decrease and are no longer detected on all of the sensor pairs. At the edge position, the frequencies for the highest Reynolds number no longer match those from the flow characterisation data. At the outside position, some sensor pairs still detect the vortex shedding frequencies as first or second peaks, but for others the dominant frequencies have reduced as the robot is moved into the freestream flow. The magnitude of the dominant frequencies showed a trend of decreasing as the robot was moved out of the Kármán vortex street, Table 6.14.

Position	Centre	Edge	Outside
8.6 $\times 10^3$	10	10	10
17.0 $\times 10^3$	50	50	40
22.6 $\times 10^3$	100	40	50

Table 6.12: Peak-to-peak amplitude values of the pressure signals when the robot is placed in the centre, edge and outside positions at Reynolds numbers relative to the cylinder of 8.6 $\times 10^3$, 17.0 $\times 10^3$ and 22.6 $\times 10^3$.

Reynolds number	Centre	Edge	Outside	DPIV	Strouhal
11.0 $\times 10^3$	0.195	0.195	0.15±0.05	0.20	0.198
21.9 $\times 10^3$	0.391	0.488	0.25±0.15	0.51	0.393
29.0 $\times 10^3$	0.586	0.488	0.34±0.05	0.63	0.522

Table 6.13: Dominant frequencies extracted from the pressure signals when the robot was positioned in the centre, at the edge and outside of the Kármán vortex street at Reynolds numbers relative to the cylinder of 8.6 $\times 10^3$, 17.0 $\times 10^3$ and 22.6 $\times 10^3$. Values with variation are given if two frequencies were detected across the four sensor pairs.

Sensor pair	1	2	3	4
Centre				
11.0 $\times 10^3$	1.62	1.17	1.26	1.19
21.9 $\times 10^3$	17.69	12.41	9.46	7.65
29.0 $\times 10^3$	59.90	32.19	22.23	19.02
Edge				
11.0 $\times 10^3$	2.54	1.99	1.21	0.78
21.9 $\times 10^3$	33.10	14.52	10.64	9.34
29.0 $\times 10^3$	14.53	10.51	6.92	5.38
Outside				
11.0 $\times 10^3$	0.63	0.53	0.47	0.56
21.9 $\times 10^3$	10.44	6.35	4.91	4.32
29.0 $\times 10^3$	10.63	5.41	3.54	2.62

Table 6.14: Magnitudes of the dominant frequencies for each of the sensor pairs along the side of the robot head at the centre, edge and outside positions at Reynolds numbers relative to the cylinder of 8.6 $\times 10^3$, 17.0 $\times 10^3$ and 22.6 $\times 10^3$.

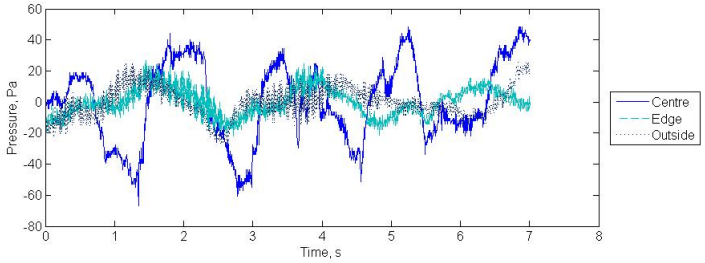

(a)

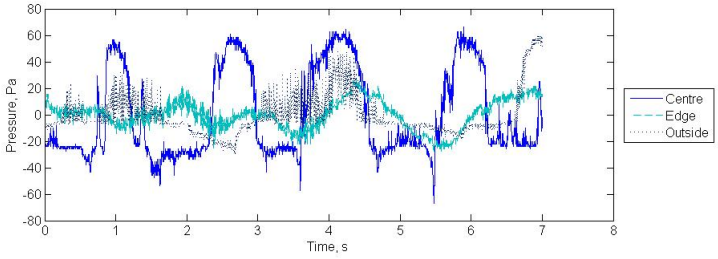

(b)

Figure 6-29: Pressure plots from (a) the right-hand side and (b) the left-hand side of the robot when it was positioned in the centre, at the edge and outside of the Kármán vortex street at a Reynolds number relative to the cylinder of 22.6 $\times 10^3$.

By examining the DPIV and pressure data together it was found that a negative (clockwise) vortex approaching the nose caused a peak on the right-hand sensor and a trough on the left-hand sensor, and a positive (anticlockwise) vortex approaching the nose caused a trough on the right-hand sensor and a peak on the left-hand sensor, Figure 6-31 to 6-33. The vortex was, on average, 1.13 cylinder diameters in front of the robot when a peak or trough occurred, Table

6.15. No values are given for the edge and outside positions at Re = 8.6 $\times 10^3$ as there was no clear pattern of peaks and troughs within the pressure data to detect a vortex. It can be seen that the distances from the robot nose to the vortex are smaller than the wavelength, or half wavelength, of the Kármán vortex street produced and presented within Chapter 4.

	Centre Position	Edge Position	Outside Position	Normalised Wavelength
11.0 $\times 10^3$	0.87±0.19	-	-	3.94
21.9 $\times 10^3$	0.84±0.14	1.10±0.43	1.39±0.10	3.60
29.0 $\times 10^3$	1.33±0.30	0.97±0.17	1.42±0.20	3.46

Table 6.15: Normalised distance of the vortex in front of the nose of the robot at the start of the peaks and troughs within the pressure signals when the robot was in the centre, edge and outside positions. The normalised wavelength for the associated Kármán vortex street is also given.

Moving laterally: summary

The normalised size and circulation of the vortices remained approximately constant with increasing flow speed. As the robot is moved out of the centre of the Kármán vortex street, the pressure pattern begins to reduce in clarity from the clear oscillations at a phase difference of 180° between the sides of the head, to a less pronounced pattern. The peak-to-peak amplitudes of the pressure signals decrease as the robot is moved out of the Kármán vortex street, with the edge and outside positions giving similar values. In addition, the dominant frequency detected decreases as the robot moves out from the central position behind the cylinder, and stops matching the vortex shedding frequency of the flow. The magnitude of the frequencies decrease significantly when outside of the Kármán vortex street when compared to the central position. By examining the DPIV and pressure data together it was found that a negative (clockwise) vortex approaching the nose caused a peak on the right-hand sensor and a trough on the left-hand sensor, and a positive (anticlockwise) vortex approaching the nose caused a trough on the right-hand sensor and a peak on the left-hand sensor. The vortex was, on average, 1.13 cylinder diameters in front of the robot when a peak or trough occurred.

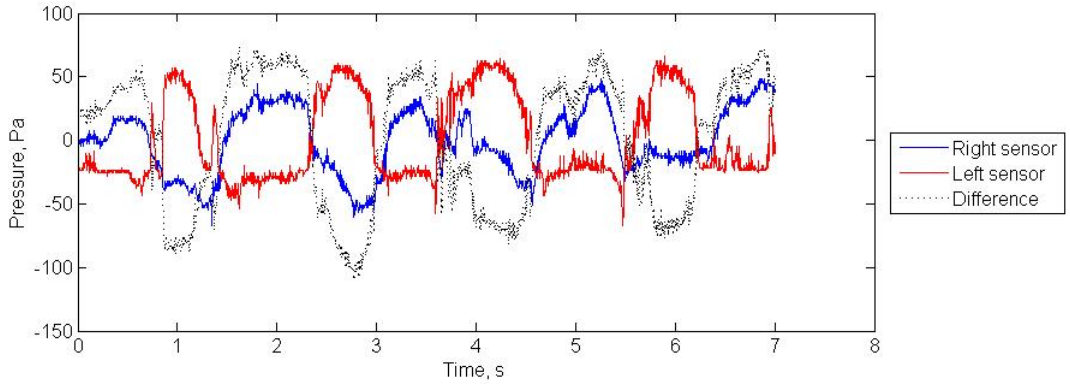

(a)

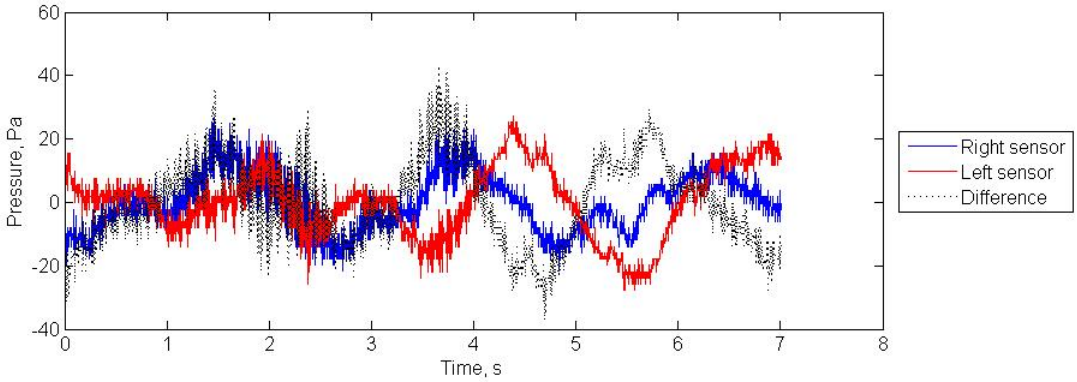

(b)

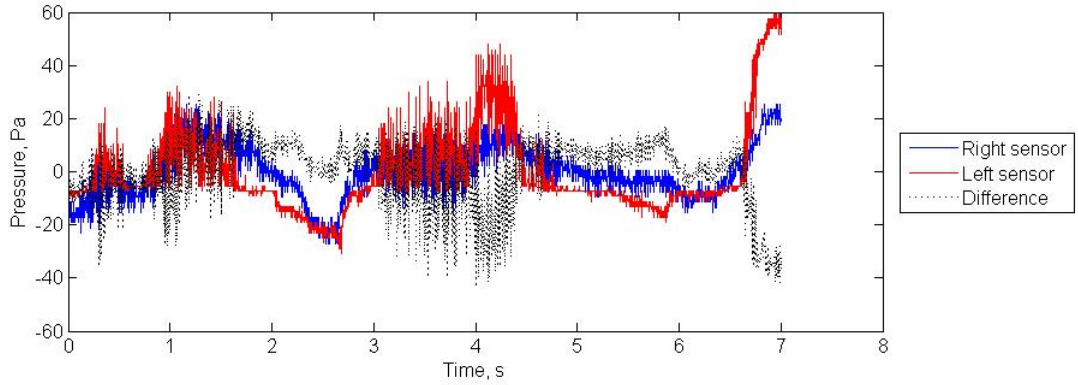

(c)

Figure 6-30: Pressure plots from the robot positioned (a) in the centre, (b) at the edge and (c) outside of the Kármán vortex street at a Reynolds number relative to the cylinder of 22.6 $\times 10^3$.

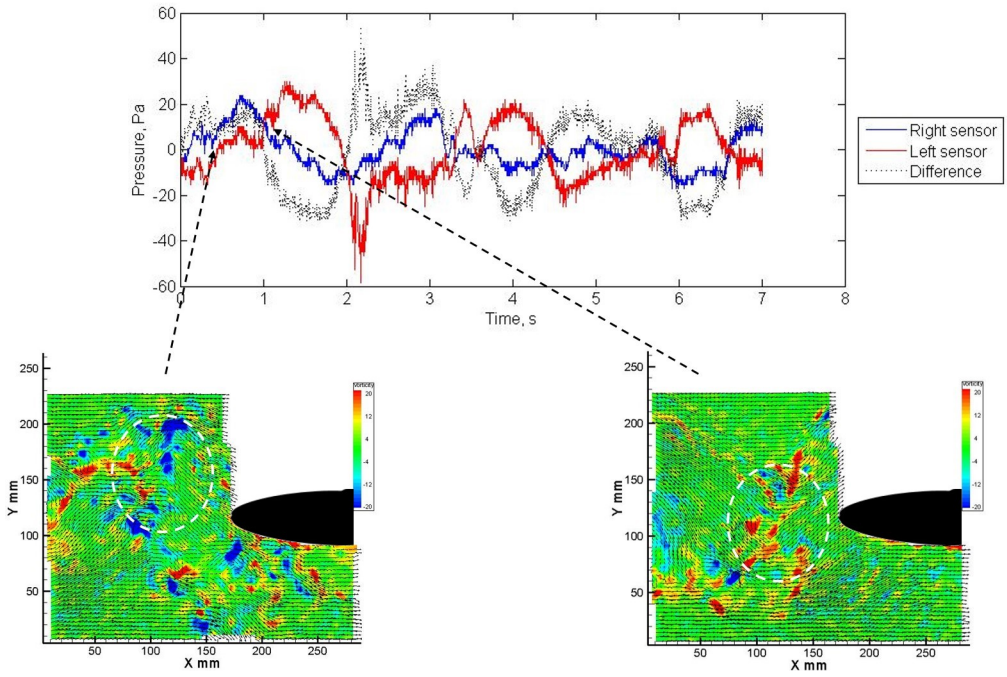

Figure 6-31: Pressure plots and associated DPIV frames from the robot positioned in the centre of the Kármán vortex street at a Reynolds number relative to the cylinder of 17.0 $\times 10^3$. These images illustrate the frames within the DPIV capture that correspond to the peaks and troughs of the pressure signals. A peak on the left-hand pressure sensor is linked to an oncoming positive vortex and a peak on the right-hand sensor is linked to an oncoming negative vortex.

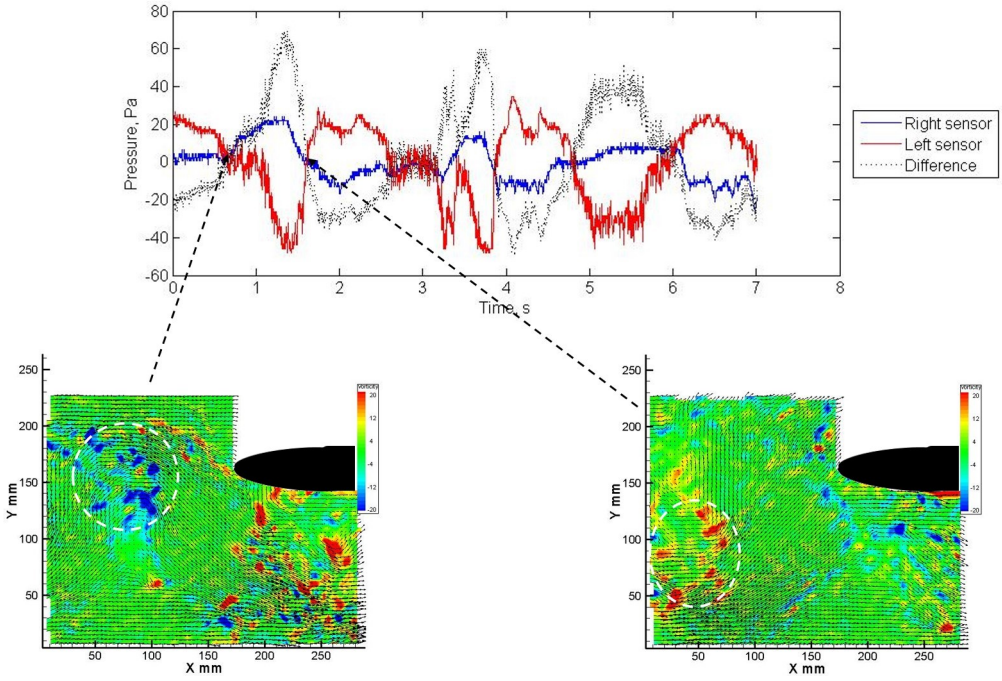

Figure 6-32: Pressure plots and associated DPIV frames from the robot positioned at the edge and of the Kármán vortex street at a Reynolds number relative to the cylinder of 22.6 $\times 10^3$. These images illustrate the frames within the DPIV capture that correspond to the peaks and troughs of the pressure signals. A peak on the left-hand pressure sensor is linked to an oncoming positive vortex and a peak on the right-hand sensor is linked to an oncoming negative vortex.

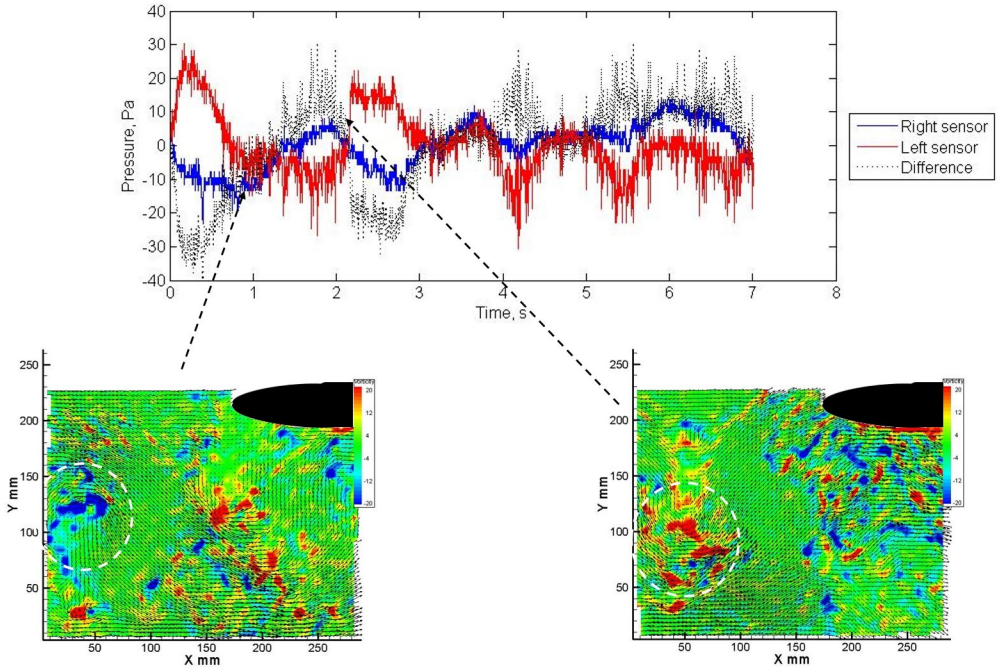

Figure 6-33: Pressure plots and associated DPIV frames from the robot positioned outside of the Kármán vortex street at a Reynolds number relative to the cylinder of 22.6 $\times 10^3$. These images illustrate the frames within the DPIV capture that correspond to the peaks and troughs of the pressure signals. A peak on the left-hand pressure sensor is linked to an oncoming positive vortex and a peak on the right-hand sensor is linked to an oncoming negative vortex.

6.2.5 The effect of head angle

A fish will not always be able to keep its head straight in to the direction of flow. The experiments, that were initially carried out in steady flow Section 6.1, were, therefore, repeated in the Kármán vortex street to gain an understanding of the pressure signals that can occur in an unsteady flow regime when the head is angled to the oncoming flow. The 45mm diameter cylinder was used at Re = 21.9 $\times 10^3$ for all of the head angles; 0°, ±5°, ±10°, ±20°, ±30° and ±40°, Figure 6-4, with the robot positioned three diameters downstream of the cylinder.

As all of the experiments were carried out using the same cylinder size and flow speed the Kármán vortex street characteristics remained approximately constant for each of the head positions. The average normalised circulation for the experiments was 0.28±0.05 and the average normalised size of the vortices was 0.42±0.07.

The pressure plots of the robot at 0°, 10° 20° 30° and 40° are shown in Figures 6-34 and 6-35. They show that there is little change until the ±20° angles. After this point, the pattern of peaks and trough that has signified the Kármán vortex street begins to disappear, along with the phase angle between the sides of the head. The peak-to-peak amplitudes of the pressure

signals remain approximately constant at 30 – 40Pa. These amplitudes begin to reduce at the higher angles of attack (above $\pm 20°$), but not in a coherent pattern.

The dominant frequency detected was 0.88 ± 0.1Hz, until $\pm 40°$, where the dominant frequency begins to drop, particularly at the nose, where the distance from the cylinder wake is greatest. It was also found that the magnitudes of the dominant peaks decrease as the head is angled away from the direction of flow; up to $\pm 10°$, the frequency magnitude reaches above 20. From $\pm 20°$ to $\pm 40°$ the magnitudes decrease to below 10. This could, therefore, be used as an indication of whether the robot is positioned in the centre of the wake, facing into the flow.

By examining the DPIV and pressure data together it was found that a negative (clockwise) vortex approaching the nose caused a peak on the right-hand sensor and a trough on the left-hand sensor, and a positive (anticlockwise) vortex approaching the nose caused a trough on the right-hand sensor and a peak on the left-hand sensor, Figures 6-36 to 6-41. The vortex was, on average, 1.38 cylinder diameters in front of the robot when a peak or trough occurred, Table 6.16.

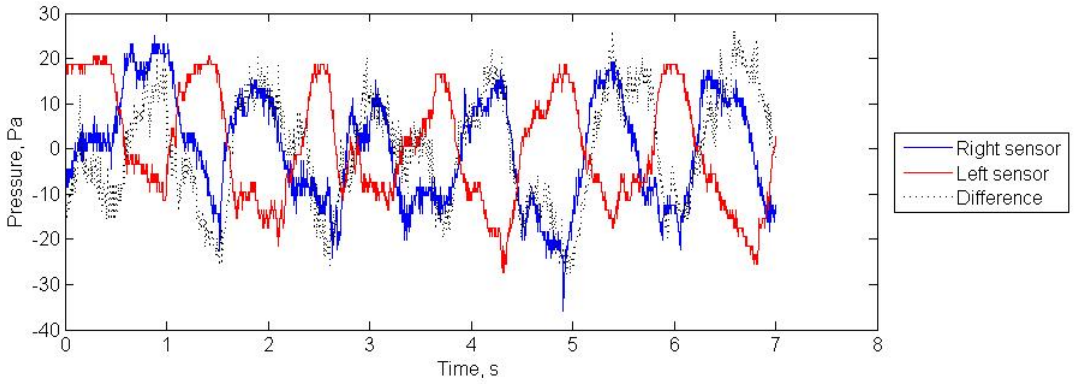

(a)

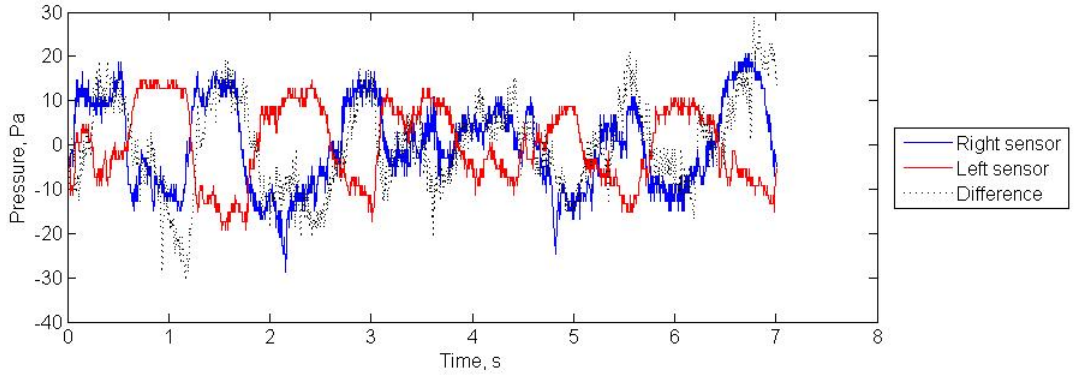

(b)

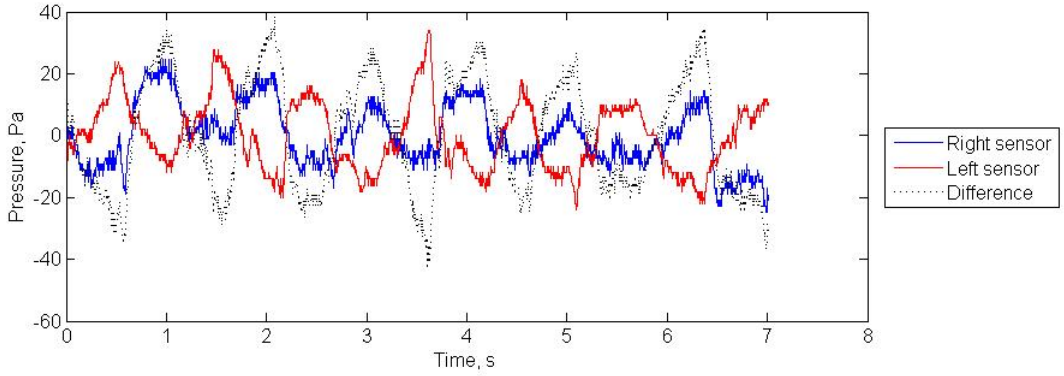

(c)

Figure 6-34: Pressure plots from the robot positioned at (a) 0°, (b) 5° and (c) 10°. Although only the positive angles have been presented here, they are representative of the negative angles of the head position relative to the flow.

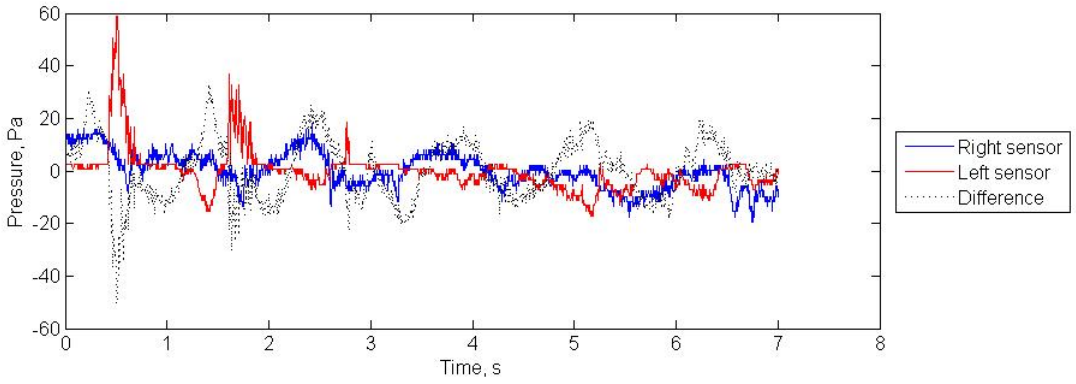

(a)

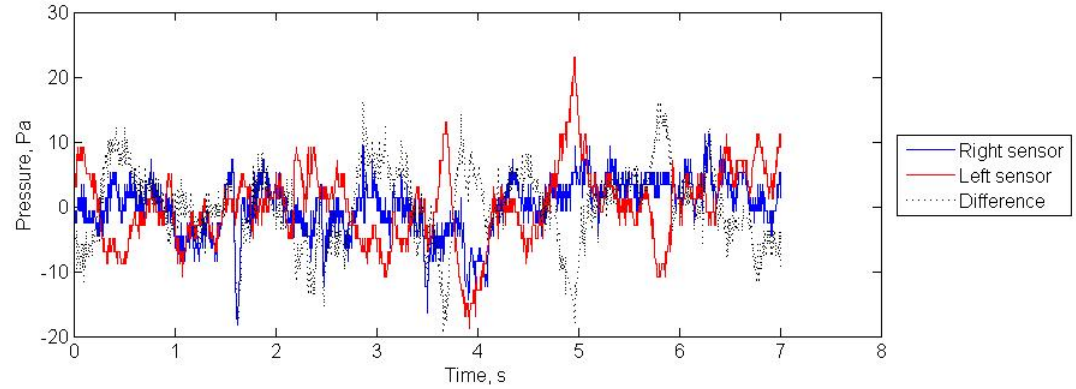

(b)

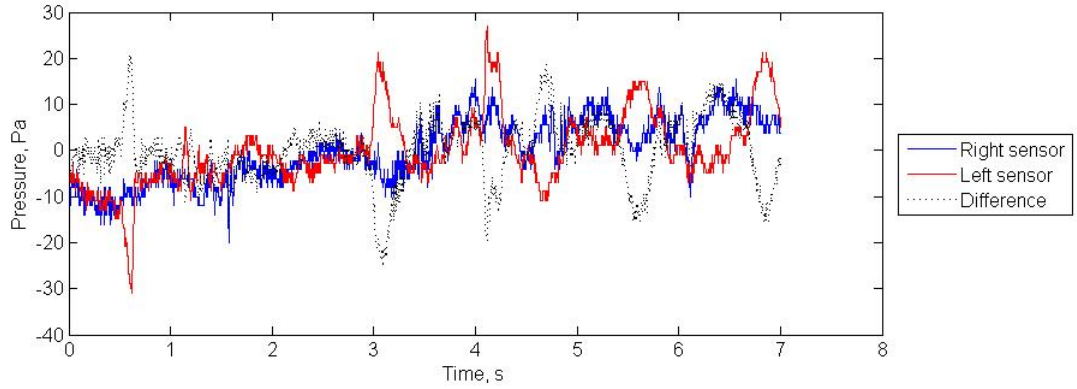

(c)

Figure 6-35: Pressure plots from the robot positioned at (a) 20°, (b) 30° and (c) 40°. Although only the positive angles have been presented here, they are representative of the negative angles of the head position relative to the flow.

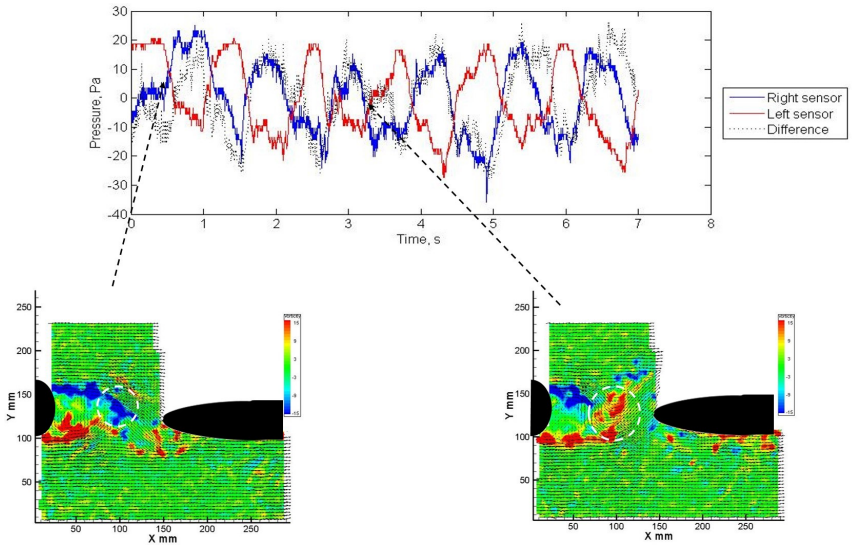

Figure 6-36: Pressure plots, with associated DPIV frames, from the robot positioned at 0°. Although only the positive angles have been presented here, they are representative of the negative angles of the head position relative to the flow. The DPIV frames are linked to the peaks and troughs within the pressures signals. A peak on the left-hand pressure sensor is linked to an oncoming positive vortex and a peak on the right-hand sensor is linked to an oncoming negative vortex.

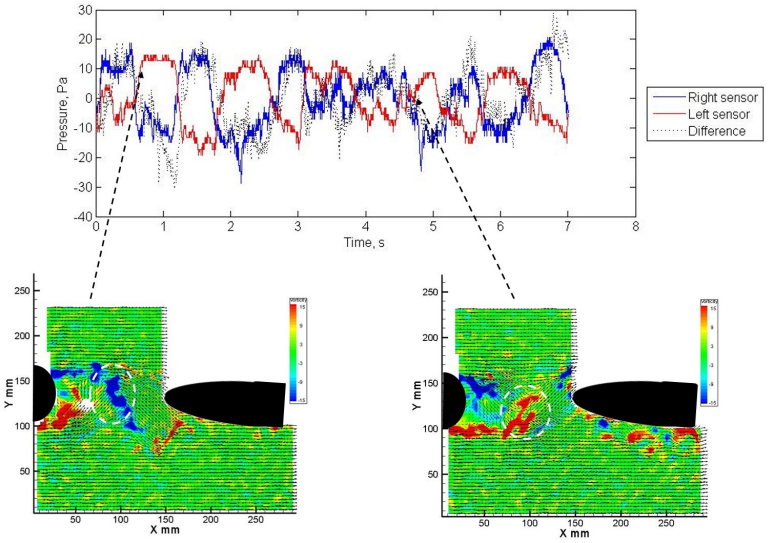

Figure 6-37: Pressure plots, with associated DPIV frames, from the robot positioned at 5°. Although only the positive angles have been presented here, they are representative of the negative angles of the head position relative to the flow. The DPIV frames are linked to the peaks and troughs within the pressures signals. A peak on the left-hand pressure sensor is linked to an oncoming positive vortex and a peak on the right-hand sensor is linked to an oncoming negative vortex.

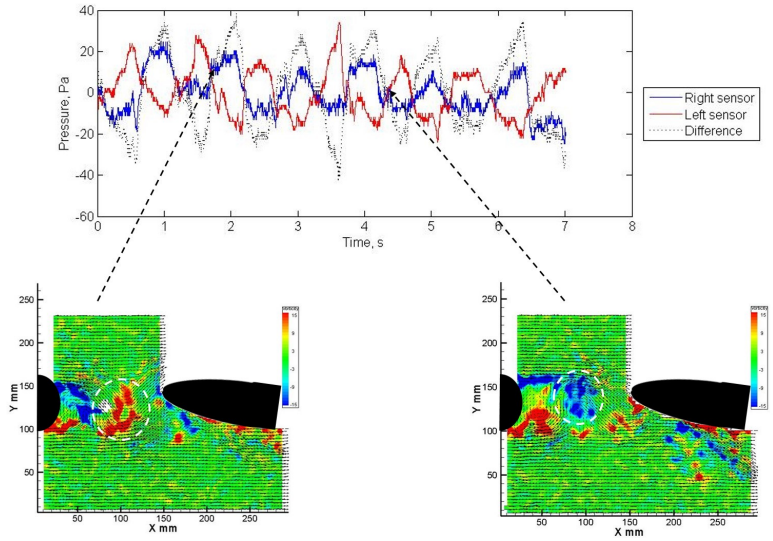

(a)

Figure 6-38: Pressure plots, with associated DPIV frames, from the robot positioned at 10°. Although only the positive angles have been presented here, they are representative of the negative angles of the head position relative to the flow. The DPIV frames are linked to the peaks and troughs within the pressures signals. A peak on the left-hand pressure sensor is linked to an oncoming positive vortex and a peak on the right-hand sensor is linked to an oncoming negative vortex.

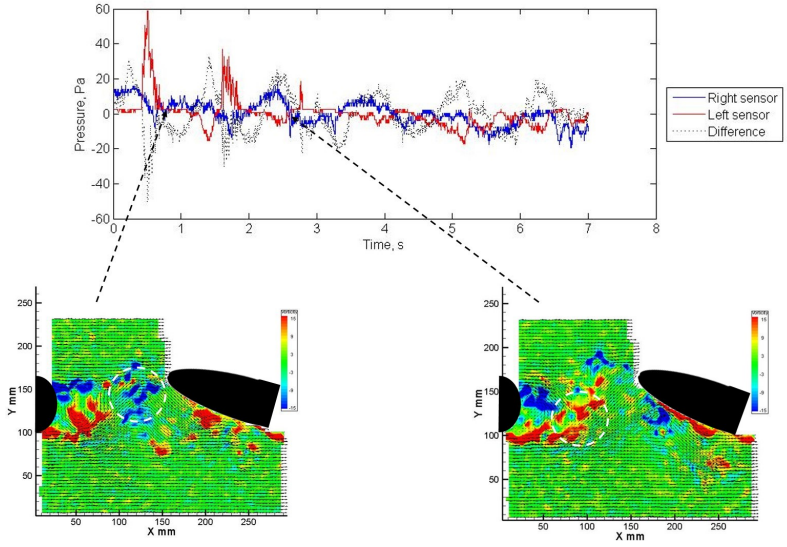

Figure 6-39: Pressure plots, with associated DPIV frames, from the robot positioned at 20°. Although only the positive angles have been presented here, they are representative of the negative angles of the head position relative to the flow. A peak on the left-hand pressure sensor is linked to an oncoming positive vortex, illustrated within the DPIV frames, and a peak on the right-hand sensor is linked to an oncoming negative vortex.

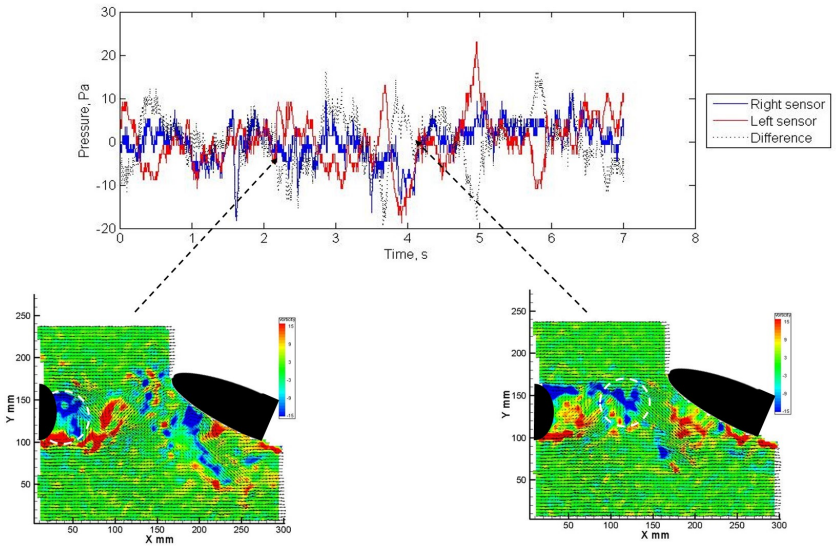

Figure 6-40: Pressure plots, with associated DPIV frames, from the robot positioned at 30°. Although only the positive angles have been presented here, they are representative of the negative angles of the head position relative to the flow. A peak on the left-hand pressure sensor is linked to an oncoming positive vortex, illustrated within the DPIV frames, and a peak on the right-hand sensor is linked to an oncoming negative vortex.

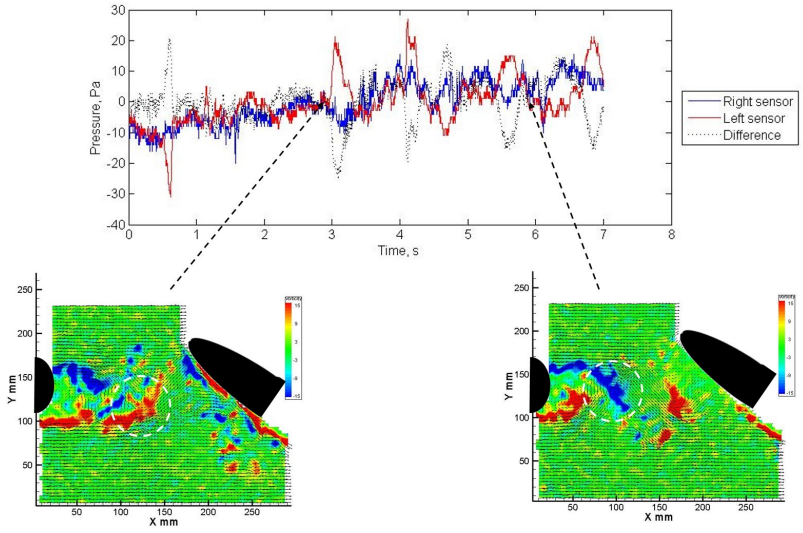

Figure 6-41: Pressure plots, with associated DPIV frames, from the robot positioned at 40° . Although only the positive angles have been presented here, they are representative of the negative angles of the head position relative to the flow. A peak on the left-hand pressure sensor is linked to an oncoming positive vortex, illustrated within the DPIV frames, and a peak on the right-hand sensor is linked to an oncoming negative vortex.

Position	Normalised vortex distance from robot nose
40°	1.37±0.57
30°	1.74±0.31
20°	1.26±0.31
10°	1.27±0.25
5°	1.52±0.54
0°	1.36±0.17
−5°	0.97±0.18
−10°	1.15±0.11
−20°	1.12±0.42
−30°	1.67±0.35
−40°	1.74±0.34

Table 6.16: Distances of the vortices from the nose of the robot, with changing head angle. The frames chosen are those at the start of the peaks and troughs of the pressure plots. The values are normalised by the cylinder diameter. The error given is the standard deviation.

Head at angles: summary

By angling the robot head into a Kármán vortex street, it was found that the pressure signals begin to lose their characteristic pattern with increasing angles beyond 20°. In addition, the phase angle between the two sides of the head decreases as the angle increases. The peak-to-peak pressure amplitudes stayed approximately constant across all angles. The dominant frequency was extracted from the pressure signals, and found to remain approximately constant until ±40°, where it began to decrease. The magnitudes of the frequencies detected decreased with increasing head angle. A negative vortex approaching the nose caused a peak on the right-hand sensor and a trough on the left-hand sensor, and a positive vortex approaching the nose caused a trough on the right-hand sensor and a peak on the left-hand sensor. These vortices were, on average, 1.38 cylinder diameters in front of the nose.

6.3 Experiments with the robot held stationary: discussion

Experiments have been completed with a rigid, fusiform-shaped robot held stationary within the flow tunnel. Initially experiments were carried out in steady flow, with the robot facing the flow and then with the robot turned by angles up to $\pm 40^\circ$ away from the centreline. The robot was then placed in a Kármán vortex street. A number of different scenarios were tested by either changing the Kármán vortex street characteristics by changing the flow speed or the cylinder size or altering the position of the robot within the Kármán vortex street, either moving towards the cylinder, moving laterally out of the cylinder wake, or angling the head by up to $\pm 40^\circ$. Three different flow speeds were used throughout these experiments giving Reynolds numbers relative to the robot of 39.7 $\times 10^3$ to 104.4 $\times 10^3$ for the steady flow experiments and 2.2 $\times 10^3$ to 22.6 $\times 10^3$ relative to the cylinders for the Kármán vortex street experiments. Synchronised DPIV and pressure data were captured and analysed for each of these experiments.

From the steady flow experiments, it was found that the flow travelled smoothly around the robot, both when it was facing the direction of flow and when it had been angled. The pressure data did not show any significant pattern; any peaks or troughs present are expected to be due to slight variations in the flow speed within the flow tunnel. The peak-to-peak amplitudes of the pressure signals were found to increase with increasing flow speed. No clear dominant frequencies were extracted from the pressure signals, and all magnitudes were below 2.5.

There were a number of results found to be common throughout the Kármán vortex street experiments; these are listed below.

- The normalised size and circulation of the vortices showed the same trends as found in the flow characterisation experiments; they remained constant with increasing flow speed, but decreased with increasing cylinder size.
- The pressure signals showed a 180° phase angles between either side of the head when the robot was in the centre of the Kármán vortex street, facing the direction of flow. This angle decreased as the robot was moved away from this position, whether laterally out of the street or with the head angled whilst within the street.
- The peak-to-peak amplitudes of the pressure signals increased with increasing flow speed, but remained approximately constant with increasing cylinder size. The values were greatest when the robot was positioned directly in the centre of the Kármán vortex street and decreased as the robot was moved out of this position.
- The dominant frequency extracted from the pressure signals closely matched the values calculated from the DPIV data when there was no robot present in the flow. This value altered when the robot was moved out of the Kármán vortex street. The magnitudes of

the frequencies increased with increasing flow speed and reduced as the robot was moved out of the Kármán vortex street.

- A peak occurred on the right-hand sensor, corresponding to a trough on the left-hand sensor, when a negative (clockwise) vortex was approaching the nose. Alternatively, a positive (anticlockwise) vortex approaching the robot caused a trough on the right-hand sensor and a peak on the left-hand sensor.

- On average, the vortices were 1.35±0.26 cylinder diameters in front of the nose when the peak or trough occurred. This is smaller than the calculated wavelength, or half wavelength, from the DPIV data when no robot was present in the flow.

- The sinusoidal pattern that the pressure signals detected, indicative of the Kármán vortex street, was strongest when the robot was in the centre of the cylinder wake. As the robot was moved laterally out of the Kármán vortex street the pressure signals lost this sinusoidal pattern.

These results show that there are indications within the pressure signals of when the robot is positioned within the Kármán vortex street. A characteristic oscillatory pattern within the pressure signal, with a 180° phase difference between the sensors on the opposing sides of the head indicates the presence of the Kármán vortex street. The peaks and troughs of this oscillatory pattern correspond well with the pattern of approaching vortices. It is suggested here that it is the preceding vortex (to the one approaching) that causes the peak and trough of the pressure signal. An approaching negative (clockwise) vortex occurs when there is a peak on the right-hand sensor and a trough on the left-hand sensor. The preceding vortex would be positive, and would be travelling over the left-hand side of the head as the negative vortex approaches. It is suggested that it is this vortex that causes the low-pressure signal on the left-hand side of the robot, with the flow of the central street on the right-hand sensors causing the higher pressure signal. This pattern would, therefore, agree with the results of Bartol et al [31] who correlated a low pressure spike over a model of a boxfish with an area of attached, concentrated vorticity. The peaks and troughs occurred when the vortices were 1.35±0.26 cylinder diameters upstream of the nose of the robot, for each of the flow speeds and cylinder sizes tested, which was lower than the calculated wavelength or half-wavelength of the Kármán vortex streets from the flow characterisation experiments. The oscillatory pattern of the pressure signals could, therefore, be used to predict the approach of oncoming vortices such that the robot could move to either avoid or intercept them. The work presented here, therefore, supports hypothesis one, presented in Chapter 2, that the pressure signal detected at, or near, the front of a fusiform shape can be used to determine the relative position of vortices to the fusiform shape.

The properties of the Kármán vortex street and pressure signal were also examined to determine whether they correlate. The normalised size of the vortices remained constant with increasing flow speed, but decreased with increasing cylinder size. This suggests that the absolute size of the vortices remains approximately constant with increasing flow speed as the

normalisation used only the cylinder size but remains approximately constant with cylinder size. The normalised circulation of the vortices also remained approximately constant with increasing flow speed, but decreased with increasing cylinder size. For the circulation, this indicates that as the flow speed increases, the absolute circulation increases but the absolute values remain approximately constant with increasing cylinder size. The pressure signal was found to have a peak-to-peak amplitude and frequency magnitudes that increased with increasing flow speed, but remained constant with increasing cylinder size. These properties could, therefore, be used as indicators of the absolute circulation values of the vortices within the flow. This result supports hypothesis two presented, that the properties of the pressure signal alter corresponding to changing properties of the vortices present in the flow.

The results presented in this chapter have shown that a pressure sensor array on-board a fusiform shaped robot can detect the Kármán vortex street present. Properties of the pressure signal can be used to indicate whether the robot is positioned within the centre of the Kármán vortex street, or if it has been moved outside either laterally or by angling the head to the oncoming flow. The relative distance of the vortex upstream of the nose has also been determined using characteristics of the pressure signal. These results could be used within a navigational strategy for a robot in a known unsteady flow, such that the vortices could be detected and a relative vortex strength could be determined. If the vortices can be detected, the robot can therefore either avoid the unsteady flow completely, or could use unsteady flows by avoiding or intercepting the vortices within the Kármán vortex street, mimicking the Kármán gait displayed by fish, to potentially increase its swimming efficiency. However, the results of this chapter have only shown that the Kármán vortex street can be detected with a stationary robot the following chapter details studies with a moving robot within steady and unsteady flows, to test the hypotheses in a more complex environment.

Chapter 7

Experiments with a Moving Robot

This chapter details the experiments in which the robot was mounted on a linear motor rig and, therefore, could move within the working section of the flow tunnel. Having determined that there are specific patterns within the pressure data that are associated with the vortices within the flow, these experiments investigate whether these patterns are still present when the robot is moving through the flow.

The results of the previous chapter supported the hypotheses set out in Chapter 1. The pressure signal was shown to detect the vortices within Kármán vortex streets and was used to determine their relative position. Additionally, the properties of that pressure signal could be used to deduce characteristics about the vortices present. However, the results related to a fish-like robot placed stationary within the flow, which is an unrealistic situation for an autonomous fish-like robot. Therefore, it is important to test these hypotheses when the robot is moving. In order to investigate a moving robot, the robot was attached to a linear motor rig so that a set of motions could be used and the pressure and DPIV data were captured as before. The linear motor rig limits the motions to simple straight lines; these could be in any direction by adjusting the orientation of the rig to the working section of the flow tunnel. The range of the motions was limited by the size of the working section of the flow tunnel and the speed at which the robot could be moved without significant interference from the rig; the latter presented as a visible shaking of the robot.

The robot was placed first in steady flows and then in Kármán vortex streets; the results are presented in the following sections.

7.1 Steady Flow

Initially, the movements were carried out in steady flow; this gave a baseline of the results, particularly any results arising from to the motion of the robot. Two main movements were investigated; moving forwards parallel to the flow and moving laterally within the flow.

7.1.1 Forward motion

The robot was moved forwards within the flow tunnel at Reynolds numbers relative to the robot of 78.6 $\times 10^3$ and 104.4 $\times 10^3$, with an oscillatory frequency of 0.08Hz for the linear motor rig. The total motion used was a forward and backward motion, although data was only captured over the forward motion section. The total distance moved (forward-and-backward) was set to be 125mm, with a maximum speed of approximately 4.7cm s^{-1}. The movement is illustrated in Figure 7-1.

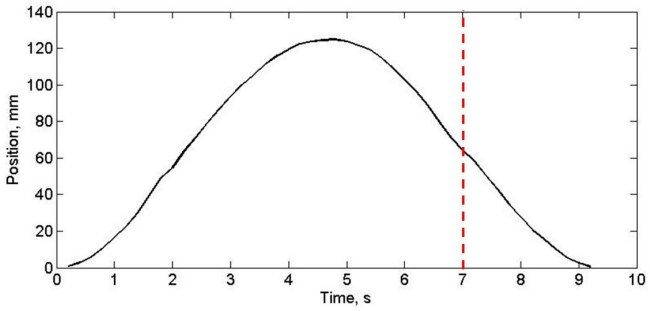

Figure 7-1: The forward movement of the robot within the flow tunnel in steady flow conditions, with the end point of the DPIV capture shown by the red dotted line.

From the DPIV, Figure 7-2 (a), it can be seen that the flow travels smoothly around the robot in both directions with faster flow (indicated by the narrower streamlines) around the front of the robot, as for when the robot was held stationary. The speed of motion of the robot is significantly lower than the bulk flow speed, meaning that the overall perturbation to the flow from the robot's movement is minimal.

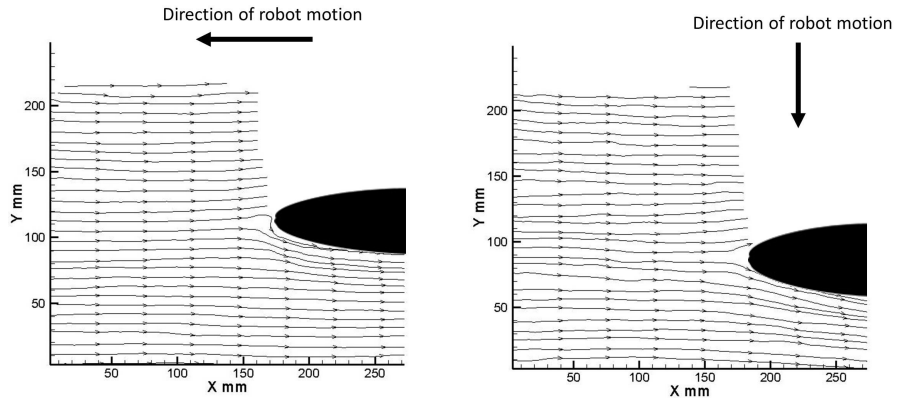

(a) (b)

Figure 7-2: DPIV images of the robot moving (a) forwards and (b) laterally within the working section of the flow tunnel in steady flow for which Re = 21.9 $\times 10^3$. These show instantaneous streamlines around the robot, but are representative of those throughout the capture.

The pressure signals, Figure 7-3, show very little pattern for the majority of the capture. However, towards the end of the plot both the right and left hand signals synchronise and show a strong oscillatory behaviour. The start of this section of the pressure signal corresponds to the point at which the robot begins to turn around and is expected to be due to the vibrations from the linear motor rig changing the acceleration of the robot. The peak-to-peak amplitude of the pressure signals increase with increasing flow speed, from 40Pa to 50Pa, as was shown in the previous chapter with the stationary robot.

In addition, a frequency analysis was completed on the pressure signals, to extract the dominant frequencies. The results showed no clear signal present across the sensor array, except at approximately 50Hz. It is expected that this higher frequency component is due to the linear motor rig, as it was not present in the stationary robot data. The magnitude of the frequencies showed a maximum of 5.3 for a 50Hz, with all other frequencies detected with much lower magnitudes.

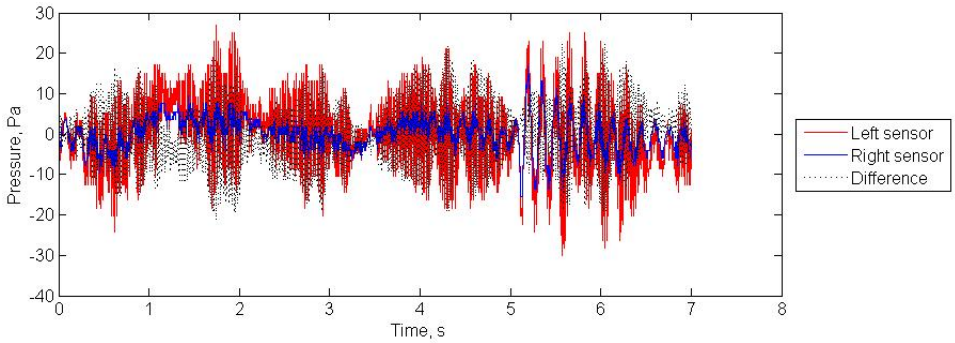

Figure 7-3: Pressure plot from the robot when moving forward in steady flow at Reynolds number relative to the robot of 78.6 $\times 10^3$. This is indicative of all flow speeds tested.

7.1.2 Lateral motion

Next, the robot was moved laterally within the flow tunnel again at Reynolds numbers of 78.6 $\times 10^3$ and 104.4 $\times 10^3$ at an oscillatory frequency of 0.08Hz for the linear motor rig, Figure 7-4. The total distance moved was set to be 180mm and had a maximum speed of approximately 6cm s^{-1}.

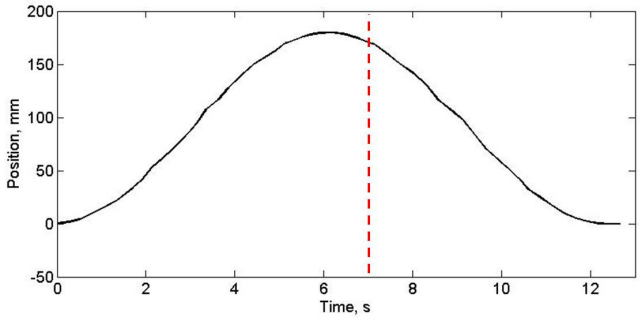

Figure 7-4: The lateral movement of the robot within the flow tunnel within steady flow conditions, with the end point of the DPIV capture shown by the red dotted line.

The DPIV captures, Figure 7-2 (b) show that the flow travels smoothly around the robot, even though the movement is perpendicular to the direction of flow. Slightly increased flow speed, indicated by the bunched streamlines, is present next to the robot in the direction of travel. Once again, the speed of the robot was significantly lower than the flow speed to give minimal disturbance to the flow and the sensors.

The pressure signals show little pattern. There is no clear indication here of the point at which the robot turns around to re-trace its course across the flow tunnel, unlike the previous motion. The trace shows that the right-hand sensor (on the back of the head compared to the direction of motion) gave a gradual decrease of pressure across the movement, whereas the left sensor (on the forward side of the head with respect to the direction of motion) gave

an approximately steady signal. The peak-to-peak amplitude of the pressure signals increased with increasing flow speed, from 10Pa to 20Pa.

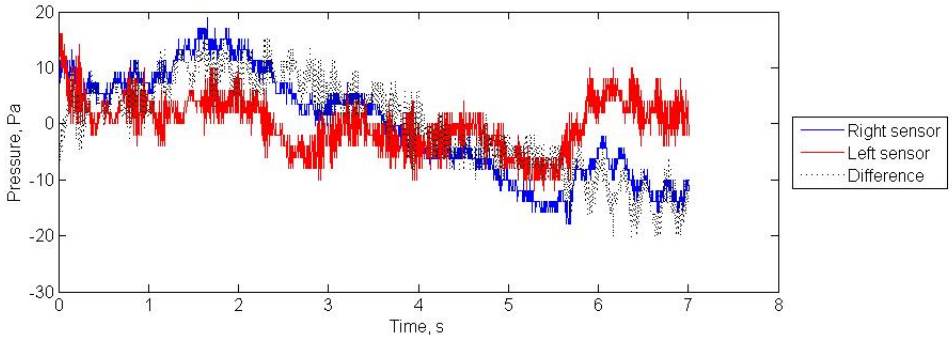

Figure 7-5: Pressure plot from the robot when moving laterally in steady flow at a Reynolds number relative to the robot of 78.6 $\times 10^3$. This is indicative of all flow speeds tested.

The dominant frequencies were also extracted from the pressure signals. No clear dominant frequency was detected, except at approximately 50Hz, as for the previous motion. The magnitudes of the frequency increase with increasing flow speed, with a maximum magnitude detected of 5 for a frequency of 0.1953Hz at the lowest flow speed to a maximum of 15 for a frequency of 0.098Hz at the highest flow speed.

7.1.3 Steady flow: summary

The experiments with the robot moving in steady flows, both forwards and laterally, have shown that the motion does not significantly disturb the bulk flow field. The pressure signal for the forward motion shows a strong indication of the time at which the robot changes direction, with a synchronised oscillation captured from sensors on both sides of the head. This is not present in the pressure signals for the lateral motion. The peak-to-peak amplitudes of the pressure signals increase with increasing flow speed, as was found previously. No single dominant frequency was extracted from the pressure signals, but a peak at approximately 50Hz was found. As this was not present when the robot was held stationary, but is present for both forward-backward and lateral motion, it is expected that this frequency initiates with the linear motor rig. The magnitude of the frequencies was found to increase with increasing flow speed.

7.2 Kármán vortex street

Having completed the steady flow experiments, the same two motions were used in conjunction with Kármán vortex streets. In addition, the lateral motion experiments were extended to include a set where the oscillation speed was increased to match the vortex shedding of the cylinder. The motion was then timed such that the robot could either avoid or intercept the vortices. This latter experimental set was carried out to better mimic the fish's behaviour

within the Kármán vortex street; as presented in Chapter 5, the fish would move laterally in phase with the Kármán vortex street, intercepting the vortices. The robot was moved to both intercept and avoid the vortices so that the different pressure signals could be compared, to better map the possible situations of an autonomous robotic fish.

7.2.1 Forward motion

The forward motion matched that from the steady flow experiments, at an oscillatory frequency of 0.08Hz for the linear motor rig. The 45 and 100mm diameter cylinders were used to create Kármán vortex streets at flow speeds of 19.65 and 26.09cm s^{-1}, giving flows with Reynolds numbers relative to the cylinder from 7.7 $\times 10^3$ to 22.6 $\times 10^3$. The speed of the robot's movement was kept constant throughout all of these experiments as it was not required to produce dimensionally similar results, but rather explore the differences within the flow regimes produced and what could be detected by the pressure sensor array. The robot was placed at three diameters downstream from each cylinder and moved 125mm or 200mm for the 45 and 100mm diameter cylinders respectively. This takes the robot to approximately one diameter downstream of the cylinder when it changes direction and begins to move backwards; Figure 7-6.

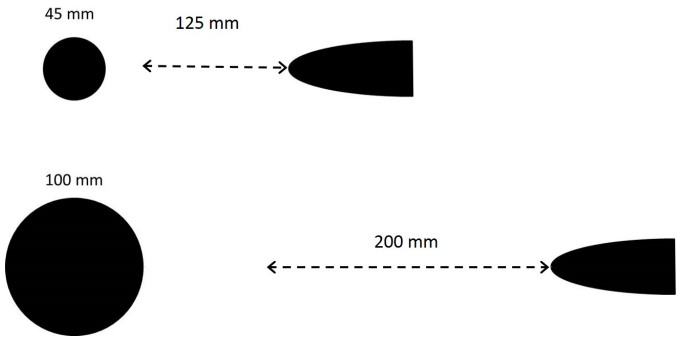

Figure 7-6: Diagram showing the movement and distance of the robot during forward motion behind both the 45 and 100mm diameter cylinders.

The DPIV results, Figure 7-7 show that the size of the vortices behind both the 45 and 100mm diameter cylinders is similar to that from the flow characterisation experiments. The results for the 100mm diameter cylinder show slightly smaller vortices were calculated when the robot was present. The circulation of the vortices, Figure 7-8, is similar behind the 45mm diameter cylinder when the robot is present compared to the flow characterisation, but for the 100mm diameter cylinder the circulation has reduced. This will be, in part, due to the slightly smaller vortices that have been calculated, as the circulation is defined as the sum of the vorticity in a given area.

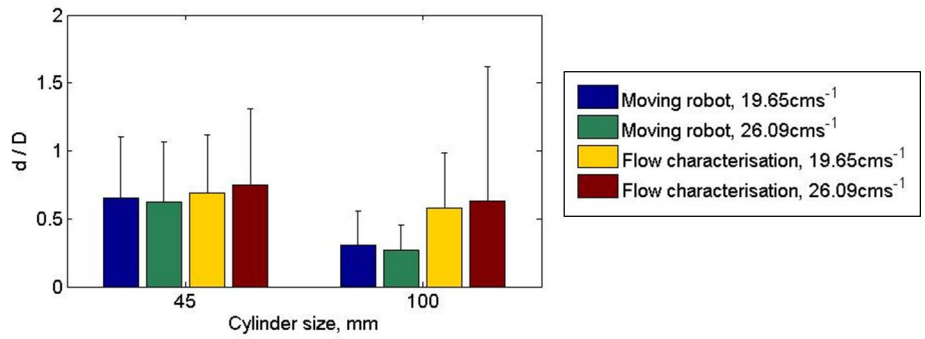

Figure 7-7: Normalised vortex size at flow speeds of 19.65 and 26.09cm s^{-1} behind the 45 and 100mm diameter cylinders as the robot moves towards the cylinders. The values calculated from the flow characterisation data are also given.

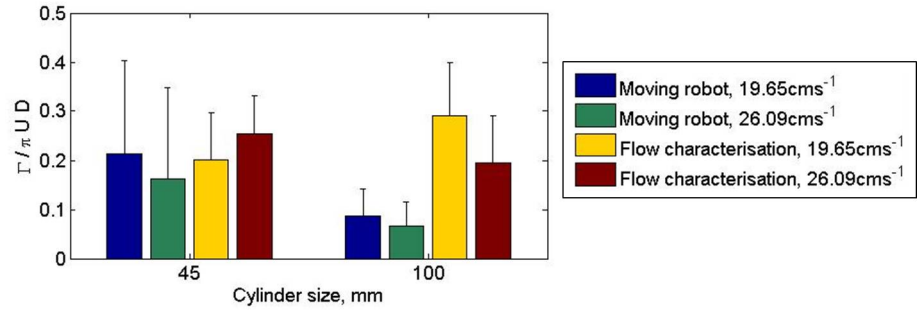

Figure 7-8: Normalised vortex circulation at flow speeds of 19.65 and 26.09cm s^{-1} behind the 45 and 100mm diameter cylinders as the robot moves towards the cylinders. The values calculated from the flow characterisation data are also given.

The pressure plots, Figure 7-9, show similar trends to those from the stationary robot experiments, with approximately 180° phase difference for the majority of the capture. Towards the end of the signal, the same behaviour as seen in the steady flow experiments of matched, high frequency oscillations can be seen. The onset of the high frequency oscillations matches the point at which the robot changes direction, as was found for the steady flow results. The peak-to-peak amplitudes of the pressure, Table 7.1, increased with increasing cylinder size, but did not show a constant trend of increasing with increasing flow speed as had been seen previously.

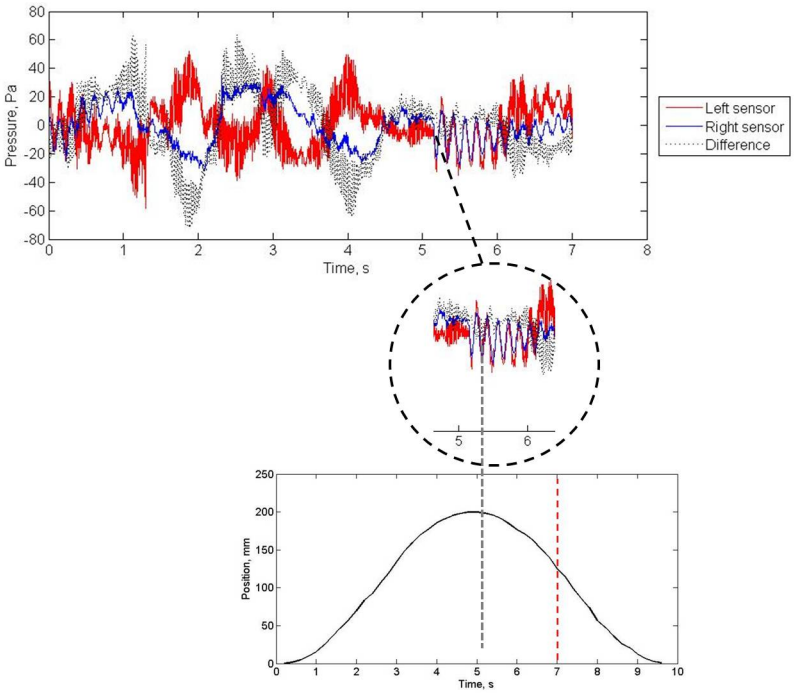

Figure 7-9: Pressure plot from the robot when moving forwards behind the 100mm diameter cylinder at Re = 21.9 $\times 10^3$. This is indicative of all flow speeds tested. The onset of the high frequency oscillations is highlighted and matched to the movement plot. This shows that these oscillations matches the point at which the robot changes direction.

	Flow Speed cm s^{-1}	
Cylinder Size mm	19.65	26.09
45	50	30
100	80	90

Table 7.1: Maximum peak-to-peak pressure amplitudes from the on-board sensors for forwards motion in Kármán vortex streets created by 45 and 100mm diameter cylinders at Reynolds numbers of 21.9 $\times 10^3$ and 29.0 $\times 10^3$.

Additionally, the dominant frequencies were extracted from the pressure signals, Table 7.2. These frequencies are close to those calculated from the Strouhal number and extracted from the flow characterisation data, indicating that the vortex shedding frequencies can still be detected whilst the robot is moving. There was an additional peak signal at approximately 50Hz, as for the robot moving in steady flow. This is expected to be due to the linear motor rig used for the movement. The magnitude of the frequencies was examined and found to increase with increasing flow speed and to increase with increasing cylinder size, Table 7.3. As for the stationary robot experiments, the maximum magnitude is found on the sensor pair closest to the nose.

As noted, the pattern of the pressure signals is similar to that observed in the stationary

robot experiments. By examining the pressure frames at which the peaks and troughs of the signal occur and matching them to the DPIV frames, synchronised by the LED, it was found that, as previously, a positive (anticlockwise) vortex approaching the robot created a peak on the left-hand sensor and a trough on the right-hand sensor; and a negative (clockwise) vortex approaching the robot created a trough on the left-hand sensor and a peak on the right-hand sensor; Figure 7-10. This pattern is evident until the robot gets very close to the cylinder, at which point the pressure signal settles to an approximately steady signal. The pressure signal then oscillates with no phase difference between the sides of the head as the robot is changing direction. It is expected that, as this latter effect is due to the vibrations from the linear motor rig changing the acceleration of the robot, this would not be present in an autonomous fish-like robot, but rather it is an artefact of the experimental set-up and equipment used. By examining the pressure plots and the DPIV, it was found that the pressure sensors detected the vortices at normalised distances of 0.6 – 1.5; as the robot moved towards the cylinder, the distance between the nose and the vortices decreased. The pressure signals do not appear to change with decreasing distance to the vortex.

		Pressure signal	Flow characterisation	Strouhal
45mm				
	19.65cm s^{-1}	0.8789 - 1.074	0.943	0.873
	26.09cm s^{-1}	1.367	1.3897	1.1595
100mm				
	19.65cm s^{-1}	0.3906	0.51135	0.393
	26.09cm s^{-1}	0.6836	0.6305	0.5218

Table 7.2: Dominant frequencies extracted from the pressure signals whilst moving forwards within Kármán vortex streets created behind 45 and 100mm diameter cylinders at 19.65 and 26.09cm s^{-1}. The values extracted from the DPIV data from the flow characterisation experiments and values calculated using the Strouhal number are also given.

Sensor pair		1	2	3	4
45mm					
	19.65cm s^{-1}	3.57	3.35	3.58	3.40
	26.09cm s^{-1}	11.37	6.67	7.10	6.90
100mm					
	19.65cm s^{-1}	20.72	11.01	14.5	10.88
	26.09cm s^{-1}	23.90	17.87	15.12	9.016

Table 7.3: Magnitudes of the dominant frequencies extracted from the pressure signals whilst moving forwards within Kármán vortex streets created behind 45 and 100mm diameter cylinders at 19.65 and 26.09cm s^{-1}.

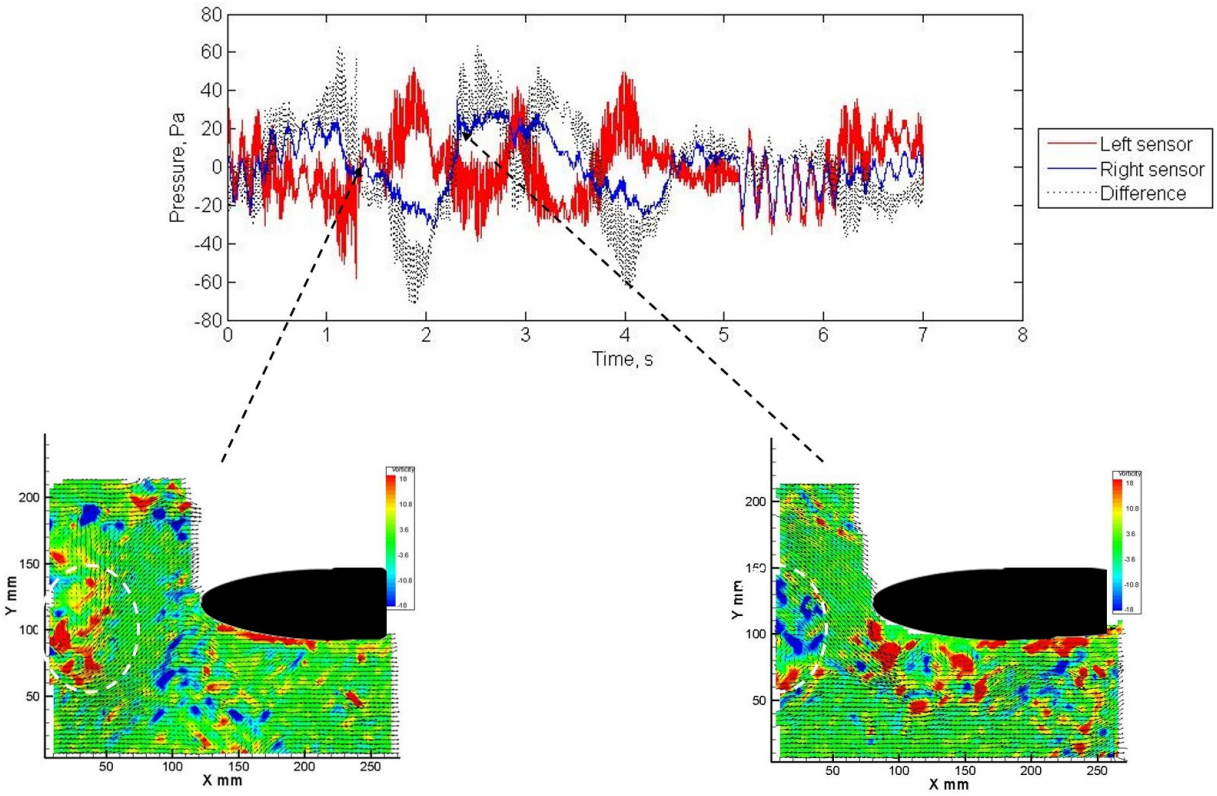

Figure 7-10: Plot showing the pressure plot and associated DPIV images with the robot behind the 100mm diameter cylinder at Re = 21.9 $\times 10^3$. The left-hand image shows an approaching anti-clockwise/positive vortex, corresponding to a trough in the right-hand pressure signal. The left-hand image shows the robot moved further towards the cylinder, and an approaching clockwise/negative vortex, corresponding to a peak on the right-hand sensor.

Moving forwards: summary

The results of the robot moving forwards towards the cylinder are in keeping with the results found with the stationary robot at one, two and three diameters downstream of the cylinder. The normalised size and circulation of the vortices present within the flow remain approximately constant with increasing flow speed, but decrease with increasing cylinder size. The pressure signals showed the characteristic sinusoidal pattern that indicated the Kármán vortex street. The peak-to-peak amplitudes of the pressure signals increased with increasing cylinder size but did not show a consistent trend of increasing with increasing flow speed. The dominant frequencies were extracted from the pressure signals and found to be similar to those calculated from the flow characterisation data from Chapter 4. The magnitudes of the frequencies increased with increasing flow speed and increasing cylinder size, with the highest values given by the sensor pair closest to the nose. In addition, the peaks and troughs of the pressure signals correspond to vortices present in the flow; a positive vortex approaching the robot created a peak on the left-hand sensor and a trough on the right-hand sensor, and vice versa for the

negative vortices. The pressure signals stop showing this pattern once the robot is close to the cylinder (around one cylinder diameter), such that it cannot detect vortices any more; at this point the robot's direction was changed, so that it started moving away from the cylinder. This turning point was presented by a high frequency oscillation in the pressure signals, that was matched on both sides of the head.

7.2.2 Lateral Motion

In addition to the forward motion, the robot was moved laterally across the flow tunnel, through different cylinder wakes. Three cylinder sizes were used, with the robot placed three diameters downstream of the cylinders, Figure 7-16. For the initial experiments, the motion matched the speeds and set-up as in the steady flow experiments, where the robot moved slowly across the tank. Furthermore, a set of experiments was carried out where the frequency of the motion was similar to the vortex shedding frequency of the cylinder; the robot's motion was then timed such that the robot would either move around or intercept the vortices present in the cylinder wake. These experiments are detailed below.

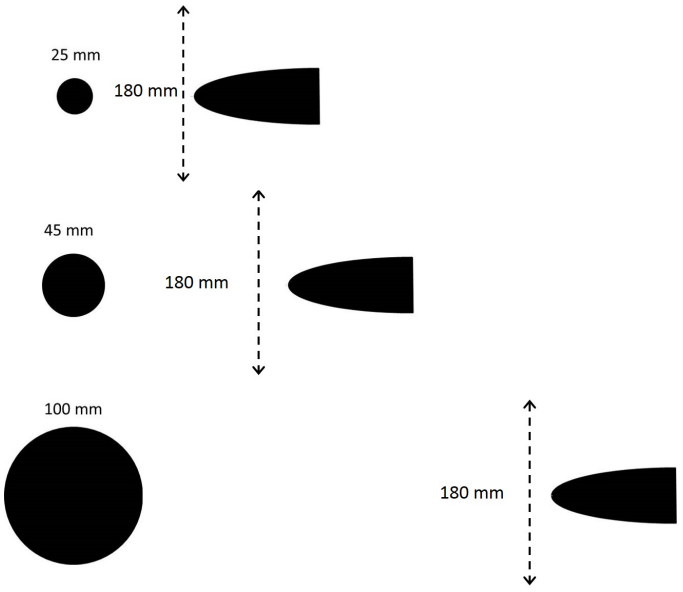

Figure 7-11: Diagram showing the movement and distance of the robot during lateral motion behind the 25, 45 and 100mm diameter cylinders.

The DPIV data, Figure 7-12, show that the normalised size of the vortices is similar to those from the flow characterisation experiments. There is a trend of decreasing normalised size with increasing cylinder diameter. The normalised circulation, Figure 7-13, is slightly higher than for the flow characterisation results, except for the 100mm diameter cylinder, where the values have reduced.

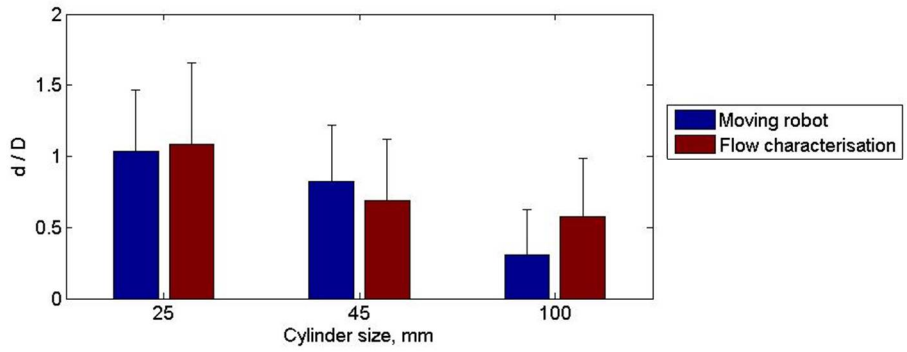

Figure 7-12: Normalised vortex size at a flow speed of 19.65cm s^{-1} behind the 25, 45 and 100mm diameter cylinders as the robot moves laterally through the cylinder wakes.

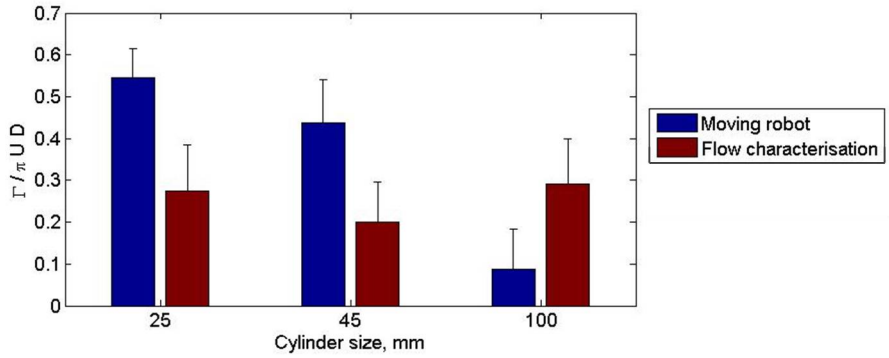

Figure 7-13: Normalised vortex circulation at a flow speed of 19.65cm s^{-1} behind the 25, 45 and 100mm diameter cylinders as the robot moves laterally through the cylinder wakes.

Through the Kármán vortex street

The robot was positioned at three cylinder diameter lengths downstream of the cylinder. The linear motor rig was set to oscillate at 0.08Hz; the total distance moved was set to be 180mm, with a maximum speed of motion of 5.0cm s^{-1}. The three cylinders, of 25, 45 and 100mm diameter were used with flow speeds of 19.65 and 26.09cm s^{-1}, giving flows with Reynolds numbers relative to the cylinder from 4.3 $\times 10^3$ to 22.6 $\times 10^3$. Here, the motion speed and distance travelled is kept constant throughout all experiments, due, in part, to the restriction of the size of the flow tunnel such that a greater movement could not be used, but mostly because the focus is on determining the effects of the movement through different flow regimes produced by the varying cylinder sizes and flow speeds.

The pressure plots, Figure 7-14, show the characteristic sinusoidal pattern as the robot moves through the Kármán vortex street. Outside of the area of the cylinder wake, the pressure plot shows a much smoother signal, Figure 7-15. The signal also shows the trait of 180° phase

difference within the Kármán vortex street between the two sides of the head, as was found previously. The peak-to-peak amplitude of the pressure signals increased with increasing flow speed and increasing cylinder size, Table 7.4, as was found previously. In addition, it can be seen from Figure 7-15, that the peak-to-peak amplitude increased when the robot was passing through the wake of the cylinder, as opposed to when it was outside of the wake. The amplitudes are found to approximately double, when the robot's sensors were within the Kármán vortex street. This is an aspect of the pressure signal that can be used to detect the Kármán vortex street. By calculating the time taken for the robot to traverse through the wake, and given the speed of motion of the robot, it was estimated that the wake width behind the 25mm diameter cylinder was approximately 6cm and the wake width behind the 45mm diameter cylinder was approximately 10.5cm. The pressure signal behind the 100mm diameter cylinder did not show a change to indicate the robot had moved out of the wake. These wake widths are both approximately 2.5 times greater than the wake widths calculated from the flow characterisation data. This is likely to be due to the interference of the robot with the wake.

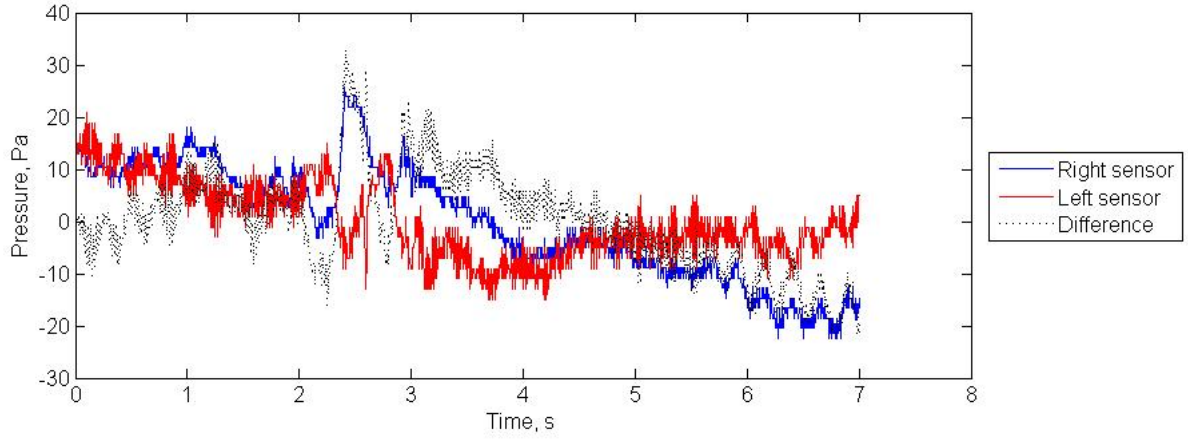

(a)

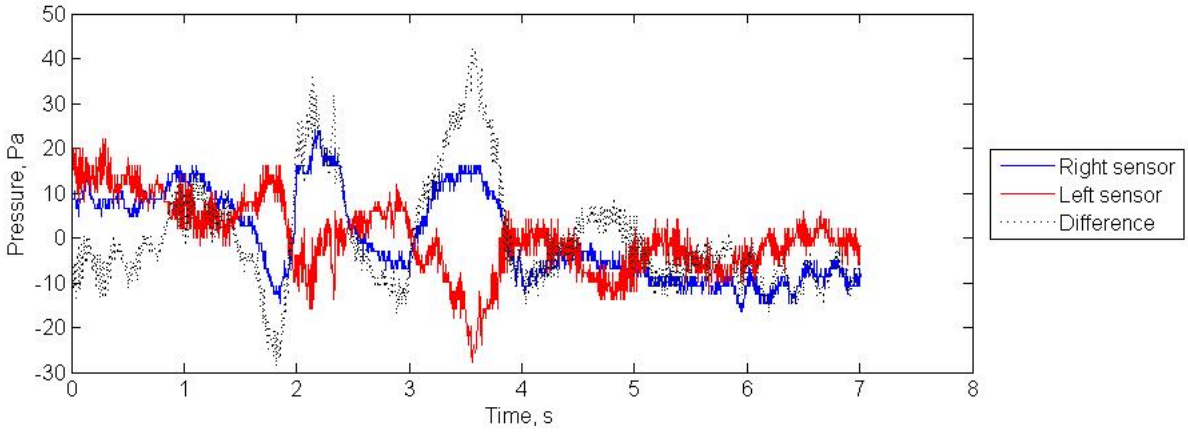

(b)

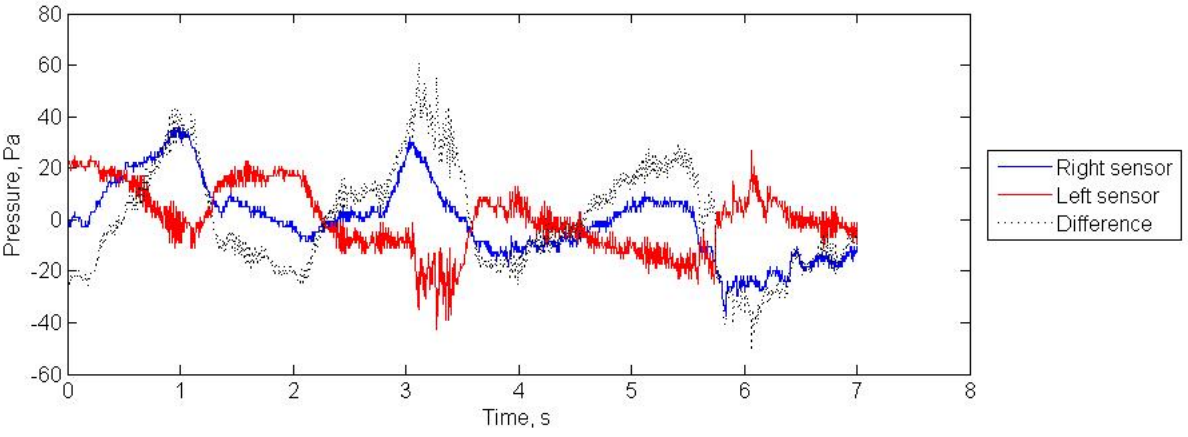

(c)

Figure 7-14: Pressure signals from the robot whilst moving laterally through the Kármán vortex street at a flow speed giving Re = 21.9 $\times 10^3$ behind (a) the 25mm, (b) the 45mm and (c) the 100mm diameter cylinders.

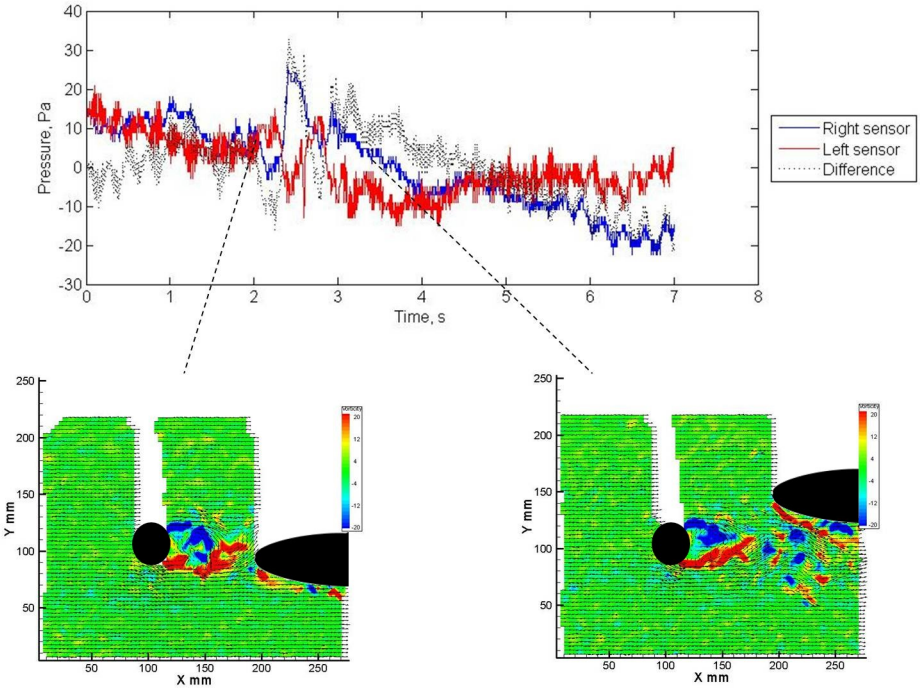

(a)

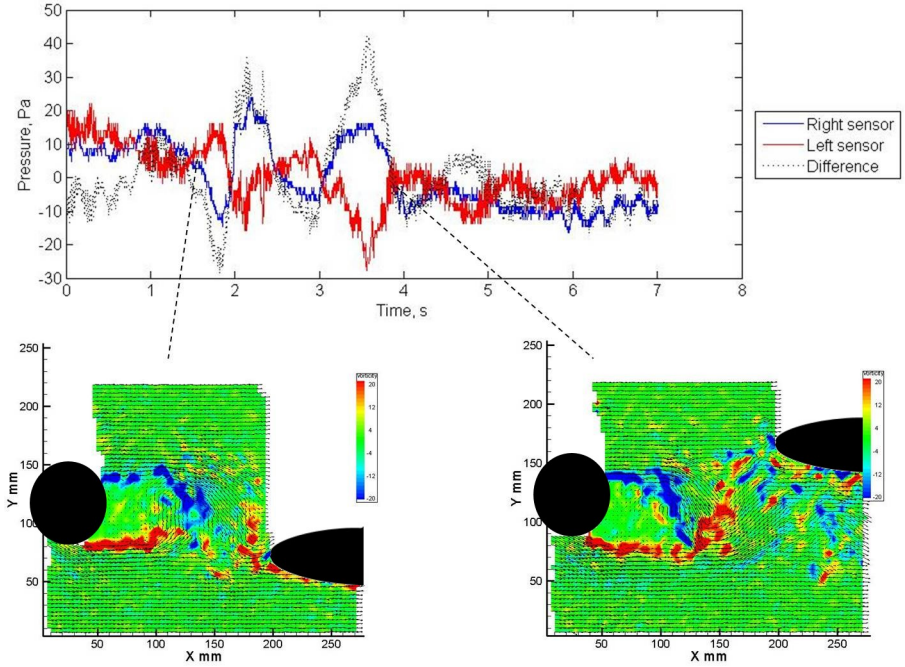

(b)

Figure 7-15: Images illustrating the position of the robot at the changing point of the pressure signals, where the peak-to-peak amplitudes double for (a) the 25mm diameter cylinder and (b) the 45mm diameter cylinder. The DPIV images are plots of vorticity, with red indicating positive vorticity and blue negative vorticity.

The dominant frequencies were also extracted from the pressure signals. For the experiments using the 25mm diameter cylinder, the vortex shedding frequencies were not clearly detected except at the highest flow speed, but a signal at approximately 4Hz was found at all flow speeds. It is not clear what this frequency is related to. For the experiments with the 45mm diameter cylinder, the vortex shedding frequencies were detected, Table 7.5, but not necessarily as the dominant peak as the 4Hz was again present. Conversely, the experiments using the 100mm diameter cylinder detect the vortex shedding frequencies as the peak frequencies, Table 7.5, and the 4Hz peak is not present. The magnitudes of the frequencies were examined and found to increase with increasing cylinder size and increasing flow speed, Table 7.6. Again, the maximum values are found from the sensor pair closest to the nose.

	Flow Speed $\mathrm{cm\,s^{-1}}$		
Cylinder Size mm	9.92	19.65	26.09
25	10	10	45 / 15
45	10	35 / 15	70 / 40
100	20 / 10	40 / 40	80 / 40

Table 7.4: Peak-to-peak pressure amplitude values from the on-board sensors for lateral motion through Kármán vortex streets created by 25, 45 and 100mm diameter cylinders at Reynolds numbers of 21.9 $\times 10^3$ and 29.0 $\times 10^3$. The two numbers given indicate the value when the robot is passing through the Kármán vortex street (on the left), and the value when the robot is outside of the Kármán vortex street (on the right).

	Pressure signal	Flow characterisation	Strouhal
25mm			
$9.92\mathrm{cm\,s^{-1}}$	4.102	0.88	0.792
$19.65\mathrm{cm\,s^{-1}}$	4.102	1.81	1.572
$26.09\mathrm{cm\,s^{-1}}$	2.148	1.808	2.087
45mm			
$9.92\mathrm{cm\,s^{-1}}$	0.488	0.693	0.44
$19.65\mathrm{cm\,s^{-1}}$	0.781	0.943	0.873
$26.09\mathrm{cm\,s^{-1}}$	1.27	1.39	1.16
100mm			
$9.92\mathrm{cm\,s^{-1}}$	0.195	0.204	0.198
$19.65\mathrm{cm\,s^{-1}}$	0.488	0.511	0.393
$26.09\mathrm{cm\,s^{-1}}$	0.586	0.631	0.522

Table 7.5: Dominant frequencies extracted from the pressure signals whilst moving forwards within Kármán vortex streets created behind 25, 45 and 100mm diameter cylinders at 9.92, 19.65 and $26.09\mathrm{cm\,s^{-1}}$. The values extracted from the DPIV data from the flow characterisation experiments and values calculated using the Strouhal number are also given.

The sinusoidal pattern within the Kármán vortex street follows the same pattern as has been described previously; a positive (anticlockwise) vortex approaching the robot created a peak on the left-hand sensor and a trough on the right-hand sensor; and a negative (clockwise) vortex approaching the robot created a trough on the left-hand sensor and a peak on the right-hand sensor; Figure 7-16.

Sensor pair		1	2	3	4
25mm					
	9.92cm s^{-1}	5.35	4.81	2.47	2.16
	19.65cm s^{-1}	2.01	1.91	4.56	4.75
	26.09cm s^{-1}	7.43	2.91	2.98	3.78
45mm					
	9.92cm s^{-1}	1.87	1.96	4.20	5.05
	19.65cm s^{-1}	10.48	4.36	4.36	5.40
	26.09cm s^{-1}	14.40	3.98	6.31	5.47
100mm					
	9.92cm s^{-1}	10.51	4.74	6.40	5.58
	19.65cm s^{-1}	23.47	9.10	11.42	8.99
	26.09cm s^{-1}	40.18	16.50	18.30	14.33

Table 7.6: Magnitudes of the dominant frequencies extracted from the pressure signals whilst moving forwards within Kármán vortex streets created behind 25, 45 and 100mm diameter cylinders at 9.92, 19.65 and 26.09cm s^{-1}.

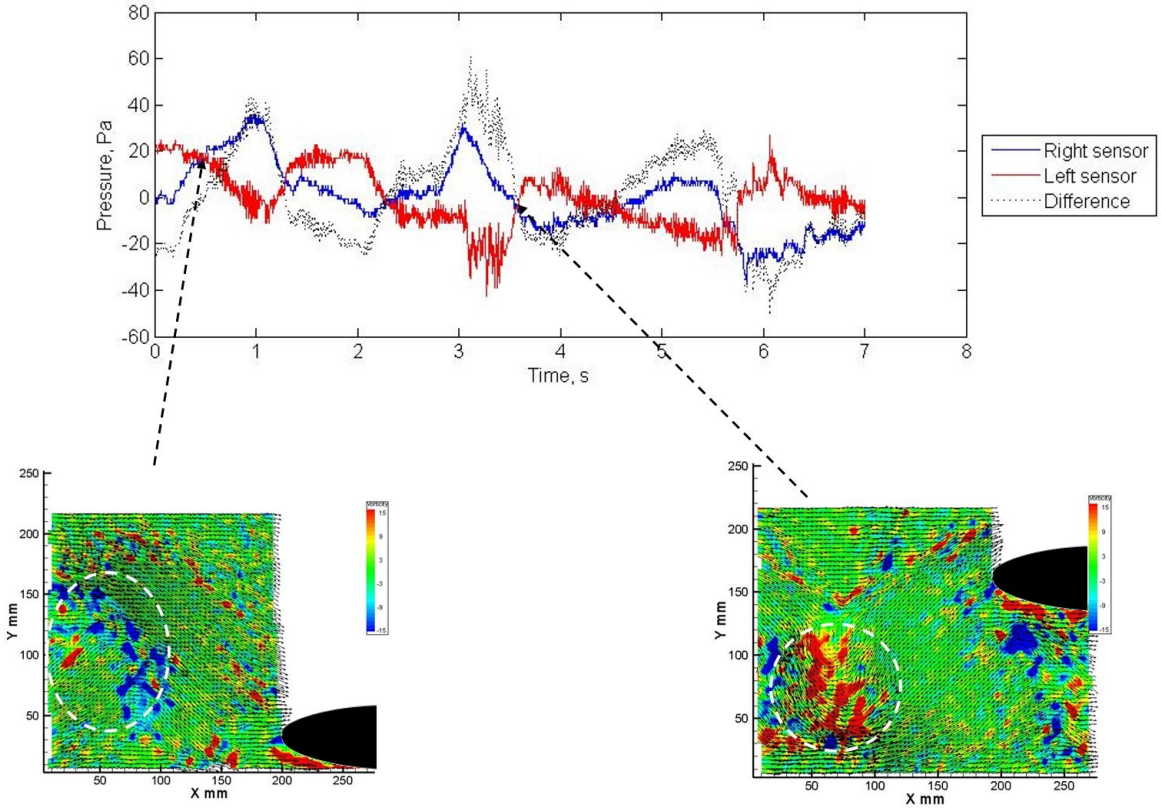

Figure 7-16: Plot showing the pressure plot and associated DPIV images with the robot behind the 100mm diameter cylinder at Re = 21.9 $\times 10^3$. The left-hand image shows an approaching clockwise/negative vortex, corresponding to a peak in the right-hand pressure signal. The left-hand image shows the robot moved further towards the back of the working section of the flow tunnel, and an approaching anti-clockwise/positive vortex, corresponding to a trough on the right-hand sensor.

The peaks and troughs occurring in the pressure plots are associated with vortices; it was found, by examining the pressure and DPIV together, that for the 25mm diameter cylinder the robot could be a normalised lateral distance of 2 cylinder diameters away from the vortices of the wake when the pattern was detected. For the 45 and 100mm diameter cylinders this reduced to a normalised lateral distance of 0.8 cylinder diameters. This is illustrated in Figure 7-17.

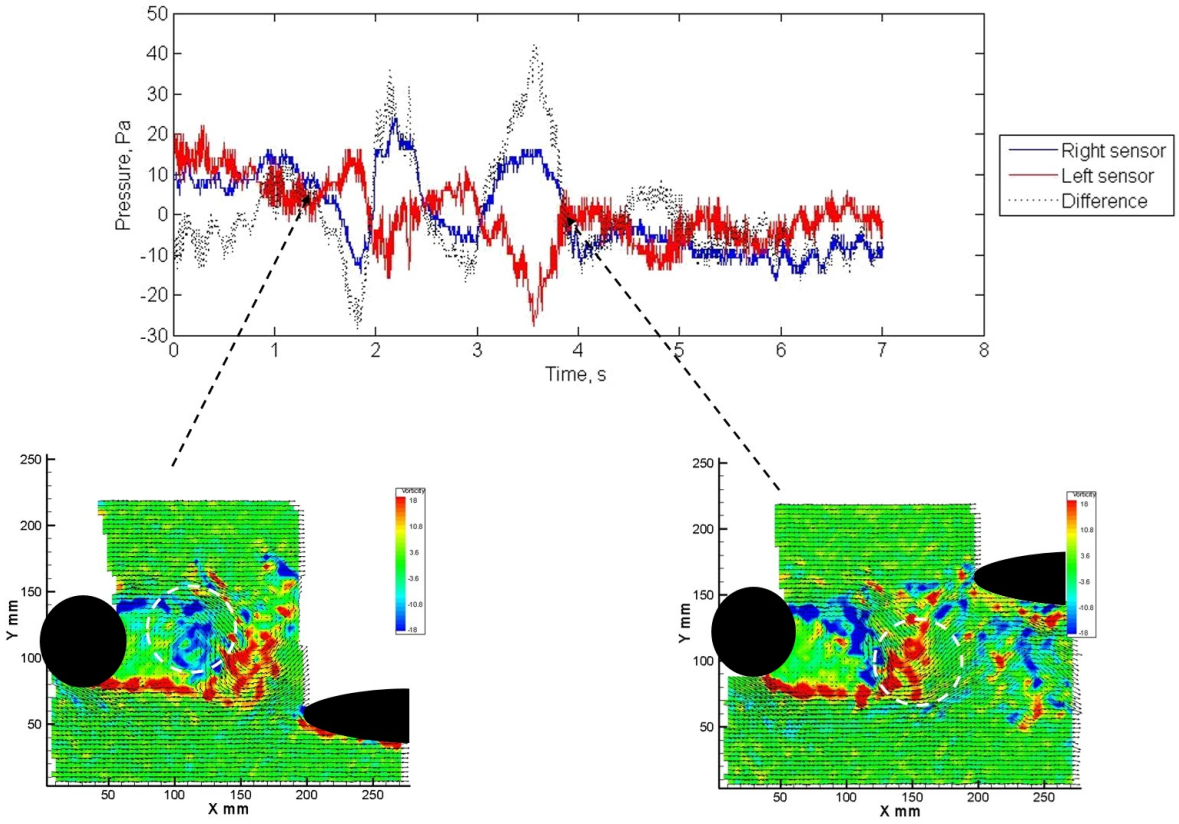

Figure 7-17: Plot showing the positions of the robot at the maximum distance away from the wake of the 45mm diameter cylinder at Re = 21.9 $\times 10^3$ that the Kármán vortex street is detected by the pressure sensors.

Slaloming

The linear motor rig was set to oscillate at 0.36Hz, which approximately matched the vortex shedding frequency of the Kármán vortex street used (0.393Hz). This allows the robot to either slalom between the vortices produced, or move to intercept the vortices as they travel downstream from the cylinder. The total distance moved was set to be 150mm with a maximum speed of approximately 8.5cm s^{-1}. The movement is illustrated in Figure 7-18. The 100mm diameter cylinder was used at a Reynolds number relative to the cylinder of 17.0 $\times 10^3$. The robot was positioned 300mm (three diameters) downstream of the cylinder. The robot was placed within the Kármán vortex street and visually observed; the movement was then started

such that the robot would intercept or avoid the vortices. This was repeated successfully three times for each experiment set to ensure that the position of the robot relative to the vortices was as required.

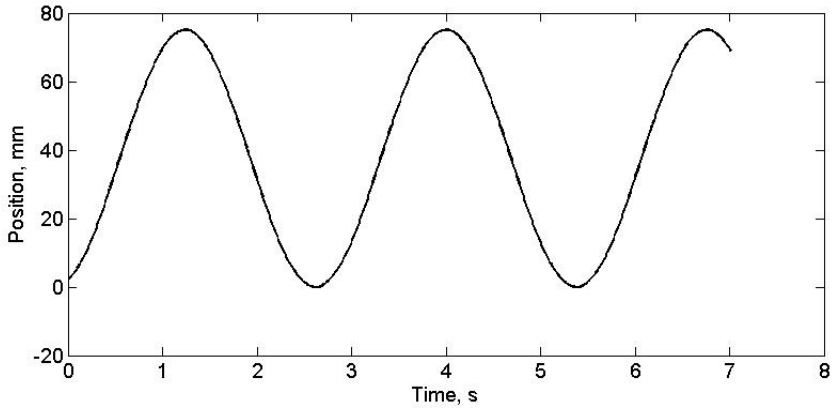

Figure 7-18: Illustration of the oscillatory movement of the robot within the Kármán vortex street behind the 100mm diameter cylinder at a Reynolds number relative to the cylinder of 17.0 $\times 10^3$.

The pressure plots from the slaloming robot are given in Figure 7-19. The characteristic sinusoidal pattern, with a 180° phase difference between either side of the head, is present. By overlaying the movement, Figure 7-20, it can be seen that the pressure signals do not directly align with the movement. Therefore, it is expected that the pressure signals are capturing the vortices present in the flow and not just the movement of the robot. The peak-to-peak amplitudes of the pressure signals were 30Pa and 50Pa when the robot avoids and intercepts the vortices respectively. These have decreased slightly when compared to when the robot was moving through the Kármán vortex street, with values of 40Pa and 80Pa. This decrease in the amplitudes could be used as an indication that the robot is in phase, or directly out of phase, with the vortices rather than simply moving through the Kármán vortex street. The pressure signals were also processed to extract the dominant frequencies. For each of the runs, the dominant frequency was found to be 0.3906Hz, which is similar to that of the vortex shedding frequency calculated from the Strouhal number, of 0.393Hz. The magnitudes of the frequency were greatest in the front-most sensor pair, with a maximum of 20.4 when the robot intercepted the vortices and 12.3 when the robot avoided the vortices. These then decreased with sensor distance from the nose to values of 9.3 and 6.2 respectively.

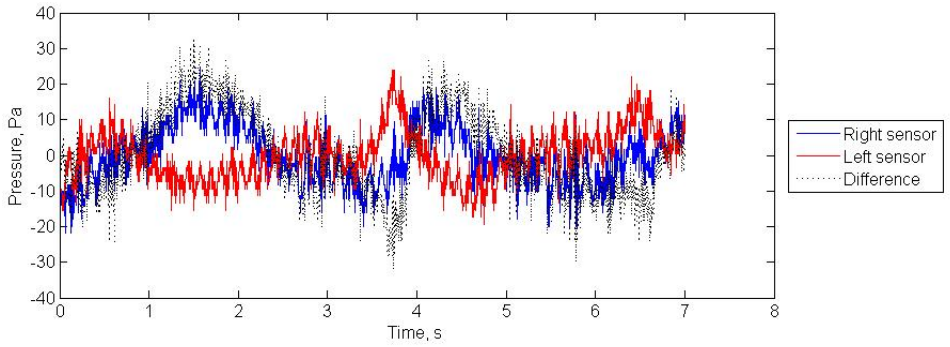

(a)

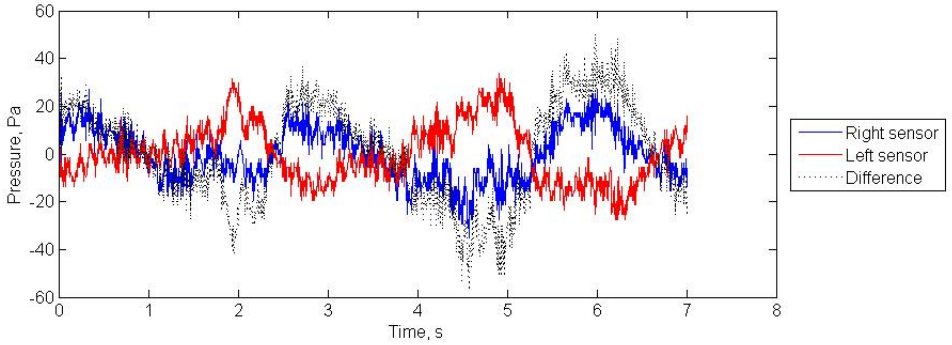

(b)

Figure 7-19: Pressure signals from the robot whilst slaloming through the Kármán vortex street in flow of Re = 21.9 $\times 10^3$ behind the 100mm diameter cylinder when the robot was set to (a) avoid the vortices and (b) intercept the vortices.

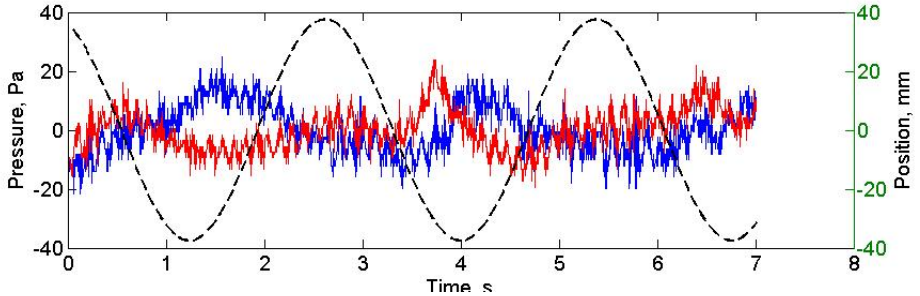

Figure 7-20: Pressure signals from the robot whilst slaloming through the Kármán vortex street in flow of Reynolds number relative to the cylinder 21.9 $\times 10^3$ behind the 100mm diameter cylinder, overlaid with the motion of the robot. The pressure signals and motion were synchronised used the LED to ensure that the motion and signals could be compared.

The pressure plots show the same pattern as has been found for all of the previous experiments; the peaks and troughs of the pressure signals correspond to vortices present in the flow where

a positive vortex approaching the robot created a peak on the left-hand sensor and a trough on the right-hand sensor, and vice versa for the negative vortices. This is illustrated by Figure 7-21.

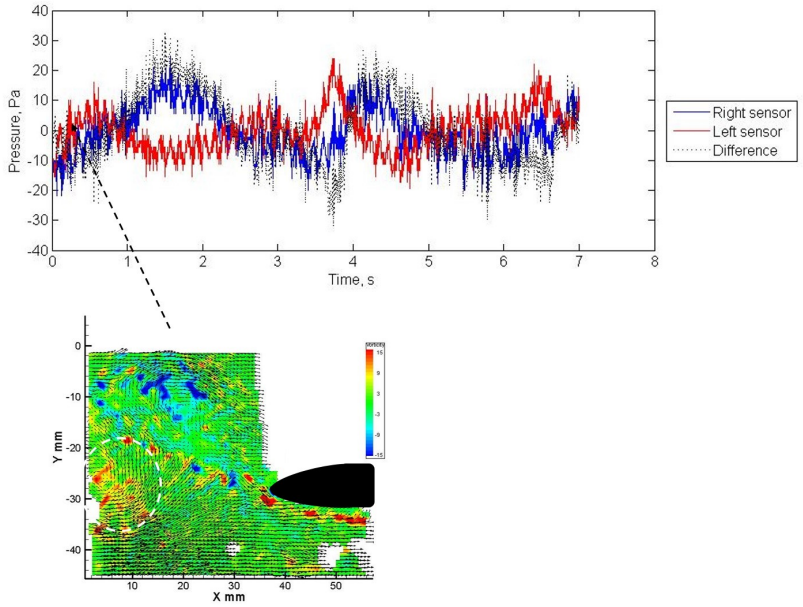

(a)

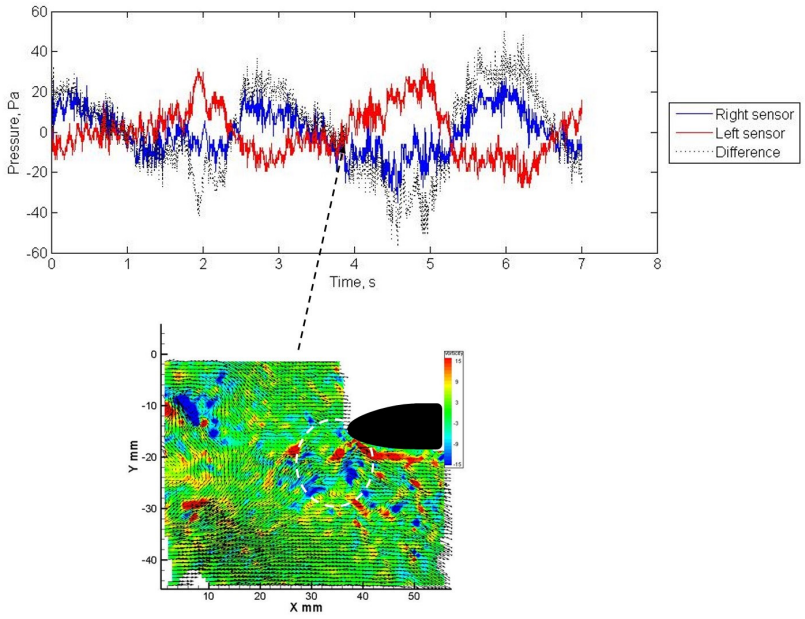

(b)

Figure 7-21: Pressure plot with associated DPIV image showing the position of the robot in relation to the pressure plot for (a) the robot timed to avoid vortices and (b) the robot timed to intercept the vortices. These plots show the oncoming vortices at the onset of the peaks within the pressure sensors, as has been seen previously.

Lateral motion: summary

The DPIV data showed that the normalised size and circulation of the vortices followed the trends found previously; they stay approximately constant with increasing flow speed and decrease with increasing cylinder size. When the robot is moved laterally through the Kármán vortex street, the characteristic sinusoidal pattern that indicates the presence of the Kármán vortex street is present in the pressure signals. However, this pattern is only seen when the robot is within two cylinder diameters of the vortices present in the cylinder wake for the 25mm cylinder, and within 0.8 cylinder diameters for the 45 and 100mm diameter cylinders. The peak-to-peak amplitudes of the pressures increase with increasing flow speed and cylinder size, as was found previously. The dominant frequencies detected matched well with the expected vortex shedding frequencies of the flow. The magnitudes of the frequencies also increased with increasing flow speed and cylinder size, with the greatest value generally found on the sensor pair closest to the nose.

When the robot is moved at the vortex shedding frequency within the Kármán vortex street, such that it can slalom to avoid or intercept the vortices, the pressure signals again show the characteristic sinusoidal pattern that indicates the presence of a Kármán vortex street. The peak-to-peak amplitudes of the pressure signals have reduced when compared to the same cylinder size and flow speed combination for a stationary robot or for the robot moving both laterally within the Kármán vortex street. Otherwise there is no clear indication that the robot is slaloming within the Kármán vortex street as opposed to holding station within the Kármán vortex street.

7.3 Experiments with a moving robot: discussion

Experiments have been carried out with the fish-like robot moving forwards and laterally in both steady flows and within cylinder wakes. The movements were initially carried out at slow robot speeds; the final experiment consisted of a slalom motion of the robot, with a frequency of motion close to the vortex shedding frequency such that the robot could either avoid or intercept the vortices. Synchronised DPIV and pressure data were captured and analysed for each of these experiments.

From the steady flow experiments, it was found that there was no discernible bulk flow disturbance from the motion of the robot. From the forward motion experiments, the pressure plots showed a distinct change in pattern at the point at which the robot changed direction and began to travel backwards; this was not evident within the lateral motion pressure signals.

The DPIV data from the Kármán vortex street experiments shows that, in general, the trends match those found from the flow characterisation experiments with the normalised size and circulation remaining approximately constant with increasing flow speed and decreasing with

increasing cylinder size. The normalised size and circulation of the vortices is a little lower for the 100mm diameter cylinder results.

The dominant frequencies extracted from the pressure signals for the Kármán vortex street experiments detected the vortex shedding frequencies when the robot was within the Kármán vortex street. The exception to this was when the robot was moving laterally through the Kármán vortex street behind the 25mm diameter cylinder, when a frequency of approximately 4Hz was detected, and for the 45mm diameter cylinder the vortex shedding frequencies were not necessarily the dominant peaks. The magnitudes of the frequencies were examined and found to increase with increasing flow speed and cylinder size. When the vortex shedding frequency was not detected, the magnitudes of the frequencies present were low.

The pressure plots for all robot movements showed the oscillatory pattern and 180° phase difference between sides of the head that is the characteristic of the robot present in a Kármán vortex street. The peak-to-peak amplitudes of the pressure increased with increasing flow speed and increasing cylinder size. When the robot was slaloming within the Kármán vortex street, the peak-to-peak amplitudes decreased when compared to the robot moving laterally through the Kármán vortex street, with vortex avoidance giving the lowest value.

As for the stationary robot experiments, the peaks and troughs of the pressure signals with the robot in a Kármán vortex street correspond to the approach of vortices; a peak on the right-hand sensor, corresponding to a trough on the left-hand sensor, occurred when a negative (clockwise) vortex was approaching the nose. Alternatively, a trough on the right-hand sensor and a peak on the left-hand sensor indicated a positive (anticlockwise) vortex approaching the robot. As before, it is deduced from these signals that it is the opposing directional vortex that is travelling across the sensors causing the peak or trough.

When the robot was moved laterally through the Kármán vortex streets, the pressure sensors would only detect the street when they were 2 diameters away for the 25mm diameter cylinder, which decreased to 0.8 diameters for the 45 and 100mm diameter cylinders. The pressure signals showed the characteristic sinusoidal pattern when the robot was within this area, with the pressure signals much smoother outside of this range. The wake widths were estimated from these areas of higher peak-to-peak amplitude signals and were found to be approximately 2.5 times that calculated from the flow characterisation data. It is suggested this increase is due to interference from the robot.

The results of this chapter have shown that the Kármán vortex street can be detected by a moving robot, both when moving slowly compared to the bulk flow speed and when moving at a frequency similar to the vortex shedding frequency. As the robot moved laterally through the cylinder wake the characteristic sinusoidal pattern appeared when the robot was close to the wake, but smoothed considerably as the robot moved out of the street. This is a clear indicator

of the presence of an unsteady, bluff body wake that could be used by an autonomous fish-like robot to detect an unsteady wake. The street, and the vortices present, were detected when they were within 2 cylinder diameters of the robot nose in the lateral direction, and between 0.6 and 1 cylinder diameters upstream of the nose. This work, therefore, supports hypothesis one, that the pressure signal detected at, or near, the front of a fusiform shape could be used to determine the relative position of vortices to the fusiform shape.

The peak-to-peak amplitudes and frequency magnitudes were found to increase with increasing flow speed, but remained constant with increasing cylinder size. Additionally, when the robot was outside of the Kármán vortex street, the peak-to-peak amplitudes and the frequency magnitudes were low. These can, therefore, be used as indicators for the absolute circulation of the vortices, which increase with increasing flow speed but remain approximately constant with increasing cylinder size. This work, therefore, supports hypothesis two, that the properties of the pressure signal would alter corresponding to changing properties of the vortices present in the flow.

The experiments in which the robot was slalomed within the Kármán vortex street show no clear indications that the robot is moving faster than previously, or whether the robot is avoiding or intercepting the vortices within the flow.

Chapter 8

Conclusions

The objective of this work was to link the local and global flow fields around a fish-like robot in steady and unsteady flow and, therefore, determine the correlation between the global fluid phenomena and the local pressure measurements taken from on-board the robot. This study has provided the initial work that could be used in navigational strategies for autonomous underwater robots. By understanding the local patterns that the global flows can cause, the different flows that a robot may encounter can be monitored and possibly used for energy saving swimming routines.

8.1 Literature

A study of the literature has shown a growing interest in biomimetic fish-like robots. Four key elements were identified that can be used as inspiration from fish: its shape, its body motions, its sensing systems and its behaviours or global motions. The final element to be considered is the environment in which it is placed. There have been a number of studies that have investigated flexible foils in steady flows [129–141], with others taking it further and developing flexible robots [142–151]. These studies have, for the most part, focussed on the body movements of the fish in an attempt to emulate the body waveform a fish creates whilst swimming. Additional experiments have been carried out with flexible foils in Kármán vortex streets, but these have been constrained, passive models, with the focus of the studies often on positions for maximum thrust production. The lateral line sensing system of fish have been investigated and shown to detect both the velocity and pressure fields within a flow. A number of studies have been presented on trying to emulate the neuromasts of the lateral line [164–167]. The global movements of the fish alter depending on its environment; the global movement within the Kármán vortex street was termed the Kármán gait by Liao et al [19]. This is a motion that has had little focussed investigation until recently. In addition to this work, a small number of studies were identified that examined both the pressure and velocity fields around fish or fish-like models. Windsor et al [33, 34] presented work using DPIV and CFD to couple the velocity measured and the pressure predicted around a blind Mexican cave fish in open water

and when moving towards a wall. These studies were completed in steady flows, with a gliding fish to provide minimal disturbance to the flow field. Additionally, Bartol et al [31,32] measured the velocity and the pressure around models of boxfish in steady flow. They were examining the flow close to the body of the models, and were able to link low pressure signals with areas of concentrated, attached vorticity.

The review of the literature exposed a gap as no work was found that investigated the link between the global velocity flow field and the local pressure field around a fish-like robot in unsteady flows. Therefore, the experiments in this study were designed to close this gap, by placing a fusiform shape robot, with an integrated artificial lateral line in both steady and unsteady flows and capturing the local and global flow fields. The local flow field was detected using the artificial lateral line which was an embedded array of pressure sensors on the head of the robot. The global flow field was captured using DPIV, which allowed a large area of the flow field around the robot to be imaged. These two measurement techniques were synchronised so that the results could be matched. To give inspiration for the positions and motions of the robot within the experiments, live fish were studied in both steady and unsteady flows to determine their global movements.

At the outset of this work, two hypotheses were proposed; that the pressure signal detected at, or near, the front of a fusiform shape can be used to determine the relative position of vortices to the fusiform shape; and that the properties of the pressure signal alter corresponding to changing properties of the vortices present in the flow. The hypotheses were tested by placing the robot within steady flows and then within a number of different Kármán vortex streets. These latter regimes were created using different cylinder sizes and different flow speeds. At first, the robot was held stationary at different positions relative to the cylinder. The robot was then attached to a linear motor rig and moved either forwards within the working section of the flow tunnel or laterally across the tank. Initially these motions were carried out at slow speeds, with a final experiment increasing the oscillation of movement to match the vortex shedding frequency. This experiment was designed to better emulate the global motion of the fish seen in experiments. The results of this work support these hypotheses.

8.2 Environmental characterisation

Initially, the flow within the working section of the flow tunnel was characterised over a range of flow speeds and using a number of cylinders of different sizes to create Kármán vortex streets. The steady flow experiments showed a variation in the flow speed across the width of the working section, within 17% of the average flow speed value; however, this is a steady flow, such that this pattern remained constant with time. The turbulence intensity value indicated that the flow within the working section of the flow tunnel was turbulent. This background flow is more characteristic of a natural setting, in which fish or fish-like robots would operate, than a laminar flow. The Kármán vortex streets were characterised using six different parameters;

- wake width;
- wake wavelength;
- flow speed variation across the wake;
- vortex shedding frequency;
- vortex size; and
- vortex strength.

The Kármán vortex streets produced span the intermediate subcritical shedding regime [93]. The normalised wake wavelength stayed approximately constant with changing cylinder size and flow speed and was similar to those presented by Brede et al [94] and Karasaduni and Funakoshi [171]. The normalised wake width was found to be of a similar width to the size of cylinder. The velocity within the cylinder wake decreased to a minimum at a central position behind the cylinder, as presented by Liao et al [19], Anagnostopoulous [76] and Nishioka and Sato [172]. The vortex shedding frequencies were close to those calculated using the Strouhal relationship, with a Strouhal number of 0.2. The normalised size of the vortices created stayed approximately constant with increasing flow speed and decreased with increasing cylinder size. They were of similar magnitude to those presented by Lam [67]. The normalised circulation of the vortices followed this same trend, staying approximately constant with increasing flow speed but decreasing with increasing cylinder size. The values calculated fit well with those presented by Williamson [174] and Brede et al [94]. The Kármán vortex streets produced, therefore, fit well with those found within the literature, despite a turbulent background flow. This gave confidence to the parameters used to characterise the flow and to the flows being produced within the flow tunnel.

8.3 Experiments with fish

Having characterised the flow field within the working section of the flow tunnel, experiments with live fish were completed to gain inspiration for the robotic experiments. Rainbow trout were placed in both steady flows and Kármán vortex streets and DPIV was used to capture the surrounding flow field. Two main behaviours were investigated; the global motion of the fish within the flow tunnel in both steady and unsteady flows; and the position of the fish with respect to the vortex position in the Kármán vortex streets. It was found that the fish would hold station in x but drift backwards or laterally within the flow tunnel. Conversely, the fish exhibited a clear oscillatory movement pattern when in the Kármán vortex street. The frequency of this oscillatory pattern was similar to that of the vortex shedding frequency of the Kármán vortex street, and the amplitude of this motion matched the wake width closely. Additionally, it was found that the fish would move to approach the vortices within the flow, rather than avoid them, which is opposite to the results reported by Liao et al [19]. This could

be due to the slower flow speeds tested here compared to those used by Liao et al. These results were then used to inspire the motions used for the robot experiments that followed.

8.4 Experiments with the robot held stationary

For the initial experiments with the robot in the flow tunnel, the robot was held stationary in both steady and unsteady flows. By keeping the robot stationary for each data set, the complexity of the experiment was reduced, thereby allowing the hypotheses to be tested in the simplest scenarios. The steady flow experiments showed that the fusiform shape allowed the flow to travel smoothly around the robot; this was true both when the robot was facing into the flow and when the head was positioned at various angles relative to the direction of flow. The pressure signals did not show any clear patterns, with any oscillation assumed to be noise due to the non-uniform flow. The peak-to-peak amplitudes of the pressure signals were found to increase with increasing flow speed, to values no greater than 25Pa. No clear dominant frequencies were extracted from the pressure signals, and all frequency magnitudes were below 2.5Pa.

Having determined the background flow field and pressure signals that occur with the robot in steady flow, the robot was next placed in Kármán vortex streets. A number of different studies were undertaken; changing the flow speed; changing the cylinder size; placing the robot nearer to the cylinder; placing the robot laterally away from the centre-line of the cylinder; and placing the head at a number of angles relative to the direction of flow. For each of these studies, synchronised DPIV and pressure data at the front of the robot were captured. From all of these experiments, the following conclusions were drawn:

- The normalised size and circulation of the vortices present in the flow followed the same trends found in the flow characterisation experiments: they stayed approximately constant with increasing flow speed and decreased with increasing cylinder size.
- The pressure signals, when the robot was present in the Kármán vortex streets, followed a sinusoidal pattern. There was a 180° phase difference between the pressure signals from either side of the head when the robot was facing into the direction of flow. This angle decreased as the robot was moved away from the central position, whether by moving laterally out of the street, or with the head positioned at angles within the street, until it reached 0°.
- The dominant frequency extracted from the pressure signals closely matched the values calculated from the DPIV data during the flow characterisation experiments. As the robot was moved out of the centre of the Kármán vortex street, the frequency no longer matched the vortex shedding frequency. The magnitudes of the frequencies were also extracted, and found to increase with increasing flow speed. When in the Kármán vortex street the magnitudes were large, up to 60Pa, but when the robot was moved out the Kármán vortex street the magnitudes dropped to values below 1Pa.

- The peak-to-peak amplitude of the pressure signals were found to increase with increasing flow speed, with values reaching up to approximately 100Pa. The values were, in general, higher than those measured with the robot in steady flow, except at the lowest flow speeds tested.
- A peak occurred on the right-hand sensor, corresponding to a trough on the left-hand sensor, when a negative (clockwise) vortex was approaching the nose. Alternatively, a positive (anticlockwise) vortex approaching the robot caused a trough on the right-hand sensor and a peak on the left-hand sensor.
- On average, the vortices were 1.35±0.26 cylinder diameters in front of the nose when the peak or trough occurred. This is smaller than the calculated wavelength, or half wavelength, from the DPIV data when no robot was present in the flow.

From examining these results it can be seen that the presence of the Kármán vortex street can be detected by the on-board pressure sensors, which produce a characteristic sinusoidal pattern, with a 180° phase difference between the sides of the head. By extracting the dominant frequencies and their magnitudes from these signals the vortex shedding frequency can be determined; this, in itself, can help to give an indication of the possible size of the object and the flow speed present, although more information would be needed to determine these parameters explicitly. The peak-to-peak amplitude could be used in conjunction with this, as it also increases with increasing flow speed, but remains approximately constant with increasing cylinder size. This can be used as an indicator of absolute strength of the vortices, which was found to increase with increasing flow speed but remain approximately constant with increasing cylinder size.

Any alterations in the pressure pattern, the phase angle or the frequency detected and its magnitude indicate that the robot is moving away from the centreline of the Kármán vortex street. The characteristic pattern of the pressure signal has also been used to determine that the peaks and troughs of the pressure signal occur when a vortex is approaching the robot and the vortices are, on average, 1.35±0.26 cylinder diameters upstream from the nose of the robot. This distance is approximately one-third of the normalised wake wavelength calculated from the flow characterisation data. It is suggested that the peaks and troughs occurring within the pressure signal are caused by the vortices travelling directly over the sensors, although this was not captured with the DPIV in this study. Instead, only the approaching vortices can be tracked. A trough on a pressure signal would indicate the presence of a vortex, whilst the higher-pressure on the opposing side is due to the direction of the flow from the central street impinging directly on to the pressure sensors. This would agree with the result found by Bartol et al [31], that low pressure signals were correlated with areas of concentrated, attached vorticity on the body of the model. Therefore, it is the presence of a vortex across the pressure sensors that causes the characteristic signal, and can be used to predict the approach of the oncoming vortex of opposite directional rotation. Subsequently, the periodic nature of the pressure signal can be used to predict the presence on an oncoming vortex, its rotational direction and, therefore, its likely lateral position relative to the robot. This can then be used within

the navigational strategy so that the autonomous robot would be able to avoid or intercept the vortices. This work has, therefore, supported the hypotheses presented in Chapter 1.

8.5 Experiments with a moving robot

The complexity of the experiments were then increased so that the robot was moving within the flows, as an autonomous robot would be able to freely move within its environment and would not be fixed in place. The robot was again tested in steady and unsteady flows. Two motions were used; moving the robot forwards (into the direction of flow travel) and moving the robot laterally, across the direction of flow travel. Initially the movements were carried out at slow speeds, but in the final experimental set the oscillatory speed of the robot was increased to match the vortex shedding frequency and the robot was slalomed to either avoid or intercept the vortices within the Kármán vortex street.

The results of the steady flow experiments showed that there was little disturbance to the bulk flow field from the movement of the robot. For the forwards motion, there was a clear indication within the pressure signals at the point at which the robot turned around. This was not present in the lateral motion results. The peak-to-peak amplitude of the pressure signals was found to be higher than for the stationary robot in steady flow, but was again found to increase with increasing flow speed. There were no clear patterns in the dominant frequencies extracted from the pressure signals, except a consistent peak at approximately 50Hz, which is expected to be due to the motion and its associated equipment. The magnitudes of the frequencies in steady flow were all low, below 15Pa.

The DPIV results of the Kármán vortex street showed similar results to the flow characterisation experiments, where the normalised size and circulation of the vortices remained approximately constant with increasing flow speed and decreased with increasing cylinder size.

When the robot was moved forwards within the Kármán vortex street, the characteristic sinusoidal pattern seen in the stationary robot results was present. The peak-to-peak amplitudes of the pressure signals increased with increasing cylinder size, but did not increase consistently with increasing flow speed. The dominant frequencies extracted were close to those of the vortex shedding frequency, with the highest magnitude values occurring on the sensor pair closest to the nose of the robot. The magnitudes of the frequency were also found to increase with increasing cylinder size and increasing flow speed, with values up to 24Pa. The peaks and troughs of the pressure signal were linked with the oncoming vortices, where a peak on the right-hand sensor, corresponding to a trough on the left-hand sensor, occurred when a negative (clockwise) vortex was approaching the nose, and vice versa. The vortices were detected when they were between 0.6 and 1.5 cylinder diameters upstream of the robot, with the shorter distances occurring as the robot moved closer to the cylinder. There is no indication in the pressure plots of this decreasing distance to the vortices.

The robot was then moved laterally across the cylinder wake. The pressure signals now showed the characteristic sinusoidal pattern in only a part of the signal window; when the robot was passing through the central Kármán vortex street. Outside of these sections, the pressure signals were much smoother. This is shown by the peak-to-peak amplitudes of the pressures signals, which were generally low outside of the cylinder wake (between 10 and 40Pa) but approximately doubled when the robot was passing through the Kármán vortex street, to 20 to 80 Pa. These areas of higher amplitude signal were used to estimate a wake width; these values were consistently 2.5 greater than the values calculated from the flow characterisation data. However, this result could be used to deduce the approximate size of the object creating the wake. The dominant frequencies were extracted from the pressure signals and were, generally, close to the vortex shedding values of the flow characterisation data. The magnitudes of the frequencies were extracted, and increased with increasing cylinder size and flow speed as before, with the greatest values found on the sensor pair closest to the nose. For the smallest cylinder at the lower flow speeds, the vortex shedding frequency could not be extracted, or was not the dominant peak as these runs were dominated by a 4Hz signal. It is suggested that this was due to the motion of the robot and the smallest Kármán vortex streets created did not produce a strong enough signal across the sensors to be easily detected. The peaks and troughs within the pressure signal occurred with approaching vortices in the same pattern as found previously, with a peak on the left-hand sensor corresponding to a trough on the right-hand sensor occurring when a positive (anti-clockwise) vortex was approaching and vice versa.

The final experiment completed was to move the robot at a similar oscillation frequency to the vortex shedding frequency and the movement timed so that the robot could either avoid the vortices, or approach (and for the robot intercept) the vortices as was seen in the fish behaviour. The pressure signals again showed the characteristic sinusoidal pattern present in the Kármán vortex street. Overlaying the pressure signals and the motion of the robot showed that the pressure signal was not just due to the robots motion. This was also clear as the peaks and troughs of the pressure signals again linked to the approach of vortices within the flow. The peak-to-peak amplitudes of the signals were lower than when the robot was slowly moved laterally through the Kármán vortex street, with the lowest value when the robot was avoiding the vortices. The dominant frequency was close to that of the calculated vortex shedding frequency both when the robot avoided and intercepted the vortices. The magnitudes of the frequency was greatest when the robot was timed to intercept the vortices. Therefore, the combination of the lower frequency magnitude and lower peak-to-peak amplitude of the pressure signal could be used as an indication that the robot was avoiding vortices, rather than intercepting them. However, there is no clear indication in the results whether the robot is avoiding or intercepting the vortices.

The work presented here has supported the hypotheses presented in Chapter 1, that the pressure signal detected at, or near, the front of a fusiform shape can be used to determine the

relative position of vortices to the fusiform shape and that the properties of the pressure signal alter corresponding to changing properties of the vortices present in the flow. The position of the vortices when upstream of the robot and when the robot was moved laterally out of the vortex street were calculated, using the characteristic sinusoidal pattern that occurred when the robot was in the Kármán vortex street. In addition, it was found the the peak-to-peak amplitude of the pressure signal and the magnitude of the dominant frequencies detected could be used as indicators for the relative strength of the vortices present within the flow. This was found in both the stationary and the moving robot experiments. The results of the moving robot were also able to indicate a wake width; although this value was consistently larger than previously calculated, an approximate object size causing the wake could be estimated and therefore the relative size of the vortices could be inferred.

8.6 Future Work

The work in this study can be considered the initial stages in fully mapping the pressure signals that correspond global flow phenomena using artificial lateral lines on fish-like robots. Further work on this topic which will help to develop and consolidate this new understanding could include:

- Increasing the number of flow fields tested; the current work has carried out these experiments, and shown that the pressure sensors can be used to detect Kármán vortex streets. However, by increasing the number of flow speeds, cylinder sizes and also flow phenomena, for example testing the robot in a fully turbulent field, the map of the global field would be greatly increased.

- Increasing the range of movement available by the robot; the robot used for these experiments was moved using a linear motor rig. The range of movement could include turning and swimming at the same time, or allowing for an autonomously swimming robot, to explore the influence of these motions on the local and global flow fields.

- Adding a flexible tail to the robot; a fixed, rigid tail was attached to the fish-like robot for the presented experiments. However, including a flexible tail, whether it is used as the main mode of propulsion or whether it is added to increase the commonality between the robot and a fish, would help determine whether the motion of a flexible tail would alter the signals detected by the pressure sensors.

- Adding more sensors to the robot; for example, also including velocity sensors to the artificial lateral line to better simulate the total lateral line as present on fish. Sensors such as MEMS sensors to detect velocity that are currently being researched [164, 165] could be added on to the robot. It is possible that, by increasing the amount and type of data collected, the accuracy of the flow prediction using the sensors data could be increased.

8.7 Final word

The work presented here has investigated the literature available and found few studies linking the local and global flow fields (measured using pressure and velocity respectively) around a fish-like object, particularly when moving in the flow. Work by Windsor et al [33,34] and Bartol et al [31, 32] linked the velocity and pressure around a fish or fish-like model respectively, but only in steady flows, with no relative motion of the fish or model. Therefore, to fill this gap in the literature, experiments with a fusiform-shaped fish-like robot with an on-board pressure sensor array have been carried out with the robot placed in both steady and unsteady flows when held stationary and when moving within the flows.

This work can be considered as the initial stages in producing a map of global flow fields using on-board pressure sensing arrays using fish-like robots. This map of information could then be used within navigational strategies, such that an autonomous fish-like robot would be able to determine the flow fields surrounding it, and even whether there may be the potential for energy-saving swimming-routines. For example, a robot could be set to swim slowly through a flow field. If the pressure sensors showed a section of increased peak-to-peak amplitude activity with a sinusoidal pattern and 180° phase-difference between the two sides of the head, a Kármán vortex street may be present. By swimming through this section again, and holding station when the higher amplitude signals occur, it is likely the robot would be stopped within 2 cylinder diameters laterally of the centre of the wake, and likely less (concluded from the distances to the wake from the laterally moving robot). By extracting the dominant frequencies and comparing them to frequencies present when there is no sinusoidal pattern and low peak-to-peak amplitudes, a vortex shedding frequency may be present, if the magnitudes are much higher and there is good agreement in all the sensor pairs along the side of the head. If the occurrence of the peaks and troughs is then examined, the position of the vortices at approximately 1.3 cylinder diameters could be assumed. This would, therefore, give a relative size of the object ahead, as a lower dominant frequency would indicate a larger object (for a given flow speed). Absolute values relating to the street would need greater information, such as the flow speed present, but it is suggested that sufficient information could be extracted to enable a robot to swim within the Kármán vortex street if required. In addition, with further work artificial lateral lines could be used to allow a number of fish-like robots to swim in formation, or track each other, without the need for set swimming routes to be pre-determined. Given the number of uses that fish-like robots could be put to, further developing them, their movements and their capabilities can aid in the maintenance, protection and exploration of the vast underwater landscapes that are present on this planet.

Bibliography

[1] The fly shop. website, 2014.

[2] M. Sfakiotakis, D. Lane, J. Bruce, and C. Davies. Review of fish swimming modes for aquatic locomotion. *IEEE Journal of Oceanic Engineering*, 24:237–252, 1999.

[3] Koichi Hirata. Principles of the swimming fish robot. National Maritime Research Institute Website, 2001.

[4] Alexis Hall. Mechanoreception. Website, 2014.

[5] CILIA. $www.cilia - bionics.org$. Website, October 2009.

[6] Princeton University. www.princeton.edu. website, February 1997.

[7] Arunn Narasimhan. unrulednotebook.wordpress.com/2009/03/12/avenue-de-henri-benard/, November 2009.

[8] Festo. $www.festo.com/cms/en_corp/13611.htm$. Website, 2013.

[9] Evo Logica. $www.evologics.de/en/products/glider/index.html$. Website, 2010.

[10] C.C Lindsey. Form function and locomotory habits in fish. *Fish Physiology*, 8:1–100 1–100, 1978.

[11] George V. Lauder and Eric D. Tytell. Hydrodynamics of undulatory propulsion. *Fish Biomimetics*, 23:927–939, 2005.

[12] B. Ahlborn. *Zoological Physics. Quantitative Models of Body Design, Actions, and Physical Limitations of Animals.* Springer, 2004.

[13] J. J. Videler, U. K. Müller, and E. J. Stamhuis. Aquatic vertebrate locomotion: wakes from body waves. *Journal of Experimental Biology*, 202:3423–3430, November 1999.

[14] U. K. Müller, B. L. E. van den Heuvel, E. J. Stamhuis, and J. J. Videler. Fish foot prints: morphology and energetics of the wake behind a continuously swimming mullet (*Chelon Labrosus* risso). *Journal of Experimental Biology*, 200:2893–2906, August 1997.

[15] H. Bleckmann and R. Zelick. Lateral line system of fish. *Integrative Zoology*, 4:13–25, 2009.

[16] A. Schmitz, H. Bleckmann, and J. Mogdans. Organisation of the superficial neuromast system in goldfish, *Carassius auratus*. *Journal of Morphology*, 269:751–761, 2008.

[17] Matthew J. McHenry, James A. Strother, and Sietse M. van Netten. Mechanical filtering by the boundary layer and fluid-structure interaction in the superficial neuroamst of the fish lateral line system. *Journal of comparative physiology a-neuroethology sensory neural and behavioural physiology*, 194:795–810, 2008.

[18] F.E. Fish and G.V. Lauder. Passive and active flow control by swimming fishes and mammals. *Annual Review of Fluid Mechanics*, 38:193–224, 2006.

[19] James C. Liao, David N. Beal, George V. Lauder, and Michael S. Triantafyllou. The kármán gait: novel body kinematics of rainbow trout swimming in a vortex street. *Journal of Experimental Biology*, 206:1059–1073, 2002.

[20] James C. Liao, David N. Beal, George V. Lauder, and Michael S. Triantafyllou. Fish exploiting vortices decrease muscle activity. *Science*, 302:1566–1569, 2003.

[21] Bernard Massey and John Ward-Smith. *Mechanics of Fluids*. Taylor and Francis, eighth edition, 2006.

[22] Sheldon I. Green, editor. *Fluid Vortices*. Kluwer Academic Publishers, 1995.

[23] C. H. K. Williamson. The existence of two stages in the transition to three-dimensionality of a cylinder wake. *Physics of Fluids*, 321:3165, 1988.

[24] M. Rosen. Water flow about a swimming fish. *NOTS Technical Publication. U.S Naval Ordnance Test Station, China Lake*, 1959.

[25] C. H. K. Williamson. Three-dimensional vortex dynamics in bluff body wakes. *Experimental Thermal and Fluid Science*, 12:150–168, 1996.

[26] David L. Hu, Thomas J. Goreau, and John W. M. Bush. Flow visualisation using tobacco mosaic virus. *Experiments in Fluids*, 2008.

[27] Charles G. Lomas. *Fundamentals of Hot-Wire Anemometry*. Cambridge University Press, 1986.

[28] P. W. Bearman. On vortex street wakes. Technical report, National Physical Laboratory, Aerodynamics Division, 1966.

[29] Brian Cantwell and Donald Coles. An experimental study of entrainment and transport in the turbulent near wake of a circular cylinder. *Journal of Fluid Mechanics*, 136:321–374, 1983.

[30] Mitsuaki Funakoshi. Evolution of voriticty regions of kármán-vortex-street type. *Fluid Dynamics Research*, 15:251–269, 1995.

[31] Ian K. Bartol, Malcolm S. Gordon, Morteza Gharib, Jay R. Hove, Paul W. Webb, and Daniel Weihs. Flow patterns around the carapaces of rigid-bodied, multi-propulsor boxfishes (teleostei: Ostraciidae). *Integrative and Comparative Biology*, 42:971–980, 2002.

[32] Ian K. Bartol, Morteza Gharib, Paul W. Webb, Daniel Weihs, and Malcolm S. Gordon. Body-induced vortical flows: a common mechanism for self-corrective trimming control in boxfishes. *Journal of Experimental Biology*, 208:327–344, 2005.

[33] Shane P. Windsor, Stuart E. Norris, Stuart M. Cameron, Gordon D. Mallinson, and John C. Montgomery. The flow fields involved in hydrodynamic imaging by blind mexican cave fish (*Astyanax fasciatus*). part I: open water and heading towards a wall. *Journal of Experimental Biology*, 213:3819–3831, 2010.

[34] Shane P. Windsor, Stuart E. Norris, Stuart M. Cameron, Gordon D. Mallinson, and John C. Montgomery. The flow fields involved in hydrodynamic imaging by blind mexican cave fish (*Astyanax fasciatus*). part II: gliding parallel to a wall. *Journal of Experimental Biology*, 213:3832–3842, 2010.

[35] R. Venturelli, O. Akanyeti, F. Visentin, J. Jezov, L. D. Chambers, G. Toming, J. Brown, M. Kruusmaa, W. M. Megill, and P. Fiorini. Hydrodynamic pressure sensing with an artificial lateral line in steady and unsteady flows. *Bioinspiration and Biomimetics*, 7:1–12, 2012.

[36] O. Akanyeti, L. D. Chambers, J. Jezov, J. Brown, R. Venturelli, M. Kruusmaa, W. M. Megill, and P. Fiorini. Self-motion effects on hydrodynamic pressure sensing; part i. forward-backward motion. *Bioinspiration and Biomimetics*, 8:1–10, 2013.

[37] L. D. Chambers, O. Akanyeti, R. Venturelli, J. Jezov, J. Brown, M. Kruusmaa, P. Fiorini, and W. M. Megill. A fish perspective: detecting flow features while moving using an artificial lateral line in steady and unsteady flow. *Journal of the Royal Society Interface*, 11, 2014.

[38] Hans J. Lugt. The dilema of defining a vortex. *Recent developments in theoretical and experimental fluid mechanics: compressible and incompressible flows*, pages 309 – 321, 1979.

[39] M. S. Chong, A. E. Perry, and B. J. Cantwell. A general classification of three dimensional flow fields. *Physics of Fluids A*, 2:765–777, 1990.

[40] C. R. Hunt, A. A. Wray, and P. Moin. Eddies, streams and convergence zones in turbulent flows. In *Studying Turbulence using Numerical Simulation Databases Proceedings of 1988 Summer Program*, 1988.

[41] Jinhee Jeong and Fazle Hussain. On the identification of a vortex. *Journal of Fluid Mechanics*, 285:69–94, 1995.

[42] J. Sung and J. Y. Yoo. Near-wake vortex motions behind a circular cylinder at low reynolds number. *Journal of Fluids and Structures*, 17:261–274, 2003.

[43] W. Kim, J. Sung, J. Y. Yoo, and M. H. Lee. High-definition piv analysis of vortex shedding in the cylinder wake. *Journal of Visualization*, 7:17–24, 2004.

[44] T. von Kármán. On the mechanism of the drag a moving body experiences in a fluid. *Progress in Aerospace Sciences*, 1911. Translated by E. Krause and A. Henze, Institute of Aerodynamics, RWTH Aachen University. in 2013.

[45] E. T. S. Walton. On the motion of vortices near a circular cylinder in a stream of liquid. *Proceedings of the Royal Irish Academy. Section A: Mathematical and Physical Sciences*, 38:29–39, 1928.

[46] Ian Taylor and Marco Vezza. Prediction of unsteady flow around square and rectangular section cylinders using a discrete vortex method. *Journal of Wind Engineering and Industrial Aerodynamics*, 82:247–269, 1999.

[47] Muammer Ozgoren. Flow structure in the downstream of square and circular cylinders. *Flow Measurement and Instrumentation*, 17:225–235, 2006.

[48] H. F. Wang and Y. Zhou. The finite-length square cylinder near wake. *Journal of Fluid Mechanics*, 638:453–490, 2009.

[49] R.R. Clements and D.J. Maul. The repesentation of sheets of vorticity by discrete vortices. *Progress in Aerospace Sciences*, 16:129–146, 1975.

[50] F. H. Barnes and I. Grant. Vortex shedding in unsteady flow. *Journal of Wind Engineering and Industrial Aerodynamics*, 11:335–344, 1983.

[51] Abdollah Shadaram, Mahdi Azimi Fard, and Noorallah Rostamy. Experimental study of near wake flow behind a rectangular cylinder. *American Journal of Applied Sciences*, 8:917–926, 2008.

[52] Shaun A. Johnson, Mark C. Thompson, and Kerry Hourigan. Predicted low frequency structures in the wake of elliptical cylinders. *European Journal of Mechanics B/Fluids*, 23:229–239, 2004.

[53] Oksana Stalnov, Vitali Palei, Ilan Fono, Kelly Cohen, and Avi Seifert. Experimental estimation of a d-shaped cylinder wake using body-mounted sensors. *Experiments in Fluids*, 42:531–542, 2007.

[54] A. de Vecchi, S. J. Sherwin, and J. M. R. Graham. Wake dynamics of external flow past a curved circular cylinder with the free-stream aligned to the plane of curvature. *Journal of Fluids and Structures*, 24:1262–1270, 2008.

[55] A. J. Baxendale and I. Grant. Vortex shedding from two cylinders of different diameters. *Journal of Wind Engineering and Industrial Aerodynamics*, 23:427–435, 1986.

[56] A.T. Sayers and A. Saban. Flow over two cylinders of different diameters: The lock-in effect. *Journal of Wi*, 51:43–54, 1994.

[57] Robert J. Martinuzzi and Brian Havel. Vortex shedding from two surface-mounted cubes in tandem. *International Journal of Heat and Fluid Flow*, 25:364–372, 2004.

[58] J. C. Hu and Y. Zhou. Flow structure behind two staggered circular cylinders. part i. downstream evolution and classification. *Journal of Fluid Mechanics*, 607:51–80, 2008.

[59] A. Alper Oner, M. Salih Kirkgoz, and M. Sami Akoz. Interaction of a current with a circular cylinder near a rigid bed. *Ocean Engineering*, 35:1492–1504, 2008.

[60] SiYing Wang, LaiBing Jia, and XieZhen Yin. Kinematics and forces of a flexble body in karman vortex street. *Chinese Science Bulletin*, 54:556–561, 2009.

[61] N. Adil Ozturk, Azize Akkoca, and Besir Sahin. Piv measurements of flow past a confined cylinder. *Experiments in Fluids*, 44:1001–1014, 2008.

[62] E. D. Obasaju, P. W. Bearman, and J. M. R. Graham. A study of forces, circulation and vortex patterns around a circular cylinder in oscillating flow. *Journal of Fluid Mechanics*, 196:467–494, 1988.

[63] Y. Yokoi and K. Kamemoto. Vortex shedding from an oscillating circular cylinder in a uniform flow. *Experimental Thermal and Fluid Science*, 8:121–127, 1994.

[64] C. W. Ng, V. S. Y. Cheng, and N. W.M. Ko. Numerical study of vortex interactions behind two circular cylinders in bistable flow regime. *Fluid Dynamics Research*, 19:379–409, 1997.

[65] J. S. Tao, X. Y. Huang, and W. K. Chan. A flow visualisation study on feedback control of vortex shedding from a circular cylinder. *Journal of Fluids and Structures*, 10:965–970, 1996.

[66] J. Wu and J. Sheridan. The wake of an orbiting cylinder. *Journal of Fluids and Structures*, 11:617–626, 1997.

[67] K. M. Lam. Vortex shedding flow behind a slowly rotating circular cylinder. *Journal of Fluids and Structures*, 25:245–262, 2009.

[68] J. Wu, J. Sheridan, M. C. Welsh, and K. Hourigan. Three-dimensional vortex sturctures in a cylinder wake. *Journal of Fluid Mechanics*, 312:201–222, 1996.

[69] Fulvio Scarano and Christian Poelma. Three-dimensional vorticity patterns of cylinder wakes. *Experiments in Fluids*, 47:69–83, 2009.

[70] A. Rao, J. Leontini, M.C. Thompson, and K. Hourigan. Three-dimensionality in the wake of a rotating cylinder in a uniform flow. *Journal of Fluid Mechanics*, 717:1–29, 2013.

[71] H. Glauert. The characteristics of a karman vortex street in a channel of finite breadth. *Proceedings of the Royal Society of London A: Mathematical Physical and Engineering Sciences*, 120:34–46, 1928.

[72] *On the Action of Viscosity in Increasing the Spacing Ratio of a Vortex Street*, volume 154, 1936.

[73] Fernando L. Ponta. Vortex decay in the kármán eddy street. *Physics of Fluids*, 22:online, 2010.

[74] Hassan Aref and Eric D. Siggia. Evolution and breakdown of a vortex street in two dimensions. *Journal of Fluid Mechanics*, 109:435–463, 1981.

[75] Peter Plaschko and Eberhard Berger. Periodic flow in the near wake of straight circular cylinders. *Physics of Fluids*, 5:1718–1724, 1993.

[76] P. Anagnostopoulos. Computer-aided flow visualisation and vorticity balance in the laminar wake of a circular cylinder. *Journal of Fluids and Structures*, 11:33–72, 1997.

[77] T. S. Morton. An estimate of the circulation generated by a bluff body. *Journal of Scientific and Mathematical Research*, 2:12–19, 2008.

[78] *Vortex dynamics of wakes*, 2008.

[79] Uğur Oral Ünal, Mehmet Atlar, and Ömer Gören. Effect of turbulence modemodel on the computation of the near-wake flow of a circular cylinder. *Ocean Engineering*, 37:387–399, 2010.

[80] Garrett Birkhoff. A new theory of vortex streets. *Proceedings of the National Academy of Sciences*, 38:409 – 410, 1952.

[81] Garrett Birkhoff. Formation of vortex streets. *Journal of Applied Physics*, 24:98–103, 1953.

[82] P. C. Jain and B.S. Goel. Shedding of vortices behind a circular cylinder. *Computers and Fluids*, 4:137–142, 1976.

[83] James Carl Schatzman. *A model for the von Kármán vortex street*. PhD thesis, California Institute of Technology, 1981.

[84] P. G. Saffman. and J. C. Schatzman. Properties of a vortex street of finite vortices. *SIAM Journal on Scientific and Statistical Computing*, 2:285–295, 1981.

[85] P. G. Saffman and J. C. Schatzman. Stability of a vortex street of finite vortices. *Journal of Fluid Mechanics*, 117:171–185, 1982.

[86] P. G. Saffman. and J. C. Schatzman. An inviscid model for the vortex-street wake. *Journal of Fluid Mechanics*, 122:467–786, 1982.

[87] Paolo Luzzatto-Fegiz and Charles H. K. Williamson. Structure and stability of the finite-area von kármán street. *Physics of Fluids*, 24:066602, 2012.

[88] Pedram Rouchan and X. L. Wu. Universal wake structures of kármán vortex streets in two-dimensional flows. *Physics of Fluids*, 17:073601, 2005.

[89] Boye Ahlborn, Mae L. Seto, and Bernd R. Noack. On drag, strouhal number and vortex-street structure. *Fluid Dynamics Research*, 30:379–399, 2002.

[90] Alan Elcrat, Bengt Fornberg, Mark Horn, and Kenneth Miller. Some steady vortex flows past a circular cylinder. *Journal of Fluid Mechanics*, 409:13–27, 2000.

[91] B. N. Rajani, A. Kandasamy, and Sekhar Majumdar. Numerical simulation of laminar flow past a circular cylinder. *Applied Mathematical Modelling*, 33:1228–1247, 2009.

[92] M. M. Zdravkovich. Conceptual overview of laminar and turbulent flows smooth and rough circular cylinders. *Journal of Wind Engineering and Industrial Aerodynamics*, 33:53–62, 1990.

[93] M. M. Zdravkovich. *FLOW AROUND CIRCULAR CYLINDERS VOL 1: FUNDAMENTALS*. Oxford University Press, 1997.

[94] M. Brede, H. Eckelmann, and D. Rockwell. On secondary vortices in the wake. *Physics of Fluids*, 8:2117 – 2124, 1996.

[95] T. Igarashi. Flow characteristics around a circular cylinder with a slit (1st report, flow control and flow patterns). *Bulletin of the JSME*, 21(154):656–664, 1978.

[96] A. Agrawal and A. K. Prasad. Properties of vortices in self-similar tubulent jet. *Experiments in Fluids*, 33:565–577, 2002.

[97] C. Norberg. An experimental investigation of the flow around s circular cylinder: influence of aspect ratio. *Journal of Flu*, 258:287–316, 1994.

[98] Saul S. Abarbanel, Wai Sun Don, David Gottlieb, David H. Rudy, and James C. Townsend. Secondary frequencies in teh wake of a circular cykinder with vortex shedding. *Journal of Fluid Mechanics*, 225:557–574, 1991.

[99] J. P. Batham. Pressure distributions on circular cylinders at critical reynolds numbers. *Journal of Fluid Mechanics*, 57:209–228, 1973.

[100] P. W. Bearman. On vortex shedding from a circular cylinder in teh critical reynolds number regime. *Journal of Fluid Mechanics*, 37:577–585, 1969.

[101] R.B. Green and J.H. Gerrard. Vorticity measurements in the near wake of a circular cylinder at low reynolds numbers. *Journal of Fl*, 246:675–691, 1993.

[102] Oliver Pust and Christoph Lund. The kármán vortex street - ldv and piv measurements compared with cfd. In R. J. Adrian, D. F. G Dur ao, F. Durst, M. V. Heitor, M. Maeda, and J. H. Whitelaw, editors, *Laser Techniques Applied to Fluid Mechanics Selected papers from the 9th International Symposium, Lisbon, Portugal 13-16 July 1998*. Springer, 2000.

[103] A. S. Banerjee, A. C. Mandal, and J. Dey. Particle image velocimetry studies of an incipient spot in the Blasius boundary layer. *Experiments in Fluids*, 40:928–941, 2006.

[104] Thilo Hölscher, Javier Rodriguez-Rodriguez, Wilko G. Wilkening, Juan C. Lasheras, and Hoi Sang U. Intraoperative brain ultrasound: A new approach to study flow dynamics in intracranial aneurysms. *Ultrasound in Medicine and Biology*, 32:1307–1313, 2006.

[105] Geoffrey R. Spedding and Anders Hedenström. Piv-based investigations of animal flight. *Experiments in Fluids*, 46:749–763, 2009.

[106] Eize J. Stamhuis and John V. Videler. Quantitative flow analysis around aquatic animals using laser sheet particle image velocimetry. *Journal of Experimental Biology*, 198:283–294, 1995.

[107] M. Raffel, C. Willert, S. Wereley, and J. Kommpenhans. *Particle Image Velocimetry: A Practical Guide*. Springer, second edition, 1998.

[108] R. J. Adrian. Statistical properties of particle image velocimetry measurements in turbulent flows. In D. F. G . Durao, R. J. Adrian, T. Asanuma, F. Durst, and J. H. Whitelaw, editors, *Laser Anemometry in Fluid Mechanics*, volume III, pages 115 – 129. 1988.

[109] R. D. Keane and R. J. Adrian. Theory of cross-correlation analysis of piv images. *Applied Science Research*, 49:191–215, 1992.

[110] J Westerweel. Fundamentals of digital particle image velocimetry. *Measurement Science and Technology*, 8:1379–1392, August 1997.

[111] N. Fujisawa and Y. Oguma. Measurement of pressure field around a NACA0018 airfoil from PIV velocity data. *Journal of Visualization*, 11:281–282, 2008.

[112] N Fujisawa, S Tanahashi, and K Srinivas. Evaluation of pressure field and fluid forces on a circular cylinder with and without rotational oscillation using velocity data from piv measurement. *Measurement Science and Technology*, 16:989 – 996, 2005.

[113] Maarten Vanierschot and Eric Van den Bulck. Planar pressure field determination in the initial merging zone of an annular swirling jet based on stereo-piv measurements. *Sensors*, 8:7596–7608, 2008.

[114] R. Gurka, A. Liberzon, D. Hefetz, D. Rubinstein, and U. Shavit. Computation of pressure distribution using piv velocity data. urapiv.wordpress.com/projects/pressure/, 1999.

[115] Kobra Gharali and David A Johnson. Pressure and acceleration determination methods using piv velocity data. In *PROCEEDINGS OF THE ASME FLUIDS ENGINEERING DIVISION SUMMER CONFERENCE*, August 2008.

[116] S.Y. Jaw, J.H. Chen, and P.C. Wu. Measure of pressure distribution from piv experiments. *Journal of Visualization*, 12:27–35, 2009.

[117] James C. Liao. The role of the lateral line and vision on body kinematics and hydrodyanmic preference of rainbow trout in turbulent flow. *Journal of Experimental Biology*, 209:4077–4090, 2006.

[118] James C. Liao. A review of fish swimming mechanics and behaviour in altered flows. *Philosophical transactions of the royal society biologial sciences*, 362:1973–1993, 2007.

[119] Kirsten Pohlmann, Jelle Atema, and Thomas Breithaupt. The importance of the lateral line in nocturnal predation of piscivorous catfish. *Journal of Experimental Biology*, 207:2971–2978, 2004.

[120] B. Chagnaud, H. Bleckmann, and J. Engelmann. Neural responses of goldfish lateral line afferents to vortex motions. *The Journal of Experimental Biology*, 209:327–342, 2006.

[121] D. N. Beal, F. S. Hover, M. S. Triantafyllou, J.C. Liao, and G. V. Lauder. Passive propulsion in vortex wakes. *Journal of Fluid Mechanics*, 549:385–402, 2005.

[122] B. Chagnaud, H. Bleckmann, and M. Hofmann. Kármán vortex street detection by the lateral line. *Journal of Comparative Physiology A*, 193:753–763, 2007.

[123] Arthur B. Dubois, Giovanni A. Cavagna, and Richard S. Fox. Pressure distribution on the body surface of swimming fish. *Journal of Experimental Biology*, 60:581–591, 1974.

[124] James Lighthill. Estimates of pressure differences across the head of a swimming clupeid fish. *Philosophical Transactions of the Royal Society of London*, 341:129–140, 1993.

[125] M. J. McHenry, K. B. Michel, and U.K. Müller. Hydrodynamic sensing does not facilitate active drag reduction in the golden shiner (notemigonus crysoleucas). *Journal of Experimental Biology*, 213:1309–1319, 2009.

[126] Eliot G. Drucker and George V. Lauder. Locomotor forces on a swimming fish: three-dimensional vortex wake dynamics quantified using digital particle image velocimetry. *Journal of Experimental Biology*, 202:2393–2412, August 1999.

[127] J. Sakakibara, M. Nakagawa, and M. Yoshida. Stereo-PIV study of flow around a maneuvering fish. *Experiments in Fluids*, 36:282–293, August 2003.

[128] Jennifer C. Nauen and George V. Lauder. Quantification of the wake of rainbow trout (oncorhynchus mykiss) using three-dimensional stereoscopic digital particle image velocimetry. *Journal of Experimental Biology*, 205:3271–3279, 2002.

[129] M. R. Amiralaei, H. Alighanbari, and S.M. Hashemi. Flow field characteristics study of a flapping airfoil using computational fluid dynamics. *Journal of fluids and structures*, 27:1068–1085, 2011.

[130] Gen-Jin Dong and Xi-Yun Lu. Numerical analysis on the propulsive performance and vortex shedding of fish-like travelling wavy plate. *International journal for numerical methods in fluids*, 48:1351–1373, 2005.

[131] Ramiro Godoy-Diana, Catherine Marais, Jean-Luc Aider, and José Eduardo Wesfreid. A model of the symmetry breaking of the reverse bénard-von kármán vortex street produced by a flapping foil. *Journal of Fluid mechanics*, 622:23–32, 2009.

[132] R. Gopalkrishnan, M. S. Triantafyllou, G. S. Triantafyllou, and D. Barrett. Active vorticity control in a shear flow using a flapping foil. *Journal of Fluid Mechanics*, 274:1–21, 1994.

[133] R.F. Huang and J.S. Wu. Effects of cylinder wake on separated boundary layer of a wing. *AIAA Journal*, 45:247–256, 2007.

[134] David Lentink, Florian T. Muijres, Frits J. Donker-Duyvis, and Johan L. van Leeuwen. Vortex-wake interactions of a flapping foil that models animal swimming and flight. *Journal of Experimental Biology*, 211:267–273, 2007.

[135] Florian T. Muijres and David Lentink. Wake visualization of a heaving and pitching foil in a soap film. *Experiments in Fluids*, 43:665–673, 2007.

[136] Q. Liao, G.-J. Dong, and X.-Y. Lu. Vortex formation and force characteristics of a foil in the wake of a circular cylinder. *Journal of Fluids and Structures*, 19:491–510, 2004.

[137] Teis Schnipper, Anders Anderson, and Tomas Bohr. Vortex wakes of a flapping foil. *Journal of Fluid Mechanics*, 633:411–423, 2009.

[138] T. K. Sengupta, T. T. Lim, Sharanappa V. Sajjan, S. Ganesh, and J. Soria. Accelerated flow past a symmetrical arofoil: experiments and computations. *Journal of Fluid Mechanics*, 591:255–288, 2007.

[139] M. S. Triantafyllou, A. H. Techet, Q. Zhu, D. N. Beal, F. S. Hover, and D. K. P. Yue. Vorticity control in fish-like propulsion and maneuvering. *Integrative and Comparative Biology*, 42:1026–1031, 2002.

[140] Qiang Zhu. Optimal frequency for flow energy harvesting of a flapping foil. *Journal of Fluid Mechanics*, 675:495–517, 2011.

[141] Alexandra H Techet, Franz S Hover, and Michael S Triantafyllou. Separation and turbulence control in biomimetic flows. *Flow, Turbulence and Combustion*, 71:105 – 118, 2003.

[142] Pablo Valdivia y Alvarado. *Design of a Biomimetic Compliant DEvices for Locomotion in Liquid Environments*. PhD thesis, Massachusetts Institute of Technology, 2007.

[143] Christoph Brücker and Horst Bleckmann. Vortex dynamics in the wake of a mechanical fish. *Experiments in Fluids*, 43:799–810, July 2007.

[144] Baofeng Gao and Shuxiang Guo. Fluid dynamic analysis of an icpf actuated fish-like underwater microrobot with 3 dof. In *Proceedings of the 2011 IEEE International Conference on Mechatronics and Automation*, 2011.

[145] G. V. Lauder, P. G. A. Madden, J. L. Tangorra, E. Anderson, and T. V. Baker. Bioinspiration from fish for smart material design and function. *Smart Materials and Structures*, 20, 2011.

[146] Eunjeong Lee. Design of a soft and autonomous biomimetic micro-robotic fish. *IEEE Conference on Industrial Electronics and Applications*, 5:240–247, 2010.

[147] J. H. Long Jr, N. M. Krenitsky, S. F. Roberts, J. Hirokawa, J. de Leeuw, and M. E. Porter. Testing biomimetic structure in bioinspired robots: How vertebrae control the stiffness of the body and the behaviour of fish-like swimmers. *Integrative and Comparative Biology*, pages 1–18, 2011.

[148] Paul Riggs, Adrian Bowyer, and Julian Vincent. Advantages of a biomimetic stiffness profile in pitching flexible fin propulsion. *Journal of Bionic Engineering*, 7:113–119, 2010.

[149] A. B. Phillips, J. I. Blake, B. Smith, S. W. Boyd, and G. Griffiths. Nature in engineering for monitoring the oceans: towards a bio-inspired flexble autonomous underwater vehicle operating in unsteady flow. *Journal of Engineering for the Maritime Environment*, 224:267–278, 2010.

[150] Mohsen Siahmansouri, Ahmad Ghanbari, and Mir Masoud Seyyed Fakhrabadi. Design, implementation and control of a fish robot with undulating fins. *International Journal of Advanced Robotic Systems*, 8:61–69, 2011.

[151] T. Salumäe and M. Kruusmaa. A flexible fin with bio-inspired stiffness profile and geometry. *Journal of Bionic Engineering*, 8:418–428, 2011.

[152] J. M. Anderson, K. Streitlien, D. S. Barrett, and M. S. Triantafyllou. Oscillating foils of high propulsive efficiency. *Journal of Fluid Mechanics*, 360:41–72, 1998.

[153] D. S. Barrett, M. S. Triantafyllou, D.K. Yue, M. A. Grosenbaugh, and M. J. Wolfgang. Drag reduction in fish-like locomotion. *Journal of Fluid Mechanics*, 392:183–212, 1999.

[154] F. S. Hover, O. Haugsdal, and M. S. Triantafyllou. Effect of angle of attache profiles in flapping foil propulsion. *Journal of Fluids and Structures*, 19:37–47, 2004.

[155] K. Parker, J. Soria, and K. D. Ellenrieder. Thrust measurements from a finite-span flapping wing. *AIAA Journal*, 45:58–70, 2007.

[156] K. Streitlien. On thrust estimates for flapping foils. *Journal of Fluids and Structures*, 12:47–55, 1998.

[157] Tianmiao Wang, Li Wen, Jianhong Liang, and Guanhao Wu. Fuzzy vorticity control of a biomimetic robotic fish using a flapping lunate tail. *Journal of Bionic Engineering*, 7:56–65, 2010.

[158] Silas Alben. Passive and active bodies in vortex-street wakes. *Journal of Fluid Mechanics*, 642:95–125, 2010.

[159] Zheng Ren and Kamran Mohseni. A model of lateral line of fish for vortex sensing. In *40th AIAA Fluid Dynamics conference, June 28th-July 1st*, 2010.

[160] Donald Rockwell. Vortex-body interactions. *Annual Review of Fluid Mechanics*, 30:199–229, 1998.

[161] Adrian Klein and Horst Bleckmann. Determination of object position, vortex shedding frequency and flow velocity using artificial lateral line canal. *Beilstein Journal of Nanotechnology*, 2:276–283, 2011.

[162] Yingchen Yang, Jack Chen, Jonathan Engel, Saunvit Pandya, Nannan Chen, Craig Tucker, Sheryl Coombs, Douglas L. Jones, and Chang Liu. Distant touch hydrodynamic imaging with an artificial lateral line. *Proceedings of the National Academny of Sciences of the Univted Staes of America*, 103:18891–18895, 2006.

[163] J. G. Peng and Z. Y. Zhou. Numerical simulation and experimental studies on a new type flow sensor. *Journal of Physics: International Symposium on Instrumentation Sceince and Technology*, 48:239–244, 2006.

[164] Yingchen Yang, Nam Nguyen, Nannan Chen, Michael Lockwood, Craig Tucker, Huan Hu, Horst Bleckmann, Chang Liu, and Douglas L. Jones. Artificial lateral line with biomimetic nneuromast to emulate fish sensing. *Bioinspiration and Biomimetics*, 5:1–9, 2010.

[165] A. Qualtieri, F. Rizzi, M. T. Todaro, A. Passaseo, R. Cingolani, and M. De Vittorio. Stress-drive ain cantilever-based flow sensor for fish lateral line system. *Microelectronic Engineering*, (doi:10.1016/j.mee.2011.02.091), 2011.

[166] Vicente I. Fernandez, Stephen M. Hou, Franz S. Hover, Jeffrey H. Lang, and Michael S. Triantafyllou. Lateral-line-inspired mems-array pressure sensing for passive underwater navigation. Technical report, Massachusetts Institute of Technology (MIT) (Sea Grant), 2007.

[167] Vicente I. Fernandez, Stephen M. Hou, Franz S Hover, Jeffrey H. Lang, and Michael S. Triantafyllou. Development and application of distributed mems pressure sensor array for auv object avoidance. Technical report, Massachusetts Institute of Technology (MIT) (Sea Grant), 2009.

[168] Evonik Industries. Vestosint data sheet.

[169] Matt Stegmeir and Tyson Strand. Introduction to piv. Webinar, March-April 2010.

[170] University of Bath Ethical Committee. Code of ethical practice for research/experimentation involving the use of animals., May 2007.

[171] T. Karasudani and M. Funakoshi. Evolution of a vortex street in the far wake of a cylinder. *Fluid Dynamics Research*, 14:331–352, 1994.

[172] Michio Nishioka and Hiroshi Sato. Measurements of velocity distributions in the wake of a circular cylinder at low reynolds numbers. *Journal of Fluid Mechanics*, 65:97–112, 1974.

[173] Yang-Moon Koh. Vorticity and viscous dissipation in an incompressible flow. *Korean Society of Mechanical Engineers Journal*, 8:35 – 42, 1994.

[174] C. H. K. Williamson. Vortes dynamics in the cylinder wake. *Annual Review of Fluid Mechanics*, 28:477–539, 1996.